Superfluid Vortices in Four Spatial Dimensions

by

Ben McCanna

A thesis submitted to the
University of Birmingham
for the degree of
DOCTOR OF PHILOSOPHY

School of Physics and Astronomy
College of Engineering and Physical Sciences
University of Birmingham
March 24, 2022

Abstract

Quantized vortices in two and three-dimensional superfluids have been studied as an important area of physics for many decades. These are topological defects forming points in 2D and lines in 3D about which the superfluid can circulate. Recent experimental developments in "synthetic dimensions" and other fields has led to broad interest in the quantum simulation of physical systems in higher dimensions, with a particular focus on topological phases such as quantum Hall systems. However, most theoretical works in 4D have focused on topological models without interactions. This has motivated us — via the analogy between rotating superfluids and the quantum Hall effect — to study the behaviour of hypothetical four-dimensional superfluids under rotation. In this thesis we begin to establish the basic phenomenology of vortices in rotating 4D superfluids, using a minimal 4D GPE model. We find that vortices in four dimensions form planes (or more generally surfaces), and that "double rotations" which arise in 4D can stabilise stationary states with orthogonal vortex planes intersecting at a point. Investigating this behaviour further, we find more general vortex stationary states based on intersecting skew planes which have cores composed of connected smoothly curved surfaces. These results suggest that vortices in four dimensional superfluids can lose their individual character, even in the absence of dynamics, which is a fascinating departure from the physics of vortices in lower dimensions. In future this work opens up many avenues of research, including the study of more experimentally relevant models, investigation of more complex topological defects in 4D, and the possibility of closed vortex surfaces.

Acknowledgements

My first and deepest thanks goes to my supervisor, Hannah Price. She has taught me about so much interesting physics and has made me feel part of a lively international research community these past few years. She also never ran out of patience or support for me, despite my best efforts.

Secondly, I would like to thank my secondary supervisor, Mike Gunn. Our conversations about research were infrequent, but they saved me from a lot of frustrating dead-ends. Plus he always had something interesting and completely unrelated to talk about!

Thank you to my Dad for proofreading this thesis so quickly and enthusiastically, as well as to Chris Oliver for reading over a particularly dense section. Thanks also to my whole family for always being there for me, and to all my PhD friends and former housemates for all the games and laughs we have shared.

Lastly, I want to thank Nach for so much love and support these past few years. Despite everything that has happened, in our lives and in the world, you have made me happier than I ever thought I could be.

แด่ณัช

Contents

Outline

This thesis is primarily composed of three chapters, the second and third of which are presented as publication-style papers. As first author of each of these papers I performed all the analytical and numerical calculations and was responsible for the majority of the writing. My supervisor, Hannah Price, advised me on the direction of the project and assisted with writing and editing the papers.

Chapter 1 is a review of the theoretical and experimental background to this thesis, as well as the motivations that inspired this work.

Chapter 2 details our initial original results and consists of the following published paper: B. McCanna and H. M. Price, "Superfluid vortices in four spatial dimensions," *Phys. Rev. Res.*, vol. 3, p. 023 105, 2021. DOI: 10.1103/PhysRevResearch.3.023105.

Between Chapters 2 and 3 we have an interlude discussing the connections between our initial results and the wider theoretical background that inspired this work 2.

Chapter 3 presents many further results, and consists of the following manuscript in preparation: B. McCanna and H. M. Price, "Skewed and curved vortex surfaces in stationary states of four dimensional superfluids," 2022, in preparation.

Lastly we have a conclusion summarising the work and discussing future research avenues.

Chapter 1

Background and Motivation

"Why do we tell stories? To try to make sense of a world that can be terrifying and enormous. I don't know that your story will long be known. I don't know who will remain to tell it, but it did happen — and it did matter."

Brennan Lee Mulligan, *Exandria Unlimited: Calamity*

In this introductory chapter, we will begin by reviewing the physics of vortices in two and three-dimensional superfluids, using the Gross Pitaevskii mean-field theory. Then, motivated by the equivalence between rotation and magnetic fields, we will discuss the quantum Hall effect in two and four dimensions, highlighting some similarities and differences between the two. Finally, we will discuss the experimental methods that can realise higher-dimensional physics, with a particular focus on "synthetic dimensions" as these have greatest potential to implement interacting topological 4D models.

Note also that as the bulk of this thesis is composed primarily of two scientific papers, extensive introductory material is also naturally included in later chapters. This includes further detailed reviews of the physics of quantum vortices in 2D and 3D superfluids; an in-depth discussion of rotations in 2D, 3D and 4D; an introduction of the 4D Gross-Pitaevskii equation; and further details about the numerical and analytical methods to be used in this thesis.

1.1 Vortices in Superfluids

Quantum superfluid vortices have long been studied as a classic example of a topological defect. This concept will be briefly explained later but for now we note that it is an inhomogeneity in a system that is extremely long lived and stable due to some associated topological invariance. This invariance arises in an ordered system with a continuous broken symmetry [3]. In superfluids this symmetry is the $U(1)$ symmetry associated with global quantum phase changes [4], and a simple description of this ordered phase is given by Gross Pitaevskii mean field theory, which we will now review.

1.1.1 The Gross-Pitaevskii Equation

Recall that the Schrodinger equation for any quantum system is given by $H|\Psi\rangle = i\hbar\partial_t|\Psi\rangle$, where H is the Hamiltonian and $|\Psi\rangle$ is the state vector, or wavefunction. We begin by considering this equation for a collection of N identical interacting bosons. In this case $|\Psi\rangle$ is a many-body state and the corresponding Hamiltonian is given by

$$H = \sum_{j=1}^{N}\left[-\frac{\hbar^2}{2m}\nabla_j^2 + V_{\text{ext}}(\boldsymbol{r}_j)\right] + \sum_{1\le j<k\le N} U(\boldsymbol{r}_j - \boldsymbol{r}_k), \tag{1.1}$$

where m is the mass of the bosonic particles, $\boldsymbol{r}_j$ is the position vector of the j-th boson, $V_{\text{ext}}(\boldsymbol{r})$ is an external potential, or "trap", and $U(\boldsymbol{r}_j - \boldsymbol{r}_k)$ is the interaction potential between the particles. For sufficiently weak (or vanishing) interactions this system forms a Bose-Einstein Condensate (BEC), meaning that a macroscopic number of bosons occupy the same single-particle state [5]. Furthermore, a weakly interacting BEC exhibits superfluidity: flow without any viscosity below a certain critical velocity [5].

A BEC can be described at the mean-field level by an *order parameter* $\psi(\boldsymbol{r}, t)$, a complex function which can roughly be thought of as the wavefunction of the macroscopically occupied state. Mathematically, this function is used as the single-particle factors in the

Hartree-Fock approximation of $|\Psi\rangle$, given by [5, 6]

$$\Psi(\boldsymbol{r}_1, \boldsymbol{r}_2, ..., \boldsymbol{r}_N, t) = \prod_{j=1}^{N} \left[\frac{1}{\sqrt{N}} \psi(\boldsymbol{r}_j, t) \right], \tag{1.2}$$

which essentially states that all the particles are in the same state, $\psi/\sqrt{N}$. In order for this approximation to work, we must also replace the interparticle interaction, $U(\boldsymbol{r}_j - \boldsymbol{r}_k)$, with a contact pseudopotential [6], $g\delta(\boldsymbol{r}_j - \boldsymbol{r}_k)$, where g is called the interaction strength. This parameter must be chosen so that the pseudopotential reproduces the s-wave scattering length of the original potential.

With these approximations in place we can calculate observables using ψ, rather than having to deal with the many-body wavefunction. In particular, we can compute the energy as the expectation value of H, given by $E = \langle \Psi | H | \Psi | \Psi | H | \Psi \rangle$. Ignoring terms of order which leads to the following functional of ψ

$$E[\psi] = \int_{SF} \left[\frac{-\hbar^2}{2m} |\nabla \psi|^2 + V_{\text{ext}} |\psi|^2 + \frac{g}{2} |\psi|^4 \right] \mathrm{d}^D r, \tag{1.3}$$

where SF denotes the entire superfluid under consideration, D is its dimensionality, and we have ignored terms of order $1/N$ or smaller.

We can use our mean-field state [Eq. (1.2)] as a variational ansatz for the ground state of H, simply by minimising the energy $E[\psi]$ with respect to ψ. However, we must also apply the constraint that the many body wavefunction is normalized, that is $\langle \Psi | \Psi | \Psi \rangle = 1$. This translates to the following normalization condition for the order parameter

$$N = N[\psi] \equiv \int_{SF} |\psi|^2 \mathrm{d}^D r, \tag{1.4}$$

which fixes the number of particles. This means that we should actually minimise the grand canonical energy $F[\psi] = E[\psi] - \mu N[\psi]$, where $\mu = \partial E / \partial N$ is the chemical potential which serves as a Lagrange multiplier enforcing the normalization condition. Setting the functional derivative $\delta F[\psi]/\delta \psi^*$ to zero gives us the time independent version of the well-

known Gross-Pitaevskii Equation (GPE) [5]:

$$-\frac{\hbar^2}{2m}\nabla^2\psi + V_{\text{ext}}\psi + g|\psi|^2\psi = \mu\psi. \tag{1.5}$$

Naturally, this equation has solutions which are constant in time. This equation is also known as the non-linear Schrödinger equation, since it resembles the Schrödinger equation but with an extra nonlinear term and with μ replacing the energy. We can also look at dynamics of the superfluid by retaining the time dependence in $\psi(\boldsymbol{r}, t)$ and minimizing the action

$$\mathcal{S}[\psi] = \int_{t_1}^{t_2} \left(E[\psi] - i\hbar \int_{SF} \psi^* \frac{\partial}{\partial t}\psi \mathrm{d}^D r \right) \mathrm{d}t, \tag{1.6}$$

over a time-interval spanning between times t_1 and t_2. This gives the time dependent version of the GPE [5]:

$$i\hbar\frac{\partial}{\partial t}\psi = \left[-\frac{\hbar^2}{2m}\nabla^2 + V_{\text{ext}}(\boldsymbol{r}) + g|\psi|^2 \right] \psi. \tag{1.7}$$

Comparing this to the time-independent version in Eq. (1.5), we see that stationary solutions of the GPE evolve according to $\psi(\boldsymbol{r}, t) = e^{-i\mu t/\hbar}\psi(\boldsymbol{r})$, with the chemical potential once again taking the role that energy plays in ordinary quantum mechanics.

We can define other physical parameters by de-dimensionalizing Eq. (1.5). If we let $r \to \xi r$, $\psi \to \sqrt{n}\psi$, and choose these scaling parameters to satisfy[1]

$$\frac{\hbar^2}{m\xi^2} = gn = \mu, \tag{1.8}$$

then we arrive at the following dimensionless equation for the stationary state

$$\left[-\frac{1}{2}\nabla^2 + \frac{1}{\mu}V_{\text{ext}}(\xi\boldsymbol{r}) + |\psi|^2 - 1 \right] \psi = 0. \tag{1.9}$$

[1]Note that many authors define the healing length with a 2 in the denominator of Eq (1.8).

All external parameters are now in the potential, which means that the homogeneous ($V_{\text{ext}}(\boldsymbol{r}) = 0$) superfluid is scale invariant; a change in any external parameter — such as m or g — simply amounts to a rescaling of the natural units, which are ξ, n, and μ. The new physical quantities defined by Eq. (1.8) are ξ, the *healing length*; and n, the background density of the homogeneous superfluid. In particular, the healing length is the scale over which ρ returns to the constant value n as you move away from a local depletion, provided the condensate is homogeneous at large distances. For example, if we take Eq. (1.9) in 1D with $V_{\text{ext}} = 0$ then the corresponding equation for $f(x) = |\psi(x)|$ is

$$\left[-\frac{1}{2}\frac{\partial^2}{\partial x^2} + f^2 - 1\right] f = 0, \tag{1.10}$$

assuming a constant phase. Imposing a hard wall boundary condition $f(0) = 0$ fixes the solution to $f(x) = \tanh(x)$. Back in dimensionful quantities, we have

$$\psi(x) = \sqrt{n}\tanh\left(\frac{x}{\xi}\right), \tag{1.11}$$

such that the superfluid heals away from a hard wall over a typical distance of ξ [5, 6].

1.1.2 Hydrodynamic equations

It can often be useful to recast the GPE in terms of the hydrodynamic equations, which are so-called because they bear a resemblance to the hydrodynamic theory of classical fluids. To see this, note that Eq. (1.4) allows us to identify $|\psi|^2$ with the density, $\rho(\boldsymbol{r}, t)$, of the superfluid, which motivates the so-called Madelung transformation of the order parameter: $\psi = \sqrt{\rho}\,\mathrm{e}^{iS}$, where $S(\boldsymbol{r}, t)$ is the phase of the superfluid. Substituting this form into the time-dependent GPE (1.7) gives a complex equation that can be separated into the following two real equations:

$$\frac{\partial \rho}{\partial t} + \frac{\hbar}{m}\nabla \cdot (\rho \nabla S) = 0, \tag{1.12}$$

and

$$\hbar\frac{\partial S}{\partial t}+\frac{\hbar}{2m}|\nabla S|^2+g\rho+V_{\text{ext}}-\frac{\hbar^2}{2m\sqrt{\rho}}\nabla^2\sqrt{\rho}=0. \tag{1.13}$$

The first of these is a continuity equation, ensuring that the number of particles in a closed system is conserved. The divergence term therefore defines a particle current $\boldsymbol{j}=\rho\boldsymbol{v}$, with a corresponding velocity field $\boldsymbol{v}=\hbar\nabla S/m$ for the superfluid. Taking the gradient of Eq. (1.13) then gives us the following hydrodynamic equation for $\boldsymbol{v}$

$$m\frac{\partial \boldsymbol{v}}{\partial t}+\nabla\left(\frac{1}{2}mv^2+g\rho+V_{\text{ext}}-\frac{\hbar^2}{2m\sqrt{\rho}}\nabla^2\sqrt{\rho}\right)=\boldsymbol{0}. \tag{1.14}$$

The energy [Eq. (1.3)] can also be rewritten in terms of these hydrodynamic variables as

$$E=\int_{SF}\left[\frac{1}{2}m\rho v^2+V_{\text{ext}}\rho+\frac{1}{2}g\rho^2+\frac{\hbar^2}{2m}|\nabla\sqrt{\rho}|^2\right]\mathrm{d}^D r. \tag{1.15}$$

If we ignore the final terms in Eqs. (1.14) and (1.15) (which are known as the "quantum pressure") then these equations plus the continuity equation, $\partial_t\rho+\nabla\cdot(\rho\boldsymbol{v})=0$, describe an inviscid classical fluid with pressure equal to $g\rho^2/2$, and no explicit dependence on $\hbar$. This approximation holds when the density is varying slowly over the scale of the healing length, such as when the trap takes many healing lengths to reach the energy scale of the chemical potential, or if there is no external potential and the system is large compared to the healing length [5].

1.1.3 Rotation of a superfluid

Even in the "classical" limit where ρ is constant, superfluidity can be peculiar. The definition of the velocity field as $\boldsymbol{v}\propto\nabla S$ ensures that superfluid flow is irrotational, due to the identity $\nabla\wedge\nabla S=\boldsymbol{0}$ [5, 6]. This holds as long as the second order mixed partial derivatives of S — corresponding to $\partial_x v_y$, for example — are continuous (Clairaut's theorem). Applying Stokes' theorem to a region A of superfluid then gives that the

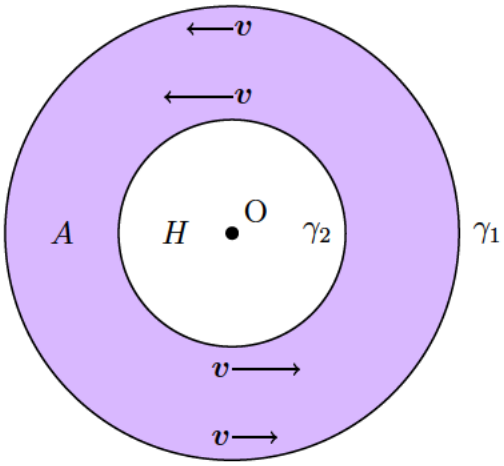

Figure 1.1: Superfluids can rotate with discrete values of angular momentum in a multiply connected domain such as the region A shown here, which has boundaries denoted by $\gamma_{1,2}$ and which encloses a central hole H. When the system is rotated around an axis through the origin (at the center of the hole), the velocity field $\boldsymbol{v}$ inside the superfluid region must increase towards the origin, as indicated here by the length of the solid arrows.

circulation of fluid along the boundary ∂A vanishes

$$\oint_{\partial A} \boldsymbol{v} \cdot \mathrm{d}\boldsymbol{l} = \int_A \nabla \wedge \boldsymbol{v} \cdot \mathrm{d}\boldsymbol{S} = 0. \tag{1.16}$$

However, this constraint does not always prevent circulation of a superfluid. Consider the 2D region A in Fig. 1.1. This domain is not *simply connected*: loops that enclose the central hole H (such as the boundaries $\gamma_{1,2}$) cannot be contracted to a point in A. This also means that the boundary ∂A is the disjoint union $\gamma_1 \cup \gamma_2$ and Eq. (1.16) becomes

$$\oint_{\gamma_1} \boldsymbol{v} \cdot \mathrm{d}\boldsymbol{l} - \oint_{\gamma_2} \boldsymbol{v} \cdot \mathrm{d}\boldsymbol{l} = 0, \tag{1.17}$$

where the minus sign comes from the opposite orientation of the two curves. The flow is therefore curl-free provided the circulation — which need not vanish — is equal around both boundaries.

Note that we did not require A to be the entire superfluid, or for it to have a circular boundary, so the circulation in fact takes the same value around any loop that encloses H. This value is proportional to the change in phase around such a loop, which can be

seen by substituting the definition of $\boldsymbol{v}$ into Eq. (1.16), giving [5, 7]

$$\oint_\gamma \boldsymbol{v} \cdot \mathrm{d}\boldsymbol{l} = \oint_\gamma \frac{\hbar}{m} \nabla S \cdot \mathrm{d}\boldsymbol{l} = \frac{\hbar}{m} \left[\Delta S\right]_\gamma . \tag{1.18}$$

This quantity does not necessarily vanish since there is no requirement for S to be single-valued. However, the order parameter, $\psi = \sqrt{\rho} e^{iS}$, must be single valued, which means that any discontinuities in S must come in integer multiples of 2π. Therefore the circulation of a superfluid is quantized in integer multiples of h/m.

This has interesting consequences for the velocity field; γ_2 must be shorter than γ_1, so the velocity has to decrease with distance from the hole in order to maintain the same circulation. If we assume circular symmetry and a velocity field that is everywhere tangent to the concentric circles of A then Eqs. (1.17) and (1.18) gives us a velocity field and associated phase profile of

$$v = k \frac{\hbar}{mr}, \quad S = k\theta \tag{1.19}$$

where (r, θ) are polar coordinates with respect to O, the centre of H, and the integer k is called the *winding number* [4], as it counts how many times the phase winds around the unit circle for one loop H. The winding number is a *topological invariant*: it cannot be changed by a continuous deformation of the order parameter [3]. Intuitively speaking this is guaranteed by the quantization of k, as there is no continuous way to change one integer into another. Note that there is a deeper way to think about topological invariants that finds use in many areas of mathematics and physics. This is called *homotopy theory* [3, 8, 9], which we briefly outline for the interested reader in Appendix B.

Now, to introduce the concept of a vortex, we consider continuously shrinking the hole H to its centre point O. Since k remains fixed the inner velocity on γ_2 must increase without bound as this curve approaches O [c.f. Eq. (1.19)]. Correspondingly, the phase profile [Eq. (1.19)] approaches a branch point singularity at O as the rest of H becomes "filled in". Focusing on this limit, we analyze the *hydrodynamic* energy of the fluid: the

first term of Eq. (1.15), corresponding to the kinetic energy of the flow. Using Eq. (1.19) for the circular velocity field gives

$$E_h = \pi k^2 \frac{\hbar^2}{m} \int \frac{\rho(r)}{r} \mathrm{d}r. \tag{1.20}$$

Note that the independence of ρ from θ follows from the continuity equation using the fact that $\nabla \cdot \boldsymbol{v} = 0$, and the assumption $\partial_t \rho = 0$. This energy integral has a divergent contribution from the neighbourhood of O unless $\rho \to 0$ as $r \to 0$. We can quantify this decay more precisely as follows: using Eq. (1.19) for the velocity field in Eq. (1.14) we find a $1/r^2$ singularity in the kinetic term $(mv^2/2)$. This can only be cancelled by the quantum pressure. Asymptotic balance of these two terms gives

$$\frac{k^2}{r^2} \sim \frac{1}{r\sqrt{\rho}} \frac{d}{dr} \left(r \frac{d}{dr} \sqrt{\rho} \right) \quad \text{as } r \to 0, \tag{1.21}$$

where $f(x) \sim g(x)$ as $x \to x_0$ means that $\lim_{x \to x_0} f(x)/g(x) = 1$. Assuming a power law decay, $\sqrt{\rho} \propto r^m$, we obtain that $m = k$, the winding number. What we have just found is the well-known density profile in the vicinity of a *vortex* core [5, 6], with Eq. (1.19) describing the circular flow and phase winding around the core.

1.1.4 Quantum vortices

As we just discovered, quantum vortices are small holes in a superfluid or superconductor about which the phase winds and the fluid circulates [5–7]. They are a type of *topological defect*, which is a region of an ordered system where the order is lost and cannot continuously be restored due to an associated topological invariant [3]. For quantum vortices this invariant is the winding number. Other examples of topological defects include optical vortices [10], dislocations in crystals [3] and disclinations in liquid crystals [11].

The previous section described how single-component (i.e. spinless) quantum fluids can be described by a complex scalar order parameter, which vanishes at a vortex core. Setting both the real and imaginary parts to zero defines regions of *codimension* 2, mean-

ing that vortex cores occupy $D-2$ dimensional subregions of a D dimensional condensate. Intuitively this makes sense, as there should be two linearly independent vectors orthogonal to the vortex at every point along the core to define the local plane of rotation.

In two dimensions, the full (dimensionless) density profile of a point vortex is found by substituting the ansatz $\psi_k(r,\theta) = f_k(r)\,\mathrm{e}^{ik\theta}$ into Eq. (1.9), assuming circular symmetry and no external potential ($V_{\text{ext}} = 0$), with $f_k(r)$ being a real function. This leads to the following equation

$$\left[-\frac{1}{2r}\frac{\partial}{\partial r}r\frac{\partial}{\partial r} + \frac{k^2}{2r^2} + f_k^2 - 1\right] f_k = 0, \tag{1.22}$$

with boundary conditions $f_k(0) = 0$, and $f_k(r) \to 1$ as $r \to \infty$. We have already dealt with the first limit and concluded that $f_k(r) \propto r^{|k|}$ as $r \to 0$. The second condition states that the superfluid density eventually returns to the homogeneous value, or that the presence of the vortex should become unnoticeable far away from the core. Note that Eq. (1.22) describes not only a point vortex in 2D, but a single-vortex profile in any number of dimensions with the symmetries we assumed earlier in calculating the vortex energy. Solving this equation in general requires numerical methods; in Appendix A we outline a standard method based on imaginary time evolution [12], which is used for numerical results throughout this thesis. The result of such a calculation is shown in Fig. 1.2 where we plot the numerically obtained function $f_1(r)$ for a vortex with winding number $k = 1$, as a function of the distance from the vortex core.

We can find the hydrodynamic energy of a single vortex in a homogeneous superfluid in arbitrary dimensions provided we assume certain symmetries. Let the order parameter be independent of the directions parallel to the vortex core, and let $\boldsymbol{v}$ be given by the circular flow in Eq. (1.19). This corresponds to, for example, a straight vortex line in an otherwise uniform 3D condensate. From this point on in the text we shall refer to a configuration satisfying both of these conditions as a *flat* vortex, since it generalises a straight vortex line to arbitrary dimensions.

Using r and θ for the polar coordinates in the plane of rotation orthogonal to the

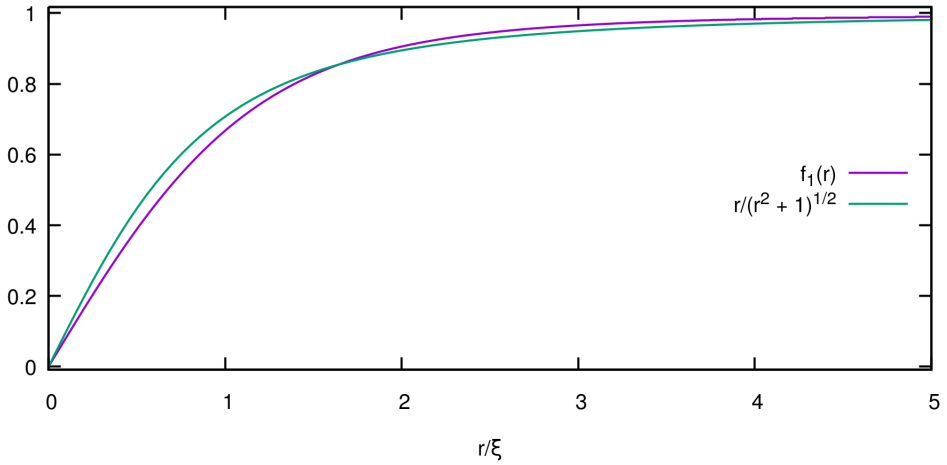

Figure 1.2: Numerical solution (purple), and a variational approximation (green), of the modulus of a 2D vortex order parameter (with winding number $k = 1$) as a function of the distance r from the vortex core. As can be seen, the profile goes smoothly to zero at the origin, and approaches the constant background density (which is equal to one in these dimensionless units) at large distances.

vortex core, we have

$$E_{\mathrm{h}} = k^2 V \frac{\hbar^2}{mR^2} \int_0^R \frac{\rho(r)}{r} \mathrm{d}r, \tag{1.23}$$

where V is the volume of the superfluid, and R is its radius in the rotating plane. This is just Eq. (1.20) with a different prefactor to correct for dimensionality. We will approximate the density as a constant n outside some core radius r_c, where $\xi \ll r_c \ll R$. This allows us to split Eq. (1.23) into two parts: the small core energy,

$$E_{\mathrm{core}} = k^2 \mu N \frac{\xi^2}{R^2} \int_0^{r_c} \frac{\rho(r)}{n} \frac{dr}{r}, \tag{1.24}$$

and the kinetic energy induced in the entire fluid

$$E_{\mathrm{kin}} = k^2 \mu N \frac{\xi^2}{R^2} \ln\left(\frac{R}{r_c}\right). \tag{1.25}$$

Here, we have reintroduced the chemical potential $\mu = \hbar^2/m\xi^2$, and particle number $N = nV$ of the homogeneous state since these are equal to those of the vortex state up to small corrections [5]. We can compare these energies using a variational approximation

to the density profile. For a vortex with winding number $k = 1$, such a variational approximation yields $\rho(r) \approx nr^2/(r^2 + \xi^2)$, the square root of which is shown in Fig. 1.2 to bear good agreement to the numerical solution for $f_1(r)$. From this, we then obtain

$$\frac{E_{\text{core}}}{E_{\text{kin}}} \approx \frac{\ln\left(\frac{r_c^2}{\xi^2} + 1\right)}{2\ln\left(\frac{R}{r_c}\right)}. \tag{1.26}$$

Since $\ln(1 + x^2) \sim 2\ln(x)$ as $x \to \infty$, we therefore require that $R/r_c \gg r_c/\xi$ in order to ignore the core energy in favour of the fluid kinetic energy. A more careful analysis [5] using the numerical solution to Eq. (1.22), gives the total energy difference between the state with a single vortex of charge k and the uniform state with equal N as

$$E_k(R) = k^2 \mu N \left(\frac{\xi}{R}\right)^2 \ln\left(2.06\frac{R}{\xi}\right). \tag{1.27}$$

Vortices are therefore energetically unfavourable unless some rotational force is applied to the superfluid. In such a rotating frame the energy is reduced by an amount $\boldsymbol{\Omega} \cdot \boldsymbol{L}$, where $\boldsymbol{\Omega}$ is the oriented frequency of rotation, and $\boldsymbol{L}$ is the angular momentum of the superfluid given by

$$\boldsymbol{L} = \int_{SF} m\rho \boldsymbol{r} \wedge \boldsymbol{v} \mathrm{d}^3 r. \tag{1.28}$$

For a flat vortex of winding k, the angular momentum is $L = Nk\hbar$ and is directed in the plane orthogonal to the vortex core. The vortex energy in the rotating frame is therefore given by $E_k(R) - Nk\hbar\Omega$; setting this to zero gives the *critical frequency* at which a single vortex becomes the ground state as

$$\Omega(R) = \frac{E_k(R)}{Nk\hbar} = k\frac{\hbar}{mR^2}\ln\left(2.06\frac{R}{\xi}\right). \tag{1.29}$$

Similarly, we can look at the energy of multi-vortex configurations, under the assumption that the phase is additive. Consider two flat parallel vortex lines in a 3D superfluid separated by a distance d in the rotation plane. Let S_j be the phase profile associated

with each vortex, where $j = 1$ or 2, and the corresponding velocity fields be $\boldsymbol{v}_j = \hbar\nabla S_j/m$. The total phase profile is simply $S = S_1 + S_2$, therefore the velocity fields add together, and we obtain the hydrodynamic energy as

$$E_{\mathrm{h}} = \int_{SF} \frac{1}{2} m\rho(\boldsymbol{v}_1 + \boldsymbol{v}_2)^2 \mathrm{d}^3 r = E_1 + E_2 + E_{\mathrm{int}}, \tag{1.30}$$

where E_j is the individual energy of vortex j, and the vortex-vortex interaction energy E_{int} is given by

$$E_{\mathrm{int}} = \int_{SF} m\rho \boldsymbol{v}_1 \cdot \boldsymbol{v}_2 \mathrm{d}^3 r. \tag{1.31}$$

We will calculate this hydrodynamic interaction using essentially the same argument as in [3]. We begin by factoring out any constants and performing the integral out of the rotation plane, since ψ is independent of this direction, resulting in

$$E_{\mathrm{int}} = \frac{\hbar^2 V}{m\pi R^2} \int_P \rho\nabla S_1 \cdot \nabla S_2 \mathrm{d}^2 r, \tag{1.32}$$

where the remaining integral is over the common plane of rotation, denoted by P. Let us define two polar coordinate systems (r_j, θ_j) centred on each of the vortices, as in Fig. 1.3, such that $S_j = k_j\theta_j$. We will also define a branch cut, denoted by Σ, in the definition of θ_1, in order to make θ_1 — and hence S_1 — single-valued. The two sides of the cut we will denote $\Sigma_\pm$, and we will take the cut in the negative x direction such that $\theta_1 = \pm\pi$ on $\Sigma_\pm$, as shown in Fig 1.3.

Now that S_1 is single-valued will can integration by parts to write

$$\int_P \rho\nabla S_1 \cdot \nabla S_2 \mathrm{d}^2 r = \int_\Sigma S_1 \left(\rho\nabla S_2\right) \cdot \mathrm{d}\boldsymbol{\Sigma} - \int_P S_1 \nabla \cdot \left(\rho\nabla S_2\right) \mathrm{d}^2 r, \tag{1.33}$$

where the first term is a boundary integral over the two sides of the branch cut Σ. We can further simplify things by excluding a region around each vortex core from the integral. This is the same trick we used before: introducing a core radius r_c between the scales of ξ

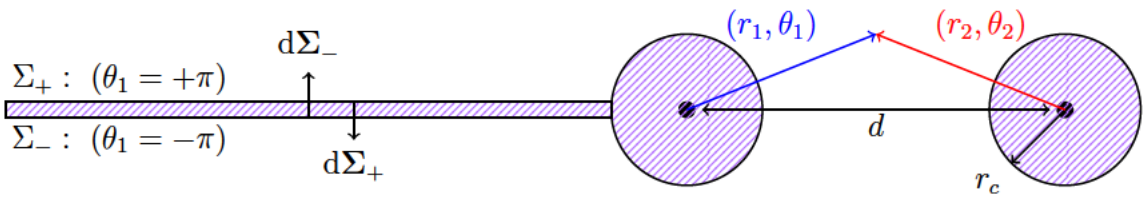

Figure 1.3: Two parallel flat vortex lines shown as a cross-section along their common plane of rotation. The vortex cores are indicated by black dots and are separated by a distance d. The annotated red and blue lines indicate the two polar coordinate systems $((r_j, \theta_j))$ defined with respect to each vortex core. We have to introduce a branch cut, $\Sigma_+ \cup \Sigma_-$, to define a single-valued phase S_1, of one of the vortices. The regions shaded in pink are the vortex cores $(r_j < r_c)$, and the branch cut, which are both excluded from the interaction energy integral. The line elements perpendicular to either side of the branch cut are denoted by $\mathrm{d}\boldsymbol{\Sigma}_\pm$. Note that the width of the branch cut can be arbitrarily small, whereas we require $r_c \gg \xi$ to use the homogeneous approximation. Adapted from Fig. 9.3.1 in Ref. [3].

and the condensate radius R. We can then approximate ρ with its homogeneous value n outside these excluded regions shown in Fig 1.3, and use the fact that for these circularly symmetric phase profiles, we have $\nabla^2 S_i = 0$ to remove the second term[2]. Eq. (1.33) now becomes

$$\int_P \rho \nabla S_1 \cdot \nabla S_2 \mathrm{d}^2 r \approx n \int_{\tilde{\Sigma}} S_1 \nabla S_2 \cdot \mathrm{d}\boldsymbol{\Sigma}, \tag{1.34}$$

where $\tilde{\Sigma}$ denotes the part of the branch cut that lies outside the excluded vortex core [c.f. Fig 1.3]. Note that at this point the calculation is now approximate, due to our treatment of the vortex core and the density profile.

We now simply have the integral over the branch cut $\tilde{\Sigma} = \tilde{\Sigma}_+ \cup \tilde{\Sigma}_-$, given by

$$\int_{\tilde{\Sigma}} S_1 \nabla S_2 \cdot \mathrm{d}\boldsymbol{\Sigma} = \int_{\tilde{\Sigma}_+} S_1 \nabla S_2 \cdot \mathrm{d}\boldsymbol{\Sigma}_+ + \int_{\tilde{\Sigma}_-} S_1 \nabla S_2 \cdot \mathrm{d}\boldsymbol{\Sigma}_- \tag{1.35}$$

By definition, along each of the lines $\tilde{\Sigma}_\pm$ the phase S_1 takes the values $S_1 = \pm k_1 \pi$, respectively, so we may substitute these values into the above to obtain the hydrodynamic

[2] This more generally follows from the continuity equation if ρ is constant [3]

interaction as

$$E_{\text{int}} \approx nVk_1\frac{\hbar^2}{mR^2}\left(\int_{\tilde{\Sigma}_+}\nabla S_2\cdot \mathrm{d}\boldsymbol{\Sigma}_+ - \int_{\tilde{\Sigma}_-}\nabla S_2\cdot \mathrm{d}\boldsymbol{\Sigma}_-\right) \tag{1.36}$$

If we perform these integrals in the (r_2, θ_2) coordinate system then the perpendicular line elements take the form $\mathrm{d}\boldsymbol{\Sigma}_\pm = \pm\hat{\boldsymbol{\theta}}_2\mathrm{d}r_2$, so using $\nabla S_2 = \frac{k_2}{r_2}\hat{\boldsymbol{\theta}}_2$ we have

$$E_{\text{int}} \approx 2nVk_1k_2\frac{\hbar^2}{mR^2}\int_{d+r_c}^{R}\frac{\mathrm{d}r_2}{r_2}, \tag{1.37}$$

where we recall that d is the separation of vortex cores. Now, provided that this separation is much larger than the core size, i.e. $d \gg r_c$, then to leading order our final result is given by [3, 5, 6]

$$E_{\text{int}} \approx 2k_1k_2\mu N\left(\frac{\xi}{R}\right)^2\ln\left(\frac{R}{d}\right), \tag{1.38}$$

where again we have rewritten in terms of the chemical potential μ and particle number N. We can use this expression and Eq. (1.27) for the single-vortex energy to rewrite the total energy of a pair of vortices as

$$E_{\text{h}} = \mu N\left(\frac{\xi}{R}\right)^2\left[(k_1+k_2)^2\ln\left(\frac{R}{r_c}\right) - 2k_1k_2\ln\left(\frac{d}{r_c}\right)\right]. \tag{1.39}$$

There are two very important things to note about this. One is that if $k_2 = -k_1$ then the energy has no logarithmic divergence with system size [3, 5]. This is because at large distances the velocity fields of such a vortex-antivortex pair cancel, and so the kinetic energy of the flow is finite. The second conclusion we can draw is that if $k_1 = k_2 = 1$ the first term is the energy of a single vortex of winding number 2, and the second term is negative if $d > \xi/2.06$. This means that multiple singly charged vortices are always energetically preferred to multiply charged vortices. Therefore, when rotated at a frequency above the critical frequency (Eq. (1.29)) for multiply charged vortices, a system will typically prefer to host an appropriate number of $k = 1$ vortices rather than

a corresponding smaller number of vortices with higher winding numbers. In the limit of large rotation, this leads to an Abrikosov [13] (triangular) lattice of vortices, which has been observed in various experiments with ultracold atoms [14–16].

1.1.5 Rotation as an artificial magnetic field

So far in this section we have shown how rotation of a 2D or 3D superfluid can stabilise vortices, and in the later chapters of this thesis we will present original work investigating vortices in a hypothetical 4D superfluid undergoing rotation. While the model we use is far from experimental applicability (as discussed further in Chapters 2 and 3), our work is ultimately motivated by the prospect of realising 4D physics in the lab using "synthetic dimensions", an idea which we will briefly explore in Sec. 1.3. However, it turns out that it makes little sense to talk about physically rotating a plane that includes a synthetic dimension, although this is not an issue thanks to another idea known as "synthetic" or "artificial" gauge fields [17–23].

In the context of synthetic dimensions, this idea will be explained in more detail in Sec. 1.3, but for now it suffices to say that it is often possible — and sometimes quite simple — to implement something that is equivalent to a magnetic field within a synthetic dimension scheme, even if the constituent particles, such as ultracold atoms, are electrically neutral. This idea is also commonly applied to trapped ultracold atoms in real space, allowing experiments to stabilise vortices in these systems using an artificial gauge field [17, 24, 25]. Here we will give a brief review of the equivalence between rotation and magnetic fields, to motivate our study of rotating 4D superfluids.

While it is true that magnetic fields classically cause circular orbits, it is not immediately obvious that this is related to a system which is physically rotating. However, as we shall now briefly review, it can be shown that the Coriolis force in a rotating reference frame is in fact mathematically equivalent to the Lorentz force from a magnetic field [26]. To see this, consider the Hamiltonian of a particle in a potential $V(\boldsymbol{r})$ and in a frame

rotating with angular frequency Ω in the x–y plane, given by

$$H = -\frac{1}{2m}\boldsymbol{p}^2 + V(\boldsymbol{r}) - \Omega\left(xp_y - yp_x\right), \tag{1.40}$$

where the first term is the usual kinetic energy, the second term is the potential energy, and the third term is the reduction in energy in the rotating frame due to the angular momentum term $\boldsymbol{\Omega}\cdot\boldsymbol{L}$ introduced above, which here simplifies to $\Omega L_{xy} \equiv \Omega(xp_y - yp_x)$.

This can be rewritten as follows [26]

$$H = -\frac{1}{2m}\left[\boldsymbol{p} - m\Omega\left(x\hat{\boldsymbol{y}} - y\hat{\boldsymbol{x}}\right)\right]^2 + V(\boldsymbol{r}) - \frac{1}{2}m\Omega^2\left(x^2 + y^2\right), \tag{1.41}$$

where $\hat{\boldsymbol{x}}$ and $\hat{\boldsymbol{y}}$ are unit vectors in the x and y directions, respectively. The Hamiltonian is now suspiciously familiar: the first term, which includes the Coriolis force, can be thought of as a free particle of charge q_{eff} in a uniform magnetic field of strength $B_{\textbf{eff}}$, where $q_{\text{eff}}B_{\text{eff}} = 2m\Omega$. The last term, which generates the centrifugal force, can be thought of as an upturned harmonic oscillator potential, which is not related to a magnetic field. Instead this can be viewed simply as a modification of the potential $V(\boldsymbol{r})$. For this reason we can consider rotation and magnetic fields to be equivalent. We will therefore spend the next section exploring the quantum mechanics of a charged particle in a magnetic field.

1.2 The Quantum Hall Effect

In this section, we will review how particles moving in magnetic fields can lead to the so-called 2D and 4D quantum Hall effects. Ongoing research interest in these phenomena is a part of the underlying motivation behind this thesis; however, many of the details behind these effects (such as their associated topological energy-band invariants) will not be important in our work, and so we keep this discussion brief.

1.2.1 The 2D Quantum Hall Effect

In 1980, von Klitzing et. al. [27] discovered that a 2D electron gas (2DEG) subjected to low temperatures and a strong perpendicular magnetic field exhibits exact quantization of the Hall conductance. This quantity determines the linear response of the current in one direction of a 2DEG when an electric field is applied in the perpendicular direction within the 2D plane, and a magnetic field is applied out of the plane. The discovered quantization of the Hall conductance, now known as the 2D quantum Hall effect (QHE), can be expressed as the following linear response equation [28]

$$j^{\mu} = \frac{e^2}{h} C_1 \varepsilon^{\mu\nu} E_{\nu}, \tag{1.42}$$

where C_1 is an integer that depends on the applied magnetic field strength, j^{μ} is the current density, E_{ν} is the applied electric field, μ and ν run over the Cartesian axes x and y within the 2D plane, and $\varepsilon^{\mu\nu}$ is the 2D Levi-Civita symbol. An idealised model of this system (in the absence of the electric field) is given by the 2D Hamiltonian for a free spinless particle of charge e in a magnetic field [29]

$$H = \frac{1}{2m} \left(\hat{\boldsymbol{p}} - e\boldsymbol{A} \right)^2, \tag{1.43}$$

where $\boldsymbol{A}$ is the electromagnetic vector potential. This simple model predicts a set of equally spaced and highly degenerate energy levels, known as Landau levels, with energies given by $E = \hbar(eB/m)(n + 1/2)$, where B is the magnetic field strength, and n is the integer Landau level index. The degeneracy of these levels is then indexed by the angular momentum quantum number m, in the plane of the field [29, 30], which can in turn be related to the coordinates of the centres of the semiclassical cyclotron orbits [30]. In a system of area A, the number of degenerate energy levels for each value of n is approximately $eBA/2\pi\hbar$, which is equal to the magnetic flux threading the system in units of the flux quantum h/e [29, 30].

Another model for a 2DEG, which takes into account the effects of a lattice, is the Harper-Hofstadter model. First studied by Harper in 1955 [31], this is the tight-binding model of charged spinless non-interacting particles on a 2D square lattice, with a magnetic field applied out of the plane. The Hamiltonian, in second quantized form in the Landau gauge, is given by [28]

$$H = -J \sum_{x,y} \left(a^\dagger_{x+1,y} a_{x,y} + e^{2\pi i \Phi x} a^\dagger_{x,y+1} a_{x,y} + \text{h.c.} \right), \tag{1.44}$$

where Φ is the magnetic flux per plaquette of the lattice, J is the hopping strength, h.c. denotes the Hermitian conjugate and $a^\dagger_{x,y}$, a_{xy} are the creation and annihilation operators for a particle at the lattice site with coordinates (x, y). Hofstadter studied this model in further detail in 1976 [32], and showed that the energy spectrum as a function of Φ has an unexpected and beautiful fractal structure — now known as Hofstadter's butterfly — resulting from the commensurability or incommensurability of the magnetic unit cell with the lattice. In the limit that the flux per plaquette goes to zero, this model recovers the continuum limit of Landau levels. Note that in this thesis we will always consider a continuum model, leaving the inclusion of a lattice to future work.

Using the Harper-Hofstadter model, Thouless et. al. [33] in 1982 were able to calculate the Hall response [Eq. (1.42)] and explain its precise quantization by showing that the integer C_1 is a *topological invariant*, called the first Chern number, here summed over the set of occupied states when the Fermi level lies in a gap. In a simple two-band model, C_1 concretely counts how many times the occupied eigenstates wind over the Bloch sphere as momentum sweeps out the 2D Brillouin zone [30], which is topologically a torus.

Physically, the topological invariance of C_1 means that it can only change when the gap closes and reopens. This closing and reopening process can occur as the magnetic field B is increased, and can be theoretically understood by fixing a Fermi energy and then studying the evolution of the Hofstadter's butterfly spectrum as the magnetic flux increases. Alternatively, one can do the same thing in the continuum limit by looking at

the Landau levels, whose spacing is proportional to B. In either case, the closing and reopening of the gap occurs when an energy level passes through the Fermi energy. As each energy level in these models can be labelled by a non-zero value of the Chern number, the change in the number of occupied states corresponds to the experimentally observed jumps in the Hall response.

The topological invariance of the Hall effect makes it incredibly robust against disorder, and indeed any variation of the Hamiltonian that does not close the gap. This makes the measured response [Eq. (1.42)] independent of many material parameters, allowing a very precise and universal way to measure the fundamental quantum of conductance e^2/h which in turn has been used to redefine the kilogram [34]. Quantum Hall systems were also the first discovered topological phase of matter, which has grown into an extensive and cutting edge field of modern physics [28]. While topological phases already exhibit unconventional phenomena at the single-particle level, even more exotic physics has been demonstrated in the presence of strong interactions. These interactions, combined with the non-trivial topology of the electron states, leads to the fractional quantum Hall effect when the Fermi energy lies within one of these highly degenerate bands [35]. Fractional quantum Hall states are strongly correlated phases characterized by quasiparticles with fractional electric charge and anyonic (neither bosonic nor fermionic) exchange statistics, leading to Hall conductivity plateaus at fractional values of e^2/h [35].

Finally, note that the QHE is not limited to electrons in magnetic fields, nor to solid state systems, or even charged particles. It was shown by Haldane in 1988 [36] that an applied magnetic field is not necessary for the 2D QHE, but that instead what is required is that time reversal symmetry is broken. There are a multitude of ways to break this symmetry in experiments, many of which are equivalent to an external magnetic field. Firstly, as we mentioned in Sec. 1.1.4, rotation of a system can effectively mimic a magnetic field for neutral particles [26], which is a technique that is frequently used to stabilise vortices in cold bosonic gases. Secondly, there are now many methods to generate artificial gauge fields for neutral atoms in a trap [17, 21, 37] or an optical lattice [19, 21,

38–41], or using various "synthetic dimension" schemes [20] which will be discussed in Sec. 1.3. These synthetic dimension techniques are also one way in which experiments may realise 4D phenomena of the kind that is presented in this thesis. As part of the broader context of our work, we will therefore now briefly discuss the 4D QHE.

1.2.2 The 4D Quantum Hall Effect

A great deal of theoretical work has gone into classifying topological phases of matter, such that we now have a complete classification, e.g. for gapped systems of non-interacting fermions [42, 43]. What has become especially clear from this is that the existence and nature of topological phases depends on the dimensionality of the system considered. In particular, it has been shown that every even dimensional space has its own quantum Hall effect, meaning that we can talk about the 4D QHE, 6D QHE, 8D QHE and so on [28]. Here we will discuss the simplest version of the 4D QHE (corresponding to the Abelian 4D QHE). In fact, this served as the original motivation and inspiration for the work presented in this thesis, as in a sense, by studying vortices in 4D rotating superfluids, we are investigating whether new and interesting physics can emerge from adding weak interactions to a version of this 4D topological model.

Importantly, in four dimensions, the magnetic field can no longer be considered a vector. This is because magnetic fields are fundamentally associated with rotation in 2D planes; the only reason we can describe them with a vector in 3D is that there is a unique axis normal to any plane in $\mathbb{R}^3$. In 4D, the normal to any plane is another plane, and so this trick fails. Instead, one can define a magnetic field in any number of dimensions as an antisymmetric 2-tensor, with components given by $B_{ij} = \partial_i A_j - \partial_j A_i$. Now let us consider a 4D magnetic field applied through two completely independent planes simultaneously, that is, such that the only nonzero components are B_{xz} and B_{yw}. It is then impossible to define this field with just a single component, regardless of the basis used. This is something that cannot occur in 3D or below, and this underpins the Abelian 4D QHE. Note that equivalent arguments apply to the angular momentum

operator in higher dimensions, and it is for this reason that we have chosen to study 4D superfluids undergoing so-called "double rotation", which are rotations that occur through two completely independent orthogonal planes (e.g. x–y and z–w) at once; these concepts will be introduced in more detail in Chapter 2.

Similar to 2D, we can write down a continuum model of a 4DEG under magnetic fields in both the xz and yw planes using the Hamiltonian $H = H^{LL}_{xz}(B_{xz}) + H^{LL}_{yw}(B_{yw})$, where $H^{LL}_{jk}(B)$ is the 2D Landau level Hamiltonian [Eq (1.42)] in the j–k plane with field strength B. The spectrum of this simple 4D model is just a sum of the 2D spectra, given by

$$E = \hbar(eB_{xz}/m)(n_{xz} + 1/2) + \hbar(eB_{yw}/m)(n_{yw} + 1/2), \tag{1.45}$$

where n_{xy}, and n_{zw} are independent Landau level indices in the two planes.

Similarly, we can include a lattice by writing a 4D Harper-Hofstadter Hamiltonian as a sum of 2D versions as follows: $H = H^{HH}_{xz}(\Phi_{xz}) + H^{HH}_{yw}(\Phi_{yw})$, where $H^{HH}_{jk}(\Phi)$ is the 2D Harper-Hofstadter Hamiltonian [Eq. (1.44)] in the j–k plane with a flux of Φ per plaquette. Just as in the case of the 2D QHE, this lattice model allows for a direct calculation of the response equations in terms of topological invariants of the eigenstates. This calculation has been done, as part of a proposal to implement the 4D Harper-Hofstadter Hamiltonian in a system of ultracold atoms using a particular synthetic dimension scheme [44]. The authors found that if one applies an electric field E_y in the y direction, and a weak perturbing magnetic field $\tilde{B}_{zw}$ in the z–w plane, then the response equations are

$$j^w = \frac{\Phi_{xy}}{2\pi a^2}\frac{e^2}{h}C_1^{yw}E_y, \tag{1.46}$$

$$j^x = \frac{e^3}{h^2}C_2 E_y \tilde{B}_{zw}, \tag{1.47}$$

where a is the lattice spacing, C_1^{yw} is the first Chern number of the system in the y–w plane, and C_2 is a 4D topological invariant called the second Chern number. It is this new integer invariant that characterizes the 4D QHE. Furthermore, in the Abelian 4D

QHE we have described here, C_2 is related to the first Chern numbers of the system in the x–z and y–w planes. For the lowest energy band, this relationship is simply given by a product: $C_2 = C_1^{xz} C_1^{yw}$. Note that, because this model generates a nontrivial second Chern number via first Chern numbers, the linear 2D quantum Hall response still occurs, as seen in Eq (1.46).

We can intuitively understand these response equations — but not their quantization — classically, if we recall that the first and second Chern numbers have been generated by the magnetic fields B_{xz} and B_{yw} (corresponding to the fluxes Φ_{xz} and Φ_{yw}). Firstly, Eq. (1.46) is just the 2D Hall effect: the electric field E_y generates a current in the y direction, which is then deflected into the w direction by the magnetic field component B_{yw}. With this in mind, we can interpret Eq. (1.47) as describing how this w current (resulting from E_y) is in turn deflected, first into the z direction by the field $\tilde{B}_{zw}$, and then the corresponding z current is deflected into the x direction by the original field B_{xz}. Of course the interesting part is how quantum mechanics causes this response to be quantized according to C_2; this is simply a semiclassical picture akin to the cyclotron orbits of the 2D QHE.

An intriguing fact about the 4D QHE effect is it can coexist with time reversal symmetry in more complex models, which must therefore have vanishing first Chern numbers. In contrast to the two band model that can characterise the first Chern number, a minimal model for the time-reversal symmetric 4D QHE involves two doubly-degenerate bands, and so is a four band model. In such a four band model, the second Chern number counts how many times the eigenstates of the two occupied bands wind over a higher-dimensional Bloch 4-sphere S^4, as the momentum varies over the Brillouin zone 4-torus T^4 [28].

Such non-Abelian versions have also been studied in previous works [45, 46], which have shown that such a system has a similar nonlinear Hall response to that in Eq. (1.47), given by

$$j^\mu = \frac{e^3}{2h^2} C_2 \epsilon^{\mu\nu\sigma\tau} E_\nu \tilde{B}_{\sigma\tau}, \tag{1.48}$$

where E_ν and $\tilde{B}_{\sigma\tau}$ are applied perturbing electric and magnetic fields, and $\epsilon^{\mu\nu\sigma\tau}$ is the 4D Levi-Civita symbol. Note that, in contrast to the Abelian model, strong magnetic fields are not required for C_2 to be nonzero, and in these models the nonlinear Hall response can be observed in the absence of the linear 2D response, making this a truly higher-dimensional effect that cannot be understood in terms of lower dimensions.

As we have previously mentioned, experimental schemes have been devised in recent years to explore this kind of higher-dimensional physics in our 3D world. One such scheme goes by the name of topological pumping [47–57]; this involves theoretically taking a 4D (for example) Bloch Hamiltonian and replacing one or more of the quasimomentum components with tuneable external parameters. This allows the Hamiltonian to be reinterpreted as a two, or three-dimensional model with these extra "pump" parameters. Then, by experimentally implementing this Hamiltonian and varying the pump parameters, one can sample the abstract higher-dimensional momentum space and find signatures of the higher-dimensional topology. This has been achieved experimentally in the context of cold atoms [55], photonics [56], acoustics [57–59]. Of course, topological pumping cannot fully realise higher-dimensional dynamics, since the pump parameters have to be varied with time in order to explore the higher-dimensional space. This also means that interacting 4D models cannot be straightforwardly investigated in this way.

Another possible method consists of directly engineering a higher-dimensional lattice by increasing the connectivity of a physical system. For example, a 2D square lattice can be embedded in 1D by taking a sequence of chains and adding in long range links to connect like sites of adjacent chains. There have been proposals to implement this idea in experiments using superconducting qubits [60], and photonic lattices [61], although in practice it is usually challenging to engineer the long range hops required. However, this technique has been experimentally successful in the platform of electrical circuits [62, 63], since changing connectivity here simply amounts to rewiring the circuit. In this case, the experiment was designed to implement the non-Abelian 4D QHE, although this equivalence only holds in a certain frequency window and so does not provide full access

to this phenomenon. However, as we have already mentioned, there is a far broader set of experimental techniques collectively referred to as synthetic dimensions, which have the potential for simulating the full physics of 4D physical systems in the real world.

1.3 Synthetic Dimensions

The general idea of a synthetic dimension is to take a set of local internal states or degrees of freedom of a physical system and then couple them together [20, 62, 64–88], for example via an external driving field. These states are then reinterpreted as sites along a lattice, with state transitions interpreted as hops between lattice sites. This is depicted schematically in Fig. 1.4, with the left panel showing that internal states on their own can form a 1D chain once externally coupled, and the right panel showing a 2D square lattice constructed by pairing this synthetic dimension with a real one. The right panel also shows a flux of α per plaquette, indicating one of the most appealing features of this idea: there is often a simple way to introduce an artificial gauge field by engineering the transitions with the required Peierls phases.

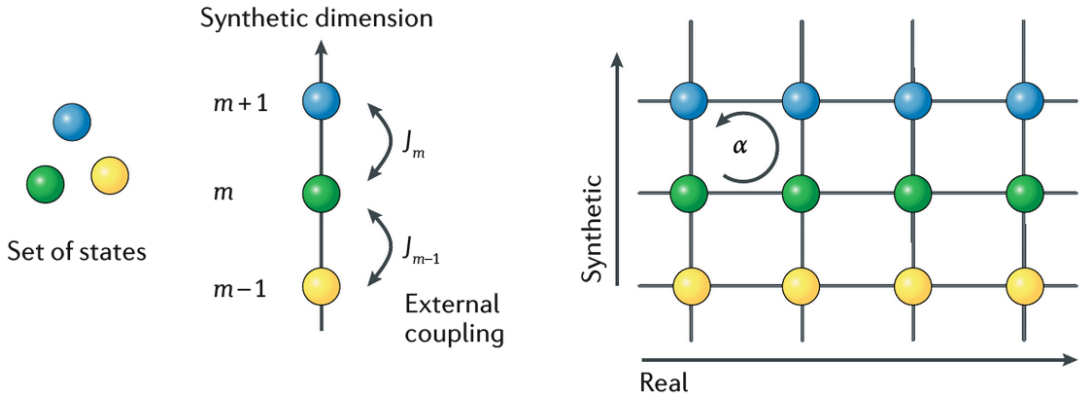

Figure 1.4: A basic schematic of a synthetic dimension. (Left) An internal set of states indexed by m are externally coupled together, leading to a 1D lattice with a potentially position-dependent hopping strength J_m. (Right) Combining this synthetic dimension with a 1D lattice in real space leads to a 2D lattice, where there is often a natural way to include an artificial flux of α per plaquette. From [89]

The idea of using synthetic dimensions to experimentally simulate higher-dimensional physics was first suggested by Boada et al. [66] in 2012, where two concrete proposals were

given using ultracold atoms. One of these methods was later extended by Celi et al. [20] to allow for an artificial magnetic field through the plane defined by a real dimension and the synthetic one. Here we will briefly explain this particular scheme to illustrate how synthetic dimension experiments work in practice, and what intricacies can arise.

The proposal uses identical atoms in a set of hyperfine states with constant total hyperfine quantum number F, but differing values of the projection, m_F, of this observable in a given direction [20, 66]. The synthetic dimension is built out of these states, with m_F acting as the site index, such that there are $2F + 1$ sites from $m_F = -F$ to F. Coupling between the states is achieved via Raman transitions — simultaneous absorption and emission of two photons of differing polarisations [90] — which increase or decrease the value of m_F by one. The atoms are also allowed to hop between the sites of an optical lattice in real space, which provides up to three additional dimensions. This scheme can therefore (in principle) naturally extend to 4D, since the internal states used are completely independent of the position of the atoms in real space [44, 66]. (Note that in certain other synthetic dimension schemes the combination with real dimensions is not possible and so all dimensions must be synthetic [89].)

To illustrate this scheme in more detail, we will focus here on a one-dimensional real-space lattice, such that Fig. 1.5 shows the set up: the red lasers and the real magnetic field $B_0\boldsymbol{e}_z$ lift the degeneracy of the m_F states and confine atoms to the optical lattice sites, while the blue and green Raman beams generate hopping in the spin dimension. As depicted, the green(blue) laser has polarisation in(out of) the plane. An atom absorbing a photon from one beam while emitting one into the other undergoes a net change in the direction, but not the magnitude, of F. This changes the value of m_F while keeping F fixed.

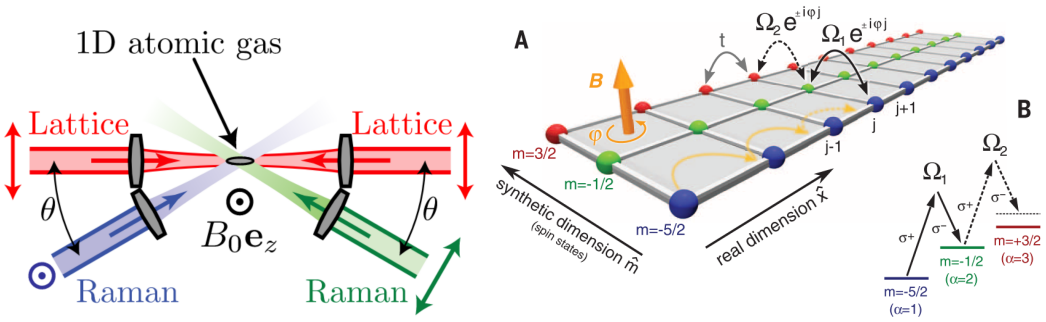

Figure 1.5: Experimental setup for the 2D real/spin space hybrid lattice (Left, from [20]). Schematic of the synthetic lattice (A), and an illustration of the Raman transitions between Zeeman-split m_F states (B) here for ^{173}Yb atoms. (Right, from [68]).

The trick that incorporates a synthetic gauge field into the lattice is that the Raman transitions are designed to also induce a net change of the atom's momentum in the optical lattice direction [20]. This is mathematically and physically equivalent to minimal coupling; a magnetic vector potential $\boldsymbol{A} = By\hat{\boldsymbol{x}}$ will shift the x-momentum of a charged particle by an amount linear in its position in the y direction. Therefore, the 2D lattice defined by the m_F states and real-space positions contains an artificial magnetic field acting on the neutral atoms. As shown in Fig 1.5, this is achieved simply by changing the orientation of the Raman beams with respect to the optical lattice [20]. The field strength can be tuned by changing the tilt angle of the beams, since this alters the x-component of momentum of the Raman photons, which is what determines the momentum transfer associated with a spin-hop.

This particular synthetic lattice scheme was implemented experimentally in 2015 by Stuhl et al. [67] and Mancini et al. [68] independently. These experiments were limited to two- and three-leg ladders as in Fig. 1.5, however they were able to image the topological edge states on the spin-boundaries associated with the flux piercing the lattice. More recently, this experimental set-up has been used to generate a synthetic dimension of 17 sites by using Dysprosium atoms which have a much larger low-lying manifold of internal states available [86]. One peculiarity of this scheme is that the hopping strength in the synthetic dimension is nonuniform: it depends on the position m_F. This translates to a position-dependent mass in the continuum limit, which is not particularly well-defined as

mass and momentum therefore no longer commute.

Another important detail is that interactions can be, to a good approximation, completely nonlocal in the synthetic dimension. Physically this makes sense: if two atoms on the same optical lattice site attract or repel each other, they are unlikely to care whether they are in the same hyperfine state or not. Depending on the atomic species, this leads to many-body models with $SU(N)$ symmetry, where N is the number of synthetic lattice sites, which have generated a lot of interest as they can lead to many exotic states [62]. However it is also desirable to be able to engineer synthetic dimensions with contact — or at least somewhat local — interactions. Recently, there have been proposals for how to achieve this, e.g. by using a spatial magnetic field gradient to separate states with different m_F values in space [86].

Synthetic dimensions as a field has also greatly expanded since its inception, and there are now a large number of different experimental schemes. Table 1.1 gives an overview of many of these schemes, showing the variety in experimental platforms that are used. This wide range of physical systems and types of state used means that each synthetic dimension scheme can have very particular quirks and limitations. However, some of these details are more common, such as: position dependent hopping, nonlocal interactions, lattices with a limited number of sites, and hard-wall boundary conditions. Fortunately, topological features (such as Chern numbers) can be robust even to unusual variations such as these, as previously mentioned [62].

None of these common details are unavoidable, of course, and we will now discuss a proposal which does in fact manage to avoid them, albeit at the cost of other complexities. This scheme, suggested by Ozawa and Carusotto in 2017 [77] potentially allows for completely local interactions and an artificial gauge field. Their idea was to use a lattice of ring resonators to trap photons, with the angular position, θ, within each resonator serving as a "curled up" extra dimension. Hopping on the lattice is naturally achieved via evanescent coupling between the rings, and if a nonlinear optical medium is used then photons in the same resonator can interact. In this case the angular displacement of two

Physical System	Type of states	Type of coupling	No. of synthetic dimensions studied
Atoms [20, 67, 68, 86]	Hyperfine states	Raman lasers	1
Atoms [71, 75]	Electronic states	Clock lasers	1 (only 2 sites)
Atoms [81]	Angular momentum of molecules	Microwaves	1–2
Atoms [70, 72]	Momentum states	Bragg transitions	No upper limit
Atoms and photons [91, 92]	Spatial eigenmodes	Shaking	1–3
Photons [69, 76, 82]	Orbital angular momentum	Spatial light modulator	1
Photons [73, 74]	Frequency modes	Temporal modulation	No upper limit
Photons [77]	Angular coordinate of resonator	Dispersion of resonator	1 (continuous dimension)
Photons [64, 65, 78, 83]	Arrival time of pulses	Coupled optical paths of different lengths	1–2
Generic [79, 84, 85]	Floquet states	Temporal modulation	No upper limit
Bosons [87]	Multi-particle configurations	Particle hopping	No upper limit
Atoms [80, 88]	Rydberg states	Millimetre waves	1 (6 sites)

Table 1.1: Summary of different synthetic dimension schemes showing the type of physical system, state, and coupling used, as well as the number of dimensions implemented. Adapted from [89]

photons is an essential part of the interaction potential, and effectively local interactions are feasible [77].

Additionally, designing the lattice such that the radius of resonators varies linearly with one of the lattice directions, x, causes an x-dependent shift in the angular mode index of the photons, which acts as an artificial magnetic field in the x–θ plane. This does, however, present a challenge for extending this proposal to the 4D QHE, which would require the lattice of ring resonators to be three-dimensional. The varying size of the resonators in the x direction could then interfere with the evanescent coupling in the other directions. The Abelian 4D QHE would also require another magnetic field, in the y–z plane. There is a well-known way to implement a synthetic gauge field in a lattice of ring resonators [93], but it is not clear that this can be straightforwardly incorporated into the above proposal. Finally, we note that this proposal is unusual

among synthetic dimension methods in that the synthetic dimension, θ, is continuous and has periodic boundary conditions. Periodic boundaries would also present a complication for the physics of rotating superfluids to be studied in this thesis, and would certainly impact the type of vortices that can form in such a system. However, it is far more common to have a discrete synthetic dimension with open boundary conditions, and henceforward we will not consider periodic boundary conditions along any of the dimensions.

1.4 Motivation and summary

In this chapter we have covered the physics of vortices in two and three-dimensional superfluids, and described how rotating such a system is analogous to an applied magnetic field. This then led us to a discussion of the quantum Hall effect, first in 2D, and then in 4D where two types are possible: the Abelian 4DQHE which requires time reversal symmetry break (e.g. with rotation or a magnetic field) and the Non-Abelian 4DQHE which does not. We briefly discussed the inspiration for this project: to see if adding weak interactions to a 4DQH system could lead to interesting physics that could not be understood in terms of lower dimensions. Lastly, we described the recent experimental breakthroughs that have motivated theoretical interest in higher dimensions, with a particular focus on synthetic dimensions as a potential way to realise an interacting 4DQH system.

To reach this weakly interacting 4DQH regime requires the combination of local interactions and an artificial gauge field in two independent planes at once. Needless to say, implementing both of these features of a synthetic dimension in the same experiment is an open and interesting challenge, and it is not entirely clear which platform will be successful in this. For this reason, we have chosen to study a model which is far from experimental relevance, but is the natural generalisation of the description of a superfluid in lower dimensions. That is, we are starting from the 4D GPE, assuming four equivalent continuous dimensions with contact interactions as will now be introduced in Chapter 2. This means that the generality of our results is not limited by details that can be par-

ticular to the experimental set-up, and future work can build upon ours by introducing whatever features are needed to connect with a given experiment

Chapter 2

Superfluid Vortices in Four Spatial Dimensions

"Behold me - I am a Line, the longest in Lineland, over six inches of Space" - "Of Length," I ventured to suggest. "Fool", said he, "Space is Length."

Edwin Abbott, *Flatland: A Romance of Many Dimensions*

Superfluid vortices in four spatial dimensions

Ben McCanna* and Hannah M. Price
School of Physics and Astronomy, University of Birmingham, Edgbaston, Birmingham B15 2TT, United Kingdom

(Received 22 May 2020; revised 31 October 2020; accepted 25 March 2021; published 10 May 2021)

Quantum vortices in superfluids have been an important research area for many decades. Naturally, research on this topic has focused on two-dimensional (2D) and 3D superfluids, in which vortex cores form points and lines, respectively. Very recently, however, there has been growing interest in the quantum simulation of systems with four spatial dimensions; this raises the question of how vortices would behave in a higher-dimensional superfluid. In this paper, we begin to establish the phenomenology of vortices in 4D superfluids under rotation, where the vortex core can form a plane. In 4D, the most generic type of rotation is a "double rotation" with two angles (or frequencies). We show, by solving the Gross-Pitaevskii equation, that the simplest case of equal-frequency double rotation can stabilize a pair of vortex planes intersecting at a point. This opens up a wide number of future research topics, including into realistic experimental models; unequal-frequency double rotations; the stability and potential reconnection dynamics of intersecting vortex surfaces; and the possibility of closed vortex surfaces.

DOI: 10.1103/PhysRevResearch.3.023105

I. INTRODUCTION

Quantum vortices are fundamental topological excitations of superfluids, which have been widely studied for many years [1–7]. Unlike a lot of many-body phenomena, vortices can be understood at the mean-field level through the Gross-Pitaevskii equation (GPE) [1]. A superfluid vortex consists of a local density depletion within the "vortex core," around which the superfluid circulates. In two-dimensional (2D) and 3D superfluids, this vortex core forms a point and a line, respectively, as sketched in Fig. 1. Vortices have an associated energy cost but can be stabilized by rotation of the superfluid [2,3] or, equivalently, by artificial magnetic fields [8–10].

While research has so far naturally focused on vortices in 2D and 3D superfluids, there is growing interest in simulating systems with four spatial dimensions. This is thanks to experimental and theoretical investigations of 4D physics in topological pumping [11–13], high-dimensional parameter spaces [14–17], and electric circuits with high connectivity [18–22], as well as proposals for engineering 4D systems using "synthetic dimensions" [23,24]. The latter, in particular, opens up the prospect of being able to explore higher-dimensional superfluids with artificial gauge fields. In this approach, "synthetic dimensions" are built by coupling together the internal states of cold atoms [25–35], photonic systems [24,36–42], and other platforms [43–46]. Such degrees of freedom are then reinterpreted as lattice coordinates in a new direction, increasing the effective system dimensionality, while providing straightforward ways to realize artificial magnetic fields [47] and hence mimic rotation in a higher-dimensional space.

The potential of synthetic dimensions for reaching 4D with (for example) ultracold bosonic atoms [23,33] motivates the question of how superfluid vortices behave in higher dimensions. In this paper, we take an initial step in this direction by exploring the 4D GPE under rotation, with local atom-atom interactions. This is chosen as a minimal model, which naturally extends a standard textbook problem to 4D in order to establish basic aspects of 4D vortex physics. More realistic models for experiments will depend on the specific synthetic-dimension implementation chosen and are likely to include other effects, such as lattices and unusual interactions with respect to the synthetic dimension, that will further enrich the possible vortex states but will go beyond this paper. We also note that while our main motivation for studying the 4D GPE is as an initial stepping stone towards possible synthetic-dimension experiments, this model is also plausible as a description of low-temperature interacting bosons in a hypothetical 4D universe (see Appendix A and Refs. [48–50]) and so is of mathematical interest for generalizing classic results about superfluid vortices to higher dimensions.

To investigate vortices in 4D, we must first appreciate that rotations (or equally, magnetic fields) in higher dimensions can have a fundamentally different form; all rotations in two and three dimensions are so-called "simple rotations," while in 4D, generic rotations are "double rotations" [51]. This difference will be discussed in more detail later but can be understood in brief by noting that in 2D or 3D every rotation has a single rotation plane and angle, while in 4D there can be two independent rotation planes, e.g., the xy and zw planes, each with their own angle of rotation.

In this paper, we show that equal-frequency double rotation of a 4D superfluid can stabilize a vortex structure formed by two vortex planes intersecting at a point, while a simple rotation stabilizes a single vortex plane, as sketched in Fig. 1. We obtain our results, firstly by using a phase ansatz to nu-

*

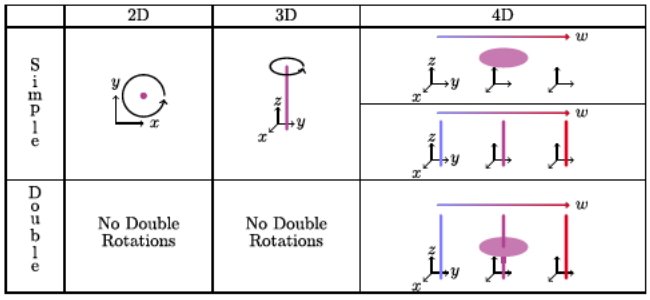

FIG. 1. Sketch of minimal vortex structures, stabilized for different system dimensionalities (columns) and types of rotation (rows). Here, "simple" and "double" indicate rotations with one or two planes of rotation, respectively, as discussed in the text. In 2D and 3D, only simple rotations exist, stabilizing vortex cores as a point and line, respectively, about which the superfluid rotates (black arrow). In 4D space (shown as 3D cross sections colored according to w value), both types of rotation exist, leading to a richer vortex phenomenology. In 4D, equal-frequency double rotations can lead to a new type of vortex configuration consisting of two vortex planes intersecting at a point, while simple rotations stabilize a single vortex plane. In these sketches, a vortex plane appears either as a line persisting for all w (lines of varying color) or as a plane for a particular w value (purple disk), depending on the rotation plane. Note that in the 4D column we have omitted the arrow indicating superfluid motion.

merically solve an effective 2D radial equation and secondly by numerically solving the full 4D GPE under rotation. This generalization of superfluid vortices to higher dimensions opens up many avenues of future research, such as questions concerning the unequal-frequency case; reconnections of vortex planes; possible curvature of vortex surfaces; and more realistic setups capturing experimental details.

II. REVIEW OF VORTICES IN 2D AND 3D SUPERFLUIDS

We begin by reviewing the basic properties of 2D and 3D vortices, in order to lay the groundwork for our discussion of 4D superfluids. We consider systems of weakly interacting bosons described by a complex order parameter, ψ, which obeys the time-independent GPE with no external potential [1]

$$-\frac{\hbar^2}{2m}\nabla^2\psi + g|\psi|^2\psi = \mu\psi, \tag{1}$$

where m is the particle mass, g is the interaction strength, and μ is the chemical potential. A hydrodynamic description can be obtained from this equation by substituting $\psi = \sqrt{\rho}e^{iS}$, where ρ is the superfluid density and S is the phase [1]. The velocity field, $\mathbf{v} = \frac{\hbar}{m}\nabla S$, is irrotational wherever S is well behaved. A consequence of this property is that a superfluid supports quantized vortices. This can be seen by noting that the superfluid circulation around a closed loop C is quantized as

$$\oint_C \mathbf{v}\cdot d\mathbf{r} = \frac{\hbar}{m}[\Delta S]_C, \tag{2}$$

where $[\Delta S]_C$ is the phase winding [3]. Since ψ is single valued, we must have $[\Delta S]_C = 2\pi k$, where k is the integer winding number (or vortex charge) [1]. Smoothly deforming the loop cannot change k as long as vortices are avoided. This can only be true if $\mathbf{v}$ diverges as $1/r$ as the distance r from a vortex core goes to zero. Since particles cannot have infinite velocity, ρ must vanish in this same limit. The region of density depletion is known as the vortex core; in 2D, this is localized around a point, and in 3D around a line, as shown in Fig. 1. More generally, vortices must be localized in two directions.

As is well known, the density profile around the vortex core can be calculated directly by applying the GPE to a homogeneous superfluid with a single vortex [1]. By defining the uniform background density n, the healing length ξ can be introduced, which satisfies $\hbar^2/m\xi^2 = gn = \mu$ [52] and which physically is the distance over which ρ typically varies. Hereafter, we rescale $\mathbf{r} \to \xi\mathbf{r}$, and $\psi \to \sqrt{n}\psi$ such that Eq. (1) becomes dimensionless as

$$-\tfrac{1}{2}\nabla^2\psi + |\psi|^2\psi = \psi. \tag{3}$$

A rotationally symmetric vortex state in 2D has the form $\psi = f_k(r)e^{ik\theta}$, where (r,θ) are polar coordinates centered on the vortex core, $f_k(r)$ is real, and k is the winding number. Substituting this into Eq. (3) gives [1]

$$-\frac{1}{2}\left(\Delta_r - \frac{k^2}{r^2}\right)f_k + f_k^3 - f_k = 0, \tag{4}$$

where $\Delta_r = \partial^2/\partial r^2 + (1/r)\partial/\partial r$. This equation has no closed-form solution but does admit the asymptotic forms $f_k(r) = O(r^{|k|})$ as $r \to 0$, and $f_k(r) = 1 - O(r^{-2})$ as $r \to \infty$ [3]. The crossover between these two behaviors occurs at around the healing length. Note that a straight vortex line in an otherwise homogeneous and isotropic 3D superfluid has this same profile, with (r,θ) defined in the plane perpendicular to the vortex line [1].

Using this density profile, the energy cost of a vortex relative to the ground state can be evaluated. For a singly charged vortex ($k = 1$) the energy can be written as

$$E_1(R) = \mu N\left(\frac{\xi}{R}\right)^2 \ln\left(2.07\frac{R}{\xi}\right), \tag{5}$$

where N is the number of bosons and R is the radius of the superfluid in the plane orthogonal to the vortex core. Equation (5) is valid in any number of dimensions. Vortices can be energetically stabilized by rotation (or equivalently, an artificial magnetic field), whereby Eq. (1) is modified in 3D by adding the term $-\mathbf{\Omega}\cdot\mathbf{L}\psi$ to the left-hand side, with $\mathbf{L} = -i\hbar\mathbf{r}\times\nabla$ being the angular momentum operator and $\mathbf{\Omega}$ being the frequency vector [1]. This term reduces the energy of a state containing a vortex aligned with the rotation, making it more energetically favorable.

III. SIMPLE AND DOUBLE ROTATIONS

Given the intrinsic link between rotation and vortices, we will now discuss the different types of rotations possible in 4D, as compared with lower dimensions, in preparation for our discussion of vortices in 4D superfluids below.

In three dimensions or fewer, every rotation is "simple"; this means that the rotation is specified by a rotation angle $\alpha \in (-\pi, \pi]$ and a plane of rotation which is unique up to

translation. Under rotation, the points on the plane of rotation remain on the plane but are displaced through the angle α. Generalizing to D-dimensional space, simple rotations have $D-2$ eigenvectors with eigenvalue 1, all of which are orthogonal to every vector in the rotation plane. For example, a rotation about the z axis in 3D has the xy plane (defined by $z=0$) as its rotation plane and fixes any point along the z axis. We may write this as a matrix in the standard basis as

$$\begin{pmatrix} \cos\alpha & -\sin\alpha & 0 \\ \sin\alpha & \cos\alpha & 0 \\ 0 & 0 & 1 \end{pmatrix}. \tag{6}$$

We can think of this as a rotation of 2D space (spanned by x and y) extended into a third (z) direction. Similarly, simple rotations in 4D can be thought of as rotations of 3D space extended into a fourth direction. Labeling the fourth axis as w, our previous example becomes a rotation about the zw plane (defined by $x=y=0$), given in matrix form by

$$\begin{pmatrix} R(\alpha) & 0 \\ 0 & I \end{pmatrix}, \quad \text{where } R(\alpha) = \begin{pmatrix} \cos\alpha & -\sin\alpha \\ \sin\alpha & \cos\alpha \end{pmatrix} \tag{7}$$

and I is the 2D identity. Note that there are six Cartesian coordinate planes in 4D, so the rotation group SO(4) has six generators, and the representation of these generators (which physically describe angular momentum) as spatial vectors no longer works in 4D as it does in 3D. The set of fixed points of a simple rotation in 4D are a plane, not a line, and this fixed plane is completely orthogonal to the plane of rotation, by which we mean that every vector in one plane is orthogonal to every vector in the other.

In contrast to 2D and 3D, in four dimensions, we can also have "double rotations," which generically have only one fixed point, and two completely orthogonal planes of rotation each with a corresponding rotation angle [51]. To visualize this, consider a double rotation in the xy and zw planes represented by the matrix [53]

$$\begin{pmatrix} R(\alpha) & 0 \\ 0 & R(\beta) \end{pmatrix}, \tag{8}$$

for angles $\alpha, \beta \in (-\pi, \pi]$. For those familiar with certain 4D quantum Hall models, this is analogous to generating a second Chern number by applying magnetic fields in two completely orthogonal planes [12,13,23,24,54]. Double rotations are in fact the generic case of rotations in 4D, as if either α or $\beta = 0$, the rotation reduces to the special case of simple rotation discussed above [51]. From here on we will refer to the two planes of rotation as planes 1 and 2, respectively, and focus only on so-called "isoclinic" double rotations for which $\alpha = \beta$.

Before continuing, it is worth noting that isoclinic rotations have an additional symmetry. To see this, we remember that, as introduced above, generic double rotations have one fixed point and two planes of rotation, with corresponding angles $\alpha, \beta \in (-\pi, \pi]$. Vectors in $\mathbb{R}^4$ which do not lie in these rotation planes are displaced through an angle between α and β [51]. However, if $\alpha = \beta$, then this means that every vector is displaced by the same angle. As a consequence, for a given isoclinic rotation there is a continuum of pairs of completely orthogonal planes that can each be thought of as the two planes of rotation. In other words, isoclinic rotations therefore no longer have two unique planes of rotation, although they still have a single fixed point. However, numerically, we break this degeneracy since the phase winding of our initial state picks out the xy and zw planes in particular. We can also anticipate that a more experimental model would likely break this symmetry too, e.g., through the inclusion of lattices or through inherent differences between real and "synthetic" spatial dimensions.

IV. VORTEX PLANES IN 4D

Now that we have discussed some of the geometry of rotations in 4D, we are ready to study the associated vortex physics. As above, we consider a superfluid described by the GPE in the absence of external potentials, but now with atoms free to move in four spatial dimensions.

The simplest case to consider is that of a 4D superfluid under a constant simple rotation. As shown in Eq. (7), a simple rotation can be viewed as a 3D rotation extended into a fourth dimension, hence stabilizing a vortex plane, as sketched in Fig. 1. The corresponding order parameter profile is $\psi = f_k(r_1)e^{ik\theta_1}$, where (r_1, θ_1) are plane polar coordinates in the plane of rotation and $f_k(r)$ is the solution of Eq. (4). As this is independent of the other two coordinates, the vortex core becomes a plane; this is directly analogous to the extension of a point vortex in 2D into a line in 3D. We have verified this result numerically, as shown in Appendix B 1. This can be understood as the natural extension of vortices into 4D, as the extra dimension plays no role, and the vortex plane is homotopically characterized by a $\mathbb{Z}$ topological winding number, as in 2D and 3D. For a more detailed discussion of homotopy classification of vortex planes in 4D, see Appendix C.

In contrast, we expect that double rotation, being an intrinsically 4D (or higher) phenomenon, will lead to more interesting vortex configurations. To address this problem, we look for the ground states of the 4D GPE in a doubly rotating frame

$$\left[-\frac{\hbar^2}{2m}\nabla^2 + g|\psi|^2 - \Omega_1 L_1 - \Omega_2 L_2\right]\psi = \mu\psi, \tag{9}$$

where Ω_j and L_j are the rotation frequency and angular momentum operator in plane j. In Cartesian coordinates (x, y, z, w), $L_1 = -i\hbar(x\partial_y - y\partial_x)$, and $L_2 = -i\hbar(z\partial_w - w\partial_z)$. For simplicity we will adopt double polar coordinates $(r_1, \theta_1, r_2, \theta_2)$, defined by

$$(x, y, z, w) = (r_1\cos\theta_1, r_1\sin\theta_1, r_2\cos\theta_2, r_2\sin\theta_2),$$

such that $L_j = -i\hbar\partial_{\theta_j}$. The simple rotation case discussed before corresponds to $\Omega_2 = 0$, where the vortex core spans plane 2. In this paper we focus on equal-frequency doubly rotating superfluids; that is, $\Omega \equiv \Omega_1 = \Omega_2$.

The fact that L_1 and L_2 generate a double rotation means that they commute. We may look for a solution which is a simultaneous eigenstate of both angular momentum operators; therefore we propose an ansatz for the ground state under

rotation of the form

$$\psi(\mathbf{r}) = f(r_1, r_2)e^{ik_1\theta_1 + ik_2\theta_2}, \tag{10}$$

where $f(r_1, r_2)$ is real and the k_j are integer phase winding numbers in each rotation plane. This phase profile corresponds to the superfluid circulating in both planes simultaneously, about both vortex cores. We have suppressed the dependence of f on each k_j for brevity, and in all numerical results both winding numbers are 1. This state exhibits a phase singularity when either $r_j = 0$, so we require $f(0, r_2) = f(r_1, 0) = 0$ from the same reasoning as in 2D and 3D. In other words, this describes a pair of completely orthogonal vortex planes that intersect at a single point as illustrated in Fig. 1 and that are characterized by $\mathbb{Z} \times \mathbb{Z}$ topological winding numbers (see Appendix C). Intersection of two planes at a point is only possible in 4D or higher and, in fact, is the generic case in 4D. This is in contrast with 3D, where the intersection of lines is a special case, and so vortex lines intersect and reconnect at specific times [55–58].

To examine our ansatz, we now proceed to numerically solve for the density profile, under this phase constraint. Substituting the ansatz [Eq. (10)] into the GPE [Eq. (1)] in 4D, and dedimensionalizing in the same way as in the 2D case, we obtain the following equation for $f(r_1, r_2)$:

$$-\frac{1}{2}\left(\Delta_{r_1} - \frac{k_1^2}{r_1^2} + \Delta_{r_2} - \frac{k_2^2}{r_2^2}\right)f + f^3 - f = 0, \tag{11}$$

where $\Delta_{r_j} = \partial^2/\partial r_j^2 + (1/r_j)\partial/\partial r_j$. Since each vortex produces only a local density depletion, we expect that $f(r_1, r_2) \sim f_{k_2}(r_2)$ as $r_1 \to \infty$ and equally for $(1 \leftrightarrow 2)$, where $f_k(r)$ is the point vortex solution of Eq. (4). Note that this limiting "boundary condition" can be satisfied by a separable product ansatz, $f_{k_1}(r_1)f_{k_2}(r_2)$, of 2D density profiles in each plane. However, this form fails to solve the full equation due to the nonlinear f^3 term. This product form therefore gives a natural approximation to compare with, and we expect it to fail significantly only in the vicinity of the origin, where both $f_{k_j}(r_j)$ differ appreciably from unity.

To verify this, and find the full density profile, we have solved Eq. (11) by imaginary time evolution within a discretized grid in (r_1, r_2) space with hard-wall boundary conditions at a radius $R = 100\xi$ in each plane ($r_j = R$) and at the origin in each plane ($r_j = 0$). The latter condition is required due to the centrifugal term diverging at the vortex cores; consequently, the precise location of the vortex cores was an assumption in these calculations. We used a forward Euler time discretization and second-order finite differences in space. We chose a large value of R compared with ξ so that we could examine the vortex cores within a homogeneous region. (Future studies could include the effect of additional trapping potentials, such as harmonic traps along some or all directions.) We were able to achieve a resolution of 0.05ξ, and the calculations were converged until the relative change in chemical potential and particle number over one time step converged below 10^{-14}.

The results for $k_1 = k_2 = 1$ are shown in Fig. 2(a), where we observe the expected local density depletion around the vortex cores when either $r_1 = 0$ or $r_2 = 0$. We also compare our numerical solution with the product approximation, $f_1(r_1)f_2(r_2)$, in Fig. 2(b); we observe that the product approximation is very accurate except within a distance of roughly $\gtrsim\xi$ from the intersection point, as expected. Immediately around the intersection, the product approximation fails, overestimating the density by a factor of about $4/3$.

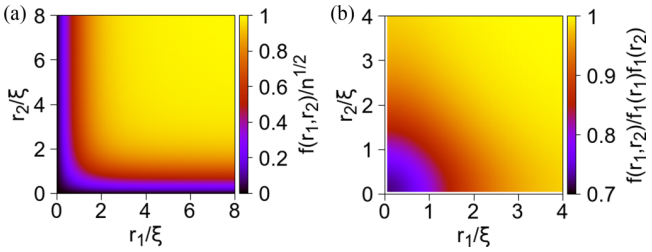

FIG. 2. (a) Numerical solution of Eq. (11) for $f(r_1, r_2)$, with $k_1 = k_2 = 1$, showing the density profile for an intersecting pair of vortex planes in 4D, as a function of the two polar radii. (b) The ratio of the solution in (a) to the product approximation $f_1(r_1)f_1(r_2)$, where $f_j(r_j)$ is the well-known 2D vortex profile governed by Eq. (4). This shows that the product approximation works well away from the intersection as expected but fails in a small region around $r_1 = r_2 = 0$. Numerical parameters and details are given in the main text.

Just as in the 2D case we can use our calculation of the density profile to find the energy of this vortex configuration relative to the state with no vortices. Defining independent radii R_j in each plane, such that $r_j \leqslant R_j$, we find numerically (see Appendix B 4) that the energy is approximately given as

$$E_{k_1,k_2}(R_1, R_2) = E_{k_1}(R_1) + E_{k_2}(R_2), \tag{12}$$

where $E_k(R)$ is the single-vortex energy given in Eq. (5). This can be understood from the superfluid kinetic energy $\int \rho v^2 d^4r$, which is the main contribution to the energy of a vortex. The velocity field is given by $\mathbf{v} = \mathbf{v}_1 + \mathbf{v}_2$, where $\mathbf{v}_j = \frac{k_j}{r_j}\hat{\theta}_j$ is the velocity induced by vortex j. As $\mathbf{v}_j$ lies in plane j, we see that $\mathbf{v}_1 \cdot \mathbf{v}_2 = 0$ and so the hydrodynamic vortex-vortex interaction term, $\int \rho \mathbf{v}_1 \cdot \mathbf{v}_2 d^4r$, vanishes. The total kinetic energy integral therefore splits into a sum of the individual kinetic energies. Note that this argument relies on the assumptions that the two vortex cores have no curvature and are completely orthogonal to each other.

In order to confirm the existence and stability of the intersecting vortex plane state, we have performed imaginary time evolution with the 4D GPE under both simple and double rotation [Eq. (9)] directly on a 4D Cartesian grid within a 4D ball of radius $R = 8.25\xi$ with a hard-wall boundary. A hypersphere rather than a hypercube was chosen as the majority of the 4D volume of a hypercube is taken up by regions "in the corners," that is, outside of the hypersphere that just fits inside. This allowed us to relax our above constraint on the phase profile, at the cost of smaller numerical system sizes. Again, we used the forward Euler method for time discretization and second-order finite differences in space. We were able to obtain resolutions of up to 0.2ξ, and by repeating simulations at different resolutions, we checked that our main conclusions were qualitatively insensitive to the coarse graining of the numerics. At the system sizes and resolutions we have been able to reach, the homogeneous region extends over a

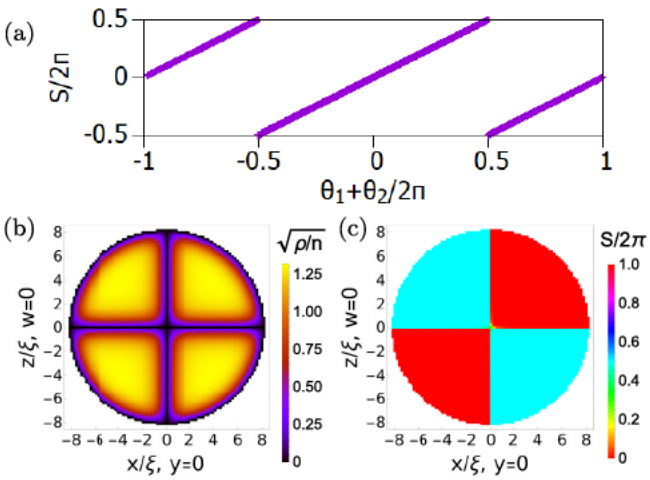

FIG. 3. Numerical results from imaginary time evolution of the doubly rotating 4D GPE in a ball geometry of radius $\sim 8\xi$, given an initial state with phase profile $\theta_1 + \theta_2$ and additional noise. (a) The phase of the final state at each point within the 4D ball vs the sum of the two polar angles, showing perfect agreement with the phase profile of our ansatz [Eq. (10)]. The density (b) and phase (c) profiles of the final state for the 2D slice in which $y = w = 0$; these are consistent with our ansatz, as well as the density profile shown in Fig. 2. We can interpret this final state as containing two vortex planes, one at $x = y = 0$ and one at $z = w = 0$. Further 2D cuts of this state are given in Appendix B 2.

few healing lengths. The calculations were converged to an accuracy threshold of 10^{-12}. A benefit of performing calculations with all four coordinates is that we were able to test our ansatz by allowing the phase to evolve and by removing the boundary condition at $r_j = 0$ mentioned previously. More precisely, we used an initial state with homogeneous density away from the edge of the ball and a phase profile given by $\arctan2(y, x) + \arctan2(w, z)$ for the doubly rotating case and $\arctan2(y, x)$ for the singly rotating case. We tested the robustness of our results to noise (up to 20% of the background value) added to the real and imaginary parts of the initial ψ. Note that we measure the applied frequency in units of the critical frequency of a single vortex in a homogeneous 2D disk of the same radius as our 4D ball; this is given (in our units) by [59]

$$\Omega_{\text{crit}}^{\text{2D}} = \mu \, \ln(2.07R/\xi)\left(\frac{R}{\xi}\right)^2. \tag{13}$$

For the results shown in Fig. 3 both the frequencies of rotation used were roughly $2.5\Omega_{\text{crit}}^{\text{2D}}$. Further work could investigate the effect of double rotation with unequal frequencies.

For a suitable range of frequencies Ω we find good agreement between the stationary state obtained from the full 4D numerics and our ansatz for two intersecting vortex planes, as shown in Fig. 3. Figure 3(a) shows that the phase profile of the state after relaxation perfectly agrees with that of the ansatz. Figures 3(b) and 3(c) show the density and phase profiles, respectively, for the 2D cut in which $y = w = 0$. As can be seen the density drops to zero along the lines $x = 0$ and $z = 0$, corresponding to the intersections of each vortex core with the plane of the cut, as expected. Further two-dimensional cuts of this state are given in Appendix B 2.

In this paper, we have shown that the simple rotation of an idealized 4D superfluid can stabilize a vortex plane, while equal-frequency double rotations can lead to two vortex planes intersecting at a point which do not interact hydrodynamically. This significantly extends the phenomenology of superfluid vortices, demonstrating that new effects can emerge in higher spatial dimensions even within mean-field theory.

It is important to note that we have studied an idealized model, which allows us to explore vortex physics in 4D without experimental details that depend on how the synthetic dimension is implemented [25–32,35]. The main differences between our work and possible experiments are, firstly, that the majority of practical implementations would lead to (tight binding) lattice models, whereas we have considered four continuous dimensions as a theoretical first step. Adding a lattice should introduce rich additional effects particularly when the lattice spacing is comparable to or greater than other length scales. However, when this spacing is very small, it should be possible to approximate a lattice model with a continuum model in the mean-field regime as we have considered here. Furthermore, synthetic-dimension schemes can include unusual effects, which are very dependent on the specific experimental implementation. In terms of the tight-binding description previously mentioned, these complications can include position-dependent hopping strengths, limited numbers of sites, and long-range interactions [25–31,35]. For the sake of generality as well as simplicity we have therefore chosen an idealized model, which can then be adapted in different ways for promising experimental scenarios in further work. We also note that Eq. (1) has SO(4) (4D rotational) symmetry, which would be broken in any experiment due to inequivalence of the synthetic and real spatial dimensions. Numerically, we break this symmetry with the phase ansatz, which was assumed in the radial case and imposed on the initial state in the Cartesian case. However, we do still assume an SO(2) symmetry in each of the xy and zw planes to obtain the effectively 2D radial equation [Eq. (11)] and simplify the corresponding numerics. In the Cartesian case, we also chose a boundary condition (a hard wall at some radius from the origin) that preserved these in-plane symmetries. In synthetic-dimension experiments, on the other hand, the most common boundary condition is an open boundary condition which is independent of the other dimensions [25–32,35]. Hence a more experimentally relevant geometry would involve one or more dimensions which have their own independent hard-wall boundary conditions, for example, a "spherinder" boundary specified by $\{\mathbf{r} \in \mathbb{R}^4 | x^2 + y^2 + z^2 = R^2\} \cup \{\mathbf{r} \in \mathbb{R}^4 | w = \pm L\}$ for some R and L. Investigating the effect of breaking one or both of these in-plane rotational symmetries geometrically is an interesting and natural next step for future work.

As well as a first step towards understanding future experimental models, this work also opens up many interesting theoretical research directions. Natural next steps include the study of 4D superfluids doubly rotating at unequal frequencies and 4D generalizations of previously studied questions from 2D and 3D [2,3]. Firstly, closed vortex surfaces in 4D would naturally generalize the vortex loops that arise in 3D [1], but with potentially an even richer classification when

nonorientability and surfaces of higher genus are included [60]. Secondly, vortex lines in 3D are known to dynamically reconnect upon intersection [55–58], whereas here we have shown that completely orthogonal intersecting vortex planes in 4D form a stationary state stabilized by rotation. It is an open question whether vortex planes reconnect if they are not completely orthogonal, and this question could have relevance to the general case of unequal-frequency double rotation. For example, intuitively, we would expect that an adiabatic change from $\Omega_2 = \Omega_1$ to $\Omega_2 > \Omega_1$ would cause the vortex in plane 2 (inducing rotation in plane 1) to tilt towards plane 1 to benefit from the now larger rotational energy discount in plane 2. Finally, in the longer term this work opens up questions related to the inclusion of strong interactions and the 4D fractional quantum Hall effect, as well as the study of models with more interesting order parameter spaces [61,62], potentially hosting non-Abelian vortices.

ACKNOWLEDGMENTS

We thank Tomoki Ozawa, Mike Gunn, Iacopo Carusotto, Mark Dennis, and Russell Bisset for helpful discussions. This work is supported by the Royal Society via Grants No. UF160112, No. RGF\EA\180121, and No. RGF\R1\180071, as well as by the EPSRC.

APPENDIX A: THE 4D GPE FOR AN IDEALIZED 4D BOSONIC GAS

The 4D GPE is a natural and mathematically simple generalization of the 3D GPE, allowing for easy comparison to superfluid vortex physics in lower dimensions. In this section, we also point out that the 4D GPE can be motivated as the proper description of interacting bosons in a hypothetical 4D universe and so is an interesting theoretical model in its own right. As is well known, the use of the GPE to describe a system of interacting bosons relies on taking the Hartree-Fock approximation and replacing the interaction potential by a contact (Dirac delta) potential. The latter trick is in turn justified by looking at the low-energy limit of the solutions for two-particle scattering. In this limit, the solutions are spherically symmetric (s wave) and correspond to solutions for a contact interaction with the same scattering length as the original potential. While this argument is usually applied only in three dimensions and below, it has also been generalized to arbitrary dimensions [48–50], showing that the dimensionality only affects the contact interaction strength and the form of the short-range singularities that must be removed from the scattering equation. The interaction strength can be considered arbitrary due to scale invariance of the GPE in the absence of an external potential, and the singularities have no effect on the GPE. Hence it can be concluded that the GPE should be a valid mean-field description of interacting bosons at low energy in 4D.

APPENDIX B: ADDITIONAL NUMERICAL RESULTS

1. Simple rotations

As described in Sec. III, we expect that a simple rotation should be able to stabilize a single vortex plane, extending the concept of 2D point vortices and 3D line vortices straightforwardly to four-dimensional systems. Assuming the rotation is in plane 1 (as defined in Sec. II), this would correspond to a condensate wave function of the form

$$\psi = f(r_1, r_2)e^{ik_1\theta_1}, \tag{B1}$$

with $f(0, r_2) = 0$, and such that this wave function approximately takes the form $\psi \propto (x + iy)$ near the vortex core.

We have verified this minimal vortex structure numerically by performing imaginary time evolution on the full 4D GPE under simple rotation in the plane orthogonal to the expected vortex core [i.e., Eq. (9) with $\Omega_1 \neq 0$, $\Omega_2 = 0$] . The corresponding density and phase profiles for the numerical stationary state are shown for selected 2D cuts in Fig. 4. Here, the initial state was chosen as detailed in Sec. II, and the rotation frequency was chosen as $2\Omega^{\mathrm{2D}}_{\mathrm{crit}}$. These numerical calculations were performed within a discretized 4D hypersphere of radius 8.25ξ and with resolution 0.5ξ.

As can be seen in Fig. 4, the observed density and phase profiles are in good agreement with the single vortex plane [Eq. (B1)]. In particular, the density is depleted for the plane defined by $z = 0$ and $w = 0$, as is expected for a single vortex plane that approximately takes the form $\psi \propto (x + iy)$ near the vortex core. Depending on the 2D cut, this vortex plane appears either as a point [see Figs. 4(e) and 4(g)], as a line [see Figs. 4(a) and 4(c)], or as a plane (not shown). Furthermore, around the vortex plane, the superfluid rotates, as can be seen from the winding of the phase in Figs. 4(f) and 4(h) and from the phase jumps in Figs. 4(b) and 4(d).

2. Double rotations

As we have shown, the double rotation of a 4D superfluid can stabilize a new type of vortex configuration consisting of two vortex planes intersecting at a point. In Fig. 5, we plot the density and phase profiles for additional 2D cuts of the numerical stationary state presented in Fig. 3. As can be seen, these profiles have a much richer structure as compared with the case of a single vortex plane shown in Fig. 4, as the phase winds simultaneously around both vortex cores with two independent winding numbers. This is also in contrast to 3D systems where two vortex lines may intersect and reconnect over time, but a pair of intersecting vortices is not stabilized by rotation as a stationary state of the system.

3. Cuts of the radial profile

As discussed in Sec. III and shown in Fig. 2(b), we have numerically verified for the solution of the radial equation [Eq. (11)] that far from the intersection point of the vortex planes the corresponding density profile is well approximated by a product state of the 2D vortex profiles. To visualize this in an alternative way, we have plotted in Fig. 6(a) cuts of Fig. 2(a) for specific values of r_2 and then rescaled these by $f_1(r_2)$ in Fig. 6(b). As shown the rescaled curves approach $f_1(r_1)$ for large values of r_2, verifying the approximation as expected.

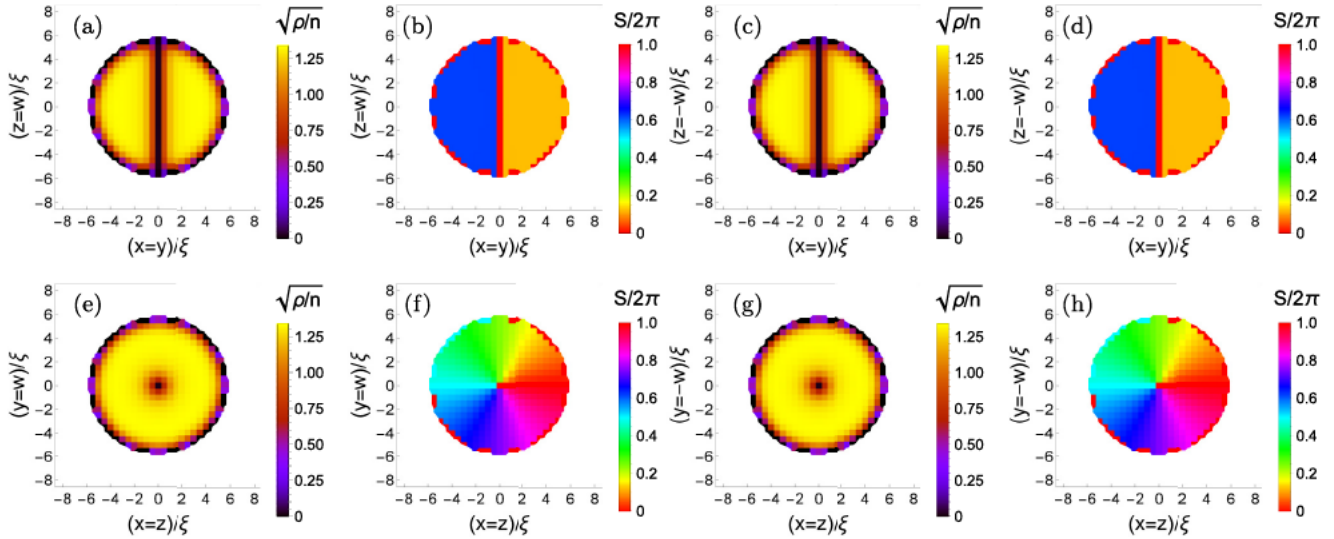

FIG. 4. Density [(a), (c), (e), and (g)], and phase [(b), (d), (f), and (h)] profiles for 2D cuts of the numerical stationary state under simple rotation. These cuts are given by (a) and (b) $x = y$ and $z = w$, (c) and (d) $x = y$ and $z = -w$, (e) and (f) $x = z$ and $y = w$, and (g) and (h) $x = z$ and $y = -w$. Numerical calculations were performed for a superfluid confined within a discretized 4D hypersphere of radius 8.25ξ and resolution 0.5ξ; this discretization is reflected in the pixelation, particularly at the boundaries of the plots. The observed density and phase profiles are in good agreement with a single vortex plane [Eq. (B1)].

4. Energy calculation for two intersecting vortex planes in a 4D superfluid

Here, we numerically verify Eq. (12), which predicts that the energy cost of two intersecting and completely orthogonal vortex planes in a 4D superfluid can be decomposed as a sum of the individual kinetic energies associated with each vortex plane in isolation.

Firstly, we used the numerical solution of the 4D radial density profile presented in Fig. 2 to calculate the energy of the intersecting vortex planes as a function of system size in each plane. We then produced a fit of this energy to the functional form of Eq. (12), with the coefficient of R_j/ξ inside the logarithm as the fitting parameter. From this we obtained 2.06, which is very close to the known coefficient of 2.07 (in our units) within the logarithmic form of the vortex energy in 2D and 3D [59]. This shows that the energy of our numerical solution for the radial equation is consistent with being a sum of two individual vortex energies.

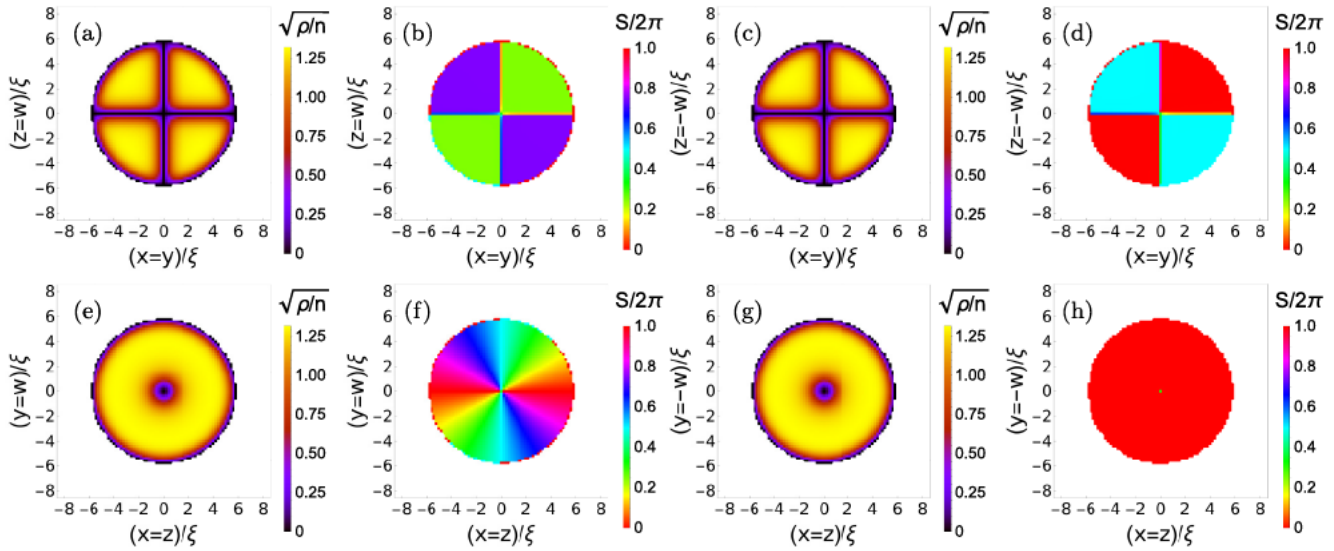

FIG. 5. Additional density [(a), (c), (e), and (g)], and phase [(b), (d), (f), and (h)] profiles along 2D cuts of the numerical stationary state studied in Fig. 3. These cuts are given by (a) and (b) $x = y$ and $z = w$, (c) and (d) $x = y$ and $z = -w$, (e) and (f) $x = z$ and $y = w$, and (g) and (h) $x = z$ and $y = -w$. The parameters and discretization are detailed in Sec. III. This discretization is reflected in the pixelation, particularly at the boundaries of the plots. The observed density and phase profiles are in good agreement with our numerical ansatz [Eq. (10)], which approximately takes the form $\psi \propto (x + iy)(z + iw)$ near the vortex cores.

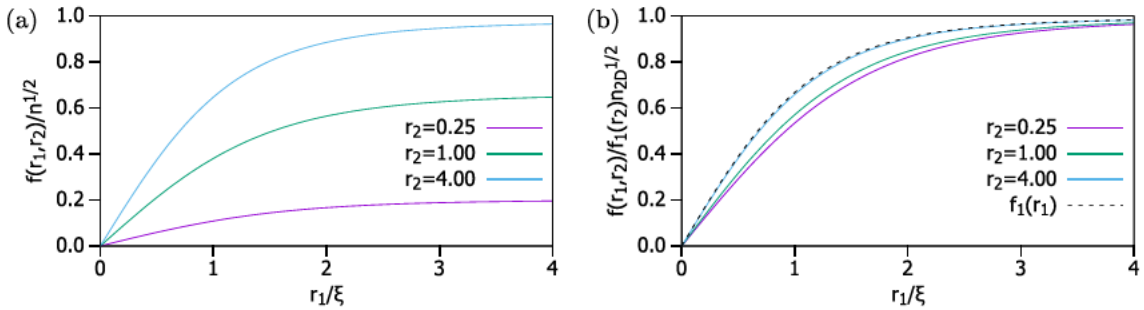

FIG. 6. (a) Cuts of Fig. 2(a), given by fixed values of r_2. (b) As in (a), but rescaled by the 2D vortex density profile $f_1(r_2)$; note the convergence to $f_1(r_1)$ for large values of r_2, showing that the order parameter can be well approximated as a product of 2D vortex profiles away from the intersection point. Close to the intersection point, this approximation breaks down, as can be seen from the deviation between these rescaled cuts in this region.

Secondly, we performed further simulations on a Cartesian 4D grid, with the same parameters as Fig. 3, except for the convergence accuracy, which was chosen to be 10^{-10} to speed up calculations. We repeated these calculations for different values of $\Omega \equiv \Omega_1 = \Omega_2$, ranging between two and three times $\Omega_{\rm crit}^{\rm 2D}$, in order to numerically verify the expected dependence of the energy on the rotation frequency. Here, we used three different initial states: one with no phase winding, one with "simple" winding in one plane, and one with "double" winding in two planes. The resulting values for E and μ as a function of Ω are shown in Fig. 7, given in units of μ_0 (the chemical potential of a homogeneous state with no vortices or hard walls but the same number of particles). We obtain straight lines for each of these data series, showing that each state has well-defined angular momentum.

For the case with no phase winding, we find that $E/\mu_0 N = 0.931$ and $\mu/\mu_0 = 1.622$ are constants which do not depend on frequency, as expected; this data series is therefore plotted with a straight line joining the dots as a guide to the eye. For the double winding case, we have performed a linear fit, obtaining $E/\mu_0 N = 1.119 - 0.083\Omega/\Omega_{\rm crit}^{\rm 2D}$ and $\mu/\mu_0 = 1.822 - 0.083\Omega/\Omega_{\rm crit}^{\rm 2D}$. The gradient, -0.083, is equal to $-2\Omega_{\rm crit}^{\rm 2D}/\mu_0$, meaning that this is the expected gradient of -2 corresponding to particles having one unit of angular momentum in each plane of rotation. For the simple winding case, we fix the gradient to be half that of the double winding line, since this state has angular momentum in only one of the two planes, and perform a linear fit with only the y intercept as a free parameter. We then obtain $E/\mu_0 N = 1.023$ and $\mu/\mu_0 = 1.722$ when $\Omega = 0$. This gives an energy cost of $0.188 = 1.119 - 0.931$ for the intersecting vortex planes and $0.092 = 1.023 - 0.931$ for the single plane, as compared with the state with no vortices. We expect from Eq. (12) that these energy costs should be related by a simple factor of 2 for this geometry, and indeed we find numerically that $0.188 - 2 \times 0.092 \simeq 0$.

APPENDIX C: HOMOTOPY THEORY FOR 4D VORTEX PLANES

Topological excitations, such as vortices, are characterized by topological invariants through homotopy theory. In this approach, the set of allowed topological charges for a given topological defect is given by the set of homotopy classes of maps from a region enclosing the defect to the order parameter manifold. Furthermore, the associated group structure of this set determines the rules for combining two such defects into one.

In 4D, a plane is enclosed by a circle, just like a line in 3D, or a point in 2D, such that the corresponding homotopy group (for a complex order parameter) is $\pi_1(S^1) = \mathbb{Z}$. This group is the same as for vortices in lower dimensions and tells us that each vortex has an integer winding number and that when two vortices combine, their winding numbers combine additively. For the case of two intersecting vortex planes the enclosing region is a 2D torus, such as the product of a circle in the xy

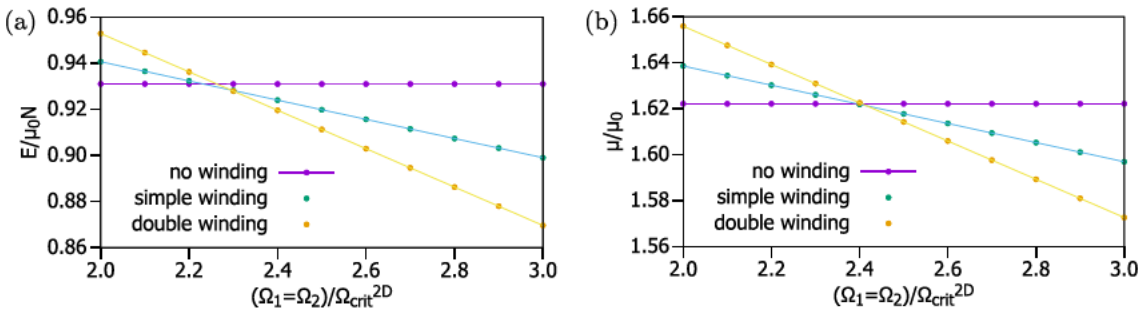

FIG. 7. (a) Energy and (b) chemical potential of numerical steady states of the 4D doubly rotating GPE [Eq. (9)] with different initial phase profiles. The lines correspond to fits and guides to the eye, respectively, as detailed in the text. The gradient and intercept of these lines give the angular momentum and energy at zero frequency, respectively, of each state, which agree with expected behavior.

plane and another circle in the zw plane. The corresponding homotopy group is therefore given by the set of homotopy classes of maps from $S^1 \times S^1$ to S^1, which is isomorphic to $\mathbb{Z} \times \mathbb{Z}$ [63]. This simply means that each vortex plane has its own winding number, and the two are independent, as expected for two vortices.

Note that this topological classification is the same as for a pair of linked vortex lines in 3D, which can also be enclosed by a torus. The configuration of 4D intersecting planes therefore offers a simple way to realize the homotopy classification of linked vortex lines within the ground state of a simple 4D GPE model. In the future, it would be interesting to generalize this model to more complicated order parameters, such as those realized in the various phases of spinor Bose-Einstein condensates (BECs) [61], as then the homotopy group would gain a richer structure, as has been studied in the context of linked line defects in liquid crystals [62].

[1] L. Pitaevskii and S. Stringari, *Bose-Einstein Condensation*, International Series of Monographs on Physics Vol. 116 (Clarendon, Oxford, 2003).

[2] N. R. Cooper, Rapidly rotating atomic gases, Adv. Phys. **57**, 539 (2008).

[3] A. L. Fetter, Rotating trapped Bose-Einstein condensates, Rev. Mod. Phys. **81**, 647 (2009).

[4] K. W. Madison, F. Chevy, W. Wohlleben, and J. Dalibard, Vortex Formation in a Stirred Bose-Einstein Condensate, Phys. Rev. Lett. **84**, 806 (2000).

[5] K. W. Madison, F. Chevy, V. Bretin, and J. Dalibard, Stationary States of a Rotating Bose-Einstein Condensate: Routes to Vortex Nucleation, Phys. Rev. Lett. **86**, 4443 (2001).

[6] M. R. Matthews, B. P. Anderson, P. C. Haljan, D. S. Hall, C. E. Wieman, and E. A. Cornell, Vortices in a Bose-Einstein Condensate, Phys. Rev. Lett. **83**, 2498 (1999).

[7] J. R. Abo-Shaeer, C. Raman, J. M. Vogels, and W. Ketterle, Observation of vortex lattices in Bose-Einstein condensates, Science **292**, 476 (2001).

[8] J. Dalibard, F. Gerbier, G. Juzeliūnas, and P. Öhberg, Colloquium: Artificial gauge potentials for neutral atoms, Rev. Mod. Phys. **83**, 1523 (2011).

[9] N. R. Cooper, J. Dalibard, and I. B. Spielman, Topological bands for ultracold atoms, Rev. Mod. Phys. **91**, 015005 (2019).

[10] T. Ozawa, H. M. Price, A. Amo, N. Goldman, M. Hafezi, L. Lu, M. C. Rechtsman, D. Schuster, J. Simon, O. Zilberberg, and I. Carusotto, Topological photonics, Rev. Mod. Phys. **91**, 015006 (2019).

[11] Y. E. Kraus, Z. Ringel, and O. Zilberberg, Four-Dimensional Quantum Hall Effect in a Two-Dimensional Quasicrystal, Phys. Rev. Lett. **111**, 226401 (2013).

[12] M. Lohse, C. Schweizer, H. M. Price, O. Zilberberg, and I. Bloch, Exploring 4D quantum Hall physics with a 2D topological charge pump, Nature (London) **553**, 55 (2018).

[13] O. Zilberberg, S. Huang, J. Guglielmon, M. Wang, K. P. Chen, Y. E. Kraus, and M. C. Rechtsman, Photonic topological boundary pumping as a probe of 4D quantum Hall physics, Nature (London) **553**, 59 (2018).

[14] S. Sugawa, F. Salces-Carcoba, A. R. Perry, Y. Yue, and I. Spielman, Second Chern number of a quantum-simulated non-Abelian Yang monopole, Science **360**, 1429 (2018).

[15] L. Lu, H. Gao, and Z. Wang, Topological one-way fiber of second Chern number, Nat. Commun. **9**, 5384 (2018).

[16] M. Kolodrubetz, Measuring the Second Chern Number from Nonadiabatic Effects, Phys. Rev. Lett. **117**, 015301 (2016).

[17] Q. Wang, K. Ding, H. Liu, S. Zhu, and C. T. Chan, Exceptional cones in 4D parameter space, Opt. Express **28**, 1758 (2020).

[18] Y. Wang, H. M. Price, B. Zhang, and Y. D. Chong, Circuit implementation of a four-dimensional topological insulator, Nat. Commun. **11**, 2356 (2020).

[19] H. M. Price, Four-dimensional topological lattices through connectivity, Phys. Rev. B **101**, 205141 (2020).

[20] R. Yu, Y. X. Zhao, and A. P. Schnyder, 4D spinless topological insulator in a periodic electric circuit, Natl. Sci. Rev. **7**, 1288 (2020).

[21] L. Li, C. H. Lee, and J. Gong, Emergence and full 3D-imaging of nodal boundary Seifert surfaces in 4D topological matter, Commun. Phys. **2**, 135 (2019).

[22] M. Ezawa, Electric circuit simulations of nth-Chern-number insulators in $2n$-dimensional space and their non-Hermitian generalizations for arbitrary n, Phys. Rev. B **100**, 075423 (2019).

[23] H. M. Price, O. Zilberberg, T. Ozawa, I. Carusotto, and N. Goldman, Four-Dimensional Quantum Hall Effect with Ultracold Atoms, Phys. Rev. Lett. **115**, 195303 (2015).

[24] T. Ozawa, H. M. Price, N. Goldman, O. Zilberberg, and I. Carusotto, Synthetic dimensions in integrated photonics: From optical isolation to four-dimensional quantum Hall physics, Phys. Rev. A **93**, 043827 (2016).

[25] O. Boada, A. Celi, J. I. Latorre, and M. Lewenstein, Quantum Simulation of an Extra Dimension, Phys. Rev. Lett. **108**, 133001 (2012).

[26] A. Celi, P. Massignan, J. Ruseckas, N. Goldman, I. B. Spielman, G. Juzeliūnas, and M. Lewenstein, Synthetic Gauge Fields in Synthetic Dimensions, Phys. Rev. Lett. **112**, 043001 (2014).

[27] M. Mancini, G. Pagano, G. Cappellini, L. Livi, M. Rider, J. Catani, C. Sias, P. Zoller, M. Inguscio, M. Dalmonte, and L. Fallani, Observation of chiral edge states with neutral fermions in synthetic hall ribbons, Science **349**, 1510 (2015).

[28] B. K. Stuhl, H.-I. Lu, L. M. Aycock, D. Genkina, and I. B. Spielman, Visualizing edge states with an atomic Bose gas in the quantum Hall regime, Science **349**, 1514 (2015).

[29] B. Gadway, Atom-optics approach to studying transport phenomena, Phys. Rev. A **92**, 043606 (2015).

[30] F. A. An, E. J. Meier, and B. Gadway, Direct observation of chiral currents and magnetic reflection in atomic flux lattices, Sci. Adv. **3**, e1602685 (2017).

[31] H. M. Price, T. Ozawa, and N. Goldman, Synthetic dimensions for cold atoms from shaking a harmonic trap, Phys. Rev. A **95**, 023607 (2017).

[32] G. Salerno, H. M. Price, M. Lebrat, S. Häusler, T. Esslinger, L. Corman, J.-P. Brantut, and N. Goldman, Quantized Hall Conductance of a Single Atomic Wire: A Proposal Based on Synthetic Dimensions, Phys. Rev. X **9**, 041001 (2019).

[33] K. Viebahn, M. Sbroscia, E. Carter, J.-C. Yu, and U. Schneider, Matter-Wave Diffraction from a Quasicrystalline Optical Lattice, Phys. Rev. Lett. **122**, 110404 (2019).

[34] L. Barbiero, L. Chomaz, S. Nascimbene, and N. Goldman, Bose-Hubbard physics in synthetic dimensions from interaction Trotterization, Phys. Rev. Research **2**, 043340 (2020).

[35] T. Chalopin, T. Satoor, A. Evrard, V. Makhalov, J. Dalibard, R. Lopes, and S. Nascimbene, Probing chiral edge dynamics and bulk topology of a synthetic Hall system, Nat. Phys. **16**, 1017 (2020).

[36] L. Yuan, Y. Shi, and S. Fan, Photonic gauge potential in a system with a synthetic frequency dimension, Opt. Lett. **41**, 741 (2016).

[37] T. Ozawa and I. Carusotto, Synthetic Dimensions with Magnetic Fields and Local Interactions in Photonic Lattices, Phys. Rev. Lett. **118**, 013601 (2017).

[38] E. Lustig, S. Weimann, Y. Plotnik, Y. Lumer, M. A. Bandres, A. Szameit, and M. Segev, Photonic topological insulator in synthetic dimensions, Nature (London) **567**, 356 (2019).

[39] L. Yuan, M. Xiao, Q. Lin, and S. Fan, Synthetic space with arbitrary dimensions in a few rings undergoing dynamic modulation, Phys. Rev. B **97**, 104105 (2018).

[40] L. Yuan, Q. Lin, A. Zhang, M. Xiao, X. Chen, and S. Fan, Photonic Gauge Potential in One Cavity with Synthetic Frequency and Orbital Angular Momentum Dimensions, Phys. Rev. Lett. **122**, 083903 (2019).

[41] L. Yuan, A. Dutt, M. Qin, S. Fan, and X. Chen, Creating locally interacting Hamiltonians in the synthetic frequency dimension for photons, Photonics Res. **8**, B8 (2020).

[42] A. Dutt, Q. Lin, L. Yuan, M. Minkov, M. Xiao, and S. Fan, A single photonic cavity with two independent physical synthetic dimensions, Science **367**, 59 (2020).

[43] Y. Baum and G. Refael, Setting Boundaries with Memory: Generation of Topological Boundary States in Floquet-Induced Synthetic Crystals, Phys. Rev. Lett. **120**, 106402 (2018).

[44] H. M. Price, T. Ozawa, and H. Schomerus, Synthetic dimensions and topological chiral currents in mesoscopic rings, Phys. Rev. Research **2**, 032017(R) (2020).

[45] P. J. D. Crowley, I. Martin, and A. Chandran, Half-Integer Quantized Topological Response in Quasiperiodically Driven Quantum Systems, Phys. Rev. Lett. **125**, 100601 (2020).

[46] E. Boyers, P. J. D. Crowley, A. Chandran, and A. O. Sushkov, Exploring 2D Synthetic Quantum Hall Physics with a Quasiperiodically Driven Qubit, Phys. Rev. Lett. **125**, 160505 (2020).

[47] T. Ozawa and H. M. Price, Topological quantum matter in synthetic dimensions, Nat. Rev. Phys. **1**, 349 (2019).

[48] K. Wódkiewicz, Fermi pseudopotential in arbitrary dimensions, Phys. Rev. A **43**, 68 (1991).

[49] F. Stampfer and P. Wagner, Mathematically rigorous formulation of the Fermi pseudopotential for higher-partial-wave scattering in arbitrary dimension, Phys. Rev. A **81**, 052710 (2010).

[50] T. T. Lê, Z. Osman, D. K. Watson, M. Dunn, and B. A. McKinney, Generalization of the Fermi pseudopotential, Phys. Scr. **94**, 065203 (2019).

[51] P. Lounesto, *Clifford Algebras and Spinors*, 2nd ed., London Mathematical Society Lecture Note Series Vol. 286 (Cambridge University Press, Cambridge, 2001).

[52] Note that many authors include the factor of $1/2$ in the definition of ξ.

[53] Any double rotation can be brought into this form by an orthogonal transform.

[54] M. Mochol-Grzelak, A. Dauphin, A. Celi, and M. Lewenstein, Efficient algorithm to compute the second Chern number in four dimensional systems, Quantum Sci. Technol. **4**, 014009 (2018).

[55] J. Koplik and H. Levine, Vortex Reconnection in Superfluid Helium, Phys. Rev. Lett. **71**, 1375 (1993).

[56] S. Nazarenko and R. West, Analytical solution for nonlinear Schrödinger vortex reconnection, J. Low Temp. Phys. **132**, 1 (2003).

[57] S. Zuccher, M. Caliari, A. W. Baggaley, and C. F. Barenghi, Quantum vortex reconnections, Phys. Fluids **24**, 125108 (2012).

[58] A. J. Allen, S. Zuccher, M. Caliari, N. P. Proukakis, N. G. Parker, and C. F. Barenghi, Vortex reconnections in atomic condensates at finite temperature, Phys. Rev. A **90**, 013601 (2014).

[59] C. Pethick and H. Smith, *Bose-Einstein Condensation in Dilute Gases* (Cambridge University Press, Cambridge, 2002).

[60] J. Gallier and D. Xu, *A Guide to the Classification Theorem for Compact Surfaces*, Geometry and Computing Vol. 9 (Springer, Berlin, 2013).

[61] Y. Kawaguchi and M. Ueda, Spinor Bose-Einstein condensates, Phys. Rep. **520**, 253 (2012).

[62] T. Machon and G. P. Alexander, Global defect topology in nematic liquid crystals, Proc. R. Soc. A **472**, 20160265 (2016).

[63] A. Hatcher, *Algebraic Topology* (Cambridge University Press, Cambridge, 2002).

Interlude: Topological aspects of intersecting vortex planes

"I tell them that if they will occupy themselves with the study of mathematics they will find in it the best remedy against the lusts of the flesh."

Thomas Mann, *The Magic Mountain*

We have just seen in Chapter 2 how the unique properties of rotations in 4D lead naturally to new vortex phenomena in four dimensional superfluids. In particular, we showed that (equal-frequency) double rotation, which does not exist in two and three dimensions, can stabilise a stationary state consisting of two completely orthogonal vortex planes that intersect at a point. Such an intersecting stationary state cannot naturally exist in 3D, since vortex lines typically only intersect as part of a dynamical process called reconnection [94]. In Chapter 3 we will investigate further questions about vortex planes, and surfaces more generally, such as the potential reconnection dynamics of vortices in 4D, and the low energy vortex states for unequal-frequency double rotation. First, however, we will explore some of the interesting topological aspects of the orthogonal intersecting state. In this interlude we will be using the Einstein summation convention.

In particular, we want to investigate whether there is any new topological invariant classifying this state in 4D. To motivate this we turn once again to the analogy between rotating superfluids and quantum Hall phases, and draw inspiration from the fact that a new invariant — the second Chern number — arises in the 4D QHE. Firstly, let us compare the mathematical form of the first Chern number C_1 and the winding number of

a superfluid. The first Chern number of a topological insulator in 2D is defined as follows

$$C_1 = \frac{1}{2\pi} \int_{BZ} F_{xy} \mathrm{d}^2 k \tag{2.1}$$

$$F_{xy} = \partial_{k_x} A_y - \partial_{k_y} A_x \tag{2.2}$$

$$\boldsymbol{A} = -i \sum_{n \text{ occupied}} \langle n, \boldsymbol{k}| \nabla_{\boldsymbol{k}} |n, \boldsymbol{k}\rangle \tag{2.3}$$

where $|n, \boldsymbol{k}\rangle$ are the eigenvectors of the system, n denotes the band index and $\boldsymbol{k}$ the momentum, $\boldsymbol{A}$ is the (Abelian) Berry connection, F_{xy} is the (Abelian) Berry curvature [28], and BZ denotes the Brillouin zone. The winding number of a superfluid, on the other hand, is

$$k = \frac{m}{2\pi\hbar} \int_{SF} \omega_{xy} \mathrm{d}^2 r \tag{2.4}$$

$$\omega_{xy} = \partial_x v_y - \partial_y v_x \tag{2.5}$$

$$\boldsymbol{v} = \frac{\hbar}{m\rho} \mathrm{Im}[\psi(\boldsymbol{r})^* \nabla \psi(\boldsymbol{r})], \tag{2.6}$$

There is a striking similarity to these equations, as well as a few key differences which we will outline. Firstly, the Berry connection and curvature are functions of momentum space, and the Chern number is an integral over the Brillouin zone torus; while the superfluid quantities are functions of real space, with the winding number integral carried out over an arbitrary superfluid geometry (SF). Secondly, the expression for the superfluid velocity field can be simplified to $\boldsymbol{v} = \hbar \nabla S/m$, while there is no such simplification for the Berry connection (due to its definition in terms of complex vectors, rather than a single complex scalar function). This of course leads to the vanishing of the vorticity ω_{xy} except along vortex lines, where it is in fact singular. For example, the velocity field of a single flat vortex, $\boldsymbol{v} = \hbar k \hat{\boldsymbol{\theta}}/mr$, leads to a vorticity of $\omega_{xy} = \hbar k \delta(r)/mr$.

Finally, the form of the Berry connection and the superfluid velocity field are not immediately analogous. We can bring both out the similarities between these two fur-

ther by making a few manipulations. Firstly, normalization of the topological insulator states, $\langle n, \boldsymbol{k}|n, \boldsymbol{k}\rangle = 1$, implies that $\langle n, \boldsymbol{k}|\nabla_{\boldsymbol{k}}|n, \boldsymbol{k}\rangle$ is pure imaginary and that the Berry connection can be rewritten as

$$\boldsymbol{A} = \sum_{n \text{ occupied}} \frac{\mathrm{Im}\left[\langle n, \boldsymbol{k}| \nabla_{\boldsymbol{k}} |n, \boldsymbol{k}\rangle\right]}{\langle n, \boldsymbol{k}|n, \boldsymbol{k}\rangle}. \tag{2.7}$$

Recalling that the superfluid density is $\rho = |\psi|^2$, we can also rewrite the superfluid velocity as

$$\boldsymbol{v} = \frac{\hbar}{m} \frac{\mathrm{Im}[\psi(\boldsymbol{r})^* \nabla \psi(\boldsymbol{r})]}{\psi(\boldsymbol{r})^* \psi(\boldsymbol{r})}. \tag{2.8}$$

Now it is clear that the only differences between these two quantities, other than the aforementioned real and momentum space mismatch, are an overall prefactor, and the fact that $\boldsymbol{A}$ is defined by a sum over multiple vector-valued states while $\boldsymbol{v}$ is defined by a single complex order parameter.

Using this somewhat formal analogy we now want to motivate a candidate topological invariant for rotating 4D superfluids. Just as we compared the winding number to the first Chern number in 2D, we are going to use the second Chern number in 4D as a guide. Since our doubly-rotating superfluid system is analogous to an Abelian (i.e. time reversal asymmetric) 4D QH system, we are going to use the Abelian Berry connection and curvature [Eqs. (2.3) and (2.2)] as before. This effectively assumes all bands are non-degenerate; for the non-Abelian 4D QHE we must generalise the Berry connection and curvature to matrices that mix degenerate bands [28]. We can therefore use the Abelian second Chern number, given by [44]

$$C_2 = \frac{1}{8\pi^2} \int_{BZ} \epsilon^{\mu\nu\sigma\tau} F_{\mu\nu} F_{\sigma\tau} \mathrm{d}^4 k, \tag{2.9}$$

such that, using our analogy, we expect a topological invariant of rotating 4D superfluids

which is proportional to

$$I = \frac{m^2}{8\pi^2\hbar^2}\int_{SF} \epsilon^{\mu\nu\sigma\tau}\omega_{\mu\nu}\omega_{\sigma\tau}\mathrm{d}^4r. \tag{2.10}$$

Consider this quantity for the intersecting orthogonal vortex plane state. The velocity field is $\boldsymbol{v} = \hbar k_1\hat{\boldsymbol{\theta}}_{\mathbf{1}}/mr_1 + \hbar k_2\hat{\boldsymbol{\theta}}_{\mathbf{2}}/mr_2$, leading to a vorticity field with only two nonzero components: $\omega_{xy} = \hbar k_1\delta(r_1)/mr_1$, and $\omega_{zw} = \hbar k_2\delta(r_2)/mr_2$. Substituting this into Eq (2.10) above, we obtain the result

$$I = \frac{m^2}{4\pi^2\hbar^2}\int_{SF} \omega_{xy}\omega_{zw}\mathrm{d}^4r, \tag{2.11}$$

$$= k_1k_2. \tag{2.12}$$

This is exactly analogous to the decomposition of the second Chern number into a product of first Chern numbers, $C_2 = C_1^{xy}C_2^{zw}$, in the lowest energy level of the 4D Harper-Hofstadter model [44]. However, this quantity is only nonzero when the two planes intersect, and, intuitively, this intersection point is not itself topologically invariant. Even if we consider both planes to be rigid, they can be separated purely via rotations and translations of the planes. For more complex order parameter fields, one can have non-Abelian vortex lines in 3D which have cannot pass through each other or reconnect, instead forming a rung when they collide [4]. This could lead to intersecting non-Abelian vortex planes which are topologically protected, and is a natural direction for future work based on this thesis.

It turns out that the quantity in Eq. (2.10) has been studied in the context of classical inviscid incompressible fluids in higher dimensions, where it is in fact an invariant of the flow-[95]. Along with the circulation in 2D, and this higher-dimensional circulation in 4D,

there is an entire family of invariants[1] of such fluids in $2m$ dimensions, given by

$$\int_D \epsilon^{i_1 j_1 i_2 j_2 \ldots i_m j_m} \omega_{i_1 j_1} \omega_{i_2 j_2} \ldots \omega_{i_m j_m} d^{2m} r, \tag{2.13}$$

where D is some region comoving with the fluid. In fact, denoting the integrand of Eq (2.13) by I_{2m}, then the integral of I_{2m}^n, for $n \in \mathbb{N}$ is also conserved in $2m$ dimensions. There is also a family of odd-dimensional invariants of these fluids, although they do not have this last property. These are given in $2m+1$ dimensions by [95]

$$\int_D \epsilon^{i_0 i_1 j_1 i_2 j_2 \ldots i_m j_m} v_{i_0} \omega_{i_1 j_1} \omega_{i_2 j_2} \ldots \omega_{i_m j_m} \mathrm{d}^{2m+1} r. \tag{2.14}$$

In 3D (i.e. $m = 1$, this quantity is the well known *helicity* of the fluid

$$\int_D \boldsymbol{v} \cdot \boldsymbol{\omega} \mathrm{d}^3 r, \tag{2.15}$$

where $(\boldsymbol{\omega})_i = \epsilon^{ijk} \omega_{jk}$ is the pseudovector form of the vorticity in 3D. The helicity can be thought of as the linking number of trajectories associated with the vorticity [95]. In 3D superfluids these trajectories are precisely the vortex lines, however direct application of Eq. (2.15) for superfluids gives a quantity that is not conserved in time [96, 97]. An alternative candidate for superfluid helicity involves another term coming directly from the phase S, and this quantity is a topological invariant, but it vanishes identically. This implies that the 4D topological invariant candidate I in Eq. (2.10) is not conserved either, because it can be related to the helicity [Eq. (2.15)] via a generalised Stoke's theorem. Given a 4D region M, we have that I in M is equal to the helicity on the boundary ∂M [98].

It seems therefore that orthogonal intersecting plane state we have discovered is tantalisingly close to realising some truly nontrivial 4D topological invariant. To pursue this

[1] sometimes referred to as topological invariants, but in a slightly different way than is used in this thesis

further it would make sense to draw analogy with the non-Abelian 4D QHE, and to investigate the possibility of non-Abelian vortices in 4D. For now, however, we move on, and in the next chapter we will see some concrete examples where the intersection point between vortex planes is not conserved.

Chapter 3

Skewed and curved vortex surfaces in 4D GPE stationary states

Je n'ai fait celle-ci plus longue que parce que je n'ai pas eu le loisir de la faire plus courte.

[I have made this longer than usual because I have not had time to make it shorter.]

Blaise Pascal

Skewed and curved vortex surfaces in stationary states of four dimensional superfluids

Ben McCanna* and Hannah M. Price†
School of Physics and Astronomy, University of Birmingham, Edgbaston Park Road, B15 2TT, West Midlands, United Kingdom

The study of superfluid quantum vortices has long been an important area of research, with previous work naturally focusing on two-dimensional and three-dimensional systems, where rotation stabilises point vortices and line vortices respectively. Interestingly, as we recently showed in Ref. [1], this physics generalises for a hypothetical four-dimensional (4D) superfluid to include vortex planes, which can have a much richer phenomenology. In particular, we showed that so-called equal-frequency "double rotations" can lead to exotic vortex structures with a core composed of two rigid orthogonal planes intersecting at a point. In this paper, we go further to study the possibility of skewed and curved vortex planes, which have no direct analogue in lower dimensions. By analytically and numerically studying the 4D Gross-Pitaevskii equation, we show that various different types of these vortex surfaces can be stabilised and favoured by double rotation with equal or unequal rotation frequencies. Our work raises open questions for further research into the physics of these vortex surfaces and suggests interesting future extensions to more realistic 4D models and to other types of topological excitations.

I. INTRODUCTION

Quantum vortices are topological excitations that play an important role in the physics of superfluids [2–10]. Such vortices are characterised by the quantized circulation of the superfluid around a local density depletion, which is called the "vortex core". As is well-studied, in a two-dimensional (2D) superfluid, the vortex core corresponds effectively to a 0-dimensional point, while for a three-dimensional (3D) superfluid, the core extends into a one-dimensional line or ring. As vortices are excitations, they are associated with an energy cost, but can be stabilised by either rotating the superfluid [4, 5], or equivalently by engineering artificial magnetic fields [11–13].

Very recently, we began in Ref. [1] to investigate the possible phenomenology of vortex structures in a four-dimensional (4D) superfluid, by studying a 4D generalisation of the Gross-Pitaevskii equation (GPE) including rotation [2]. Interestingly, the extension to 4D considerably enriches the possible vortex structures as there are fundamental differences between rotations (or equivalently, magnetic fields) in different numbers of spatial dimensions. As we shall review further below, in 2D and 3D, all rotations are "simple rotations" that can be characterised by a single rotation plane and rotation frequency, while in 4D, generic rotations are "double rotations", meaning that two completely orthogonal planes of rotation, and hence two rotation frequencies, can be identified. In Ref. [1], we explored how the simplest case of a double rotation with equal frequencies can stabilise a new type of vortex structure in which the vortex core consists of two rigid orthogonal planes intersecting at a point, with no direct analogue in lower dimensions.

In this paper, we shall go further to explore what happens as the two rotation frequencies in a 4D system are either simultaneously varied or made unequal. As we shall show, this can lead to 4D vortex structures with cores composed of skewed non-orthogonal surfaces which curve to avoid the expected intersection point. As evidence for this, we shall present both analytical and numerical calculations based on the 4D generalised GPE under rotation. We shall develop and numerically test a theory to explain the skewed vortex planes in terms of a simplified competition between the rotational energy and the hydrodynamic vortex-vortex interaction terms. For unequal and equal frequency double rotations, we find different skewed and/or curved vortex surfaces that can be comparable to or even lower in energy than a pair of rigid orthogonal vortex planes [1] for our system sizes and parameters. We also note qualitative similarities between the curvature of these vortex surfaces in 4D and the reconnection of vortex lines in 3D, raising interesting questions for future research.

Going further, we note that we have studied a *minimal* 4D mathematical model, which is motivated as a natural extension of the standard GPE description of 2D and 3D superfluids. In the future, it will also be very interesting to explore if similar structures can be found in more experimentally-realistic models, connecting with recent theoretical and experimental advances in probing higher-dimensional physics [14–27], e.g. using techniques such as "synthetic dimensions" [16, 28–52]. More generally, the rich phenomenology of curved vortex surfaces that we have begun to explore raises the possibility of finding other exotic topological excitations, such as closed vortex surfaces, which could generalise and extend the physics of vortex loops in 3D systems. Finally, our results suggest that vortices can lose some of their individual character in 4D, as the curved surfaces that we have found do not easily decompose into two separate but intersecting vortex states, unlike in Ref. [1]. This opens interesting questions, for example, about what would happen at

* [redacted]

even higher rotation frequencies, where we may expect the number of vortices to become large.

Outline of Paper

We shall begin in Section II by reviewing the basic physics of quantum vortices in both 2D and 3D superfluids, as described by the GPE equation. Then in Section III, we shall discuss in more detail the different possible types of rotations in four spatial dimensions, including simple, double and isoclinic rotations. As part of this section, we shall discuss the rotation planes of isoclinic rotations in detail, as this will be useful for later sections of the paper. In Section IV, we shall briefly review the 4D GPE and the physics of completely orthogonal 4D vortex planes, which were studied in 4D doubly-rotating superfluids with equal rotation frequencies in Ref. [1]. We shall also introduce the numerical methods to be used throughout this work. In Section V, we shall then derive the hydrodynamic energy of a pair of non-orthogonal skewed 4D vortex planes that intersect at a point, and discuss the possibility that such planes would reconnect. As we then develop in Section VI, our hydrodynamic theory predicts that, in a doubly-rotating 4D superfluid with two unequal rotation frequencies, a pair of rigid vortex planes will become skewed so as to start aligning with the higher frequency and with each other. Our numerical results verify this predicted skewness at large distances, but also show that the vortex surfaces curve near the origin to avoid the intersection point, in a manner reminiscent from reconnection. In Section VII, we shall then extend our discussion to equal-frequency double rotations, and ask whether this can favour anti-aligning skewed vortex surfaces. Numerically, we find that such skewed (and curved) structures can be comparable to or even slightly lower in energy than rigid orthogonal vortex planes for our system parameters, showing that 4D superfluids support a rich vortex phenomenology. Finally, in Section VIII, we shall summarize our results and discuss possible future extensions to this work.

II. REVIEW OF SUPERFLUID VORTICES

In this section, we shall briefly review the basic properties of quantized vortices in 2D and 3D superfluids. We shall begin by introducing the GPE and reviewing how this leads to the structure of a 2D superfluid vortex, before discussing the energy of such a state within a finite system. We shall then briefly discuss systems with multiple 2D vortices, before reviewing some aspects of vortex physics in 3D superfluids. This will lay the groundwork for the discussion of 4D vortices in Section IV onwards.

II.1. Structure of a 2D Superfluid Vortex

We consider a system of weakly-interacting bosons in the absence of an external potential as can be described by the time independent Gross-Pitaevskii equation [2]

$$-\frac{\hbar^2}{2m}\nabla^2\psi + g|\psi|^2\psi = \mu\psi, \tag{1}$$

where ψ is the complex order parameter, m is the mass of the particle, g is the interaction strength, and μ is the chemical potential. Note that a harmonic trapping potential is also often included in the GPE, as this is present in many ultracold gas experiments [2–8, 53]; however, for simplicity we will neglect all such effects and restrict our discussion to infinite systems and finite systems with hard-wall boundary conditions, as specified below.

From the order parameter, it is possible to directly define the superfluid density, phase, and velocity fields as $\rho = |\psi|^2$, $S = \mathrm{Arg}\,\psi$ and $\mathbf{v} = \frac{\hbar}{m}\nabla S$, respectively [2]. Importantly, the form of the velocity field implies that the circulation of the superfluid around any closed loop C has to be quantized with the circulation being given by

$$\oint_C \mathbf{v}\cdot\mathrm{d}\mathbf{r} = \frac{\hbar}{m}\oint_C \nabla S\cdot\mathrm{d}\mathbf{r},$$

where the integral on the right hand side gives the change in the superfluid phase around the loop C. This would be zero if S is single-valued, but since S is a phase and its value is only defined modulo 2π, so the superfluid circulation is quantized generally as [2–5, 10]

$$\oint_C \mathbf{v}\cdot\mathrm{d}\mathbf{r} = 2\pi k\frac{\hbar}{m}, \tag{2}$$

where k is an integer called the winding number. Note that continuous deformations of the loop C within the superfluid will not change the integer winding number, since $\mathbf{v}$ varies continuously so long as ψ is non-zero. This means that $k \in \mathbb{Z}$ is a topological invariant, which will be equal to zero whenever C can be continously contracted to a point. Hence, a simply-connected superfluid (i.e. one in which all loops are contractible) cannot circulate.

If a simply-connected superfluid is rotated, it therefore cannot behave as a rigid body but will instead form internal holes, called vortices, where the density goes to zero and around which the phase winds by a quantized amount [2–8, 53]. In 2D, the structure of a rotationally-symmetric vortex is described by

$$\psi(r,\theta) = |\psi(r)|e^{ik\theta}, \tag{3}$$

where (r,θ) are 2D polar coordinates centered on the vortex core. The winding number k corresponds to the topological charge of the vortex, and is conventionally taken to be positive for vortices and negative for anti-vortices. From the above ansatz, the vortex velocity field is then [2]

$$\mathbf{v} = \frac{\hbar}{m}\nabla(k\theta) = \frac{\hbar}{mr}k\hat{\boldsymbol{\theta}}, \tag{4}$$

where $\hat{\boldsymbol{\theta}}$ is the unit vector pointing along the θ direction. As required by Eq. (2), this velocity field falls off as $1/r$, and reverses direction when the sign of the winding number, k, is flipped. The angular momentum of the vortex in Eq. (3) is also quantized as

$$\mathbf{L} = \mathbf{r} \times m\mathbf{v} = \hbar k \hat{\boldsymbol{z}}$$

with respect to the axis through the center of the vortex core, with $\hat{\boldsymbol{z}}$ being the unit vector pointing out of the 2D plane, along the z direction. More generally, in a system with axial symmetry, the angular momentum is quantized only for an on-axis vortex [3].

To complete this description of the vortex state [Eq. (3)], the density-profile can be obtained numerically by solving the GPE [Eq. (1)]. When so doing, it is common to define the uniform background density as n and then rescale $\psi \to \sqrt{n}\psi$ and $\mathbf{r} \to \xi\mathbf{r}$, where ξ is the healing length, which satisfies $\hbar^2/m\xi^2 = gn = \mu$, and which physically is the distance over which ρ typically varies. (Note that often a factor of $1/2$ is included in the definition of ξ [2].) Under these rescalings, Eq. (1) becomes dimensionless as

$$-\frac{1}{2}\nabla^2\psi + |\psi|^2\psi = \psi,$$

which is then solved numerically [2, 3] to obtain a dimensionless real-valued density profile function $f_k(r) = |\psi|$. While the obtained $f_k(r)$ has no closed form, it can be shown that it asymptotically vanishes towards the vortex core as $f_k(r) = \mathcal{O}(r^{|k|})$ when $r \to 0$, and asymptotically returns to the profile of a homogeneous superfluid as $f_k(r) = 1 - \mathcal{O}(r^{-2})$ when $r \to \infty$ [5], with a crossover between these two behaviours around the healing length.

II.2. Energy of a 2D Superfluid Vortex

Within a hydrodynamic description [2, 3, 10], the energy of a 2D vortex in the absence of an external potential is made up of a kinetic contribution

$$E_{\rm kin}[\psi] = \frac{\hbar^2}{2m}\int (\nabla\sqrt{\rho})^2 \mathrm{d}^2r + \frac{m}{2}\int \rho\mathbf{v}^2\mathrm{d}^2r, \quad (5)$$

and an inter-particle interaction contribution

$$E_{\rm int}[\psi] = \frac{1}{2}g\int \rho^2\mathrm{d}^2r, \quad (6)$$

where the integrals are carried out over the area of the 2D system, which we consider to be circular with radius R and hard-wall boundary conditions.

Both of the above contributions can be estimated analytically by assuming that the density is zero within the vortex core, which we take to be circular with a radius of our healing length ξ, and constant otherwise across the system. (Note that other definitions for the size of the vortex core can be used [2, 10]; however, the following argument is only approximate and such changes do not significantly affect the relative scaling and importance of the different energy terms.) For such a simple, so-called "hollow-core", model for a vortex, the total energy difference, ΔE, between the homogeneous and the vortex state is straightforward to calculate; firstly, in the hydrodynamic kinetic energy (Eq. (5)) introduced above, the first ("quantum pressure") term vanishes so that the extra kinetic energy due to a vortex is given simply by [2]

$$\Delta E_{\rm kin} = \frac{m}{2}\int \rho\mathbf{v}^2\mathrm{d}^2r \simeq k^2\pi n\frac{\hbar^2}{m}\ln\left(\frac{R}{\xi}\right), \quad (7)$$

where n is the constant density within the system outside of the vortex core. Similarly, the interaction energy (i.e. the energy needed to make a hole in the superfluid) can be calculated as

$$\Delta E_{\rm int} \simeq \frac{1}{2}gn^2\xi^2\pi. \quad (8)$$

The latter can clearly be neglected for a large system with $R \gg \xi$, meaning that the total hydrodynamic energetic cost of a vortex can be approximated as [10]

$$E_{\rm h} \approx \Delta E_{\rm kin} \simeq k^2\pi n\frac{\hbar^2}{m}\ln\left(\frac{R}{\xi}\right) \quad (9)$$

A more accurate estimate of the energy cost relative to the uniform state can be found using the dimensionless numerical density-profile function, $f_k(r)$, in the vortex-state ansatz [Eq. (3)]. Using the grand canonical energy at fixed chemical potential μ takes care of corrections to the background density n from the core depletion. Then, using that, $\mu = \hbar^2/m\xi^2$, and $n = N/\pi R^2$, in the uniform system, where N is the total number of bosons, we may write this numerical vortex energy as

$$E_k(R) = k^2\mu N\left(\frac{\xi}{R}\right)^2\ln\left(2.07\frac{R}{\xi}\right), \quad (10)$$

which importantly is the same functional form as the simple hydrodynamic estimate [Eq. (9)], up to the numerical prefactor within the logarithm. (Note that if the healing length had instead been defined including a factor of $1/2$ as $\hbar^2/2m\xi^2 = gn = \mu$, then this numerical prefactor becomes 1.46 [2].)

Vortices can be energetically stabilised by rotation (or equivalently an artificial magnetic field) [4, 5]. In a rotating reference frame, the GPE [Eq. (1)] becomes

$$\left[-\frac{\hbar^2}{2m}\nabla^2 + g|\psi|^2 - \boldsymbol{\Omega}\cdot\hat{\mathbf{L}}\right]\psi = \mu\psi, \quad (11)$$

where $\hat{\mathbf{L}} = -i\hbar\mathbf{r}\times\nabla$ is the (3D) angular momentum operator, and $\boldsymbol{\Omega}$ is the rotation frequency vector [2]. In 2D, we can assume that $\boldsymbol{\Omega} = \Omega\hat{\boldsymbol{z}}$, and hence the energy reduction from rotation is given by $\Delta E_{\rm rot} = \Omega\langle\hat{L}_z\rangle$. As discussed above, vortices carry a finite amount of angular momentum and so are favoured by rotation.

To leading order, we can assume the superfluid has a constant density and neglect the depletion of the core, so that the energy reduction from rotation can be calculated as [2]

$$\Delta E_{\rm rot} = \Omega \langle \hat{L}_z \rangle \simeq \Omega \hbar k \pi n R^2. \tag{12}$$

(This approximation cannot be applied to the calculation of the hydrodynamic energy of a single vortex [Eq. (7)] as the $1/r^2$ dependence of the integrand gives a singular contribution from the area around $r = 0$.) As can be seen, this term reduces the energy of a state containing a vortex for which the circulation is aligned with the rotation, and raises the energy of a state (with opposite k) that is anti-aligned with the rotation. For a vortex to be energetically stabilised, the reduction in energy must be greater than (or equal to) the cost of making a vortex within the same approximations (e.g. Eq. (9)). This leads to an estimate of the critical frequency of [2]

$$\Omega_c^{2D} \simeq k \frac{\hbar}{mR^2} \ln\left(\frac{R}{\xi}\right),$$

i.e. this is the minimal rotation frequency needed to stablise a vortex with winding number k. Using the energy for the numerical vortex profile (Eq. (10)) leads to a more accurate calculation for this frequency as

$$\Omega_c^{2D} = k \frac{\hbar}{mR^2} \ln\left(2.07 \frac{R}{\xi}\right). \tag{13}$$

Note also that this critical frequency will depend on any external potentials that are present, and so will be different, e.g. with a harmonic trap [3]. However, in this paper, we will focus on untrapped systems with hard-wall boundary conditions, as mentioned above.

II.3. Multiple Vortices in a 2D Superfluid

As can be seen from Eq. (13), the critical rotation frequency is proportional to the winding number k, meaning that higher frequencies are required to stabilise vortices with higher winding numbers. However, by comparing the hydrodynamic energy with the rotation energy, it can be seen that, even at higher frequencies, it will always be energetically unfavourable (in the absence of additional external potentials) to produce a multiply charged vortex (i.e. with $|k| > 1$) as compared to multiple singly-charged vortices (with $|k| = 1$) [10].

The above argument also suggests that a pair of similarly-charged 2D vortices will interact repulsively, as it is energetically unfavourable to bring them together and merge them into a single vortex with a higher winding number. Indeed, it can be shown that, in a sufficiently large system, the interaction energy between a pair of well-separated vortices, with charges k_1 and k_2 respectively, can be approximated as [3]

$$\Delta E_{\rm pair} \propto k_1 k_2 \ln\left(\frac{R}{\Delta r}\right) \tag{14}$$

where Δr is the distance between the two vortex cores. As can be seen, this is attractive for oppositely-charged vortices (i.e. a vortex and anti-vortex pair) but repulsive for vortices with the same sign. In an infinite system, a pair of vortices will therefore continually move apart, while a vortex and anti-vortex pair can move together and annihilate. Note that Eq. (14) is derived under the approximation that the density is constant everywhere in the system, i.e. ignoring the density depletion at the vortex core. Consequently, the calculated vortex-vortex interaction energy [Eq. (14)] is only valid for separations $\Delta r \gg \xi$, and attempting to take the limit $\Delta r \to 0$ gives a logarithmic divergence. In reality, when a pair of vortices with winding numbers $k_{1,2}$ come together, they combine into a vortex with winding number $k_1 + k_2$. One can still obtain this correct result from Eq. (7) if we consider the vortices to be combined once their separation is similiar to the healing length $\Delta r \sim \xi$. This is consistent with the constant density approximation, as the latter amounts to ignoring variations on the scale of ξ or below (except in the presence of a trap).

As the rotation frequency increases therefore above the critical frequency [Eq. (13)], it will be energetically favourable to have more and more singly-charged vortices in the system. The effectively repulsive interactions between these vortices then mean that, at high enough rotation frequencies, the lowest energy state in the rotating frame exhibits a uniform array of vortices, known as an Abrikosov lattice [3, 54].

II.4. Vortices in 3D Superfluids

The above discussion can be straightforwardly generalised to describe vortices in a 3D superfluid [2, 3, 10]. In 3D, a vortex core can be approximated as an extended 1D line, which must either begin and end on the surface of the system, or else form a closed loop within the superfluid. The former structures are often referred to as "vortex lines" or "vortex filaments", while the latter are typically called "vortex rings" [10, 55–60]. As our paper is concerned with the lowest-energy vortex structures to be stabilised by rotation, we shall hereafter focus on vortex lines, although it would also be very interesting to study the analogue of vortex rings in higher dimensions.

In the simplest case, a cylindrically-symmetric vortex line in 3D can be described [10] e.g. by

$$\psi(r, \theta, z) = |\psi(r, z)| e^{ik\theta},$$

in cylindrical polar coordinates (r, θ, z), where we have assumed that the rotation axis lies along the z direction and that the rotation is sufficiently strong so as to align and straighten the vortex core. In the absence of an additional potential, the vortex structure is then invariant along the z direction and the dimensionless density profile is given by the radial function found numerically from the 2D GPE. Consequently, a 3D vortex line has the same velocity field as a 2D vortex [Eq. (4)], as well as the same

critical frequency (in a cylindrical system) [10]. The latter point can be easily appreciated by noting that, in this case, the 2D calculation for the hydrodynamic energy follows through identically up to an overall multiplicative factor in both Eq. (9) and Eq. (12), to represent the height of the system [10].

Similarly, when the rotation frequency becomes much higher than the critical frequency, many vortices enter the 3D system, and should eventually form a vortex lattice analogous to that in 2D, except with the vortex cores extended as straight lines along the rotation axis [9, 10]. It is also worth noting that, unlike in 2D, the shape and orientation of a 3D vortex line can depend, for example, on both the choice of rotation axis as well on the geometry and boundary conditions of the system [56]. For example, in 3D there can be a competition between aligning the vortex core with the rotation axis in order to capitalise on energy reduction from rotation, and minimising the length of the vortex core in the superfluid so as to minimise the interparticle interaction energy.

Another new phenomenon that emerges in 3D is the reconnection of vortex lines [61]; when two vortex lines are made to intersect in 3D, they will dynamically reconnect and move apart so as to remove the intersection point. This process plays an important role, e.g. in quantum turbulence [62], and has been studied in detail theoretically [63–70], and in various superfluid experiments [55, 71–73]. As we shall review later in Section IV, a key difference between 3D and 4D superfluids is that, in the latter case there can be an intersection point between two vortex planes in a stationary state [1]. However, as we shall go on to explore in Section V onwards, we can also find stationary states with curved vortex surfaces, in which the vortex core curves spatially in order to avoid the intersection point. As the shape of these curved surfaces is reminiscent of the shape of 3D vortex lines shortly after a reconnection event, we shall now review briefly how reconnections can be approximated analytically in 3D superfluids [64].

In 3D, vortex-line reconnection is a dynamical process in which the vortex cores approach each other, intersect, reconnect and then separate over time. At very short times before or after the moment of reconnection, Nazarenko and West showed in a seminal paper that it is possible to analytically approximate the wavefunction solution close to the reconnection point, by assuming that nonlinear effects are small [64]. This assumption is justified by noting that the wave-function is spatially continuous and vanishes at the vortex cores, meaning that the particle density is low near the reconnection point. To a first approximation, the reconnection evolution can then be described by the (dimensionless) 3D linearised time-dependent GPE

$$-\frac{1}{2}\nabla^2\psi = i\dot{\psi}$$

close to the intersection point (at $\mathbf{r} = 0$). If the wavefunction at the moment of intersection ($t = t_0$) is denoted by $\psi = \psi_0$, then after a short time interval $\Delta t = (t - t_0)$, the state evolution can be approximated as:

$$\psi = \psi_0 + i\frac{\Delta t}{2}\nabla^2\psi_0. \tag{15}$$

At $t = t_0$, a reasonable ansatz for the wave-function near the intersection point is given by [64]

$$\psi_0 = z + i(az + bx^2 - cy^2)$$

where a, b, c are some positive constants, corresponding to a state containing two straight vortex cores (defined by $\psi_0 = 0$) that intersect at the origin. According to Eq. (15), such a state will evolve dynamically to [64]

$$\psi = z - (b - c)\Delta t + i(az + bx^2 - cy^2).$$

For times both before ($\Delta t < 0$) or after ($\Delta t > 0$) the moment of reconnection, this solution describes two unconnected hyperbolae, corresponding physically to two separated and curving vortex filaments. Interestingly, even such a simple linear approach reproduces many of the observed properties of vortex reconnections found in numerical simulations, such as that the vortex lines locally approach each other in an anti-parallel configuration [64, 69]. However, as this method does not describe the behaviour far from the vortex cores, the linear approach cannot predict effects such as the far-field emission of sound waves by the reconnection event; to overcome such limitations, the linear solution can be substituted back into the GPE including nonlinear terms in order to find successive nonlinear corrections, and hence to analytically calculate a fully nonlinear analytical solution within a finite volume and finite evolution time [64].

III. ROTATIONS IN 4D

In order to further lay the groundwork for our discussion of 4D vortex structures in Section IV, we shall now review the different types of rotations that are possible with four spatial dimensions, comparing these with 2D and 3D systems. We shall begin by introducing the concepts of simple, double and isoclinic rotations, before discussing the possible rotation planes of 4D isoclinic rotations in more mathematical detail. As we shall see, this will be relevant when considering the effects of rotation in a generalised 4D GPE in later parts of this paper.

III.1. Simple, double, and isoclinic rotations

In two dimensions, rotations are completely specified by their centre and rotation angle. The centre is the one fixed point of the rotation, while all other points are angularly displaced about the centre by the rotation angle. Represented as a matrix, any rotation of 2D space will be given as

$$\begin{pmatrix} \cos\alpha & -\sin\alpha \\ \sin\alpha & \cos\alpha \end{pmatrix},$$

where $\alpha \in (-\pi, \pi]$ is the angle of rotation and we are defining the origin as the centre of rotation, as we will throughout this paper.

Similarly, rotations in three dimensions are commonly described in terms of their axis and angle of rotation. The axis is both the line of points fixed by the rotation and the centre about which the rotation occurs. One can equally define rotations in 3D by their plane of rotation, which is orthogonal to the axis of rotation. All rotations in 3D are just 2D rotations of their plane of rotation, with the third direction left unchanged. This is obvious from the matrix representation of a 3D rotation, which can always be brought into the following form

$$\begin{pmatrix} \cos\alpha & -\sin\alpha & 0 \\ \sin\alpha & \cos\alpha & 0 \\ 0 & 0 & 1 \end{pmatrix},$$

via a suitable choice of basis. The rotation plane is left invariant by the rotation but not pointwise invariant, unlike the axis. This means that points on the rotation plane remain on it after the rotation, but are rotated about the rotation axis.

Just as we can extend 2D rotations into a third direction to define 3D rotations, we may generate rotations of 4D space by extending 3D rotations into a fourth direction. In the 3D case this gave us every possible rotation, up to a change of basis. However, in 4D we can only generate a proper subset of rotations by extending our 3D definitions in this way. Members of this subset are commonly termed "simple" rotations, since they reduce to the familiar three and two dimensional cases. Simple rotations have a single rotation plane just as in the 3D case, but are centred around a plane of fixed points as opposed to an axis. This fixed plane is completely orthogonal to the rotation plane, by which we mean that every vector in one plane is orthogonal to every vector in the other. In a matrix representation, any simple rotation of 4D space can take the following form in a suitable basis

$$\begin{pmatrix} \cos\alpha & -\sin\alpha & 0 & 0 \\ \sin\alpha & \cos\alpha & 0 & 0 \\ 0 & 0 & 1 & 0 \\ 0 & 0 & 0 & 1 \end{pmatrix}. \tag{17}$$

Note that in 4D, there are six Cartesian coordinate planes, meaning that the rotation group $SO(4)$ of four-dimensional space has *six* generators, physically describing angular momentum. For this reason, the representation of these generators (and hence of angular momentum) as spatial vectors does not work in 4D, as it does in 3D.

Moreover, generic elements of $SO(4)$ are so-called "double" rotations. These new types of rotations occur simultaneously through two completely orthogonal planes of rotation (e.g. the x–y and z–w planes), each with their own rotation angle. Represented as a matrix, any double rotation can be brought into the form

$$M(\alpha, \beta) = \begin{pmatrix} \cos\alpha & -\sin\alpha & 0 & 0 \\ \sin\alpha & \cos\alpha & 0 & 0 \\ 0 & 0 & \cos\beta & -\sin\beta \\ 0 & 0 & \sin\beta & \cos\beta \end{pmatrix}, \tag{18}$$

by a suitable change of basis. This matrix form makes it clear that a double rotation can be thought of as two simultaneous simple rotations: in this case a rotation of angle $\alpha \in (-\pi, \pi]$ in the x–y plane, and one of angle $\beta \in (-\pi, \pi]$ in the $(z$–$w)$ plane. This means that any point on the x–y or z–w plane will remain on it but be rotated around the origin by an angle α or β, respectively. Points not on either rotation plane are rotated by an angle whose magnitude is strictly between $|\alpha|$ and $|\beta|$ [74], assuming that $|\alpha| < |\beta|$. Consequently, the origin is the only fixed point, as long as neither rotation angle is zero. If either angle vanishes, we recover simple rotations as a special case of double rotations.

Besides simple rotations there is another very important special class of double rotations, called "isoclinic" rotations, which will play an important role in the rest of this paper. These are the double rotations where both rotation angles are equal up to a sign, such as $M(\alpha, \alpha)$ and $M(\alpha, -\alpha)$. They come in two types known as right handed and left handed based on the relative senses of rotation in the two planes. For example, $M(\alpha, \alpha)$ is a left isoclinic rotation of the x–y and z–w planes, while $M(\alpha, -\alpha)$ is a right isoclinic rotation of these planes. All left isoclinic rotations commute with all right isoclinic ones, and any rotation of 4D space can be decomposed into a product of a left isoclinic rotation and a right isoclinic rotation [74]. However, this is not unique, as $M = M_L M_R$ can also be written as $M = (-M_L)(-M_R)$, where M_L and M_R denote left and right isoclinic rotations respectively.

III.2. Rotation Planes of an Isoclinic Rotation

In later sections of this paper, we will find it useful to take advantage of various mathematical properties of isoclinic rotations in our analysis of vortices in 4D superfluids. For that reason, we shall now discuss these special types of rotations in greater detail, focusing in particular on how to identify the rotation planes of left and right isoclinic rotations respectively.

Recall that a general double rotation will rotate a vector through an angle with magnitude between $|\alpha|$ and $|\beta|$. However, for an isoclinic rotation $\alpha = \pm\beta$, so every vector is displaced by the same given rotation angle, meaning that there is an infinite number of rotation planes. Each of these rotation planes can be described as the span of an arbitrary vector $\mathbf{v}$ and its image under the rotation (i.e. either $M_L\mathbf{v}$ or $M_R\mathbf{v}$), which means that every point in $\mathbb{R}^4$ lies on one of these rotation planes [74]. However, this does not imply that every possible 2D plane is a rotation plane (except for very special cases, as mentioned below),

nor does it mean that these rotation planes are unique: any completely orthogonal pair of them can be used as a basis to define the particular isoclinic rotation. For example, from Eq. (18) we can see that two of the rotation planes of $M(\alpha,\alpha)$ are given e.g. by the x–y and z–w rotation planes, although these are not the only rotation planes as we shall see below. This is in contrast to generic double rotations (i.e. $M(\alpha,\beta)$, with $\alpha \neq \beta \neq 0,\pi$), which have only two unique rotation planes as discussed above.

Our aim is now to mathematically identify the rotation planes of a given isoclinic rotation, which we shall denote as $M_L \equiv M(\alpha,\alpha)$, i.e. we chose our basis such that this particular rotation has the form given in Eq. (18) with $\alpha = \beta$. As we shall see, an easy way to find the corresponding rotation planes is then to use the complex representation $\mathbb{C}^2$ to represent $\mathbb{R}^4$, such that the Cartesian position vector $(x,y,z,w)^T$ is represented by $(x+iy, z+iw)^T$. Note that the natural inner product in $\mathbb{C}^2$, given in Cartesian coordinates by

$$\begin{pmatrix} x+iy \\ z+iw \end{pmatrix}^\dagger \begin{pmatrix} x'+iy' \\ z'+iw' \end{pmatrix} = xx'+yy'+zz'+ww' \\ +i(xy'-yx'+zw'-wz'),$$

contains the inner product in $\mathbb{R}^4$ as its real part. This means that any unitary matrix acting on $\mathbb{C}^2$ will be equivalent to some orthogonal matrix acting on $\mathbb{R}^4$. However, the converse is not necessarily true as unitary matrices preserve both the real and imaginary parts of the complex inner product, while orthogonal transformations need only preserve the real inner product. Nevertheless, we can say that if an orthogonal transformation of $\mathbb{R}^4$ (e.g. such as a 4D rotation) is represented by a matrix in the complex representation then that complex matrix is automatically unitary. To see this, note that the norm on $\mathbb{C}^2$ agrees with the norm on $\mathbb{R}^4$, that is

$$\begin{pmatrix} x+iy \\ z+iw \end{pmatrix}^\dagger \begin{pmatrix} x+iy \\ z+iw \end{pmatrix} = \begin{pmatrix} x \\ y \\ z \\ w \end{pmatrix}^T \begin{pmatrix} x \\ y \\ z \\ w \end{pmatrix}.$$

As any orthogonal transformation will preserve the $\mathbb{R}^4$ norm, so its $\mathbb{C}^2$ representation will preserve the corresponding complex norm, meaning that if that representation is a complex matrix it must therefore be a unitary matrix.

Returning to the particular case of double rotations, we see that in the complex representation, Eq. (18) becomes:

$$M(\alpha,\beta) = \begin{pmatrix} e^{i\alpha} & 0 \\ 0 & e^{i\beta} \end{pmatrix}, \tag{19}$$

which is indeed unitary. It is also clear that the desired left isoclinic rotation M_L can simply be represented in $\mathbb{C}^2$ as $e^{i\alpha}$ times the identity. We will now use this to show how to construct and parametrise the rotation planes of this left isoclinic rotation using this complex representation, before also discussing the case of right isoclinic rotations. Note that, in the following, rather than Cartesian coordinates, we shall primarily use double polar coordinates $(r_1,\theta_1,r_2,\theta_2)$, which are defined by $r_1e^{i\theta_1} \equiv x+iy$, and $r_2e^{i\theta_2} \equiv z+iw$, such that the complex position vector becomes $(r_1e^{i\theta_1}, r_2e^{i\theta_2})^T$ in the complex representation.

In general, a 2D plane in $\mathbb{R}^4$ can be defined as the set of solutions to a pair of simultaneous linear equations (e.g. $x=0$ together with $y=0$ defines the z–w plane passing through the origin). In contrast, in the complex representation we can define a plane using a single equation which is linear in $r_{1,2}e^{i\theta_{1,2}}$ and their complex conjugates. In other words, given four complex numbers (a_1,a_2,b_1,b_2), the equation

$$a_1r_1e^{i\theta_1} + a_2r_2e^{i\theta_2} + b_1r_1e^{-i\theta_1} + b_2r_2e^{-i\theta_2} = 0 \tag{20}$$

defines a plane passing through the origin, and any such plane can be defined (not uniquely) in this way. (For example, the above z–w plane can now be defined simply either as $r_1e^{i\theta_1}=0$ or equivalently as $r_1e^{-i\theta_1}=0$.) To get back to the real representation we then just take the real and imaginary parts of the complex equation. Note that we included the complex conjugates $r_{1,2}e^{-i\theta_{1,2}}$ in Eq. (20) so that the complex equation can have the same number of parameters as the two real equations.

As the rotation planes of M_L are invariant under M_L, to find these rotation planes we must find the equations of the form (20) that are also invariant in this way. The action of the left isoclinic rotation, M_L, is given by $\theta_{1,2} \to \theta_{1,2}+\alpha$ as introduced above, so that the image of Eq. (20) under M_L is given by

$$e^{i\alpha}\left(a_1r_1e^{i\theta_1} + a_2r_2e^{i\theta_2}\right) \\ + e^{-i\alpha}\left(b_1r_1e^{-i\theta_1} + b_2r_2e^{-i\theta_2}\right) = 0.$$

For this to reproduce Eq. (20), we require that, in general, either $a_{1,2}=0$ or $b_{1,2}=0$. Note that for the special angles of $\alpha = 0,\pi$, we recover Eq. (20) irrespective of the values of (a_1,a_2,b_1,b_2), meaning that every single plane is a rotation plane of M_L for these cases. However, these special cases are trivial as they physically correspond to, respectively, no rotation or to flipping the direction of all axes simultaneously. Focusing therefore on the general case, we identify two possibilities: either

$$a_1r_1e^{i\theta_1} + a_2r_2e^{i\theta_2} = 0, \tag{21}$$

or

$$b_1r_1e^{-i\theta_1} + b_2r_2e^{-i\theta_2} = 0.$$

However, we can map the latter equation onto the former by taking the complex conjugate of both sides and identifying $b_1^* = a_1$, and $b_2^* = a_2$. Therefore, both cases are the same and so the rotation planes of M_L are given by the solutions to the equation $a_1r_1e^{i\theta_1} + a_2r_2e^{i\theta_2} = 0$, for arbitrary complex numbers $a_{1,2}$.

In later sections of this paper, we will want to sometimes work in a coordinate system defined in relation to an arbitrary completely orthogonal pair of these rotation

planes (which we will denote as P_1 and P_2), in the same way that the coordinates $(r_1, \theta_1, r_2, \theta_2)$ are defined in relation to the x–y and z–w planes. We shall therefore now go through how such a coordinate system can be defined. To begin, let P_j be given by the solutions to

$$a_{j1} r_1 e^{i\theta_1} + a_{j2} r_2 e^{i\theta_2} = 0, \tag{22}$$

for $j = 1, 2$, and let our coordinate system defined with respect to these planes be given by $(r'_1, \theta'_1, r'_2, \theta'_2)$. Note that the coefficients a_{jk} are not all independent: once the plane P_1 is chosen, P_2 is already fixed as the orthogonal complement of P_1. For now we will not consider this constraint, but will effectively derive it later by comparing the primed and unprimed coordinate systems.

We now proceed to define the primed coordinates. Recalling that the x–y and z–w planes are defined by $r_2 e^{i\theta_2} = 0$ and $r_1 e^{i\theta_1} = 0$ respectively, we see that in our new coordinate system the planes $P_{1,2}$ should be given by $r'_{1,2} e^{i\theta'_{1,2}} = 0$ respectively. Given Eq. (22), a simple way to achieve this is to define our coordinates as follows

$$\begin{pmatrix} r'_1 e^{i\theta'_1} \\ r'_2 e^{i\theta'_2} \end{pmatrix} = \begin{pmatrix} a_{11} & a_{12} \\ a_{21} & a_{22} \end{pmatrix} \begin{pmatrix} r_1 e^{i\theta_1} \\ r_2 e^{i\theta_2} \end{pmatrix}.$$

Let us now determine the way in which the coefficients a_{jk} are constrained. This can be done by noting that the unprimed coordinates are an orthonormal system; for this to also be true of the primed coordinates, we must have that the total distance from the origin is preserved, that is

$$r'^2_1 + r'^2_2 = r^2_1 + r^2_2.$$

This condition is equivalent to requiring that the coefficients a_{jk} furnish a unitary 2×2 ($U(2)$) matrix, such that $a_{22} = e^{i\varphi} a^*_{11}$, $a_{21} = -e^{i\varphi} a^*_{12}$, and $|a_{11}|^2 + |a_{12}|^2 = 1$. This can be satisfied with the following parametrisation

$$\begin{pmatrix} a_{11} & a_{12} \\ a_{21} & a_{22} \end{pmatrix} = \begin{pmatrix} e^{i\varphi_1} \cos\eta & -e^{-i\varphi_2} \sin\eta \\ e^{i\varphi_2} \sin\eta & e^{-i\varphi_1} \cos\eta \end{pmatrix} e^{i\varphi_3} \tag{23}$$

with $\varphi_{1,2,3} \in [0, 2\pi)$, and $\eta \in [0, \pi/2)$. However, the $U(1)$ factor $e^{i\varphi_3}$ is redundant since this represents a left isoclinic rotation of the planes, just like the original rotation M_L but with a different angle. Since such a rotation leaves all the rotation planes invariant we may discard it, and we are left with the following

$$\begin{pmatrix} r'_1 e^{i\theta'_1} \\ r'_2 e^{i\theta'_2} \end{pmatrix} = \begin{pmatrix} e^{i\varphi_1} \cos\eta & -e^{-i\varphi_2} \sin\eta \\ e^{i\varphi_2} \sin\eta & e^{-i\varphi_1} \cos\eta \end{pmatrix} \begin{pmatrix} r_1 e^{i\theta_1} \\ r_2 e^{i\theta_2} \end{pmatrix}. \tag{24}$$

The above matrix is the general expression for a member of $U(2)/U(1) = SU(2)$, i.e a special unitary 2×2 matrix. We can interpret this family of matrices as the group of right isoclinic rotations [75]. To see this note that Eq. (23) is an expression in the complex representation for rotations that commute with the given left isoclinic rotation, M_L. (To see this, note that these are complex linear transformations and so they commute with i, while M_L in the complex representation is simply multiplication by $e^{i\alpha}$.) However, it is also well-known that all left isoclinic rotations commute with all right isoclinic rotations [74], whereas two isoclinic rotations of the same sense (or two generic double rotations) will only commute if they share the same rotation planes, as introduced above. In going from Eq. (23) to Eq. (24) we have factored out those left isoclinic rotations which commute with M_L, as they take the same form as M_L in the chosen basis and so have the same rotation planes. The matrix in Eq. (24) therefore is a representation of the right isoclinic rotations, as these are the remaining rotation matrices that commute with M_L.

We can also further simplify Eq. (24) by factoring out the subgroup of right isoclinic rotations which take the form $M_R \equiv M(\alpha, -\alpha)$ in our chosen basis. Letting $\varphi_2 = \varphi_1 + \varphi$, with $\varphi \in [0, 2\pi)$, we obtain

$$\begin{pmatrix} \cos\eta & -e^{-i\varphi} \sin\eta \\ e^{i\varphi} \sin\eta & \cos\eta \end{pmatrix} \begin{pmatrix} e^{i\varphi_1} & 0 \\ 0 & e^{-i\varphi_1} \end{pmatrix},$$

where the second matrix can be recognised as M_R [c.f. Eq. (19)]. Since the diagonal factor M_R just corresponds to initial rotations within the x–y, and z–w planes, it is redundant in describing the coordinate transformation [Eq. (24)] from these planes to the arbitrary rotation planes, P_j, of M_L. We can therefore discard it such that our final expression for the general transformation is

$$\begin{pmatrix} r'_1 e^{i\theta'_1} \\ r'_2 e^{i\theta'_2} \end{pmatrix} = \begin{pmatrix} \cos\eta & -e^{-i\varphi} \sin\eta \\ e^{i\varphi} \sin\eta & \cos\eta \end{pmatrix} \begin{pmatrix} r_1 e^{i\theta_1} \\ r_2 e^{i\theta_2} \end{pmatrix}, \tag{25}$$

where $\eta \in [0, \pi/2]$ and $\varphi \in [0, 2\pi)$. This is therefore the general form for a coordinate transformation from a fixed pair of rotation planes (e.g. the x–y, and z–w planes) to all other rotation planes of M_L, with all redundant parameters removed.

Interestingly, it is also clear from Eq. (25) that φ is undefined when $\eta = 0$, because the off-diagonal elements vanish. Moreover, a careful analysis shows that this also occurs at the other endpoint, $\eta = \pi/2$, as here the diagonal elements vanish, and so we can eliminate φ as follows

$$\begin{pmatrix} 0 & -e^{-i\varphi} \sin\eta \\ e^{i\varphi} \sin\eta & 0 \end{pmatrix} = \begin{pmatrix} 0 & -\sin\eta \\ \sin\eta & 0 \end{pmatrix} \begin{pmatrix} e^{i\varphi} & 0 \\ 0 & e^{-i\varphi} \end{pmatrix}.$$

This means that when $\eta = 0$ or $\pi/2$ every value of $\varphi \in [0, 2\pi)$ gives the same completely orthogonal pair of rotation planes. In other words, φ and η parameterise a 2-sphere (S^2), with the north and south pole given by $\eta = 0$ and $\pi/2$, respectively. Effectively, in going from Eq. (24) to Eq. (25), we have just taken the quotient $SU(2)/U(1) = S^3/S^1 = S^2$, which is the celebrated Hopf fibration [75]. We can therefore say that the space of all rotation planes of any given left isoclinic rotation M_L is topologically equivalent to a 2-sphere (S^2).

There is also a much quicker way of deriving Eq. (23), in other words deducing that the coordinate transformation from a fixed pair of rotation planes to all other rotation planes must be given by a unitary matrix, based on the following argument. Let the rotation which takes one rotation plane of M_L into another be given by U. The fact that M_L acts on all its rotation planes in the same way means that M_L should be invariant under a change of basis by the rotation U. In other words, we have the equation $U^{-1}M_LU = M_L$, which means that M_L and U commute. In the complex ($\mathbb{C}^2$) representation M_L is simply $e^{i\alpha}$ multiplied by the 2×2 identity matrix, and so in this representation, U must commute with i. The most general way for U to satisfy this is if U is simply a complex matrix. However, we know that U is itself a rotation, and we derived earlier that if a 4D rotation (or more generally an orthogonal transformation) in the $\mathbb{C}^2$ representation is given by a matrix, then that matrix is unitary.

Note that all of the arguments of this section can also be applied to a given right isoclinic rotation $M_R \equiv M(\alpha, -\alpha)$, provided we use a different complex representation of $\mathbb{R}^4$ where the position vector is given by $(x + iy, z - iw)^T = (r_1 e^{i\theta_1}, r_2 e^{-i\theta_2})^T$. Transformations between rotation planes of M_R — which form the left isoclinic subgroup of $SO(4)$ — then take the same form as Eq. (24), but with $e^{i\theta_2}$ and $e^{i\theta_2'}$ replaced by their complex conjugates. Then, the left isoclinic rotations of the form $M_L \equiv M(\alpha, \alpha)$ can be factored out, just as rotations of the form of M_R could be factored out of the transformations between rotation planes of M_L. Thus we can obtain an equivalent expression to Eq. (25) for the general coordinate transformation from a fixed pair of rotation planes of M_R to all other rotation planes, with all redundant parameters removed; again this equation is identical to Eq. (25) except that the second element of each of the position vectors is replaced by its complex conjugate.

Finally, consider a fluid undergoing constant rigid rotation associated with a left isoclinic rotation in time, i.e. taking $M_L(t) \equiv M(\alpha(t), \alpha(t))$ with $\alpha(t) = \omega t$, where ω is a constant frequency. Such a system can be described using any completely orthogonal pair of the rotation planes of $M_L(t)$; to see this, we define one such pair by $r_j e^{i\theta_j} = 0$ and another by $r_j' e^{i\theta_j'} = 0$, with $j = 1, 2$, where the primed and unprimed coordinates are related by Eq. (25). Then we take the $\mathbb{R}^4$ gradient of Eq. (25) as follows

$$\begin{pmatrix} \nabla\left[r_1' e^{i\theta_1'}\right] \\ \nabla\left[r_2' e^{i\theta_2'}\right] \end{pmatrix} = \begin{pmatrix} \cos\eta & -e^{-i\varphi}\sin\eta \\ e^{i\varphi}\sin\eta & \cos\eta \end{pmatrix} \begin{pmatrix} \nabla\left[r_1 e^{i\theta_1}\right] \\ \nabla\left[r_2 e^{i\theta_2}\right] \end{pmatrix},$$

and then take the complex inner product of this equation with Eq. (25) to obtain

$$\begin{pmatrix} r_1' e^{i\theta_1'} \\ r_2' e^{i\theta_2'} \end{pmatrix}^\dagger \begin{pmatrix} \nabla\left[r_1' e^{i\theta_1'}\right] \\ \nabla\left[r_2' e^{i\theta_2'}\right] \end{pmatrix} = \begin{pmatrix} r_1 e^{i\theta_1} \\ r_2 e^{i\theta_2} \end{pmatrix}^\dagger \begin{pmatrix} \nabla\left[r_1 e^{i\theta_1}\right] \\ \nabla\left[r_2 e^{i\theta_2}\right] \end{pmatrix}.$$

Expanding the inner product and evaluating the gradient we end up with a complex equation with a real part given by

$$r_1'\hat{\boldsymbol{r}}_1' + r_2'\hat{\boldsymbol{r}}_2' = r_1\hat{\boldsymbol{r}}_1 + r_2\hat{\boldsymbol{r}}_2$$

and an imaginary part given by

$$r_1'\hat{\boldsymbol{\theta}}_1' + r_2'\hat{\boldsymbol{\theta}}_2' = r_1\hat{\boldsymbol{\theta}}_1 + r_2\hat{\boldsymbol{\theta}}_2, \tag{26}$$

where the hats above symbols indicates the unit vectors in those directions. The first equation shows that the $\mathbb{R}^4$ position vector can be equally expressed in both bases, as expected. The second equation is less trivial, and can be physically interpreted as equating two velocity fields; once Eq. (26) is multiplied by the frequency ω, the RHS is a velocity field describing rigid left isoclinic rotation through the unprimed planes, while the LHS describes the same thing through the primed planes. That these two are equal shows that either pair can be used to describe such a rigidly rotating fluid, and therefore the fluid exhibits symmetry with respect to all right isoclinic rotations.

However, as mentioned above, a superfluid does not behave as a rigid body under rotation, but instead forms quantized vortices [2]. Indeed, for all the 4D superfluid vortex states that we shall study in the remainder of this paper, the 4D velocity field is significantly different to that of rigid rotation (Eq. (26)). Instead, for these states, the $SU(2)$ symmetry, associated with the set of equivalent rotation planes, is naturally broken. This leads to degeneracies between states that are oriented with respect to the different rotation planes of an isoclinic double rotation. We shall see this, first of all, in the next section where we review the case of orthogonal 4D vortex planes, which we previously studied in Ref. [1].

IV. ORTHOGONAL VORTEX PLANES IN 4D SUPERFLUIDS

So far, we have reviewed the well-known physics of vortices in 2D and 3D, and introduced the different types of rotation that become possible in 4D systems. We shall now combine these ideas in order to discuss some of the vortex structures that can emerge in a 4D superfluid under double rotation. In this section, we shall focus, in particular, on the case of orthogonal vortex planes, which we earlier described in Ref. [1]. After briefly reviewing the main findings of this previous work, we shall proceed to re-derive the hydrodynamic energy of two completely orthogonal vortex planes within a hyperspherical

system, and to introduce our numerical methods, illustrating these by presenting numerical results that complement those already published. The intention of this section is to establish a basis of comparison for when we extend our discussion to non-orthogonal 4D vortex planes in Section V.

IV.1. Structure of 4D Orthogonal Vortex Planes

As in Section II, we want to consider a superfluid described by the GPE without external potentials, but now with atoms free to move in four spatial dimensions. In the absence of rotation, a generalised 4D GPE can be written in the same form as in lower dimensions [Eq. (1)], namely [1]:

$$-\frac{\hbar^2}{2m}\nabla^2\psi + g|\psi|^2\psi = \mu\psi,$$

except now with ∇^2 corresponding to the 4D Laplacian. This serves as a minimal model in which to explore 4D vortex physics, and is a plausible mathematical description of low-temperature interacting bosons in a hypothetical universe with four spatial dimensions [1, 76–78]. In the future, it will also be interesting to consider a more tailored model moving towards a realistic 4D experiment, based, for example, on adding one or more synthetic dimensions to an ultracold bosonic gas [15, 28–38, 52]. However, the form of such a model will depend strongly on the details of the particular experimental implementation chosen, and will likely include other effects, such as lattices, unusual interaction terms and asymmetries between real and synthetic dimensions. These more experimental models therefore go beyond our current work, but raise interesting opportunities for future research as discussed briefly in our conclusions in Section VIII.

While the above 4D GPE is identical to that in lower dimensions, in the rotating frame [c.f. Eq. (11)], we have to be more careful as the angular momentum operator can no longer be treated as a vector as discussed in Section III. Instead, in 4D, the angular momentum operator is a 4x4 antisymmetric tensor, with components $\hat{L}_{\gamma\delta}$ that correspond to the angular momentum in the γ–δ plane (with $\gamma, \delta \in \{x, y, z, w\}$). The general form of the rotating-frame GPE then takes the form

$$\left[-\frac{\hbar^2}{2m}\nabla^2 + g|\psi|^2 - \sum_{\gamma\delta}\Omega_{\gamma\delta}\hat{L}_{\gamma\delta}\right]\psi = \mu\psi, \qquad (27)$$

where $\Omega_{\gamma\delta}$ is the rotation frequency associated with the γ–δ plane, and the sum runs over the six different Cartesian planes in 4D.

As can be seen from Eq. (27), the simplest situation is when there is only one plane with a non-zero rotation frequency, e.g. $\Omega_{xy} \equiv \Omega \neq 0$. This corresponds to the case of simple rotation, which can be understood as a usual three-dimensional rotation extended into 4D [c.f. Eq. (17)]. As we previously showed in Ref. [1], this sort of rotation can stabilise a single "vortex plane", where the dimensionless order parameter can be described by:

$$\psi = f_k(r_1)e^{ik\theta_1},$$

where (r_1, θ_1) are plane polar coordinates in the plane of rotation (e.g. x–y), and $f_k(r)$ is independent of the coordinates not involved in rotation (e.g. z, w) such that the radial function is the same as that found numerically from the 2D GPE [c.f. Section II]. In this case, the vortex core is a single plane (defined e.g. by $x = 0$, $y = 0$), as was also verified numerically in Ref. [1]. Physically, this can be understood as the natural extension of point vortices from 2D and line vortices from 3D into 4D, as the extra dimension plays no role.

In contrast, double rotations are an intrinsically 4D (or higher) phenomenon and so can lead to much richer vortex physics, as will be our focus in the remainder of this article. Specifically, we will focus on the 4D GPE in a doubly rotating frame

$$\left[-\frac{\hbar^2}{2m}\nabla^2 + g|\psi|^2 - \Omega_1\hat{L}_1 - \Omega_2\hat{L}_2\right]\psi = \mu\psi, \qquad (28)$$

where Ω_j and $\hat{L}_j$ are respectively the rotation frequency and angular momentum operator in plane j. For example, we could choose plane 1 as the x–y plane (i.e. $\Omega_1 \equiv \Omega_{xy}$, $\hat{L}_1 \equiv \hat{L}_{xy} = -i\hbar(x\partial_y - y\partial_x)$), and plane 2 as the z–w plane (i.e. $\Omega_2 \equiv \Omega_{zw}$, $\hat{L}_2 \equiv \hat{L}_{zw} = -i\hbar(z\partial_w - w\partial_z)$). Note that such a set-up is related to certain 4D quantum Hall models in which a nontrivial second Chern number is generated by applying magnetic fields in two completely orthogonal planes [15–18, 79].

To proceed, for simplicity we will henceforward adopt double polar coordinates $(r_1, \theta_1, r_2, \theta_2)$, defined by

$$(x, y, z, w) = (r_1\cos\theta_1, r_1\sin\theta_1, r_2\cos\theta_2, r_2\sin\theta_2),$$

such that $\hat{L}_j = -i\hbar\partial_{\theta_j}$. As $\hat{L}_1$ and $\hat{L}_2$ describe a double rotation, they commute with each other, meaning that we are able to look for simultaneous eigenstates of both angular momentum operators. As we showed in Ref. [1], for suitable equal-frequency ($\Omega_1 = \Omega_2$) rotations, a reasonable ansatz for the (dimensionless) ground-state is

$$\psi = f_{k_1,k_2}(r_1, r_1)e^{ik_1\theta_1 + ik_2\theta_2}, \qquad (29)$$

where k_1 and k_2 are the integer winding numbers in the respective rotation planes and $f_{k_1,k_2}(r_1, r_1)$ describes the 4D superfluid density profile, which is assumed to just be a function of the radii of the two planes. This ansatz describes a pair of completely orthogonal vortex planes which intersect at the origin, with the superfluid circulating simultaneously and independently in the two rotation planes with a velocity field given by

$$\mathbf{v} = \mathbf{v}_1 + \mathbf{v}_2 = \frac{\hbar}{m}\left(\frac{k_1}{r_1}\hat{\boldsymbol{\theta}}_1 + \frac{k_2}{r_2}\hat{\boldsymbol{\theta}}_2\right), \qquad (30)$$

corresponding to a superposition of 2D vortex-velocity fields in each rotation plane [c.f. Eq. (4)]. Such a vortex structure is therefore topologically characterised by the $\mathbb{Z} \times \mathbb{Z}$ topological winding numbers [1]. Note that this ansatz preferentially picks out the x–y and z–w, however, equal frequency rotations are isoclinic and hence have an infinite number of rotation planes, as we discussed in Sec. III.2. This means that suitable ansatzes could be defined with respect to any of these planes, and our choice is arbitrary.

The function $f_{k_1,k_2}(r_1, r_1)$ in Eq. (29) can be found numerically from solving the 4D GPE [Eq. (28)]. As we previously showed [1], this function appears to be close to a product ansatz $f_{k_1,k_2}(r_1, r_1) \approx f_{k_1}(r_1) f_{k_2}(r_2)$ where $f_{k_i}(r_i)$ is the 2D density profile of a vortex with winding number k_i in plane i; however, this separable approximation fails significantly near the intersection of the vortex planes near the origin due to the intrinsic nonlinearity of the GPE equation. Before presenting a numerical example of such a vortex structure, we shall first discuss the associated hydrodynamic energy and critical frequency, in an extension of the standard textbook discussion for 2D vortices that was presented in Section II.

IV.2. Hydrodynamic Energy of Completely Orthogonal Vortex Planes

As it will be helpful in the following sections, we shall here derive the hydrodynamic energy for a pair of completely orthogonal vortex planes in a 4D superfluid. As discussed in Ref. [1], we have previously studied the energy of the orthogonal-vortex structure [Eq. (29)] in a "duocylinder" geometry defined by hard-wall boundaries at $r_1 = R_1$ and $r_2 = R_2$, where R_j are the radii in the $j = 1, 2$ planes. In this geometry, the energy could be approximated by a decomposition as

$$E_{k_1,k_2}(R_1, R_2) = E_{k_1}(R_1) + E_{k_2}(R_2), \tag{31}$$

where $E_{k_j}(R_j)$ is the 2D energy [Eq. (10)] associated with having a vortex with winding number k_j in a 2D disc of radius R_j and hard-wall boundary conditions.

In this paper, we shall focus on a 4D hypersphere (or "4D ball") geometry, which is defined by having hard-wall boundaries at $r_1^2 + r_2^2 = R^2$, where R is the hyperspherical radius. This geometry is theoretically interesting in the following sections as it preserves the symmetry of isoclinic rotations [c.f. Section III] unlike the duocylinder geometry, which has boundary conditions that preferentially pick out two planes as being special.

Nevertheless, as we shall now show, we can also approximate the energy of completely orthogonal vortex planes in such a hypersphere as a decomposition into a sum of the energies of each individual plane, in an analogous manner to Eq. (31). To see this, we consider the hydrodynamics of a simplified "hollow core" vortex model, similar to that used in 2D as reviewed in Section II. Specifically, we will consider a pair of completely orthogonal vortex planes, which intersect at the origin, and we will approximate the density profile as zero within one healing length of each vortex core and at the system boundary, and equal to a constant N/V everywhere else, where N is the particle number and $V = \pi^2 R^4/2$ is the volume of the 4D ball. Following Section II, we can again neglect contributions to the hydrodynamic energy from density variations [c.f. Eq. (7)] and from interparticle interactions [c.f. Eq. (8)], leaving only

$$E_{\mathrm{h}} \approx \frac{m}{2} \int \rho \mathbf{v}^2 \mathrm{d}^4 r = \frac{m}{2} \int \rho (\mathbf{v}_1 + \mathbf{v}_2)^2 \mathrm{d}^4 r,$$

where in the second equality, we have used that the velocity field is well-described by a sum of the individual velocities for each vortex plane [c.f. Eq. (30)]. Furthermore, as $\mathbf{v}_j$ lies in plane j, it follows that $\mathbf{v}_1 \cdot \mathbf{v}_2 = 0$, i.e. that the hydrodynamic vortex-vortex interaction term vanishes, leaving us with

$$E_{\mathrm{h}} = \frac{N\hbar^2}{2Vm} \int_{\xi}^{R} r_1 \mathrm{d}r_1 \int_{-\pi}^{\pi} \mathrm{d}\theta_1 \int_{\xi}^{\sqrt{R^2 - r_1^2}} r_2 \mathrm{d}r_2 \int_{-\pi}^{\pi} \mathrm{d}\theta_2 \left(\frac{k_1^2}{r_1^2} + \frac{k_2^2}{r_2^2} \right),$$

where we have used that $v^2 = (\hbar^2/m^2)(k_1^2/r_1^2 + k_2^2/r_2^2)$ from Eq. (30).

The integration region is symmetric with respect to swapping r_1 and r_2, so each term in the integrand gives the same result, just with a different coefficient k_j^2. This means we really only need to consider one of these terms, and with the order of integration we have above, it is easiest to compute the $1/r_1^2$ term. We will also rescale $r_j \to R r_j$ and evaluate the θ integrals to give

$$\begin{aligned} E_{\mathrm{h}} &= \frac{4N\hbar^2}{mR^2} \left(k_1^2 + k_2^2\right) \int_{\frac{\xi}{R}}^{1} \frac{\mathrm{d}r_1}{r_1} \int_{\frac{\xi}{R}}^{\sqrt{1-r_1^2}} r_2 \mathrm{d}r_2 \\ &= \frac{2N\hbar^2}{mR^2} \left(k_1^2 + k_2^2\right) \int_{\frac{\xi}{R}}^{1} \frac{\mathrm{d}r_1}{r_1} \left(1 - r_1^2 - \frac{\xi^2}{R^2}\right) \\ &= \frac{2N\hbar^2}{mR^2} \left(k_1^2 + k_2^2\right) \left(1 - \frac{\xi^2}{R^2}\right) \left[\ln\left(\frac{R}{\xi}\right) - \frac{1}{2}\right], \end{aligned}$$

which to leading order in ξ/R gives us

$$E_{\mathrm{h}} = 2N \frac{\hbar^2}{mR^2} \left(k_1^2 + k_2^2\right) \ln\left(\frac{R}{\xi}\right), \tag{32}$$

This corresponds to a sum like that in Eq. (31), but for the hydrodynamic energy in this simplified constant-density model in a 4D hypersphere. Note that this equation is very similar to the point vortex energy in 2D [Eq. (9)], except we have $k_1^2 + k_2^2$ instead of k^2, and there is a geometric factor of 2 coming from the difference between the area of a disk and the 4D volume of a hypersphere. Again, just as in the 2D case, we can obtain a

more accurate energy for these orthogonal intersecting vortices by using the dimensionless numerical density-profile function $f_{k_1,k_2}(r_1, r_2)$ from our ansatz [Eq. (29)]. Using the grand canonical energy relative to the uniform state with a chemical potential given by $\mu = \hbar^2/m\xi^2$, we obtain

$$E_h \approx 2\mu N \frac{\xi^2}{R^2}\left(k_1^2 + k_2^2\right) \ln\left(2.07\frac{R}{\xi}\right), \qquad (33)$$

numerically via a fitting procedure to the form of Eq. (32), with the logarithmic prefactor as the fit parameter.

This result, without the initial factor of 2, was obtained the exact same way in our previous paper [1] for a duo-cylinder geometry given by $r_1 \leq R_1$, and $r_2 \leq R_2$. In that instance, however, the analytical calculation yielded precisely this form since the boundary conditions in the two planes were decoupled, and the energy integral therefore decomposed into a sum in the two planes. In the hyperspherical geomtery, there are less than leading order terms that we have ignored that do not have the same form. Therefore we believe that the result for a spherical geometry [Eq. (33)] is more approximate. The energy reduction from equal-frequency double rotation ($\Omega_1 = \Omega_2 = \Omega$) can be calculated as

$$\Delta E_{\rm rot} = \Omega\left(\langle \hat{L}_1\rangle + \langle \hat{L}_2\rangle\right) = \Omega N\hbar(k_1 + k_2), \qquad (34)$$

where we have used that each vortex plane independently contributes angular momentum equal to $N\hbar k_j$ [c.f. Eq.(12)]. This gives a critical frequency of

$$\Omega_c \approx 2\frac{\hbar}{mR^2}\ln\left(2.07\frac{R}{\xi}\right) \qquad (35)$$

to stabilise an orthogonal pair of $k = 1$ vortex planes. Naturally, we will present most of our results with frequencies in units of Ω_c. Note that Ref. [1] worked in units of Ω_c^{2D}, the 2D critical frequency [Eq. (13)] for a $k = 1$ point vortex in a disk of radius R. To convert between these unit conventions, we may use the fact $\Omega_c = 2\Omega_c^{2D}$.

IV.3. Numerical Methods and Results

In this section we will briefly describe the numerical methods which are then used to support our analytical results throughout the rest of this paper. We shall then illustrate these methods with an example of a structure with orthogonal vortex planes, so as to complement the results previously presented in Ref. [1] and to provide a basis for comparison with later sections of this paper.

As in our earlier work [1], the imaginary time evolution method (ITEM) is used to find solutions of the 4D GPE with double rotation [Eq. (27)]. We use second order finite differences in space and a first order explicit discretisation in time. All calculations are performed on a Cartesian grid within a 4D hypersphere of radius roughly

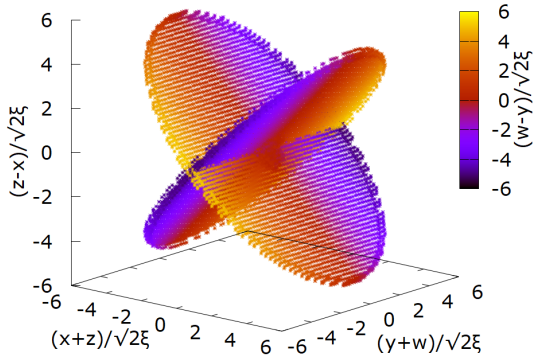

FIG. 1. Vortex core of orthogonal intersecting planes in the final state of the ITEM with parameters $\Omega_{xy} = \Omega_{zw} = 1.5\Omega_c$, and $\Delta x = 0.2\xi$, giving $R \approx 8.3\xi$. Note that the coordinates we are plotting against are rotated relative to those used in the numerics, in order to show both planes at once.

equal to $N_{\rm grid} \approx 41$ gridpoints, with a hardwall boundary condition imposed on the boundary points (defined as the points with fewer than 8 nearest neighbours). This then corresponds to a total number of gridpoints roughly equal to 1.4×10^7. The spatial step size for most calculations is set to $\Delta x = 0.5\xi$, which ensures a large system of radius $R \approx 21\xi$ to reduce the importance of boundary effects.

We calculate the predicted critical frequency Ω_c from Eq. (35) with R set to $N_{\rm grid}\Delta x - \xi$, subtracting one healing length in order to approximately account for the boundary region. As we shall see later, our numerical results suggest that, for $\Delta x = 0.5\xi$, a more accurate value for the critical frequency of $0.9\Omega_c$. This is likely due to a combination of finite size effects and the fact that Eq. (33) is an approximate result based on fitting to the function form of Eq. (32).

Our initial states are constructed in terms of a density profile and phase profile, with a degree of noise (up to 20% of the background value) then added to the real and imaginary parts of ψ. The initial density profile is chosen to be homogeneous except at the boundary where it smoothly goes to zero, while the initial phase factor is determined by the vortex configuration we expect to see at low energy for the chosen parameters. The ITEM is deemed to have converged once the relative variations in the particle number, N (calculated as the sum of $|\psi|^2\Delta x^4$), and chemical potential (the sum of the LHS of Eq. (27) multiplied by $\psi^*\Delta x^4/N$), from one iteration to the next reach below 10^{-10}. Once the ITEM reaches this threshold accuracy level we output the state and calculate the energy (using a finite difference version of Eqs (5) and (6)). We also determine the coordinates of all points making up the vortex core and separately output these, where we deem a point to be in the core if it is more than one healing length from the boundary and if the modulus of the order parameter at that location is less than the spatial resolution $\Delta x/\xi$. This latter criterion is motivated by the fact that the order parameter

goes to zero linearly as one approaches a singly charged vortex core [2]. In order to then plot the vortex core, we supplement a 3D scatter plot (showing the x, y, and z coordinates) with colour (representing the w coordinate).

To illustrate this numerical method, in Fig. 1 we show the vortex core structure obtained from ITEM under equal-frequency double rotation with parameters $\Omega_{xy} = \Omega_{zw} = 1.5\Omega_c$, and $\Delta x = 0.2\xi$, giving $R \approx 8.3\xi$. Here, the initial state (before adding noise) was chosen to have a density profile that was homogeneous within the system away from the boundaries, and a phase profile given by $\arctan 2(y, x) + \arctan 2(w, z)$, corresponding to the phase-winding expected from Eq. (29) with $k_1 = k_2 = 1$. Note that both the Cartesian grid and the initial phase profile numerically break the hyperspherical symmetry, and the symmetry associated with isoclinic rotation. However, we expect the grid effects to be small, and the phase profile simply picks out one of several degenerate states for equal frequency rotation. As in Ref. [1], the resulting stationary state is found to contain a vortex core structure consisting of a pair of intersecting completely orthogonal planes (here, corresponding to the x–y and z–w planes). Note that in plotting Fig. 1, we have rotated our coordinates according to

$$\begin{pmatrix} x \\ y \\ z \\ w \end{pmatrix} \to \frac{1}{\sqrt{2}} \begin{pmatrix} 1 & 0 & 1 & 0 \\ 0 & 1 & 0 & 1 \\ -1 & 0 & 1 & 0 \\ 0 & -1 & 0 & 1 \end{pmatrix} \begin{pmatrix} x \\ y \\ z \\ w \end{pmatrix} \tag{36}$$

in order to better depict both planes at the same time. This visualization of the vortex-core structure complements the results previously presented in Ref. [1] for the phase and density profile of the stationary state, and will serve as a useful basis for comparison to results obtained in later sections of this paper under other parameters and initial conditions.

V. NON-ORTHOGONAL VORTEX PLANES

Having introduced vortex structures composed of completely orthogonal vortex planes in the previous section, we shall now consider the possibility of a pair of non-orthogonal vortex planes in a 4D superfluid. As we shall show later in this paper, such non-orthogonal vortex planes are a natural candidate for the low energy configuration of a 4D superfluid doubly rotating at unequal frequencies. In preparation, we shall therefore derive in this section the total hydrodynamic energy of a pair of non-orthogonal vortex planes, before discussing the possibility that such vortex planes reconnect, similar to how a pair of vortex lines would reconnect in 3D [c.f. Section II].

V.1. Hydrodynamic Energy of Non-Orthogonal Vortex Planes

As in Section II and Section IV, we shall neglect the contributions from density variations and from interparticle interactions, such that the kinetic energy can be approximated as

$$E_{\rm h} \approx \frac{m}{2} \int \rho \mathbf{v}^2 \mathrm{d}^4 r = \frac{m}{2} \int \rho (\mathbf{v}_1 + \mathbf{v}_2)^2 \mathrm{d}^4 r,$$

where we have again assumed that the velocity field can be decomposed as a sum of the velocity fields associated with each of the (now non-orthogonal) vortex planes separately. From this it can be seen that in general, we can split the total hydrodynamic energy up into a sum of the energies of each individual vortex plane [c.f. Section IV.2] together with the hydrodynamic vortex-vortex interaction, which is given by

$$E_{\rm vv} = m \int \rho \mathbf{v}_1 \cdot \mathbf{v}_2 \mathrm{d}^4 r. \tag{37}$$

As we discussed above and in Ref. [1], the velocity fields $\mathbf{v}_{1,2}$ induced by two orthogonal planes were themselves everywhere orthogonal, $\mathbf{v}_1 \cdot \mathbf{v}_2 = 0$, meaning that this hydrodynamic vortex-vortex interaction between the planes vanished. However, as we shall now show, this is not true for non-orthogonal vortex planes, meaning that the vortex-vortex interaction term is non-zero in general.

In order to find $E_{\rm vv}$, we will start from the assumption that a pair of non-orthogonal vortex planes can be described by the ansatz

$$\begin{aligned} \psi &= r_1^{|k_1|} r_2'^{\,|k_2|} e^{i\left(k_1\theta_1 + k_2\theta_2'\right)} g(r_1^2, r_2'^2), \\ &= \left(x + \sigma_1 i y\right)^{|k_1|} \left(z' + \sigma_2 i w'\right)^{|k_2|} g(x^2 + y^2, z'^2 + w'^2), \end{aligned} \tag{38}$$

where the primed and unprimed coordinates are related by a double rotation given by a matrix M defined below, such that $\mathbf{r}' = M\mathbf{r}$, and $k_{1,2}$ are the winding numbers of the two vortices while $\sigma_j = \mathrm{sign}(k_j)$. The function g ensures that the density returns to the homogeneous value when both r_1 and r_2' are large compared to ξ, and is given by $g(r_1^2, r_2'^2) = \mathrm{const} \times f_{k_1,k_2}(r_1/\xi, r_2'/\xi)/r_1^{|k_1|} r_2'^{\,|k_2|}$, where $f_{k1,k2}$ is the dimensionless profile associated with the ansatz for orthogonal vortex planes in Eq. (29). In particular, g is always positive, and must satisfy the asymptotic relations

$$\begin{aligned} g(r_1^2, r_2'^{\,2}) &\sim \mathrm{const} \times \frac{f_{k_1}(r_1/\xi)}{r_1^{|k_1|}} \quad \text{as} \quad r_2' \to \infty, \\ g(r_1^2, r_2'^2) &\sim \mathrm{const} \times \frac{f_{k_2}(r_2'/\xi)}{r_2'^{|k_2|}} \quad \text{as} \quad r_1 \to \infty, \end{aligned}$$

where f_k is the dimensionless 2D vortex profile described in Sec. II.1. These asymptotics physically are the requirement that far from one of the vortex planes, the density profile is determined purely by the remaining one.

Concretely, the state in Eq. (38) contains vortex planes along $x = y = 0$ and $z' = w' = 0$ respectively, which intersect at the origin. In order to keep this ansatz general while minimizing the number of parameters, we will refer to Appendix IX, where we derive the general form of M required to describe the tilting of a plane in $\mathbb{R}^4$. The result is that, without loss of generality, we may choose the following form

$$M = \begin{pmatrix} \cos\alpha_1 & 0 & -\sin\alpha_1 & 0 \\ 0 & \cos\alpha_2 & 0 & -\sin\alpha_2 \\ \sin\alpha_1 & 0 & \cos\alpha_1 & 0 \\ 0 & \sin\alpha_2 & 0 & \cos\alpha_2 \end{pmatrix},$$

with $\alpha_{1,2} \in [0, \pi/2)$, such that

$$z' = \sin\alpha_1 x + \cos\alpha_1 z, \qquad w' = \sin\alpha_2 y + \cos\alpha_2 w. \quad (39)$$

To use this result in describing our skewed vortex planes we must assume that the vortices exist within a spherically symmetric 4D superfluid of radius R, such that $r_1^2 + r_2^2 = r_1'^2 + r_2'^2 \leq R$. Note that having a pair of orthogonal vortex planes, as discussed in the previous section, corresponds to taking $\alpha_1 = \alpha_2 = 0$, such that M becomes an identity matrix and $\mathbf{r}' = \mathbf{r}$. Given the spherical geometry we will assume, in analogy with Section IV, that the velocity fields induced by each vortex have the following simple forms

$$\mathbf{v}_1 = k_1 \frac{\hbar}{m} \frac{\hat{\boldsymbol{\theta}}_1}{r_1} \qquad \mathbf{v}_2' = k_2 \frac{\hbar}{m} \frac{\hat{\boldsymbol{\theta}}_2'}{r_2'}. \quad (40)$$

Let's first consider the special case where the matrix M is a simple rotation, meaning one of the angles $\alpha_{1,2}$ is equal to zero. In this case it is easier to use the Cartesian representation of Eq. (40), which is

$$\mathbf{v}_1 = k_1 \frac{\hbar}{m} \frac{x\hat{\boldsymbol{y}} - y\hat{\boldsymbol{x}}}{x^2 + y^2} \qquad \mathbf{v}_2' = k_2 \frac{\hbar}{m} \frac{z'\hat{\boldsymbol{w}}' - w'\hat{\boldsymbol{z}}'}{z'^2 + w'^2}.$$

Without loss of generality we can choose $\alpha_2 = 0$ such that we have $w' = w$ and $\hat{\boldsymbol{w}}' = \hat{\boldsymbol{w}}$, which is of course orthogonal to both $\hat{\boldsymbol{x}}$ and $\hat{\boldsymbol{y}}$. Therefore, the dot product between the velocity fields is given by

$$\mathbf{v}_1 \cdot \mathbf{v}_2' = k_1 k_2 \left(\frac{\hbar}{m}\right)^2 \frac{w}{z'^2 + w^2} \frac{y\hat{\boldsymbol{z}}' \cdot \hat{\boldsymbol{x}} - x\hat{\boldsymbol{z}}' \cdot \hat{\boldsymbol{y}}}{x^2 + y^2}.$$

Using Eq. (39) we have that $\hat{\boldsymbol{z}}' = \sin\alpha_1 \hat{\boldsymbol{x}} + \cos\alpha_1 \hat{\boldsymbol{z}}$, and therefore the interaction energy is given by

$$E_{\text{vv}} = k_1 k_2 \sin\alpha_1 \frac{\hbar^2}{m} \int \frac{wy\rho(x^2 + y^2, z'^2 + w^2)}{(z'^2 + w^2)(x^2 + y^2)} \mathrm{d}^4 r.$$

Keeping in mind that only x and z appear in z', we can see that the above integrand is an odd function of both y and w. This integral therefore vanishes, since our chosen geometry is symmetric with respect to both of these coordinates. In order to get a non-zero interaction potential we would need the superfluid to occupy a region that is asymmetric in both the y and w directions. This may be an interesting avenue for future work but is beyond the scope of this paper.

We shall now derive the form of the hydrodynamic interaction energy [Eq. (37)] in the special cases where M is an isoclinic rotation. There are two main reasons for this choice of rotation: firstly, an isoclinic tilt allows us to derive an analytic form for the interaction using the integral transform into non-orthogonal double polar coordinates derived in Appendix X; and secondly, in Sec. VI we will use the results we derive here to investigate possible low-energy vortex configurations in a superfluid doubly rotating at unequal frequencies, and we obtain predictions that agree closely with numerics when the frequencies are not too high. Isoclinic rotation here corresponds to the condition $\alpha_2 = \nu\alpha_1$, with $\nu = \pm 1$ denoting whether M is left $(-)$ or right $(+)$ isoclinic. Let us therefore define $\eta \equiv \alpha_1$ for simplicity and proceed. Using Eq. (39), we see that the primed coordinates now take the form

$$z' + iw' = c(z + iw) + s(x + \nu iy), \quad (41)$$

where we have applied the shorthand $c = \cos\eta$, $s = \sin\eta$.

Substituting this into Eq. (38), we find that our ansatz is given by

$$\psi = (x + \sigma_1 iy)^{|k_1|} \left[c(z + \sigma_2 iw) + s(x + \nu\sigma_2 iy)\right]^{|k_2|} g,$$

where we have suppressed the arguments of g for brevity. Note that if we have $\nu = \sigma_1\sigma_2$, then $x + \sigma_1 iy = x + \nu\sigma_2 iy$, and the planes are skewed in such a way that they are beginning to perfectly align, while $\nu = -\sigma_1\sigma_2$ corresponds to pure anti-aligning. We therefore expect that $\nu = \text{sign}(k_1 k_2)$ will give rise to a repulsive interaction between the planes, while $\nu = -\text{sign}(k_1 k_2)$ will lead to a attractive interaction [c.f. Section II.3].

In order to compute the hydrodynamic vortex-vortex interaction energy, we will first rewrite Eq. (41) in double polar coordinates as

$$r_2' e^{i\theta_2'} = c r_2 e^{i\theta_2} + s r_1 e^{i\nu\theta_1}. \quad (42)$$

As the hydrodynamic interaction energy density depends on $\rho\mathbf{v}_1 \cdot \mathbf{v}_2'$ [c.f. Eq. (37)], we must find an expression for the dot product $\hat{\boldsymbol{\theta}}_1 \cdot \hat{\boldsymbol{\theta}}_2'$ under the assumption of velocity fields of the form in Eq. (40). To do this, we will start by taking the vector gradient of Eq. (42) as

$$(\hat{\boldsymbol{r}}_2' + i\hat{\boldsymbol{\theta}}_2') e^{i\theta_2'} = c(\hat{\boldsymbol{r}}_2 + i\hat{\boldsymbol{\theta}}_2) e^{i\theta_2} + s(\hat{\boldsymbol{r}}_1 + i\nu\hat{\boldsymbol{\theta}}_1) e^{i\nu\theta_1}.$$

where we have used the primed coordinate system on the LHS and the unprimed coordinate system on the RHS. Then taking the dot product of both sides with $\hat{\boldsymbol{\theta}}_1$ gives

$$(\hat{\boldsymbol{r}}_2' \cdot \hat{\boldsymbol{\theta}}_1 + i\hat{\boldsymbol{\theta}}_2' \cdot \hat{\boldsymbol{\theta}}_1) e^{i\theta_2'} = i\nu s e^{i\nu\theta_1}.$$

Dividing through by $ie^{i\theta_2'}$ and then taking the real part of both sides gives

$$\hat{\boldsymbol{\theta}}_2' \cdot \hat{\boldsymbol{\theta}}_1 = \nu s \cos(\theta_2' - \nu\theta_1),$$

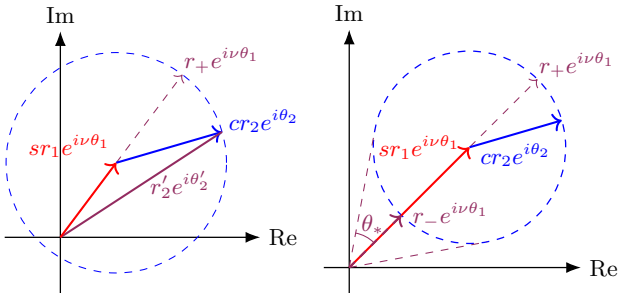

FIG. 2. A geometric/algebraic description of the two terms in Eq. (43). (Left) The first term corresponds to the region where $sr_1 < cr_2$, meaning that the complex coordinate $r'_2e^{i\theta'_2}$ encircles the origin. This means that r'_2 always reaches a minimum value of 0, and θ'_2 spans a full period, i.e. $r'_2 \in [0, r_+]$, and $\theta'_2 \in [-\pi, \pi)$. (Right) The second term corresponds to $sr_1 \leq cr_2$, which means that $r'_2e^{i\theta'_2}$ no longer winds around the origin, so r'_2 has some minimum value r_- which can be positive, and θ'_2 no longer spans a full period. This in turn means that θ'_2 takes values in the interval $[\theta_1 - \theta_*, \theta_1 + \theta_*]$, where $\theta_* \leq \pi/2$ with equality occuring when $sr_1 = cr_2$ and the blue dotted circle passes through the origin. The limits on r_1 are derived in Appendix X, and come from combining the inequalities on sr_1 and cr_2 with the spherical geometry $r_1^2 + r_2^2 \leq R^2$.

such that $\mathbf{v}_1 \cdot \mathbf{v}'_2 = \nu k_1 k_2 (\hbar/m)^2 s \cos(\theta'_2 - \nu\theta_1)/(r_1 r'_2)$, and the vortex-vortex interaction is given by

$$E_{\rm vv} = \nu k_1 k_2 \frac{\hbar^2}{m} s \int_{B^4(R)} \rho(r_1, r'_2) \frac{\cos(\theta'_2 - \nu\theta_1)}{r_1 r'_2} \mathrm{d}^4 r,$$

where $B^d(R)$ denotes the d-dimensional ball of radius R centred at the origin, which is our chosen geometry.

This integral will be as difficult to compute in the primed coordinate system as the unprimed one; however, we can greatly simplify the integrand by using the non orthogonal coordinate system defined by $(r_1, \theta_1, r'_2, \theta'_2)$, at the cost of complicating the integration limits. In Appendix X we derive the integral transformation into this non-orthogonal coordinate system for the region $B^4(1)$. To use this result we must make the substitution $\mathbf{r} \to R\mathbf{r}$ so that the integral is over $B^4(1)$ rather than $B^4(R)$, and we make the substitution $\theta'_2 = \theta + \nu\theta_1$ to simplify the cosine. Altogether, we then have

$$\begin{aligned} E_{\rm vv} = A\frac{s}{c^2} \int_0^c \mathrm{d}r_1 \int_{-\pi}^{\pi} \mathrm{d}\theta_1 \int_{-\pi}^{\pi} \mathrm{d}\theta \int_0^{r_+} \mathrm{d}r'_2 \rho \cos\theta \\ + A\frac{s}{c^2} \int_c^1 \mathrm{d}r_1 \int_{-\pi}^{\pi} \mathrm{d}\theta_1 \int_{-\theta_*}^{\theta_*} \mathrm{d}\theta \int_{r_-}^{r_+} \mathrm{d}r'_2 \rho \cos\theta, \end{aligned} \quad (43)$$

where the prefactor $A = \nu k_1 k_2 R^2 \hbar^2/m$, and the limits θ_* and $r_\pm$ are given by

$$\begin{aligned} \theta_* &= \arcsin\left[c\left(1 - r_1^2\right)^{\frac{1}{2}}/sr_1\right], \text{ and} \\ r_\pm &= sr_1\cos\theta \pm \left[c^2\left(1 - r_1^2\right) - s^2 r_1^2 \sin^2\theta\right]^{\frac{1}{2}}. \end{aligned}$$

While this integral transform is derived in great detail in Appendix X, a quick pictoral explanation for the form taken by Eq. (43) is given in Fig. 2. In particular, the fact that there are two distinct terms in this equation with different integration limits is directly related to whether $r'_2e^{i\theta'_2}$ encircles the origin (first term) or not (second term).

Now that we are using the natural coordinates for this problem, we proceed to evaluate the integrals. Similar to Section II.1, we will ignore the vortex core, and approximate the density as constant $\rho = N/V$, where N is the particle number and $V = \pi^2 R^4/2$ is the 4D volume of the system. This approximation works provided the angle η is not too close to $\pi/2$ as will be discussed later. The vortex-vortex interaction energy is then given as

$$\begin{aligned} E_{\rm vv} &= A'\frac{s}{c^2} \int_0^c \mathrm{d}r_1 \int_{-\pi}^{\pi} \mathrm{d}\theta \int_0^{r_+} \mathrm{d}r'_2 \cos\theta \\ &\quad + A'\frac{s}{c^2} \int_c^1 \mathrm{d}r_1 \int_{-\theta_*}^{\theta_*} \mathrm{d}\theta \int_{r_-}^{r_+} \mathrm{d}r'_2 \cos\theta \\ &= A'\left(J_1 + J_2\right), \end{aligned} \quad (44)$$

where the new prefactor $A' = 4\nu k_1 k_2 N\hbar^2/\pi m R^2$, and we have introduced J_1 and J_2 as shorthand to denote the two integrals. We will now deal with each of these integrals separately; focusing on the first term, we have

$$\begin{aligned} J_1 \equiv \frac{s}{c^2} \int_0^c \mathrm{d}r_1 \int_{-\pi}^{\pi} \mathrm{d}\theta \cos\theta r_+ = \frac{s}{c^2} \int_0^c \mathrm{d}r_1 \int_{-\pi}^{\pi} \mathrm{d}\theta s r_1 \cos^2\theta \\ + \frac{s}{c^2} \int_0^c \mathrm{d}r_1 \int_{-\pi}^{\pi} \mathrm{d}\theta \cos\theta \left[c^2\left(1 - r_1^2\right) - s^2 r_1^2 \sin^2\theta\right]^{\frac{1}{2}}, \end{aligned}$$

where we have carried out the integral over r'_2. The second integral on the RHS of this equation can be shown to vanish as follows

$$\int_{-\pi}^{\pi} \mathrm{d}\theta \cos\theta F(\sin^2\theta) = \left(\int_{-\pi}^{-\frac{\pi}{2}} + \int_{-\frac{\pi}{2}}^{\frac{\pi}{2}} + \int_{\frac{\pi}{2}}^{\pi} \right) \mathrm{d}\theta \cos\theta F(\sin^2\theta), = \int_{0}^{\frac{\pi}{2}} \mathrm{d}\theta \cos(\theta-\pi) F\left[\sin^2(\theta-\pi)\right]$$
$$+ \int_{-\frac{\pi}{2}}^{\frac{\pi}{2}} \mathrm{d}\theta \cos(\theta) F(\sin^2\theta) + \int_{-\frac{\pi}{2}}^{0} \mathrm{d}\theta \cos(\theta+\pi) F\left[\sin^2(\theta+\pi)\right] = \left(-\int_{0}^{\frac{\pi}{2}} + \int_{-\frac{\pi}{2}}^{\frac{\pi}{2}} - \int_{-\frac{\pi}{2}}^{0} \right) \mathrm{d}\theta \cos\theta F(\sin^2\theta) = 0,$$

which works for any arbitrary function F. This leaves us with

$$J_1 = \frac{s^2}{c^2} \int_0^c r_1 \mathrm{d}r_1 \int_{-\pi}^{\pi} \mathrm{d}\theta \cos^2\theta = \frac{\pi}{2} s^2.$$

We now turn to the second term of Eq. (44), which depends on

$$J_2 = \frac{s}{c^2} \int_c^1 \mathrm{d}r_1 \int_{-\theta_*}^{\theta_*} \mathrm{d}\theta \cos\theta \left(r_+ - r_-\right),$$
$$= \frac{2s}{c^2} \int_c^1 \mathrm{d}r_1 \int_{-\theta_*}^{\theta_*} \mathrm{d}\theta \cos\theta \left[c^2\left(1-r_1^2\right) - s^2 r_1^2 \sin^2\theta\right]^{\frac{1}{2}}.$$

This has the form of the vanishing term in J_1, except that the θ limits now do not cover a full period. In fact, the limits do not cover even half a period since $\theta_* \leq \pi/2$ (consider Fig. 2 with the blue dotted circle passing through the origin), with the consequence being that this term now contributes. To compute it we will apply the substitution $s r_1 \sin\theta = c\left(1-r_1^2\right)^{1/2} \sin u$, to give

$$J_2 = 2 \int_c^1 \mathrm{d}r_1 \frac{\left(1-r_1^2\right)}{r_1} \int_{-\pi/2}^{\pi/2} \mathrm{d}u \cos^2 u.$$
$$= -\pi \ln c - \frac{\pi}{2} s^2.$$

Putting this all together, we obtain the final result

$$E_{\mathrm{vv}} = -4 k_1 k_2 \nu N \frac{\hbar^2}{mR^2} \ln(\cos\eta).$$

We now see that our expectation regarding the sign of E_{vv} was correct: the overall sign is given by $\mathrm{sign}(\nu k_1 k_2)$ such that the interaction is positive (i.e. repulsive) when the planes are skewed in an aligning sense ($\nu = \mathrm{sign}(k_1 k_2)$), and negative (i.e. attractive) when they are anti-aligning ($\nu = -\mathrm{sign}(k_1 k_2)$.

Combining this with the result from Sec. IV.2, we have that the total hydrodynamic energy of the non-orthogonal vortex plane state is

$$E_{\mathrm{h}} = 2N \frac{\hbar^2}{mR^2} \left[\left(k_1^2 + k_2^2\right) \ln\left(\frac{R}{\xi}\right) - 2\nu k_1 k_2 \ln(\cos\eta) \right]. \tag{45}$$

Note, however, that we just derived the interaction term under the constant density approximation, while the individual hydrodynamic energies of the vortices was calculated using a hollow core model. This hollow core was needed to remove the unphysical $1/r^2$ singularity around each vortex that gives a divergent contribution to the energy, which in a mathematical sense is why vortices have cores. In contrast, the interaction energy density only goes as $1/r_1 r_2'$ which is not singular once integrated.

Recall, as per the discussion in Sec. II.3, that the same is true of point vortices in 2D: their interaction can be approximated with a constant density, but this fails to give a finite answer for the individual energies. As previously discussed, the correct answer can still be obtained if we take the vortices to be combined once their separation is of the order of ξ or below.

The question arises whether we can recover the expression for vortex combination in this 4D case. Here we have an angle between the vortex planes, given by $\pi/2 - \eta$, and we see that the interaction energy E_{vv} diverges in the limit $\eta \to \pi/2$ under the constant density approximation. This also occurred when using this approximation for point vortices in 2D as their separation distance Δr approached zero, so we see that the angular separation $\pi/2 - \eta$ is playing a similar role here in 4D as Δr did in 2D. In contrast to 2D, however, we do not have a unique value for the separation distance between the vortices, so coming up with a criterion for when they have combined seems difficult.

We will identify a natural separation as follows: each plane makes a circle of intersection with the boundary of the hypersphere, and we argue that the maximum reasonable value for the distance between the planes should be given by the minimum distance between these circles. This distance is the length of the most direct straight line between the two planes at the boundary, and — as we derive in Appendix XI — is given by $\sqrt{2}R\left(1-\sin\eta\right)^{1/2}$. This result can be obtained by naively applying the cosine rule in an analogy to lines in 2D. Setting this distance less than or equal to ξ, we have

$$\sqrt{2}R\left(1-\sin\eta\right)^{\frac{1}{2}} \leq \xi,$$

which rearranges to

$$\sin\eta \geq 1 - \frac{\xi^2}{2R^2}.$$

We want this inequality in terms of $\cos\eta$, since this is what appears in the interaction. Therefore we square both sides, which is safe as they are each non-negative, giving

$$1-\cos^2\eta \geq \left(1-\frac{\xi^2}{2R^2}\right)^2,$$

which rearranges to

$$\cos\eta \leq \frac{\xi}{R}\left(1-\frac{\xi^2}{4R^2}\right)^{\frac{1}{2}}.$$

To leading order in ξ/R, we can therefore say that the vortices are combined once $\cos\eta = \xi/R$ or less. Substituting this into Eq. (45) we obtain

$$E_{\rm h} = \frac{2N\hbar^2}{mR^2}\left(k_1+\nu k_2\right)^2 \ln\left(\frac{R}{\xi}\right),$$

which is the correct result for a vortex plane with winding number $k_1+\nu k_2$.

This concludes our discussion of the energetic properties of non-orthogonal vortex planes, the results of which we will use in Sec. VI to construct a model of superfluids doubly rotating at unequal frequencies. Next we will consider the dynamical evolution of skew vortex planes in the immediate vicinity of their intersection point.

V.2. Reconnection

Here we show that non-orthogonal vortex planes in 4D generically do not form a stationary state. In particular, we show than an initial state containing two non-orthogonal singly charged vortex planes that intersect at a point will undergo reconnection. As we shall see, in contrast to reconnections of extended vortex lines in 3D [64], the vortex core remains a single connected object at all times during this four-dimensional reconnection. However, we note that a single connected core can arise in evolved states of the 3D GPE when considering self-intersection and reconnection of vortex loops [80] or of a pair of linked vortex loops [69, 70, 81]. We follow the same analysis as in Sec. II.4 and previous works on reconnection [64]; close to a vortex core the density is small, so for short times we may describe the evolution of a vortex core with the linearised dimensionless GPE in 4D

$$-\frac{1}{2}\nabla^2\psi = i\dot{\psi}. \tag{46}$$

We will take our ansatz for non-orthogonal vortex planes [Eq. (38)] as an initial state, with $|k_1| = |k_2| = 1$, assuming an idealised case of an infinite condensate that is homogeneous away from the vortex core. Looking at the immediate vicinity of the intersection point between the planes, such that r_1 and r_2' are both small (compared to ξ), we can approximate the function g in Eq. (38) to leading order as $g(0,0)$. Any constants can then be divided out of the linear evolution [Eq. (46)], so in the immediate vicinity of either vortex core we can approximate the state as

$$\psi_0 = (x+iy)(z'+\sigma i w'),$$

where we have assumed $\sigma_1 = 1$ without loss of generality, and $\sigma = \sigma_2$ then denotes the relative sign of k_1k_2, and hence the relative orientation of the two planes. Substituting the equation for z' and w' [Eq. (39)] into our initial condition gives

$$\psi_0 = \sin\alpha_1 x^2 - \sigma\sin\alpha_2 y^2 + \text{cross-terms}, \tag{47}$$

where we have suppressed the cross-terms since they will not contribute in what follows. If we let this initial state undergo the Schrödinger evolution of Eq. (46), then after a short time Δt the evolved state is given by

$$\psi = \psi_0 + \frac{i\Delta t}{2}\nabla^2\psi_0. \tag{48}$$

The Laplacian of the initial state contains only contributions from the first two terms in Eq. (47), and is given by

$$\nabla^2\psi_0 = 2(\sin\alpha_1 - \sigma\sin\alpha_2),$$

such that the evolved state is given by

$$\psi = (x+iy)(z'+\sigma i w') + i\Delta t(\sin\alpha_1 - \sigma\sin\alpha_2). \tag{49}$$

Interestingly, if the two planes are related by an isoclinic rotation, such that $\alpha_1 = \nu\alpha_2$ then there is the possibility that $\nu = \sigma$ and the linearised equation [Eq. (48)] predicts no dynamics and hence no reconnection. This corresponds to a right iscoclinic rotation for $\nu = \sigma = 1$ and a left handed one for $\nu = \sigma = -1$. In both of these cases, however, we can use the definition of the primed coordinates [Eq. (41)] to see that, when $\nu = \sigma$

$$z' + \sigma i w' = c(z+\sigma i w) + s(x+iy),$$

such that the planes are skewed in a purely aligning sense, and their interaction according to the previous section is repulsive. This raises the possibility that such non-orthogonal purely aligning planes could form a stationary state; however, we expect that this is not true for the full nonlinear dynamics that apply at larger distances from the core. This is because the rotation M affects the function g even given the form we have assumed for it. It would be interesting in future work to test this hypothesis by applying the nonlinear analytics used for the reconnection of vortex lines in 3D [64] to these planes in 4D. Regardless, we can speculate that for purely aligning skewed planes to reconnect in the same way as the general skewed planes, the core would have to first twist near the intersection point so that — in the immediate vicinity of this point — the core forms two planes that are skewed

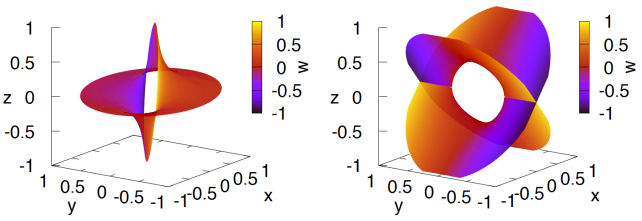

FIG. 3. Perturbed orthogonal vortex planes given by the zeroes of Eq. (50), with $a = 0.1$, $b = 0$. (Left) The vortex core in the original basis, plotted using the height ($z(x, y)$) and colour ($w(x, y)$) functions given in Eqs (52). The intersection point has become an avoided crossing, and the vortex core approaches each of the original planes as the distance from the origin increases. (Right) The same state after a rotation of the coordinates given by Eq. (36), with $z(x, y)$ and $w(x, y)$ now defined by Eqs (53).

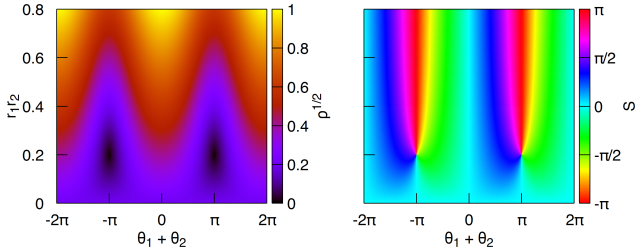

FIG. 4. Density (Left) and Phase (Right) of the perturbed orthogonal state [Eq. (54)] as a function of $r_1 r_2$ and $\theta_1 + \theta_2$ as given by Eqs (56) and (57), respectively, for $\gamma = 0.2$ and $\beta = \pi$. Note that the zeroes of the density and corresponding branch points in the phase occur at $r_1 r_2 = \gamma$ and $\theta_1 + \theta_2 = \pm\beta$. The phase winds with θ_1 and θ_2 when $r_1 r_2 > \gamma$, while it is roughly constant for $r_1 r_2 < \gamma$.

with some anti-alignment component ($\alpha_1 \neq \sigma\alpha_2$). This is reminiscent of the case in 3D, where it is well known that vortex lines are always anti-aligning very close to the reconnection point [64].

To get an idea of what the reconnected core structure looks like, consider a simpler state given by

$$\psi_\perp = (x + iy)(z + iw) - a - ib \tag{50}$$

which describes a pair of completely orthogonal planes perturbed by a complex constant, in the same way that Eq. (49) describes a pair of non-orthogonal planes perturbed by the last term which is a constant for a given value of Δt. This allows us to focus on the effect of the perturbation without the complication of the skewed planes and the time dependence of the state. The location of any vortex cores is given by the set of zeroes of the order parameter, which in this simpler case are all the points which satisfy

$$xz - yw = a, \qquad xw + yz = b. \tag{51}$$

Solving these equations for $z = z(x, y)$ and $w = w(x, y)$ gives us

$$z = \frac{ax + by}{x^2 + y^2}, \qquad w = \frac{bx - ay}{x^2 + y^2}, \tag{52}$$

which can be plotted as a surface in 3+1 dimensions, where the extra w dimension is given by colour. This is shown in the left panel of Fig. 3 for $a = 0.1$, $b = 0$. This figure shows that there is no longer an intersection at the origin, although the structure around this point is difficult to make out. We can get a clearer view by performing a double rotation, and looking at this object from a different perspective. In particular, applying the rotation given in Eq. (36) transforms Eqs (51) into

$$-x^2 + y^2 + z^2 - w^2 = 2a, \qquad -xy + zw = b,$$

which can again be solved for $z(x, y)$ and $w(x, y)$, giving

$$\begin{aligned} z^2 &= \left[A(x,y)^2 + B(x,y)^2\right]^{\frac{1}{2}} + A(x,y), \\ w^2 &= \left[A(x,y)^2 + B(x,y)^2\right]^{\frac{1}{2}} - A(x,y), \end{aligned} \tag{53}$$

where $A(x, y) = a + (x^2 - y^2)/2$, and $B(x, y) = b + xy$. These (now two-branched) solutions are plotted, for $a = 0.1$, $b = 0$ in the right panel of Fig. 3, giving a clearer view of the core structure near the origin. Again, we see that the intersection point has been replaced by a kind of avoided crossing reminiscent of the reconnection of intersecting vortex lines in 3D, but where the vortex core remains a single connected 2D region. Recall that the perturbed orthogonal state [Eq. (50)] is a simplification of the perturbed skewed state undergoing linear dynamical reconnection [Eq. (52)]. To visualise this non-orthogonal reconnecting state for small angles $\alpha_{1,2}$ we can take the picture in Fig. 3 and tilt the asymptotic plane $z = w = 0$ into $z' = w' = 0$, with the region around the origin remaining essentially the same but expanding linearly with time.

If we rewrite the perturbed orthogonal state [Eq. (50)] in double polar coordinates, we obtain

$$\psi_\perp = r_1 r_2 e^{i(\theta_1 + \theta_2)} - \gamma e^{i\beta}, \tag{54}$$

where $\gamma e^{i\beta} = a + ib$. Note that in these variables the equations for the core surface become

$$\theta_1 + \theta_2 = \beta, \quad r_1 r_2 = \gamma. \tag{55}$$

These expressions are very simple and give an immediate interpretation of γ and β, but are not as conducive to plotting and visualisation as Eqs (52) and (53). However, we can use Eq. (55) to find an expression of the minimum distance between the origin and the perturbed orthogonal core. Recall that this distance was zero for the unperturbed orthogonal state (both vortex planes passed through the origin), so this gives us a measure of the perturbation which we will use later numerically. Using $r_1^2 + r_2^2 = r^2$ we can define $r_1 = r \sin u$ and $r_2 = r \cos u$, with $u \in [0, \pi/2]$. Then, substituting this into Eq. (55), we obtain $r^2 = 2\gamma / \sin 2u$, such that the minimum value of r occurs at $u = \pi/4$, and is given by $r_{\min} = \sqrt{2\gamma}$. Furthermore, r takes this value when $r_1 = r_2 = \sqrt{\gamma}$.

We can also use the polar form Eq. (54) to plot the entire density and phase profiles by noting that this state

is only a function of the variables $r_1 r_2$ and $\theta_1+\theta_2$. Taking the modulus and argument of Eq. (54) gives

$$\rho = \left[r_1^2 r_2^2 + 2\gamma r_1 r_2 \cos(\theta_1+\theta_2-\beta)+\gamma^2\right]^{\frac{1}{2}}, \quad (56)$$

$$\tan S = \frac{r_1 r_2 \sin(\theta_1+\theta_2-\beta)}{r_1 r_2 \cos(\theta_1+\theta_2-\beta)-\gamma}, \quad (57)$$

which we have then plotted in the left and right panels, respectively, of Fig. 4, for $\gamma = 0.2$, and $\beta = \pi$. This plot clearly shows that the core — visible as dark spots in the left panel and branch points in the right panel — occurs at the values given in Eq. (55). Above $r_1 r_2 = \gamma$ the phase winds once as either θ_1 or θ_2 makes a full circle, while below it the phase becomes approximately constant. Note that we have truncated the y-axis of this plot as we expect the linearised approach to only be meaningful within about a healing length of the core structure, where the healing length is given by $\xi = 1$ in these dimensionless units. For the same reason, we only consider values of $\gamma < 1$; as we can identify $\gamma \propto \Delta t$, this is similar to the assumption that the evolution only describes short times.

To make this analogy clearer, we note that the skewed reconnecting state [Eq. (49)] at a fixed time step Δt has the same density and phase profiles as in Eqs (56) and (57), respectively, but with r_2 and θ_2 replaced by r_2' and θ_2' and with $\gamma = \Delta t(\sin\alpha_1 - \sigma \sin\alpha_2)$ and $\beta = -\pi/2$.

In this simplified linear description the perturbation governing the avoided crossing grows linearly with time for short times; it would be very interesting in future work to extend this to the nonlinear regime using analogous methods to those of Nazarenko and West [64], in order to discover the fate of these reconnected planes at later times. In particular, the question arises whether these curved vortex core structures can ever form a stationary state. As we shall see later, our numerical results show vortex core structures that are qualitatively similar to the skewed avoided crossing states we have considered here. However, these numerical vortex cores come from final states of the ITEM, which are numerical stationary states; also, these states have avoided crossing regions spanning several healing lengths, and so we do not expect these to be described by the linearised GPE [Eq. (46)].

Additionally, in this section we have assumed an infinite condensate, while our numerics uses a hardwall boundary. Once this boundary condition is imposed the off-axis nature of the avoided crossing introduces unavoidable image effects. This can be seen by evaluating the current of the reconnecting skewed state [Eq. (49)], given by $\mathrm{Im}\,(\psi^*\nabla\psi) = \rho\mathbf{v}$, and seeing that there is a radial component of the velocity at the boundary. Physically we require that the radial velocity at the boundary vanishes, otherwise the condensate would be expanding and the state would not be stationary. In fact, the 2D equivalent of Eq. (50), that is $\psi = x + iy - a - ib$, is precisely an off-axis point vortex located at the coordinates (a, b) rather than the origin, and is well known not to satisfy this boundary condition for the velocity field [82]. This condition is then usually enforced analytically with the method of images, but this is not straightforward given the complicated curved geometry of the vortex core. For this reason, analysis of these image effects is beyond the scope of this paper.

Bearing these caveats in mind, in the next section we will develop a theory of superfluids doubly rotating with unequal frequencies using intersecting non-orthogonal vortex planes as an ansatz for the ground state. Numerically, we will then observe stationary states with approximately the structure of this ansatz but with avoided crossings instead of intersections reminiscent of the reconnection physics that we have discussed in this section.

VI. UNEQUAL FREQUENCY DOUBLE-ROTATION

In this section, we will consider the behaviour of a 4D superfluid undergoing constant double rotation with unequal frequencies, given by $\Omega_{xy} = \Omega_{zw} + \Delta\Omega$ in the lab (x, y, z, w) frame. We will take $\Delta\Omega > 0$ without loss of generality, and we will also assume the superfluid occupies a hyperspherical (4D ball) region for simplicity. Note that this breaks the isoclinic SU(2) symmetry [c.f. Sec.III], which is associated with the manifold of different rotation planes when the frequencies are equal. We will begin in Section VI.1 by considering what happens to a single vortex plane in this set-up, before discussing the case of two vortex planes in Section VI.2. We shall then present our numerical results in Section VI.3.

VI.1. A single vortex plane under unequal frequency double rotation

In this section, we shall develop our intuition by considering the simple case of a single vortex plane in a system with unequal frequency double rotation. We will assume that this plane remains rigid but allow it to arbitrarily tilt in order to optimise its energy. The energy of the superfluid in the rotating frame is reduced by the amount

$$E_{\mathrm{rot}} = \Omega_{xy}\langle \hat{L}_{xy}\rangle + \Omega_{zw}\langle \hat{L}_{zw}\rangle \quad (58)$$

relative to an inertial frame. Since $\Omega_{xy} > \Omega_{zw}$ it is natural to presume that the lowest energy occurs when the vortex plane lies along the z–w plane — thereby inducing rotation in the x–y plane — such that $\langle \hat{L}_{xy}\rangle = N\hbar$ and $\langle \hat{L}_{zw}\rangle = 0$. The converse case of a vortex plane spanning the x–y plane would certainly be higher in energy, as this state would have $\langle \hat{L}_{xy}\rangle = 0$ and $\langle \hat{L}_{zw}\rangle = N\hbar$; however, it is not obvious that the superfluid energy decreases monotonically as the vortex plane is tilted from the x–y plane to the z–w plane. That is, the lowest energy overall could occur when the vortex plane is oriented somewhere between these two limits. Such a state would have positive values of both $\langle \hat{L}_{xy}\rangle$ and $\langle \hat{L}_{zw}\rangle$, and would be given as

follows

$$\psi = (x' + iy')g(x'^2 + y'^2),$$

where the primed coordinates are to be defined shortly, and the function g is given by $g(r^2) = const \times f_1(r/\xi)/r$, with f_1 the dimensionless density profile of a point vortex in 2D (see Sec. II.1). The primed coordinates are defined such that the vortex plane is given by $x' = y' = 0$, so — as derived in Appendix IX — we may assume without loss of generality that the primed coordinates are given by

$$\begin{pmatrix} x' \\ y' \\ z' \\ w' \end{pmatrix} = \begin{pmatrix} \cos\alpha_1 & 0 & \sin\alpha_1 & 0 \\ 0 & \cos\alpha_2 & 0 & \sin\alpha_2 \\ -\sin\alpha_1 & 0 & \cos\alpha_1 & 0 \\ 0 & -\sin\alpha_2 & 0 & \cos\alpha_2 \end{pmatrix} \begin{pmatrix} x \\ y \\ z \\ w \end{pmatrix}.$$

A more useful form of the order parameter for this state is given in polar coordinates, $r'_1 e^{i\theta'_1} \equiv x' + iy'$, as follows

$$\psi = r'_1 e^{i\theta'_1} g(r'^2_1).$$

In order to use this, we must express the transformation into the primed coordinate system in polar coordinates as well. Taking the combination $x' + iy'$ gives

$$r'_1 e^{i\theta'_1} = \cos\alpha_1 x + \sin\alpha_1 z + i\cos\alpha_2 y + i\sin\alpha_2 w,$$

and switching to polar coordinates and rearranging gives

$$\begin{aligned} r'_1 e^{i\theta'_1} = {} & \frac{\cos\alpha_1 + \cos\alpha_2}{2} r_1 e^{i\theta_1} + \frac{\sin\alpha_1 + \sin\alpha_2}{2} r_2 e^{i\theta_2} \\ & + \frac{\cos\alpha_1 - \cos\alpha_2}{2} r_1 e^{-i\theta_1} + \frac{\sin\alpha_1 - \sin\alpha_2}{2} r_2 e^{-i\theta_2}. \end{aligned}$$

The terms on the second line are proportional to $e^{-i\theta_j}$, and therefore generate angular momentum counter to the external rotation (since $\Omega_{xy} L_{xy} = -i\hbar\Omega_{xy}\partial_{\theta_1}$ and similarly for zw). To maximize the energy reduction from rotation we should eliminate these terms. We therefore set $\alpha_1 = \alpha_2 \equiv \eta$ to obtain the following

$$r'_1 e^{i\theta'_1} = \cos\eta\, r_1 e^{i\theta_1} + \sin\eta\, r_2 e^{i\theta_2}.$$

An expression of this same exact form [Eq. (21)] was derived in Sec. III.2 in the context of finding the rotations planes of any left isoclinic rotation in the x–y and z–w planes, i.e. a rotation M_L generated by $\hat{L}_+ = \hat{L}_{xy} + \hat{L}_{zw}$. Here, however, $r'_1 e^{i\theta'_1} = 0$ encodes the vortex plane, so we see that the vortex plane always lies in a rotation plane of M_L, regardless of the value of η. This vortex generates angular momentum in the plane orthogonal to itself, which is also a rotation plane of M_L. This is all essentially summed up by the (easily verifiable) fact that $r'_1 e^{i\theta'_1}$ is an eigenfunction of the sum of the angular momenta, $\hat{L}_+$, despite not being an eigenfunction of either component. The superfluid containing this tilted vortex therefore has the same value of $\langle \hat{L}_+ \rangle = N\hbar$ for every value of η. We can exploit this knowledge by rewriting the rotational energy [Eq. (58)] as

$$E_{\text{rot}} = \Omega_{zw} \langle \hat{L}_+ \rangle + \Delta\Omega \langle \hat{L}_{xy} \rangle. \tag{59}$$

Since the first term is constant with respect to η we therefore maximize E_{rot} by simply maximizing the second term, proportional to $\langle \hat{L}_{xy} \rangle$. This clearly occurs at $\eta = 0$, where $r'_1 e^{i\theta'_1} = r_1 e^{i\theta_1}$, and so the initial intuition was correct: a single perfectly rigid vortex plane will always want to fully align with the higher frequency.

VI.2. Two vortex planes under unequal frequency double rotation

Armed with this knowledge we now seek to find the optimal configuration of two rigid vortex planes in a doubly rotating superfluid with unequal rotation frequencies. Each vortex will want to align its angular momentum with the x–y plane as much as possible to gain from the larger rotation frequency in this plane. However, as we showed in Sec. V.1, vortex planes will interact with each other hydrodynamically once they are not orthogonal. This interaction will limit how close together (in orientation) each vortex can be and the competition between this effect and the rotational energy will determine the optimal orientation of each plane respectively. This is a simplified model of the situation, and it is worth briefly discussing the approximations we are making.

Firstly, we are going to again assume a constant density profile given by $\rho = N/V$, thereby ignoring the vortex core. As previously discussed in Section II.1, one needs to account for the core to avoid a divergent hydrodynamic energy cost of a vortex — see, for example, Eq. (7) with ξ taken to zero. However, in this case we are only interested in how the energy varies with the orientation of each vortex plane. This means we can ignore any terms which do not vary as the planes tilt. If we denote the velocity field induced by each plane by $\mathbf{v}_j$, with $j = 1, 2$ respectively, then the hydrodynamic energy can be expanded as in Section V.1 as

$$\frac{1}{2}\int \rho \mathbf{v}^2 \mathrm{d}^4 r = \frac{1}{2}\int \rho \left(\mathbf{v}_1^2 + \mathbf{v}_2^2\right) \mathrm{d}^4 r + \int \rho \mathbf{v}_1 \cdot \mathbf{v}_2 \mathrm{d}^4 r.$$

The first term is the individual hydrodynamic cost of each vortex, which diverges if we ignore the core by assuming a constant density. However, this term does not vary with orientation due to the spherical symmetry of the boundary. On the other hand, the second term, which is the hydrodynamic interaction between the planes, depends on their relative orientation but does not diverge in a constant density approximation, as explained in Sec. V.1.

We therefore ignore the constant first term, keeping only the second term which can safely be approximated using a constant density. This constant density approximation also allows us again to ignore the energy contributions from quantum pressure (the first term in Eq. (5)),

and the bosonic interaction (Eq. (6)) as is also done in Section V.1.

Secondly, we are going to assume the vortex planes remain flat and intersecting at the origin. In particular this means we are not going to consider the conclusion from Sec. V.2 that, in general, intersecting non-orthogonal vortex planes do not form a stationary state but will instead reconnect. This reconnection was found to cause the vortex surfaces to move outward near their intersection, such that they no longer intersect but instead form a single smoothly curved surface. This displacement of the cores will affect the velocity field directly, by moving the center of the circulating flow, and (if there is a hard-wall boundary) indirectly, by introducing image effects which we are as yet unable to model. Note, however, that the reconnected vortex cores (see Fig. 3) approach the original vortex planes for large values of r_1 or r_2. Therefore, if the typical size of the reconnection is small compared to the radius of the system, we may neglect these effects as they are only appreciable in a small region around the origin. With these assumptions, we now proceed to model a non-orthogonal, intersecting pair of vortex planes in a superfluid under double rotation with unequal frequencies.

As we are assuming a constant density $n = N/V$, we may take the order parameter for this configuration to be

$$\psi = n^{\frac{1}{2}} e^{i(\acute{\theta}_1 + \grave{\theta}_2)}, \tag{60}$$

where the acute ($\acute{r}$) and grave ($\grave{r}$) coordinate systems are to be defined shortly. Recall from Sec. VI.1 that the vortex planes will want to stay on one of the rotation planes of left isoclinic rotations, M_L, generated by $\hat{L}_+$. We will therefore use our result [Eq. (25)] from Sec. III.2 for the general form of such rotation planes relative to a fixed basis (in this case the lab basis, x, y, z, w). Using this result for each of the acute and grave coordinates, we have

$$\begin{pmatrix} \acute{r}_1 e^{i\acute{\theta}_1} \\ \acute{r}_2 e^{i\acute{\theta}_2} \end{pmatrix} = \begin{pmatrix} \cos\eta_1 & e^{i\varphi_1}\sin\eta_1 \\ -e^{-i\varphi_1}\sin\eta_1 & \cos\eta_1 \end{pmatrix} \begin{pmatrix} r_1 e^{i\theta_1} \\ r_2 e^{i\theta_2} \end{pmatrix}, \tag{61}$$

$$\begin{pmatrix} \grave{r}_1 e^{i\grave{\theta}_1} \\ \grave{r}_2 e^{i\grave{\theta}_2} \end{pmatrix} = \begin{pmatrix} \cos\eta_2 & e^{i\varphi_2}\sin\eta_2 \\ -e^{-i\varphi_2}\sin\eta_2 & \cos\eta_2 \end{pmatrix} \begin{pmatrix} r_1 e^{i\theta_1} \\ r_2 e^{i\theta_2} \end{pmatrix}. \tag{62}$$

where $\eta_{1,2} \in [0, \pi/2]$ and $\varphi_{1,2} \in [0, 2\pi)$, with φ_j undefined when $\eta_j = 0$ or $\pi/2$. The location of each vortex plane is then given by $\acute{r}_1 e^{i\acute{\theta}_1} = 0$ and $\grave{r}_2 e^{i\grave{\theta}_2} = 0$, respectively. The parameters $\eta_{1,2}$ denote the angle that each plane makes with the x–y (resp. z–w) plane, while $\varphi_{1,2}$ denote the direction of this tilt.

The vortex at $\acute{r}_1 e^{i\acute{\theta}_1} = 0$ is tilted by an angle η_1 away from the x–y plane, while the vortex at $\grave{r}_2 e^{i\grave{\theta}_2} = 0$ is tilted by $\pi/2 - \eta_2$ off of the same plane. Since the two vortex planes are indistinguishable, we can define the acute and grave coordinates such that the former vortex is closer to the x–y plane than the latter, which translates to the following constraint on the angles

$$\eta_1 \leq \frac{\pi}{2} - \eta_2. \tag{63}$$

Note that $\eta_1 = \eta_2 = 0$ corresponds to the configuration that we have previously studied [1] — a completely orthogonal pair of vortex planes spanning the rotation planes of the superfluid: the x–y and z–w planes, respectively. A change of basis in either of these planes redefines the φ_j variables as follows

$$\begin{pmatrix} e^{-i\alpha} & 0 \\ 0 & e^{-i\beta} \end{pmatrix} \begin{pmatrix} \cos\eta_j & e^{i\varphi_j}\sin\eta_j \\ -e^{-i\varphi_j}\sin\eta_j & \cos\eta_j \end{pmatrix} \begin{pmatrix} e^{i\alpha} & 0 \\ 0 & e^{i\beta} \end{pmatrix} = \begin{pmatrix} \cos\eta_j & e^{i(\varphi_j - \alpha + \beta)}\sin\eta_j \\ -e^{-i(\varphi_j - \alpha + \beta)}\sin\eta_j & \cos\eta_j \end{pmatrix}$$

We will choose a basis in which $-\varphi_2 = \varphi_1 \equiv \varphi$, leaving us with three free parameters, $(\eta_1, \eta_2, \varphi)$, describing the orientation of the two vortex planes relative to the lab frame. In terms of these parameters the two planes are defined by the zeroes of the following complex coordinates

$$\acute{r}_1 e^{i\acute{\theta}_1} = \cos\eta_1 r_1 e^{i\theta_1} + e^{i\varphi}\sin\eta_1 r_2 e^{i\theta_2}, \tag{64}$$

$$\grave{r}_2 e^{i\grave{\theta}_2} = \cos\eta_2 r_2 e^{i\theta_2} - e^{i\varphi}\sin\eta_2 r_1 e^{i\theta_1}, \tag{65}$$

restated here for clarity. We will now find and then minimise the sum of the rotational and hydrodynamic energies of the superfluid with respect to these three variables.

VI.2.1. Rotational Energy

Firstly, we will calculate the rotational energy, which is the expectation value of $-\Omega_{xy}\hat{L}_{xy} - \Omega_{zw}\hat{L}_{zw}$ in the state ψ [c.f. Eq. (58)]. Since this is a first order differential operator we may use the product rule on Eq. (60), e.g. for each angular momentum component as

$$\Omega_{xy}\hat{L}_{xy}\psi = n^{\frac{1}{2}}\left(e^{i\grave{\theta}_2}\Omega_{xy}\hat{L}_{xy}e^{i\acute{\theta}_1} + e^{i\acute{\theta}_1}\Omega_{xy}\hat{L}_{xy}e^{i\grave{\theta}_2}\right),$$

$$\psi^*\Omega_{xy}\hat{L}_{xy}\psi = n\left(e^{-i\acute{\theta}_1}\Omega_{xy}\hat{L}_{xy}e^{i\acute{\theta}_1} + e^{-i\grave{\theta}_2}\Omega_{xy}\hat{L}_{xy}e^{i\grave{\theta}_2}\right),$$

such that the rotational energy density is simply the sum of contributions from each vortex independently. From Section VI.1, recall that the favourable possible orientations of the two planes are limited to those which are planes of rotation of the isoclinic rotation generated by $\hat{L}_+$. This means that – as in the single vortex case we just considered – we can rewrite the rotational energy density as

$$\psi^*(\Omega_{xy}\hat{L}_{xy} + \Omega_{zw}\hat{L}_{zw})\psi = 2n\hbar\Omega_{zw} + n\Delta\Omega\left(\frac{\hat{L}_{xy}e^{i\acute{\theta}_1}}{e^{i\acute{\theta}_1}} + \frac{\hat{L}_{xy}e^{i\grave{\theta}_2}}{e^{i\grave{\theta}_2}}\right),$$

where the extra factor of 2 in the first term on the RHS arises because we now have two vortex planes instead of one [c.f. Eq. (59)]. This means that to proceed we simply have to evaluate the angular momentum of each vortex in the x–y plane. In other words, we must compute the following integral

$$\int\limits_{B^4(R)} \frac{\hat{L}_{xy} e^{i\acute{\theta}_1}}{e^{i\acute{\theta}_1}} \mathrm{d}^4 r, \tag{66}$$

and the corresponding integral for $e^{i\grave{\theta}_2}$; here, we will only show the direct calculation of the first integral, since the second follows identical logic. To begin, we will consider acting with $\hat{L}_{xy} \equiv -i\hbar\partial_{\theta_1}$ on Eq. (64) as

$$\frac{\hat{L}_{xy}\acute{r}_1 e^{i\acute{\theta}_1}}{\acute{r}_1 e^{i\acute{\theta}_1}} = \frac{\hbar \cos\eta_1 r_1 e^{i\theta_1}}{\cos\eta_1 r_1 e^{i\theta_1} + e^{i\varphi}\sin\eta_1 r_2 e^{i\theta_2}},$$

where we have also divided through by Eq. (64). Then by using the product rule, we can see that the desired integrand in Eq. (66) can be expressed as

$$\frac{\hat{L}_{xy} e^{i\acute{\theta}_1}}{e^{i\acute{\theta}_1}} = \frac{\hbar r_1 e^{i(\theta_1-\theta_2-\varphi)}}{r_1 e^{i(\theta_1-\theta_2-\varphi)} + \tan\eta_1 r_2} - \frac{\hat{L}_{xy}\acute{r}_1}{\acute{r}_1}.$$

The second term can be shown to integrate to zero as follows

$$\begin{aligned}\int\limits_{-\pi}^{\pi} \mathrm{d}\theta_1 \frac{\hat{L}_{xy}\acute{r}_1}{\acute{r}_1} &= -i\hbar \int\limits_{-\pi}^{\pi} \mathrm{d}\theta_1 \acute{r}_1^{-1} \frac{\partial \acute{r}_1}{\partial\theta_1} \\ &= -i\hbar\Big[\ln \acute{r}_1\Big]_{-\pi}^{\pi} = 0.\end{aligned}$$

In terms of the integral over θ_1, we are then left with the following

$$\int\limits_{-\pi}^{\pi} \mathrm{d}\theta_1 \frac{\hat{L}_{xy} e^{i\acute{\theta}_1}}{e^{i\acute{\theta}_1}} = \hbar \int\limits_{-\pi}^{\pi} \mathrm{d}\theta_1 \frac{r_1 e^{i(\theta_1-\theta_2-\varphi)}}{r_1 e^{i(\theta_1-\theta_2-\varphi)} + \tan\eta_1 r_2},$$

which can be evaluated as a contour integral in the complex plane. Setting $\zeta = e^{i(\theta_1-\theta_2-\varphi)}$, such that $\mathrm{d}\zeta = ie^{i(\theta_1-\theta_2-\varphi)}\mathrm{d}\theta_1$, we have

$$\begin{aligned}\int\limits_{-\pi}^{\pi} \mathrm{d}\theta_1 \frac{\hat{L}_{xy} e^{i\acute{\theta}_1}}{e^{i\acute{\theta}_1}} &= \hbar \int\limits_{|\zeta|=1} \frac{-ir_1 \mathrm{d}\zeta}{r_1\zeta + \tan\eta_1 r_2} \\ &= 2\pi\hbar\Theta\left(r_1 - \tan\eta_1 r_2\right).\end{aligned}$$

The integral over θ_2 then simply gives another factor of 2π. What is left is a fairly straightforward double integral over the two polar radii

$$\int\limits_{B^4(R)} \mathrm{d}^4 r \frac{\hat{L}_{xy} e^{i\acute{\theta}_1}}{e^{i\acute{\theta}_1}} = 4\hbar\pi^2 \int\limits_0^R r_2 \mathrm{d}r_2 \int\limits_0^{\sqrt{R^2-r_2^2}} r_1 \mathrm{d}r_1 \Theta(r_1 - \tan\eta_1 r_2),$$

where the limits reflect that the 4D hypersphere is bounded by $r_1^2 + r_2^2 = R^2$. Since both r_j are non-negative we can safely rewrite the step function as $\Theta(r_1^2 - \tan^2\eta_1 r_2^2)$, which allows us to make the substitutions $u_j = r_j^2/R^2$, such that the integral then becomes

$$\int\limits_{B^4(R)} \mathrm{d}^4 r \frac{\hat{L}_{xy} e^{i\acute{\theta}_1}}{e^{i\acute{\theta}_1}} = \hbar\pi^2 R^4 \int\limits_0^1 \mathrm{d}u_2 \int\limits_0^{1-u_2} \mathrm{d}u_1 \Theta(u_1 - \tan^2\eta_1 u_2).$$

It is now much easier to compare the step function to the integration limits, as we have that $u_1 > \tan^2\eta_1 u_2$ and $0 < u_1 < 1 - u_2$, whilst $0 < u_2 < 1$. Clearly $\tan^2\eta_1 u_2$ is non-negative, so we can make this value the new lower limit for u_1 provided it is not greater than the upper limit of $1-u_2$. This will be true for a certain range of u_2 values which satisfy the inequality

$$\begin{aligned}\tan^2\eta_1 u_2 &\leq 1 - u_2, \\ u_2 &\leq \cos^2\eta_1,\end{aligned}$$

in which case the above integral including the step function is equivalent to

$$\int\limits_{B^4(R)} \mathrm{d}^4 r \frac{\hat{L}_{xy} e^{i\acute{\theta}_1}}{e^{i\acute{\theta}_1}} = \hbar\pi^2 R^4 \int\limits_0^{c^2} \mathrm{d}u_2 \int\limits_{t^2 u_2}^{1-u_2} \mathrm{d}u_1,$$

where c and t are shorthand for $\cos\eta_1$ and $\tan\eta_1$, respectively. Evaluating this, we obtain

$$\begin{aligned}\int\limits_{B^4(R)} \mathrm{d}^4 r \frac{\hat{L}_{xy} e^{i\acute{\theta}_1}}{e^{i\acute{\theta}_1}} &= \hbar\pi^2 R^4 \int\limits_0^{c^2} \mathrm{d}u_2 \left(1 - \frac{u_2}{c^2}\right) \\ &= \hbar\frac{\pi^2}{2} R^4 \cos^2\eta_1.\end{aligned}$$

As previously mentioned the calculation for the $e^{i\grave{\theta}_2}$ term is very similar, so we simply state the result, which is

$$\int\limits_{B^4(R)} \mathrm{d}^4 r \frac{\hat{L}_{xy} e^{i\grave{\theta}_2}}{e^{i\grave{\theta}_2}} = \hbar\frac{\pi^2}{2} R^4 \sin^2\eta_2.$$

Putting these together, remembering that $n = N/V$ and $V = \pi^2 R^4/2$, we have

$$E_{\mathrm{rot}} = 2N\hbar\Omega_{zw} + N\hbar\Delta\Omega\left(\cos^2\eta_1 + \sin^2\eta_2\right),$$

for the rotational energy of two rigid, intersecting vortex planes under unequal frequency double rotation, with η_1 (resp. η_2) denoting the angle that the first (resp. second) plane is tilted compared to the x–y (resp. z–w) rotation plane.

VI.2.2. Vortex-Vortex Interaction Energy

Secondly, we consider the hydrodynamic vortex plane interaction previously derived in Sec. V.1, which, as we state again here, is calculated from

$$E_{\rm vv} = m \int \rho \mathbf{v}_1 \cdot \mathbf{v}_2 \mathrm{d}^4 r.$$

As this depends on the dot product between the velocity fields of each individual vortex, this energy is entirely dependent on the "skewness" of the two planes: an angle, which we will denote η (no subscript), that measures how far from being mutually orthogonal the vortex planes are. Simply put, we shall define η such that the angle between the two planes is $\pi/2 - \eta$. The most direct way to find η is to take the acute and grave coordinates and define a rotation transforming between them. Remembering that each of the vortex planes is a rotation plane of a left isoclinic rotation M_L, we can use our result from Sec. III.2 that the transformation between them has the following form [c.f. Eq. (24)]

$$\begin{pmatrix} \grave{r}_1 e^{i\grave{\theta}_1} \\ \grave{r}_2 e^{i\grave{\theta}_2} \end{pmatrix} = \begin{pmatrix} e^{i\phi_1}\cos\eta & e^{i\phi_2}\sin\eta \\ -e^{-i\phi_2}\sin\eta & e^{-i\phi_1}\cos\eta \end{pmatrix} \begin{pmatrix} \acute{r}_1 e^{i\acute{\theta}_1} \\ \acute{r}_2 e^{i\acute{\theta}_2} \end{pmatrix},$$

where $\eta \in [0, \pi/2]$ and $\phi_{1,2} \in [0, 2\pi)$. Substituting Eq. (62) into Eq. (61) gives a relation of this form; specifically, examining the top-left entry of the matrix allows us to relate η to η_1, η_2, and φ as follows

$$e^{i\phi_1}\cos\eta = \cos\eta_1\cos\eta_2 + e^{-2i\varphi}\sin\eta_1\sin\eta_2. \quad (67)$$

Taking particular values of φ in the above equation will give us intuition for how this parameter corresponds to the direction of the tilt, as mentioned previously, and hence allow us to deduce the form of the vortex-vortex interaction. In particular, we will examine the cases in which φ is a multiple of $\pi/2$, as this renders the RHS of Eq. (67) real and non-negative, allowing us to simplify this equation by choosing $\phi_1 = 0$. Specifically, when $\varphi = 0$ or π we have

$$\cos\eta = \cos(\eta_1 - \eta_2), \quad \rightarrow \quad \eta = |\eta_1 - \eta_2|, \quad (68)$$

while $\varphi = \pi/2$ or $3\pi/2$ gives

$$\cos\eta = \cos(\eta_1 + \eta_2), \quad \rightarrow \quad \eta = \eta_1 + \eta_2. \quad (69)$$

Note that $\cos(\eta_1 + \eta_2)$ is non-negative due to the constraint on $\eta_{1,2}$ [Eq. (63)].

To understand these special cases let's look at the equations of the vortex planes directly. Substituting $\varphi = 0$ into Eqs (64) and (65) gives

$$\acute{r}_1 e^{i\acute{\theta}_1} = \cos\eta_1(x + iy) + \sin\eta_1(z + iw),$$
$$\grave{r}_2 e^{i\grave{\theta}_2} = \cos\eta_2(z + iw) - \sin\eta_2(x + iy),$$

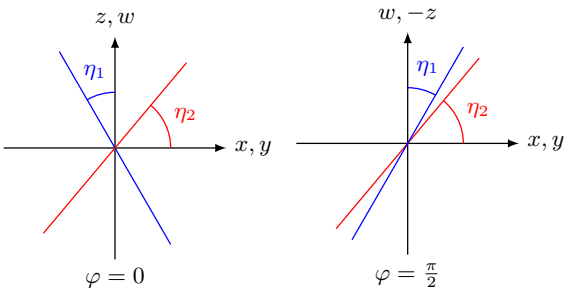

FIG. 5. A possible configuration of tilted vortex planes relative to the x–y and z–w planes, visualised as lines in 2D, for special values of φ. When $\varphi = 0$ the planes are given by Eqs (70) and (71), which describe a pair of lines in x, z space and an identical pair of lines in y, w space, plotted simultaneously in the left panel. When $\varphi = \pi/2$ we have instead Eqs (72) and (73), describing a pair of lines in x, w space and their reflection about the horizontal axis in y, z space, which we plot on the same graph here by transforming $z, w \rightarrow w, -z$. Equivalent pictures for $\varphi = \pi$ and $3\pi/2$ respectively can be found by reflection about the vertical axis.

such that the two planes are defined by

$$\acute{r}_1 e^{i\acute{\theta}_1} = 0: \quad x = -\tan\eta_1 z \ \ \& \ \ y = -\tan\eta_1 w, \quad (70)$$
$$\grave{r}_2 e^{i\grave{\theta}_2} = 0: \quad z = \tan\eta_2 x \quad \ \& \ \ w = \tan\eta_2 y, \quad (71)$$

while the same procedure for $\varphi = \pi/2$ gives

$$\acute{r}_1 e^{i\acute{\theta}_1} = 0: \quad x = \tan\eta_1 w \quad \ \& \ \ y = -\tan\eta_1 z, \quad (72)$$
$$\grave{r}_2 e^{i\grave{\theta}_2} = 0: \quad z = -\tan\eta_2 y \ \ \& \ \ w = \tan\eta_2 x. \quad (73)$$

In the $\varphi = 0$ case, Eqs (70) and (71) describe a pair of lines in the 2D (x, z) subspace, and identical lines found by taking the first lines and sending $(x, z) \rightarrow (y, w)$. Similarly, when $\varphi = \pi/2$ we have a pair of lines in the (x, w) subspace, and a pair in the (y, z) space which are related to the first pair by $(x, w) \rightarrow (y, -z)$. For $\varphi = \pi, 3\pi/2$ note that $\varphi \rightarrow \varphi + \pi$ transforms the equations for the planes simply by $z \rightarrow -z$ and $w \rightarrow -w$.

Since the equations separate into lines in 2D subspaces this way, we can visualise the planes by simply plotting these lines, as shown in Fig. 5. From the left panel of this figure it is clear that when $\varphi = 0$ (or π) the vortex planes are tilted away from the coordinate planes in the same direction. Similarly, the right panel shows that when $\varphi = \pi/2$ or $3\pi/2$ the vortices are tilted in opposite directions, and hence towards each other. Other values of φ interpolate between these two scenarios such that the two vortex planes are not tilted along a common direction. This visual understanding also agrees with the two expressions for η, given in Eqs (68) and (69).

Now we can use physical intuition to deduce – without any further calculation – the most energetically favourable value for φ for any fixed values of the parameters $\eta_{1,2}$. Recalling that the rotational energy was

independent of φ, we need only consider the interaction potential between the two vortices, given by

$$E_{\rm vv} = -4\mu N \frac{\xi^2}{R^2} \ln\cos\eta,$$

which is positive and therefore repulsive. This result was derived in Sec. V.1 in the case that $\phi_{1,2} = 0$, however these angles do not affect the interaction since they can be absorbed into the definition of $\acute{\theta}_{1,2}$ and $\grave{\theta}_{1,2}$. Since this interaction is repulsive we can clearly see that it is maximised when $\varphi = \pi/2$ or $3\pi/2$ as the vortex planes are tilted directly toward one another. Equally, in the other case where $\varphi = 0$ or π the vortices are tilted in the same direction and the interaction energy cost is minimised. Therefore, we can set $\eta = |\eta_1 - \eta_2|$ and proceed with finding the minimum energy as a function of the remaining parameters $\eta_{1,2}$. For concreteness we will also set $\varphi = 0$, but note that $\varphi = \pi$ provides an equivalent solution with the same energy.

VI 2.3. Finding the minimum

Our final step is to add the rotational and the vortex-vortex interactions energies together and to minimise the resulting sum. Firstly we will define quantities that will make the calculation simpler. Let $E^{\perp}_{\rm rot} = N\hbar(\Omega_{xy} + \Omega_{zw})$ denote the reduction in energy due to rotation of the state with orthogonal vortex planes along the x–y and z–w planes [c.f. Eq. (34)]. We then define a dimensionless energy density relative to $E^{\perp}_{\rm rot}$, given by

$$\varepsilon = \frac{R^2}{2\xi^2\mu N}(-E_{\rm rot} + E^{\perp}_{\rm rot} + E_{\rm vv}),$$

and a dimensionless frequency difference $\omega = R^2\hbar\Delta\Omega/2\xi^2\mu$. Note that in units of the critical frequency Ω_c [Eq. (35)], this dimensionless frequency is given by $\omega = \ln(2.07R/\xi)\Delta\Omega/\Omega_c$. We then must find the minimum of the following

$$\varepsilon = \omega\left(1 - \cos^2\eta_1 - \sin^2\eta_2\right) - 2\ln\cos(\eta_1 - \eta_2). \quad (74)$$

Note that we have not needed to include the absolute value on the RHS of Eq. (68), since $\cos|x| = \cos x$. Additionally, the logarithmic divergences as $\eta_1 - \eta_2 \to \pi/2$ are unphysical as there the vortex planes coincide and the constant density approximation that we took in Sec. V.1 fails.

Setting the derivatives of this energy to zero gives us the following simultaneous equations

$$\frac{\partial\varepsilon}{\partial\eta_1} = \omega\sin 2\eta_1 + 2\tan(\eta_1 - \eta_2) = 0, \quad (75)$$

$$\frac{\partial\varepsilon}{\partial\eta_2} = -\omega\sin 2\eta_2 - 2\tan(\eta_1 - \eta_2) = 0. \quad (76)$$

Firstly, examining the sign of the terms in each of these equations (recalling that $\eta_{1,2} < \pi/2$), we must have that

$$\eta_1 \leq \eta_2.$$

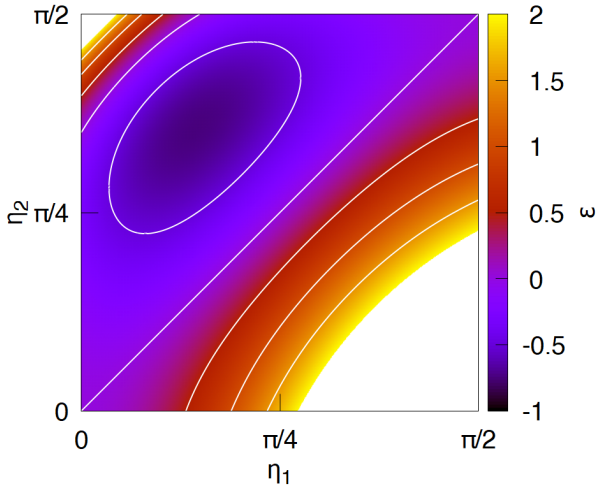

FIG. 6. Difference in dimensionless energy density [Eq. (74)] between the skew vortex plane ansatz and the orthogonal configuration as a function of the tilt angles $\eta_{1,2}$. The dimensionless frequency difference has been set to $\omega = 2$, for this value the minimum occurs at a skewness of $\eta \approx 38^\circ$ as calculated from Eq. (86). Contour lines are included as guides to the eye to highlight the degeneracy along the line $\eta_1 = \eta_2$, and the minimum in the upper left. We have omitted values of $\varepsilon > 2$ to avoid the logarithmic divergences at $(0, \pi/2)$ and $(\pi/2, 0)$.

Physically, this is because if η_1 is greater than η_2 then the force from the repulsive interaction acts in the same direction as the force from the rotational energy. Therefore we can eliminate the absolute value in Eq. (68), such that

$$\eta = \eta_2 - \eta_1. \quad (77)$$

Secondly, Eqs (75) and (76) together imply $\sin 2\eta_1 = \sin 2\eta_2$. There are two ways to satisfy this, i.e. by taking

$$\eta_1 = \eta_2, \quad (78)$$

$$\text{or} \quad \eta_1 = \frac{\pi}{2} - \eta_2. \quad (79)$$

The former case is precisely the condition that the two planes are orthogonal, which eliminates the interaction term. Substituting Eq. (78) into Eqs (75) and (76) then leads to the result $\eta_1 = \eta_2 = 0$, the state we have previously studied [1]. This state has an energy of $\varepsilon = 0$ by definition, since ε was defined relative to this state. Moreover, we also note that if we substitute Eq. (78) into Eq. (74), we see that *any* state with $\eta_1 = \eta_2$ has energy $\varepsilon = 0$. Interestingly, these orthogonal states are still all degenerate despite the isoclinic symmetry being broken when $\omega \neq 0$. The stationary point at $(\eta_1, \eta_2) = (0, 0)$ is therefore a saddle point, since it has this line of constant energy passing through it.

The latter case is much more interesting as it arises from competition between the interaction and rotational energies. Note that the relation between the tilt angles [Eq. (79)] ensures that the two planes are symmetrically

tilted with respect to the rotation planes of the superfluid; what we mean by this is that each vortex makes the same angle with the x–y plane, and also with the z–w plane. This can be seen by considering Fig. 5 and noting that the vortices are each tilted away from the x–y plane by an angle of $\pi/2-\eta_1$, and η_2 respectively. When $\eta_1 = \pi/2-\eta_2$ these two angles are equal, and the same is of course true with the angles the vortices make with the z–w plane. Using Eqs (77) and (79) we can write both the angles $\eta_{1,2}$ in terms of the skewness as follows

$$\eta_1 = \frac{\pi}{4} - \frac{\eta}{2}, \tag{80}$$

$$\eta_2 = \frac{\pi}{4} + \frac{\eta}{2}, \tag{81}$$

which makes it clear that $\eta_1 \leq \pi/4$ and $\eta_2 \geq \pi/4$. At this point it is worth restating our ansatz, since it now only depends on η. Recall that the order parameter is defined as [Eq. (60)] $\psi = n^{1/2} e^{i\acute{\theta}_1} e^{i\grave{\theta}_2}$, with these angles defined by Eqs (64) and (65). Substituting $\varphi = 0$ and the above equations for $\eta_{1,2}$, Eqs (64) and (65) become

$$\acute{r}_1 e^{i\acute{\theta}_1} = \sin\left(\frac{\pi}{4}+\frac{\eta}{2}\right) r_2 e^{i\theta_2} + \sin\left(\frac{\pi}{4}-\frac{\eta}{2}\right) r_1 e^{i\theta_1}, \tag{82}$$

$$\grave{r}_2 e^{i\grave{\theta}_2} = \sin\left(\frac{\pi}{4}+\frac{\eta}{2}\right) r_2 e^{i\theta_2} - \sin\left(\frac{\pi}{4}-\frac{\eta}{2}\right) r_1 e^{i\theta_1}, \tag{83}$$

where we have used that $\cos(\pi/4 \pm \eta/2) = \sin(\pi/4 \mp \eta/2)$. Note that we can now clearly see that two planes are arranged symmetrically, in the sense that after a rotation of angle π in the x–y plane ($\theta_1 \to \theta_1 + \pi$) the two equations Eq. (82) and (83) swap and hence the two vortex planes swap (note that this is also true for a π rotation in the z–w plane, up to a shift in the angles $\acute{\theta}_1$ and $\grave{\theta}_2$). This symmetry can also be seen in the the equations for the vortex planes, Eqs (70) and (71) which are now given by

$$z = \pm \tan\left(\frac{\pi}{4}+\frac{\eta}{2}\right) x \;\;\&\;\; w = \pm \tan\left(\frac{\pi}{4}+\frac{\eta}{2}\right) y \tag{84}$$

where $+$ and $-$ refer to the planes given by $\grave{r}_2 e^{i\grave{\theta}_2} = 0$ and $\acute{r}_1 e^{i\acute{\theta}_1} = 0$, respectively. From these equations we can actually see that this configuration is invariant under a π rotation in any one of the six coordinate planes.

We also now see from these equations that both vortices are closer in angle to the z–w plane than they are to the x–y plane. An interesting consequence of this is that when $\eta = 0$ the orthogonal state we get does not consist of vortices spanning the x–y and z–w planes. Instead the vortices occupy a pair of diagonal (in terms of the lab frame) planes, given by $z = \pm x$ and $w = \pm y$. This doesn't matter when the frequency difference is zero, as then the rotation is isoclinic and these diagonal planes are also rotation planes [c.f. Section III], but for any other value of $\Delta\Omega$ the only rotation planes are the x–y and z–w planes so it is perhaps surprising that none of these states ever occupy them.

Substituting Eqs (80) and (81) into Eq. (75) gives the following relation between ω and the optimal skewness

$$\omega = \frac{2\tan\eta}{\cos\eta}, \tag{85}$$

which rearranges to the following quadratic equation for $\sin\eta$

$$\sin^2\eta + \frac{2}{\omega}\sin\eta - 1 = 0.$$

This has only one solution for $\sin\eta$ in the interval $[-1, 1]$, given by

$$\sin\eta = \frac{\left(1+\omega^2\right)^{\frac{1}{2}} - 1}{\omega} \tag{86}$$

Physically this means that the optimal skewness vanishes in the limit that ω (i.e. the frequency difference in rotation) goes to zero, corresponding to the situation where the two vortex planes become completely orthogonal, as expected. In the opposite limit that ω becomes very large, this formula instead predicts that $\sin\eta \to 1$ and hence $\eta \to \pi/2$, meaning that the angle between the two planes goes to zero. This corresponds physically to the two planes both aligning with the z–w plane so as to maximise the energetic reduction due to the higher rotation frequency $\Omega_{xy} > \Omega_{zw}$. However, this limit should also be treated with caution, as at high enough frequencies, we expect that it will become energetically favourable to introduce more vortices and/or more complicated vortex structures, as briefly discussed at the end of the following section. We also expect there will be other contributions to the energy, which we have neglected here; for example, our assumption of a constant density profile will break down when the two vortex planes become very close together.

Now we can find the energy of this optimally skewed state; using Eqs (77), (79), and (81) the energy [Eq. (74)] becomes

$$\begin{aligned}\varepsilon &= \omega(1 - 2\sin^2\eta_2) - 2\ln\cos\eta, \\ &= \omega\cos\left(\frac{\pi}{2}+\eta\right) - \ln\cos^2\eta.\end{aligned}$$

Rearranging Eq. (85) we can quickly find that $\cos^2\eta = 2\sin\eta/\omega$, and after using $\cos(\pi/2+\eta) = -\sin\eta$ we have everything in terms of $\sin\eta$. Substituting Eq. (86) then gives the energy density for the optimal skewed statesin terms of ω as

$$\varepsilon = -\left[\left(1+\omega^2\right)^{\frac{1}{2}} - 1\right] + \ln\left\{\frac{\omega^2}{2\left[\left(1+\omega^2\right)^{\frac{1}{2}} - 1\right]}\right\} \tag{87}$$

For small and large ω we have the following asymptotics

$$\begin{aligned}\varepsilon &= -\frac{\omega^2}{2} + o(\omega^2) \text{ as } \omega \to 0, \\ \varepsilon &= -\omega + o(\omega) \text{ as } \omega \to \infty.\end{aligned}$$

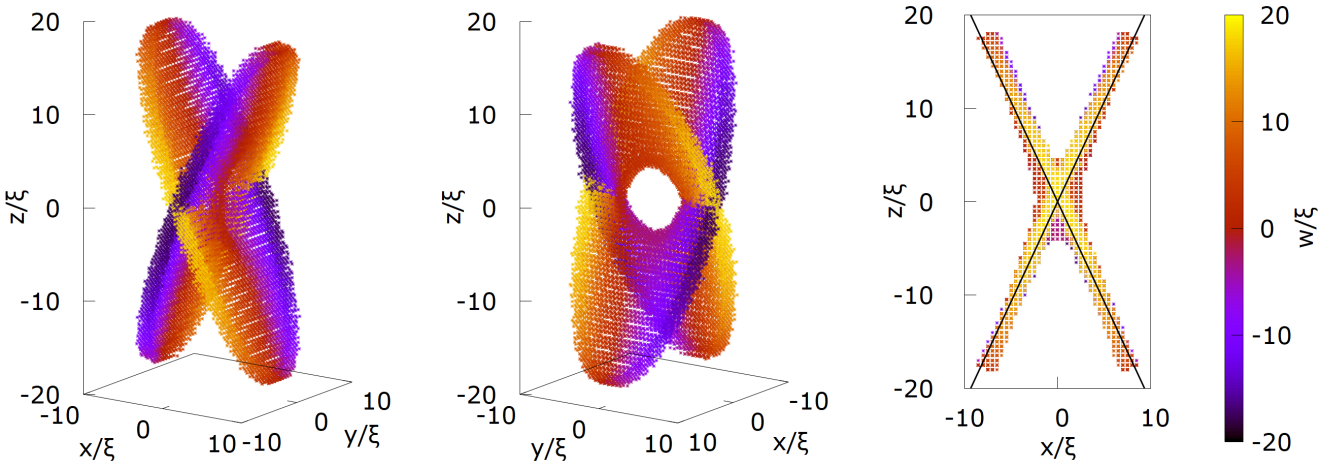

FIG. 7. Numerical vortex core in the final state of the ITEM-evolved 4D GPE under double rotation [Eq. (27)]. The spatial step size was $\Delta x = 0.5\xi$, corresponding to $R \approx 20.6\xi$. Rotation frequencies were $\Omega_{zw} = 0.85\Omega_c$, and $\Omega_{xy} \approx 1.43\Omega_c$, chosen such that the predicted skewness was precisely $\eta = 40°$. The initial phase profile was given by that of the ansatz described in Sec. VI.2, with this predicted value of η and added noise. The first two panels show two different views of the core in (x, y, z) space, with points coloured according to their w value. The overall structure resembles the skew planes of the ansatz but the second panel clearly shows how the core curves away from these planes to form an avoided crossing, reminiscent of the reconnection structures found in Sec. V.2. The final panel shows the points projected down into (x, z) space — again with w shown as colour — as well as the lines $z = \pm x \tan(\pi/4 + \eta/2)$, which the theory predicts that the core points should lie along from this perspective. The agreement between these analytical lines and numerical points is very good.

Recall that $\omega \propto R^2\Delta\Omega$, therefore these limits can be reached by decreasing (resp. increasing) either $\Delta\Omega$ or the radius R.

This energy [Eq. (87)] is also negative for all $\omega > 0$, which means our simplified model has predicted that this tilted vortex plane state is lower energy than the orthogonal state for any frequency difference $\Delta\Omega > 0$. Fig. 6 shows the energy landscape as a function of both tilt angles for dimensionless frequency difference $\omega = 2$. As expected, we see a line of constant energy along $\eta_1 = \eta_2$, a minimum energy along the line $\eta_1 = \pi/2 - \eta_2$, and a range of tilt angles for which the energy is negative.

VI.3. Numerical Results

We will now compare the above analytical predictions for tilted vortex planes to numerical results obtained using the methods described in Sec. IV.3. We choose an initial phase profile identical to that of our non-orthogonal vortex ansatz [Eq. (60)], where the acute and grave coordinates are given by Eqs (82) and (83), respectively, with a chosen value for the skewness, η. We then use Eq. (85) to calculate the frequency difference, $\Delta\Omega$, that will energetically favour the chosen value of η if the model is accurate, and then we run the ITEM with this value of $\Delta\Omega$ on our initial state with added noise.

Once the ITEM is converged we compare the geometry of the vortex core in the numerical final state with that of our predictions. Fig. 7 shows the numerical vortex core for $\Delta x = 0.5\xi$, which corresponds to a system radius of $R \approx 20.6\xi$, and with frequencies $\Omega_{zw} = 0.85\Omega_c$, and $\Omega_{xy} \approx 1.43\Omega_c$, corresponding to a predicted skewness of $\eta = 40°$. The first two panels show two different rotations of the core in (x, y, z) space, with the points coloured according to their w value (see the colourbar on the far right). Already we can see that, at large distances from the origin, the vortex cores look like the predicted tilted planes, with the symmetrically arranged with respect to the rotation planes of the superfluid. The third panel in Fig. 7 shows a side-on view where the vortex core appears approximately as a pair of lines, just as in Fig. 5. On top of these data points we have plotted the lines $z = \pm\tan(\pi/4+\eta/2)x$ [c.f. Eq. (84)] which are the predicted lines on which the numerical data should lie. As can be seen in the figure, there is excellent agreement between these numerical final states and our analytic predictions.

However, near the origin we see — most prominently in the second panel of the figure — an avoided crossing structure. This vortex core shape is qualitatively similar to that which we found analytically in Sec. V.2 by considering the linearised GPE dynamics close to the intersection point between a pair of vortex planes. However, as discussed in that section, there are some important caveats we must make when comparing these numerical results to the reconnection analytics. Firstly, the ITEM always converges towards a stationary state, whereas reconnection is a dynamical process. It is possible that the nonlinear dynamics depends on the size of the avoided crossing, leading to a stationary state at some special value. Secondly, given that our numerics is performed on a finite region with a hardwall boundary, the avoided

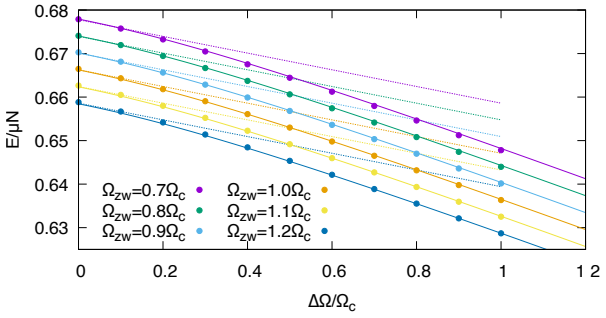

FIG. 8. Numerical (points) and analytical (solid lines) results for the energy of aligning non-orthogonal vortex states — as a function of Ω_{zw} and $\Delta\Omega$ — described in this section, as well as numerical results for the energy of the orthogonal vortex state (dotted lines). The resolution was set to $\Delta x = 0.5\xi$, giving a system radius of $R \approx 20.6\xi$. All of the analytical lines were generated by a single fit of the numerical points to Eq. (88), with E_0 and R as fitting parameters. The fit produced $E_0 \approx 0.71\mu N$ and $R \approx 19.5\xi$, and agrees excellently with the numerical data. The numerical zero-vortex ground state in this system has an energy of $E_{\rm hom} \approx 0.6697\mu N$, which suggests that the numerical critical frequency in this system is very close to $0.9\Omega_c$, where Ω_c is our predicted value [Eq. (35)].

crossing introduces image effects which were not considered in Sec. V.2. Finally, as shown in Eq. (49), there is no linear dynamics when the skew planes are tilted in a purely aligning sense, which is the case we have here. To see core plots of these predicted skew states at different values of the skewness and the spatial resolution, refer to Appendix XII.XII.1.

In addition to the above qualitative comparisons of the numerical and predicted vortex cores, we have made a quantitative analysis of the accuracy of our predicted energy [Eq. (87)]. To do this we performed the ITEM for a range of different frequencies Ω_{zw} and $\Delta\Omega$, again using our ansatz to determine the initial phase, and then calculating the energy of each final state. The procedure for these calculations was as follows; we fixed a value of Ω_{zw}, then ran the ITEM with $\Delta\Omega = \Omega_c$ on our prescribed initial state. From the final state we calculated the energy, and then to speed up calculations we used this final state as the initial state for the next ITEM run with $\Delta\Omega = 0.9\Omega_c$. This process was repeated down to the isoclinic point, $\Delta\Omega = 0$. Finally, many of these loops were run at once with different values of Ω_{zw}, so that we could explore an area in frequency space rather than just a line. The results for these energies are shown in Fig. 8, with each value of Ω_{zw} corresponding to a different colour. On top of these points we have plotted lines given by performing a single fit of this data over the area in frequency space to a redimensionalized version of Eq. (87) given by

$$E = E_0 - N\hbar\left(\Delta\Omega + 2\Omega_{zw}\right) + 2\mu N\frac{\xi^2}{R^2}\left[1 - \sqrt{1 + \frac{R^4\hbar^2\Delta\Omega^2}{4\xi^4\mu^2}} + \ln\left(\frac{R^4\hbar^2\Delta\Omega^2}{4\xi^4\mu^2}\right) - \ln\left(\sqrt{1 + \frac{R^4\hbar^2\Delta\Omega^2}{4\xi^4\mu^2}} - 1\right)\right], \quad (88)$$

where E_0 is simply the energy of the system when the vortex planes are orthogonal and there is no external rotation. Since ξ and μ are both external parameters in the numerics, the only parameters in the fit were R and E_0, the energy at $\Omega_{zw} = \Omega_{xy} = 0$. Furthermore, R is not truly a free parameter as it is determined up to boundary effects by the radius of the simulated region, which is roughly 20.6ξ. The fit produced a value of $R \approx 19.5\xi$, which is consistent if we estimate the size of the boundary region to be roughly equal to ξ. Additionally, the agreement between the numerical points and lines from the fit is excellent. We also attempted to track the energy of the theoretically predicted skew plane branch at a frequency of $\Omega_{zw} = 1.3\Omega_c$, by performing two of these iterative ITEM runs from $\Delta\Omega = \Omega_c$ down to $\Delta\Omega = 0$. Interestingly, as we decreased $\Delta\Omega$ for these runs the states we obtained increasingly diverged from the skew plane states, even down to the isoclinic point at $\Delta\Omega = 0$. For plots of these states at the isoclinic point, see Appendix XII.XII.1.

The dotted line shows the numerical energy of the orthogonal state [1] as a function of the frequencies. This was found by running the ITEM once, with $\Omega_{zw} = \Omega_{xy} = 1.2\Omega_c$, and then calculating the energy of this fixed final state for different values of Ω_{zw} and $\Delta\Omega$. As shown in Fig. 8, the energies of the orthogonal state form dotted straight lines that meet the fit lines tangentially at $\Delta\Omega = 0$, which is exactly as predicted since the skewness of the tilted state is approaching zero in this limit. Finally, note that the numerical zero-vortex ground state in this system has an energy of $E_{\rm hom} \approx 0.6697\mu N$, which is roughly equal to the energy of the skew and orthogonal vortex states when $\Omega_{zw} = 0.9\Omega_c$, and $\Delta\Omega = 0$. This means that the value of the numerical critical frequency in this system is very close to $0.9\Omega_c$, where Ω_c is our predicted value [Eq. (35)].

To get an idea of the size of the avoided crossing as a function of the frequencies, we have taken each state represented in Fig. 8 and calculated the minimum distance between its vortex core and the origin, which we denote $r_{\rm min}$. This is then plotted in Fig. 9, which shows that, in general, the avoided crossing decreases in size with both Ω_{zw} and $\Delta\Omega$. Note that these lines are not perfectly smooth and also change their ordering as $\Delta\Omega$

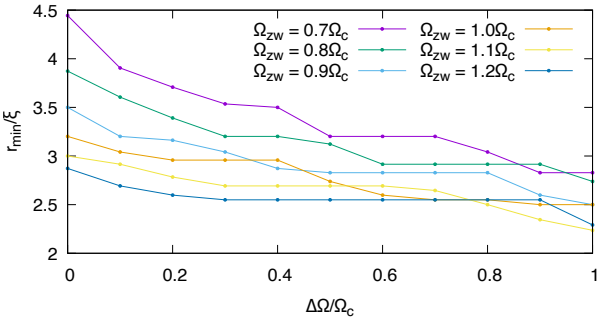

FIG. 9. Minimum distance $r_{\min}$ of the vortex core from the origin — as a function of Ω_{zw} and $\Delta\Omega$ — for the non-orthogonal numerical states whose energy is shown in Fig. 8. This quantity captures the size of the avoided crossing region seen in Figs 7 and similar final states. As shown above, this region generally shrinks as either frequency increases. These data are not particularly smooth, which may be due to some sampling error from the discretisation of the Cartesian grid

changes, suggesting that there are multiple metastable branches being sequentially followed by our numerical states. Nevertheless, these must be very close together in energy, since the fit in Fig. 8 is very good, and the long range core structure has good agreement with the predicted state.

Above we drew a qualitative comparison between the avoided crossing in the numerical states, and that seen in Sec. V.2. In that section, using linearised GPE dynamics, we found (reintroducing units) that $r_{\min} < \sqrt{2}\gamma\xi$, where γ was a perturbing term required to be much less than unity. Here, however, we can see that the $r_{\min}$ value of these numerical states is larger than 2ξ, showing that they cannot be described in this linearised regime. This is not surprising since, as previously mentioned, these are stationary states and so should have no dynamics, suggesting that a full nonlinear analysis may be required to understand this phenomenon.

Lastly, we have further tested our analytical results by using a different initial phase profile in the numerics. We still use the tilted plane ansatz [Eq. (60)], but with different values of η_1 and η_2 than those predicted. Instead of the predicted values, $\eta_1 + \eta_2 = \pi/2$ [Eq. (79)], we chose $\eta_1 = \delta$, $\eta_2 = \eta + \delta$, where η is the skewness of the theoretically predicted configuration, and δ is a small angle added to ensure all symmetries are broken. The corresponding planes still have skewness given by η, but are now asymmetric with respect to the planes of the external rotation. This initial state (with added noise) converges to the same final state as Fig. 7 under the same value of all parameters ($\Delta x = 0.5\xi$, corresponding to $R \approx 20.6\xi$ $\Omega_{zw} = 0.85\Omega_c$, $\Omega_{xy} \approx 1.43\Omega_c$, corresponding to $\eta = 40°$), showing that this predicted state is likely the ground state in this regime. However, at a higher value of $\Omega_{zw} = 1.25\Omega_c$, we find very different final states of the ITEM depending on which initial phase profile is used. Specifically, using the predicted phase profile (with added noise) we find the same final states as before, with just as good agreement to the analytics. Using the asymmetric phase profile (with added noise) described above, we find very different vortex core structures, with slightly higher energies than the theoretical states. This again shows excellent agreement with our theoretical model.

The vortex cores of these final states are shown in Fig. 10, for $\Delta\Omega$ values corresponding to $\eta = 10°$, $20°$ and $40°$, respectively. Already, in the $10°$ case we can see that our assumption of flat vortex planes is broken as there is some long-range curvature of the core. This is then exacerbated as the frequency $\Delta\Omega$ increases, with the $20°$ state clearly showing that there is almost no overall tilt of the former planes, but instead the plane at $z = w = 0$ has begun to buckle in an approximately threefold symmetric pattern, curving towards the other surface in different directions for different values of the angle θ_1. Finally, in the $40°$ figure, this curvature has become so extreme that the former plane at $x = y = 0$ appears to have become tilted and displaced as well as curved, leading to a sizeable avoided crossing where these two surfaces come together, as can be seen in the first panel. Interestingly, the second panel appears to show three parts of the vortex core surface that are parallel to each other. This suggests that this bizarre state may be limiting towards a state with multiple vortex planes parallel to the z–w plane but separated in the x–y plane. This is the expected lowest energy state for the case of high frequency simple rotation in the x–y plane (i.e. with $\Omega_{zw} = 0$) so it seems reasonable that it should also be the ground state when $\Omega_{xy} \gg \Omega_{zw}$. However, we are not quite reaching this limit in the $40°$ case, as there we have $\Omega_{xy} \approx 1.46\Omega_{zw}$. We therefore tentatively describe this strange set of states as an instance where the frequencies are large enough that the system wants more than two vortex planes but not enough for three. The planes can curve in order to become larger, thereby fitting a larger area of vortex surface in the system. Whether this is a correct description or not, it is clear that the behaviour of vortex surfaces in 4D is incredibly rich, and there is much more to be explored.

To summarise, this section showed how — in a finite 4D superfluid doubly rotating at unequal-frequencies — a pair of vortex planes in certain non-orthogonal configurations can have lower overall energy than an orthogonal pair. This energy was approximated with two terms: rotational energy from the degree of alignment between the external rotation and the superfluid angular momentum, and hydrodynamic interaction between the vortex planes. We showed that in order to benefit from the reduction in energy due to rotation, the vortex planes had to be tilted towards each other in an aligning sense, introducing a positive (i.e. repulsive) interaction energy. However, for a range of tilt angles this repulsion was more than counterbalanced by the reduction in rotational energy, giving states that were lower in energy than the orthogonal states. Finally, the lowest energy of these states — for any given frequency difference $\Delta\Omega$ — was

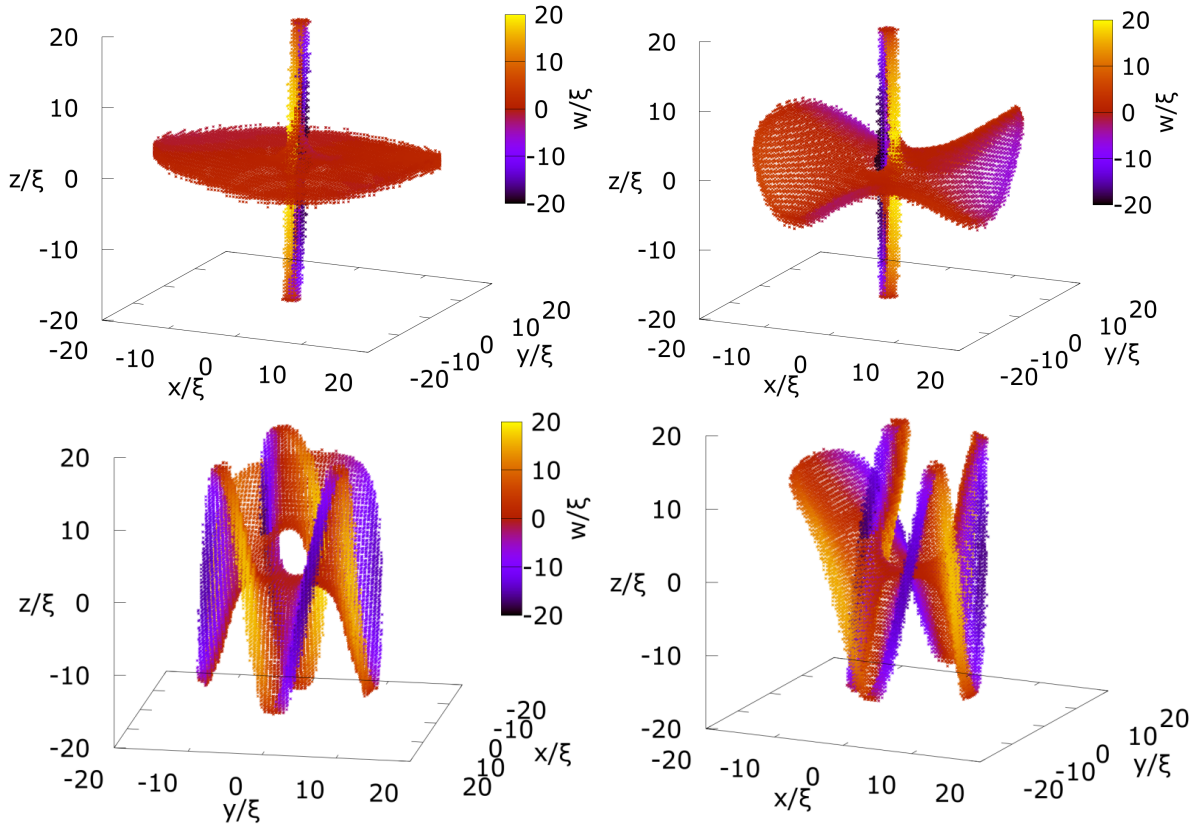

FIG. 10. Numerical vortex cores in final states of the ITEM-evolved 4D GPE under double rotation [Eq. (27)]. The spatial step size was $\Delta x = 0.5\xi$, corresponding to $R \approx 20.6\xi$. Rotation frequencies were $\Omega_{zw} = 1.25\Omega_c$, and $\Omega_{xy} \approx 1.35\Omega_c$ (Top-Left), $\Omega_{xy} \approx 1.46\Omega_c$ (Top-Right), and $\Omega_{xy} \approx 1.83\Omega_c$ (Bottom), corresponding to predicted skewness values of $\eta = 10^\circ$, 20°, and 40°, respectively. However, we used an initial phase profile corresponding to asymmetrically tilted planes — rather than the predicted symmetrically tilted ones — with added noise, as described in the main text. (Top-Left) Instead of tilting, we see that the vortex core is starting to become slightly curved even at long distances. The energy at these frequencies is $E \approx 0.6589\mu N$, while the predicted skew plane energy from the fit in Fig. 8 is $\approx 0.6544\mu N$. (Top-Right) The surface centred around $z = w = 0$ is now buckled, effectively tilting towards the other plane in different directions depending on the angle θ_1. The energy is $E \approx 0.6567\mu N$ while the skew plane energy is $\approx 0.6517\mu N$. (Bottom) The two panels show two different views in (x, y, z) space. The former x–y plane is now so curved that it has forced the other surface to become tilted and displaced, and there is an avoided crossing between them as visible in the first panel. Note that the second panel shows that parts of this surface appear to be parallel to each other. Here, the energy is $E \approx 0.6417\mu N$ while the predicted skew plane energy is $\approx 0.6407\mu N$

found by considering the optimum balance between the repulsion and rotational energy. In the following section we will consider the inverse case: vortex planes tilting in an anti-aligning sense, resulting in an increased rotational energy and a negative (i.e. attractive) interaction energy. We will use essentially the same approximations and analytics as we have in this section to investigate whether such an anti-aligning configuration can have lower energy than the orthogonal state.

VII. EQUAL FREQUENCY DOUBLE-ROTATIONS

In Ref. [1] we considered the case of a superfluid undergoing constant left isoclinic rotation in time, given by $\Omega_{xy} = \Omega_{zw} \equiv \Omega$ in the lab (x, y, z, w) frame. We showed how this type of double rotation could energetically stabilise a configuration of two completely orthogonal vortex planes that intersect at a point, as reviewed in Sec. IV. Here we will consider this case again, but with a more generalised ansatz that includes the possibility of those vortex planes tilting away from the rotation planes and towards each other, in an anti-aligning sense, in order to benefit from attractive interaction at the expense of rotational energy. We will use both analytics and numerics to investigate whether such a state can be energetically preferred to an orthogonal one.

Setting both frequencies equal to each other greatly simplifies the analysis, and introduces extra symmetry that we can exploit. Firstly, we don't have to include any tilting of the type we considered in the previous section in our ansatz, since we have $\Delta\Omega = 0$. Secondly, as shown in Sec. III.2, an isoclinic rotation does not have

a unique pair of rotation planes, but instead an infinite set of them. We also showed that the right isoclinic rotations are precisely the transformations between rotation planes of a left isoclinic rotation and vice-versa. This means that a spherically symmetric 4D system subjected to constant left isoclinic rotation in time has symmetry with respect to all right isoclinic rotations. In the case of a superfluid rotating in this way there is a degenerate set of orthogonal vortex states corresponding to the set of orthogonal pairs of rotation planes.

Therefore we will focus on configurations of two vortex planes which are each tilted off the rotation planes such that they begin to anti-align with each other. Starting with a fully general ansatz of this form we will use the right isoclinic symmetry to eliminate unnecessary parameters. As in Sec. VI, we will take the density to be constant, giving an ansatz of the following form

$$\psi = n^{\frac{1}{2}} e^{i\acute{\theta}_1} e^{i\grave{\theta}_2}, \tag{89}$$

although with the acute ($\acute{\mathbf{r}}$) and grave ($\grave{\mathbf{r}}$) coordinate systems defined in a different way to the previous section. Specifically, we will start in full generality, such that $\acute{\mathbf{r}} = \acute{M}\mathbf{r}$, and $\grave{\mathbf{r}} = \grave{M}\mathbf{r}$, where $\acute{M}$ and $\grave{M}$ are arbitrary rotations. Recall that any element M of $SO(4)$ can be written as a product of some left isoclinic rotation M_L and some right isoclinic rotation M_R, and that these always commute [c.f. Section III.2]. Therefore, we define $\acute{M} = \acute{M}_L\acute{M}_R$ and $\grave{M} = \grave{M}_L\grave{M}_R$. The relationship between the two tilted coordinate systems is then given by

$$\begin{aligned}\acute{\mathbf{r}} &= \acute{M}\grave{M}^{-1}\grave{\mathbf{r}}, \\ &= (\acute{M}_L\grave{M}_L^{-1})(\acute{M}_R\grave{M}_R^{-1})\grave{\mathbf{r}}.\end{aligned} \tag{90}$$

As shown in Sec. V.1, we require the two planes to be anti-aligning for their interaction to be attractive. In this case this means that transformation between their respective coordinate systems, (and hence the entire matrix product in Eq. (90)) must be a left isoclinic rotation. Now, the product of two left (right) isoclinic rotations is always a left (right) isoclinic rotation, and so the first factor in brackets in Eq. (90) is a left isoclinic rotation while the second factor is a right one. Therefore for $\acute{\mathbf{r}}$ and $\grave{\mathbf{r}}$ to be related by a left isoclinic rotation we must reduce the second bracketed term to the identity matrix, by setting $\acute{M}_R = \grave{M}_R \equiv M_R$.

The definitions of each of the coordinates then become $\acute{\mathbf{r}} = \acute{M}_L M_R\mathbf{r}$, and $\grave{\mathbf{r}} = \grave{M}_L M_R\mathbf{r}$. However, we can use the symmetry with respect to right isoclinic rotations to redefine $\mathbf{r} \to M_R^{-1}\mathbf{r}$, absorbing M_R into the definition of the lab frame. The acute and grave coordinates are each then related to the lab frame, and to each other by a left isoclinic rotation. In Sec. III.2 we derived the complex representation of left and right isoclinic rotations and showed how to eliminate redundant parameters when these rotations are only defined by their action on a plane. Using these results we can, finally, explicitly write down the definition of the tilted coordinates as follows

$$\begin{pmatrix} \acute{r}_1 e^{i\acute{\theta}_1} \\ \acute{r}_2 e^{-i\acute{\theta}_2} \end{pmatrix} = \begin{pmatrix} \cos\eta_1 & e^{i\varphi_1}\sin\eta_1 \\ -e^{-i\varphi_1}\sin\eta_1 & \cos\eta_1 \end{pmatrix} \begin{pmatrix} r_1 e^{i\theta_1} \\ r_2 e^{-i\theta_2} \end{pmatrix},$$

$$\begin{pmatrix} \grave{r}_1 e^{i\grave{\theta}_1} \\ \grave{r}_2 e^{-i\grave{\theta}_2} \end{pmatrix} = \begin{pmatrix} \cos\eta_2 & e^{i\varphi_2}\sin\eta_2 \\ -e^{-i\varphi_2}\sin\eta_2 & \cos\eta_2 \end{pmatrix} \begin{pmatrix} r_1 e^{i\theta_1} \\ r_2 e^{-i\theta_2} \end{pmatrix}.$$

(N.B. the difference with Eqs. (61) and (62) in the previous section is that $e^{i\grave{\theta}_2}$, $e^{i\acute{\theta}_2}$ and $e^{i\theta_2}$ are here replaced by their complex conjugates, reflecting that these coordinate systems are now related to the untilted coordinates by a left isoclinic rotation, instead of a right isoclinic rotation as previously [c.f. Section III.2].) We also already know from the previous section that the sum $\varphi_1 + \varphi_2$ can be chosen arbitrarily by a change of basis, so in this instance we will choose $\varphi_1 + \varphi_2 = \pi$. Additionally, we know difference $\varphi_1 - \varphi_2$ controls the relative direction of the tilting of the two planes. In this case we want the vortices to be tilted towards each other, so we set this difference to zero, such that $\varphi_1 = 0$, $\varphi_2 = \pi$, and

$$\acute{r}_1 e^{i\acute{\theta}_1} = \cos\eta_1 r_1 e^{i\theta_1} + \sin\eta_2 r_2 e^{-i\theta_2}, \tag{91}$$

$$\grave{r}_2 e^{i\grave{\theta}_2} = \cos\eta_2 r_2 e^{i\theta_2} + \sin\eta_2 r_1 e^{-i\theta_1}. \tag{92}$$

The skewness between the planes is then given by $\eta = \eta_1 + \eta_2$, and the angle between them is $\pi/2 - \eta$. Similarly to the previous section, we can restrict $\eta_{1,2}$ with $\eta_1 + \eta_2 \leq \pi/2$, but in reality this sum should be restricted to an even smaller value. This is because our constant-density approximation gives an unphysical divergent interaction energy as $\eta \to \pi/2$ and the vortex cores approach each other. This divergence is especially important now that we are considering attractive interaction, since it incorrectly implies the energy can decrease without bound. With this in mind we will now calculate the rotational and vortex-vortex interaction energies of this configuration, in a manner very similar to the calculations in the previous section.

VII.1. Rotational and Interaction energy

Firstly, we have the rotational energy, which will be decreased due to the vortex planes tilting off of the manifold of rotation planes of the condensate. This means that such a configuration is less energetically favourable from a rotational point-of-view. As before, the form of our ansatz allows us to write the rotational energy density as

$$\psi^*(\Omega_{xy}\hat{L}_{xy} + \Omega_{zw}\hat{L}_{zw})\psi = n\Omega\left(\frac{\hat{L}_+ e^{i\acute{\theta}_1}}{e^{i\acute{\theta}_1}} + \frac{\hat{L}_+ e^{i\grave{\theta}_2}}{e^{i\grave{\theta}_2}}\right),$$

where $\hat{L}_+ = \hat{L}_{xy} + \hat{L}_{zw}$ and where we have used that $\Omega_{xy} = \Omega_{zw} \equiv \Omega$ for equal-frequency double rotation. Again we rewrite the terms inside the brackets in terms

of the lab frame by substituting in Eqs (91) and (92). For the first term this reads

$$\frac{\hat{L}_+ \acute{r}_1 e^{i\acute{\theta}_1}}{\acute{r}_1 e^{i\acute{\theta}_1}} = \hbar \frac{\cos\eta_1 r_1 e^{i\theta_1} - \sin\eta_1 r_2 e^{-i\theta_2}}{\cos\eta_1 r_1 e^{i\theta_1} + \sin\eta_1 r_2 e^{-i\theta_2}},$$
$$\frac{\hat{L}_+ e^{i\acute{\theta}_1}}{e^{i\acute{\theta}_1}} = \hbar \left(1 - \frac{2\tan\eta_1 r_2 e^{-i(\theta_1+\theta_2)}}{r_1 + \tan\eta_1 r_2 e^{-i(\theta_1+\theta_2)}}\right) - \frac{\hat{L}_+ \acute{r}_1}{\acute{r}_1}.$$

As before this can be integrated using complex analysis, giving

$$\int_{B^4(R)} \mathrm{d}^4 r \frac{\hat{L}_+ e^{i\acute{\theta}_1}}{e^{i\acute{\theta}_1}} = \hbar \frac{\pi^2}{2} R^4 \left(1 - 2\sin^2\eta_1\right),$$
$$= \hbar V \cos 2\eta_1,$$

where $V = \pi^2 R^4/2$ is the volume of the 4D hypersphere. Similarly, the other term integrates to $\hbar V \cos 2\eta_2$ by symmetry. The rotational energy reduction is then

$$E_{\mathrm{rot}} = \int \psi^* (\Omega_{xy} \hat{L}_{xy} + \Omega_{zw} \hat{L}_{zw}) \psi \mathrm{d}^4 r$$
$$= N\hbar\Omega \left(\cos 2\eta_1 + \cos 2\eta_2\right).$$

For the interaction energy we can simply state the result, since we already know the skewness. From our calculation in Sec. V.1, we have

$$E_{\mathrm{vv}} = 4\mu N \frac{\xi^2}{R^2} \ln\cos(\eta_1 + \eta_2).$$

Similar to before, we define a dimensionless energy density relative to $E^{\perp}_{\mathrm{rot}} = 2N\hbar\Omega$ (corresponding physically to the rotational energy of two orthogonal vortex planes under equal-frequency double-rotation) as

$$\varepsilon = \frac{R^2}{4\xi^2 \mu N}(-E_{\mathrm{rot}} + E^{\perp}_{\mathrm{rot}} + E_{\mathrm{vv}}),$$

and a dimensionless frequency (not frequency difference this time) $\omega = R^2\hbar\Omega/2\xi^2\mu$, such that

$$\varepsilon = \omega \left[1 - \frac{1}{2}\left(\cos 2\eta_1 + \cos 2\eta_2\right)\right] + \ln\cos(\eta_1 + \eta_2) \quad (93)$$

Taking derivatives of this energy we find very similar results to before.

$$\frac{\partial\varepsilon}{\partial\eta_1} = \omega \sin 2\eta_1 - \tan(\eta_1 + \eta_2) = 0,$$
$$\frac{\partial\varepsilon}{\partial\eta_2} = \omega \sin 2\eta_2 - \tan(\eta_1 + \eta_2) = 0.$$

Once again we find that $\sin 2\eta_1 = \sin 2\eta_2$, such that either $\eta_1 = \eta_2$ or $\eta_1 = \pi/2 - \eta_2$. However, in this instance we can rule out the latter solution as this results in the vortices coinciding, which is a limit that our current approximations break down in. We therefore take $\eta_1 = \eta_2 \equiv \eta/2$ and proceed. Both equations above then become

$$\omega \sin\eta = \tan\eta,$$

which implies either $\sin\eta = 0$ or $\cos\eta = 1/\omega$. The former condition gives $\eta = 0$ — the orthogonal state — while the latter looks like a promising candidate for a skewed state that is lower in energy, provided $\omega > 1$. However, if we look at the energy of this state we find $\varepsilon = \omega - 1 - \ln\omega$, which is never negative. This state is therefore always higher energy than the orthogonal state. A more detailed analysis reveals that it is a saddle point in the $\eta_{1,2}$ energy landscape. Therefore, this theory predicts that for $\omega > 1$ the orthogonal state at $\eta = 0$ is a local minimum and there is an energy barrier for the states to tilt away from this. For $\omega \leq 1$, both the minimum and saddle point disappear, and the predicted energy decreases monotonically with η.

In the latter case the orthogonal state would be unstable to this form of anti-aligned tilting even to the limit $\eta_1 = \eta_2 \to \pi/4$ where the vortex planes lie on top of each other with opposite winding. Eq. (93) predicts that $\varepsilon \to -\infty$ in this limit, but this is only because our constant density approximation for the interaction energy fails as the vortex cores increasingly overlap. In reality vortices that coincide in opposite senses annihilate each other, so we can interpret the $\omega < 1$ regime as suggesting that the orthogonal state is unstable below a certain threshold frequency. Note that in units of the critical frequency, Ω_c, the dimensionless frequency is given by $\omega = \ln(2.07R/\xi)\Omega/\Omega_c$, so this threshold frequency is given in terms of the critical frequency as $\Omega_{stab} = \Omega_c/\ln(2.07R/\xi)$. This will always be smaller than Ω_c for $R > 1.32\xi$, so this stability threshold does not alter the critical frequency. Investigating this predicted stability threshold is beyond the scope of this paper but would be an interesting topic for further work.

VII.1.1. Numerical Results

Now we numerically test the analytical prediction that the orthogonal state is lower energy than any anti-aligning state for $\omega > 1$ by performing the ITEM on initial states with a phase profile corresponding to the anti-aligning ansatz [Eq. (89)] with a uniform density away from the boundary, and added noise. By symmetry we assume that $\eta_1 = \eta_2$, although the actual value of this angle must be chosen arbitrarily, as we have no predicted state to inform us. For the results presented in this section we chose an initial tilt angle of $\eta_1 = \eta_2 = 5°$.

We ran the ITEM with the parameters $\Omega = 0.75\Omega_c$, $\Delta x = 0.5\xi$, and $R \approx 20.6\xi$ on our initial state and then calculated the energy and vortex core points from the final state. The resulting vortex core is plotted in Fig. 11, and looks like a pair of slightly skewed planes at large distances from the origin. The third panel shows the core side-on, ignoring the y coordinates, and shows lines

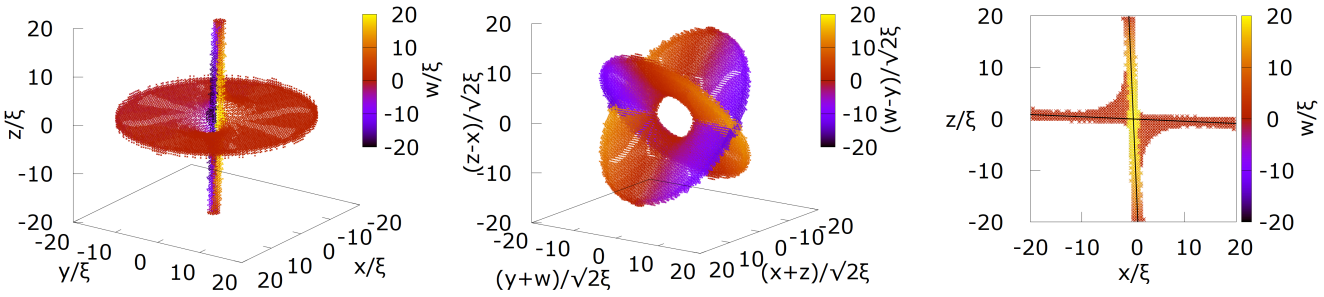

FIG. 11. Numerical anti-aligning non-orthogonal vortex core stationary state for the parameters $\Omega = 0.75\Omega_c$, $\Delta x = 0.5\xi$, and $R \approx 20.6\xi$. The first panel shows the core points in (x, y, z, w) space, with the w value represented as colour. This view shows the small tilt angle clearly, but obscures the avoided crossing region centred around the origin as one of the planes is collapsed towards the vertical axis. The second panel shows the same data after double rotation given in Eq. (36) (see the axes and colourbar labels for details), which shows the avoided crossing region clearly. The third panel shows a side-on view, along with a by-eye estimate of the tilt angle with the lines $z = -x\tan(2.5°)$ and $z = -x/\tan(2.5°)$. Note that at this frequency both this state and the orthogonal state are higher in energy than the state with no vortices.

plotted on top that give an estimate of the tilt angles by eye as $\eta_1 = \eta_2 \approx 2.5°$, such that the state has untilted slightly from our initial phase ansatz in a symmetric manner. This result suggests that the theory above is not a bad approximation: the final state that we have is close to a pair of orthogonal planes — even closer in angle than our initial phase profile.

Despite this, there is an avoided crossing region near the origin, out to radii of several healing lengths, which is qualitatively similar to the core structure derived in Sec. V.2 by considering the linearised dynamics of intersecting vortex planes. In particular, the first panel of Fig. 11 shows a core geometry somewhat similar to that of Fig. 3, with the avoided crossing obscured by the fact that much of the core is collapsing toward the vertical axis. To make the avoided crossing more visible, we rotated the coordinates according to the same double rotation [Eq. (36)] that was used to make the second panel of Fig. 3 and plotted the data against this new basis in the second panel. Again, the resulting plot looks similar to the orthogonal perturbed state, except that the avoided crossing region is much larger than that allowed by the linearised analysis in Sec. V.2. Another caveat we must make when drawing this analogy is that Fig. 11 shows the vortex core of a numerical stationary state, whereas Sec. V.2 dealt with dynamically evolving states.

We also investigate the frequency dependence of this physics by using the final state above as the initial state for another run of the ITEM with $\Omega = 0.80\Omega_c$, and then iterating this at regular frequency intervals up to $\Omega = 1.5\Omega_c$, outputting the energy and vortex core for each state. Finally, this entire loop was repeated for different values of the spatial resolution — and hence the system radius — from $\Delta x = 0.5\xi$, which gives $R \approx 20.6\xi$, down to $\Delta x = 0.25\xi$, which gives $R \approx 10.3\xi$, in steps of 0.05ξ. In order to find out whether these anti-aligning states are energetically favoured, we also found the orthogonal state for each of these system sizes and computed its energy for each of these frequencies.

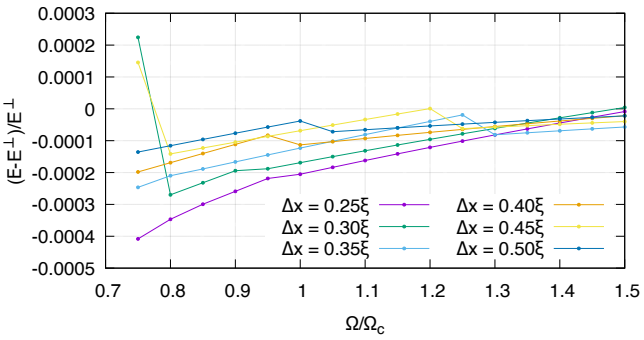

FIG. 12. Numerical results for the energy of the anti-aligning vortex states described in this section — as a function of Ω and Δx — relative to the energy of the orthogonal vortex state. Note that most of the range of the graph is above the critical frequency and this energy difference is negative except for the data point at $\Delta x = 0.3\xi$, $\Omega = 1.5\Omega_c$, and numerical outliers. This suggests that there is a sizeable region where both types of vortex states are stabilised and the anti-aligning avoided states are slightly lower energy than the orthogonal intersecting one. The two outlier points at $\Omega = 0.75\Omega_c$ are cases where the final state has vortex cores skewed according to the initial phase profile tilt angle of 5°, likely due to insufficient accuracy given how small these energy differences are.

The relative difference between these energies and orthogonal states as a function of Ω and Δx (and hence R) are plotted in Fig. 12. The two outlier points at $\Omega = 0.75\Omega_c$, corresponding to $\Delta x = 0.30\xi$ and $\Delta x = 0.45\xi$, are cases where the vortex core in the final state was formed with the tilt angle of 5°, which corresponds to the tilt in the initial phase profile, even though this configuration is clearly not the lowest energy state. This implies that our chosen accuracy threshold of 10^{-10} is slightly too high in this case, due to the very small energy differences involved. However, both of these cases then converged to the lower energy, less tilted branch

upon the next iteration at $\Omega = 0.80\Omega_c$.

As we can see, for almost all values on this graph, these slightly anti-aligned and non-intersecting states are lower energy than the orthogonal intersecting state we studied in Ref. [1]. This is even true well-above Ω_c where the vortices are energetically stabilised (compared to the no-vortex state), although the energy difference decreases in magnitude with Ω — to the point where the anti-aligned state for $\Omega = 1.5\Omega_c$ and $\Delta x = 0.3\xi$ is slightly higher in energy than the orthogonal state. Therefore, it is possible that the intersecting orthogonal state is lower in energy for a range of system sizes and frequencies. However, as previously mentioned, the energy differences are very slight, and it is possible that numerical errors may be important at this scale.

The energy difference also decreases with increasing Δx, and hence R, suggesting that in a large enough system these states either become degenerate or the orthogonal state is energetically favoured. This is to be expected from the scaling of the interaction energy relative to the rotational energy, although — as we showed earlier — these terms alone are not sufficient to predict the existence of these tilted stationary states or their reduced energy relative to the orthogonal state. Again, since the energy difference between these states is so small, the terms and effects we have ignored almost certainly become important. These include the quantum pressure and particle interaction energies, which will weakly depend on the shape of the vortex core via the density profile, but there are also other approximations we have made. Firstly, we have ignored the density profile of the vortex core completely. This does not affect the rotational energy when the cores each lie on a rotation plane, but can in principle when they do not, and will affect the vortex-vortex interaction energy regardless. Secondly, we have not accounted for the avoided crossing in our ansatz, which affects not only the density profile but the phase profile (and hence the velocity field) as well. The avoided crossing pushes the vortex core "off-axis" [c.f. Sec. V.2] which will likely reduce the angular momentum, and hence the magnitude of the rotational energy, and is also likely to affect the vortex-vortex interaction term. This off-axis nature of the core probably also induces image effects from the hard-wall boundary condition on the velocity field as discussed in Sec. V.2.

We can also estimate the size of the avoided crossing — as in Sec. VI — by calculating $r_{\min}$, the minimum distance between the vortex core and the origin. This is plotted in Fig. 13 for each of these states as a function of both Ω and Δx. Once again we see that $r_{\min} > \xi$, such that these states lie outside the linearised GPE regime considered in Sec. V.2. Furthermore, we see that, in general, the avoided crossing decreases in size with Ω, and increases with Δx (and hence system size). The former trend supports our intuition that the avoided crossing reduces the angular momentum, since higher frequencies favour higher angular momentum. The latter trend perhaps suggests that the attractive vortex-vortex interaction is not playing a large role in determining the avoided crossing size, since (for fixed particle number) the energy of this interaction decreases with increasing system size while $r_{\min}$ increases.

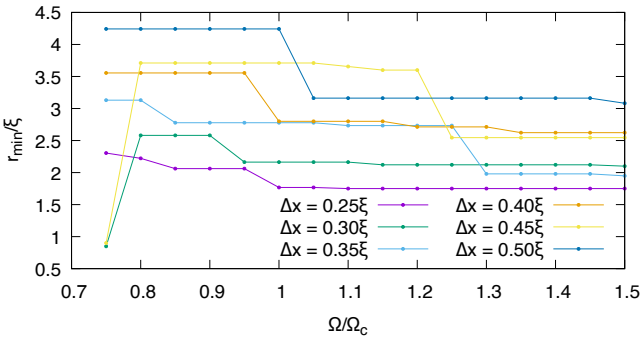

FIG. 13. The minimum distance $r_{\min}$ from the vortex core to the origin for the states described in this section, as a function of Ω and Δx, giving a measure of the size of the avoided crossing region. The data is not very smooth, suggesting there are multiple energetically-close metastable branches being explored. There may also be some sampling error due to the discretisation of the Cartesian grid. Nevertheless, the general trends are that $r_{\min}$ decreases with Ω and increases with Δx (and hence system size). The first trend makes sense if the avoided crossing is reducing the state's angular momentum, while the second trend does not have a clear explanation. Note that the outliers in this plot are the same as those of Fig. 12.

We can also see this behaviour by following the vortex core in Fig. 11 as we increase Ω up to $1.5\Omega_c$. Then we obtain a final state with the core structure shown in Fig. 14. These plots show clearly, in the second panel, the reduction in size of the avoided crossing but they also show that this state is effectively no longer skewed. Looking at the third panel, we have superimposed the lines $x = 0$ and $z = 0$ and can see that these run parallel with the data points. This means that this state is effectively the orthogonal state with an avoided crossing (similar to Eq. (50)), which is likely due to higher angular momentum being favoured at these higher frequencies. This also makes sense when comparing with Fig. 12, as the energy difference with the orthogonal state becomes very small at these frequencies. For a more detailed look at one of these avoided orthogonal states, including cuts of the density and phase profiles, at higher spatial resolution see Appendix XII.XII.2.

It is not clear whether both features of these states — the skewness of the planes and the avoided crossing — are important in lowering the energy. For this reason we have also performed the ITEM on initial states with a phase profile given by that of the orthogonal states plus a perturbation around the intersection point (as in Eq. (54) but with an unconstrained perturbation size). The final states of these numerical tests exhibit the same skewed and avoided crossing core structures as before, with the same trends in these features as the frequency

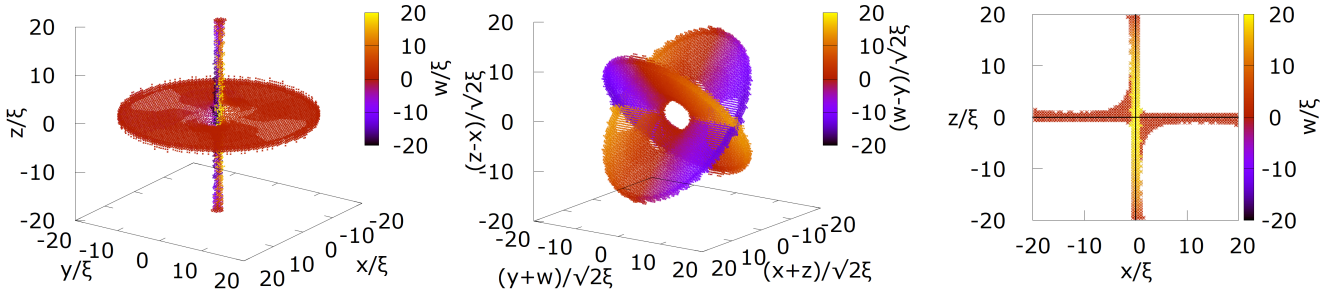

FIG. 14. As Fig. 11 but at a higher frequency of $\Omega = 1.5\Omega_c$ at which the vortex states are energetically favoured with respect to the no-vortex state. Compared to Fig. 11 this state shows a reduction in both the tilt angle and the size of the avoided crossing. The by-eye estimate in the third panel shows a tilt angle of $\approx 0°$, that is, there is no discernible tilt. This can be intuitively understood as the higher frequency causes the negative rotational energy term to have a higher weighting relative to other terms in the energy. Consequently a higher angular momentum is favoured.

and system size vary, indicating that both of these features are important. Note that if we set the perturbation to zero in the initial state the final state we obtain is the intersecting orthogonal state we previously studied [1].

Finally, we will investigate the analogy between these anti-aligning states and the linearised reconnection dynamics of Sec. V.2. To do this we have used the final state at $\Omega = 1.5\Omega_c$ and $\Delta x = 0.25\xi$, which has an avoided crossing but no discernible skewness (as in Fig. 14), so the core structure is very similar to that of analytic perturbed orthogonal state [Eq. (54)]. Then, in Fig. 15 we have plotted all of the numerical data points up to a radius of roughly 5ξ according to their value of $r_1 r_2$ and $\theta_1 + \theta_2$. These points are then coloured according to their value of $\sqrt{\rho}$ in the left panel, and S in the right panel. This was inspired by Fig. 4 in Sec. V.2, which shows the corresponding figure for the analytic perturbed orthogonal state, which depended only on $r_1 r_2$ and $\theta_1 + \theta_2$. Note that we have also added small random noise to the x and y *coordinates* of each point, to prevent points with the same value of $r_1 r_2$ and $\theta_1 + \theta_2$ from being perfectly stacked on top of each other, and hence not visible. In the case of the numerical data in Fig. 15, we can see that the density and phase plots are not single-valued in terms of these variables, as there are regions with different colours stacked on top of each other. For this reason we have plotted the points as open circles so that they don't occlude each other as much. This multivaluedness is not surprising, as the numerical state is in the nonlinear GPE regime. Nevertheless, we do find many similarities between the overall structure of this plot and Fig. 4. Firstly, the core (seen as dark spots in the density and branch points in the phase) is centred around a constant value of $r_1 r_2 = \gamma \xi^2$ with $\gamma \approx 1.75$, and $\theta_1 + \theta_2 = \pm\pi$. This was a feature of the perturbed orthogonal state, although the corresponding value of γ was constrained to be small in this linearised case. Secondly, the phase profile appears to be very close to a single-valued function of these variables, with essentially the same behaviour as the analytic phase profile of the perturbed orthogonal state. In particular, we have that for $r_1 r_2 < \gamma$ the phase is roughly constant, while for $r_1 r_2 > \gamma$ the phase winds once as either θ_1 or θ_2 makes a full circle, which is exactly what we see in Fig. 4. This suggests that there may be a similar analytic description for these numerical states — or at least their phase profile.

This section has explored the behaviour of vortices in an isoclinic doubly-rotating superfluid. We developed an analytic model that predicts that, above a certain threshold frequency, the previously studied orthogonal state is lower energy than any pair of vortex planes tilted to attractively interact. Then we presented numerical results that showed this is only approximately true, with the ITEM converging to states with a very slight skewness, sizeable avoided crossing regions, and lower energies than the orthogonal state, at least for the system sizes we considered. We have also discussed which approximations might need to be lifted in order to explain this behaviour, and compared the avoided crossings seen in these stationary states to those derived in reconnecting states in Sec. V.2.

VIII. CONCLUSIONS

In the first part of this section, we will focus on summarizing the main conclusions of our paper and highlighting the open questions that directly follow on from our study. In the second part of this section, we will then briefly discuss the more general future outlook for research into topological excitations in 4D superfluids, looking beyond the physics of the minimal model studied in this paper.

VIII.1. Summary

In this paper, we have demonstrated that stationary states of the 4D GPE under double rotation can host complicated vortex core structures consisting of skew planes and curved surfaces. This work generalises our previous study in Ref. [1], which only considered the case

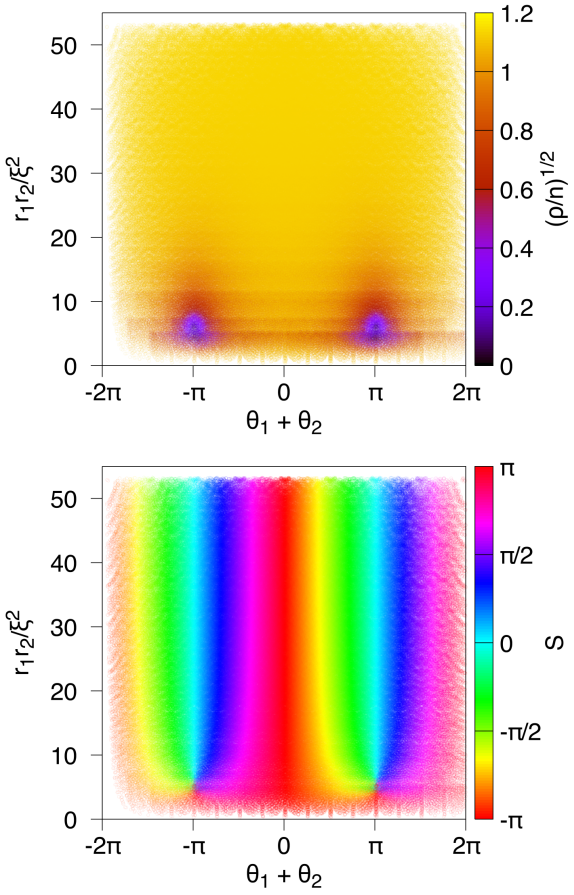

FIG. 15. Density (top) and phase (bottom) profiles of the state whose core is shown in Fig. 14. We have plotted all data points, up to a distance of roughly 5ξ from the origin, according to their value of $r_1 r_2$ and $\theta_1 + \theta_2$, in order to compare to the analytic orthogonal perturbed state [Fig. 4] which showed a similar core structure. In order to show points that are stacked below other points, we have added small random numbers to the x and y coordinates of each point and plotted them as open circles. This noise is sampled from a flat distribution ranging from $[0, 0.025\pi]$ in the x-direction and $[0, 0.25]$ in the y-direction. While neither profile is single-valued in terms of these variables, the overall structure — particularly of the phase — is very similar to that of Fig. 4.

of equal-frequency double rotation and focused on completely orthogonal and rigid vortex planes. Here, we have explored some of the other states that can be found as either of these restrictions is relaxed, and have shown that these can have similar or lower energies as compared to the rigid orthogonal vortex state in various parameter regimes. Interestingly, all of these states have no direct analogue in 2D and 3D superfluid systems under rotation, indicating that there is much more rich vortex physics still to be explored in higher spatial dimensions.

In more detail, we firstly showed in Sec. V.1 that non-orthogonal vortex planes interact hydrodynamically, in contrast to the case of orthogonal planes, and we analytically derived the form of this interaction in the special cases of planes related by an isoclinic or simple rotation. Understanding this interaction potential in the general double rotation case would be an interesting topic for future work, allowing our analytics to extend to the full configuration space of non-orthogonal vortex planes.

Secondly, in Sec. V.2 we used linearised GPE dynamics to show that the intersection point between a non-orthogonal pair of vortex planes is not stable in general, but undergoes a form of reconnection. In contrast to the reconnection of extended vortex lines in 3D, the core of the non-orthogonal vortices in 4D forms a single connected object at all times, with the intersection point replaced by an avoided crossing that expands linearly with a speed determined by the tilt angles. However, as we see later in numerics, very similar core structures can become stable, suggesting that the GPE nonlinearity may limit the predicted expansion at a certain size. Investigating this and other potential causes for the stability of avoided crossings is another possible avenue for future research.

We then approached the problem of a 4D hyperspherical superfluid doubly rotating at unequal frequencies, under the assumption that the vortices remain rigid planes. In Sec. VI.1 we showed that a single vortex plane in this system will always want to fully align with the higher of the two rotation frequencies. Then, using this result, we tackled the case of an intersecting vortex pair in Sec. VI.2, proposing a non-orthogonal such pair as an ansatz for the ground state. This was based on the observation that for both planes to benefit from the higher frequency they had to be skewed in a purely aligning sense, thereby inducing repulsive vortex-vortex interaction from our result in Sec. V.1. We built an analytic model based simply on the balance between these two energies, which predicted that a skew configuration of vortex planes could indeed have lower energy than an orthogonal one. With this model we were able to find which of these configurations was optimal, and calculated the predicted tilt-angles and energy. Comparing these results with numerics, we found excellent agreement, despite the fact that we did not account for the avoided crossing of these states that was seen numerically. However, at high frequencies we found that more exotic states with highly curved vortex surfaces were energetically favoured, suggesting the ground state of a doubly rotating superfluid is in general very complex.

Finally, we applied a modified version of this theory to the case of a superfluid under isoclinic, i.e. equal frequency, double rotation, to see whether a pair of planes skewed in an anti-aligning sense could have lower energy than an orthogonal state by benefiting from attractive vortex-vortex interactions at the expense of rotational energy. In this case, we predicted that skewed states

are unlikely to be both stable and lower energy than the orthogonal state. In particular, above a threshold frequency $\Omega_{\rm stab}$ the orthogonal state was shown to be a local minimum, with an energy barrier to any anti-aligned configuration. The frequency $\Omega_{\rm stab}$ was found to be related to, but less than, the critical frequency Ω_c, such that the orthogonal state remains stable above Ω_c. However, this result does have implications for the metastability of the orthogonal state, since below $\Omega_{\rm stab}$ the vortex planes can continuously lower their energy by tilting toward each other in an anti-aligning sense, until eventually they come together and annihilate. Numerically testing this prediction is another possible avenue of research, but for now we have focused on the region above $\Omega_{\rm stab}$. There we have found that states with a small anti-aligning skewness and a sizeable avoided crossing can be slightly lower in energy than the orthogonal intersecting state. Furthermore, the skewness in the final states decreases with frequency and appears to vanish, while the avoided crossing size decreases but not to zero. This suggests that avoided orthogonal states may be preferable to intersecting orthogonal states even at higher frequencies, although the observed energy differences decrease with system size, becoming negligible for some of the parameters tested. It is possible that intersecting and avoided orthogonal states may therefore either become degenerate in the large system limit, or alternatively that the intersecting state will become lower in energy.

As mentioned above, the results presented in this paper show that the physics of vortex surfaces in 4D can be incredibly rich, even in the absence of dynamics. The fact that curved and tilted vortex surfaces can be stable and exist at low energies in such a minimal model is a dramatic departure from the physics of lower dimensions under rotation, suggesting a vast configuration space to explore and investigate in the future.

VIII.2. General Outlook

In this paper, we have focused on a minimal theoretical model for a 4D superfluid based on the 4D GPE under rotation. This is motivated as the simplest extension of textbook 2D and 3D superfluids [c.f. Section II] into higher spatial dimensions [1]. However, in the future, it will be both interesting and relevant to go beyond this simple model to study more realistic systems with the aim of making an experimental proposal, and to explore the even richer vortex physics that will likely emerge.

Recent interest in higher spatial dimensions has been sparked by various theoretical and experimental works aimed at exploring signatures of single-particle physics in artificial 4D systems, based e.g. on topological pumping [83–94], "synthetic dimensions" [16, 28–32, 35–41, 44–50, 52, 95–123], artificial parameter spaces [19–22, 124–126] and the connectivity of classical electrical circuits [23–27]. Of these schemes that of "synthetic dimensions", in particular, may provide a way in the future to experimentally explore the physics of a 4D superfluid. In this general approach, a set of states or internal degrees of freedom are externally coupled together and then re-interpreted as lattice sites along an extra spatial dimension [28]. Such a synthetic dimension can then be combined with other real or synthetic dimensions to allow particles to explore a system with the desired effective dimensionality, such as e.g. four dimensions. Interest in this approach has grown dramatically in recent years, with significant theoretical and experimental progress in implementing synthetic dimensions across ultracold atoms [30–34, 36, 38, 99–101], photonics [16, 39, 41–43, 46, 97, 102, 108, 121, 122, 127–130], and other systems [47–50]. Within ultracold atoms, for example, synthetic dimension schemes have so far been realised based on using internal atomic states [28–31, 131], momentum states [32, 36, 132], harmonic trap states [34, 35, 52], orbital states [120], superradiant states [117], and Rydberg states [114, 119] amongst others.

While most of the progress to date has focused on lower dimensions, one recent experiment has successfully explored the single-particle dynamics of atoms in a 4D hyper-cubic synthetic lattice of momentum states [36]. There have also been proposals [15, 16] for how to use synthetic dimensions to experimentally explore a 4D quantum Hall effect [14, 15, 17, 18, 79, 133, 134], based on applying magnetic fields through two completely orthogonal 2D planes; this is analogous to a 4D system with double rotation, when viewed in the rotating frame. The development and implementation of such schemes, combined also with the inter-particle interactions necessary for superfluidity, may therefore open the way for the experimental investigation of 4D vortices in the future.

However, as we discussed in our previous paper [1], the 4D GPE that we have considered [Eq. (28)] is a toy model lacking elements which are necessary for experimental relevancy to current synthetic dimension approaches. For example, we have considered a purely hypothetical four-dimensional space that is isotropic and continuous, and we have chosen a hyperspherical hard-wall boundary to preserve the rotational symmetry. However, the motion, inter-particle interactions, and boundary conditions along any synthetic dimensions can differ from that in real space. In practice, it is likely that an experiment may contain both real and synthetic dimensions, which would break $SO(4)$ rotational symmetry. This will affect the behaviour of the tilted and curved vortex planes that we have studied, adding in additional physics that will compete with the rotational and hydrodynamic energies that we have considered. Additionally, most synthetic dimension implementations are discrete with hard-wall boundary conditions, and hence are best described by tight binding models on a lattice. It is then important to consider how many synthetic lattice sites are spanned by the typical length scales of the problem. If the answer is many, then a continuum approximation can be appropriate in the mean-field regime. If not, then a tight binding model must be used and rich physics can be expected to

arise from competition between these length scales and the synthetic lattice spacing.

Moreover, synthetic dimensions can also have features that are rarely seen in typical tight binding models, and which in themselves warrant further research. These can include nonuniform hoppings, limited system sizes, non-equilibrium effects from external driving and long-range interactions along the synthetic dimension [29, 30]. All of these are details that should be considered to make this work more experimentally relevant but they also depend strongly on the experiment in question. For this reason, and for simplicity, we have studied a minimal extension of 3D superfluid physics into 4D, in order to begin investigating what is possible in higher dimensions.

An obvious direction of future work is therefore to connect these results to experiment, by studying more complex models that take experimental details into account. We hope that such research can build upon our work by using similar techniques and ansatzes, and that more physical models will yield even richer behaviour. One simple modification that could still have interesting effects is to keep the continuous, isotropic 4D GPE model but to change the geometry to one which breaks the rotational symmetry and better reflects the boundary conditions in a synthetic dimension. A possible choice would be to pick out one or two directions as "synthetic" and give them independent hard wall boundaries (i.e. $w \in [-L, L]$, while retaining a rotationally symmetric geometry in the remaining coordinates.

There are many other interesting avenues for extending our research, aside from making the model more relevant to experiment. Our numerical stationary states with curved vortex surfaces raises the interesting possibility that other stationary states under rotation could contain closed vortex surfaces that do not meet the boundary of the system. These would be the four dimensional generalisation of vortex loops (including links and knots) in 3D [67, 69, 70, 81, 135, 136]. Additionally, there is a far richer classification of closed surfaces [137] than of closed loops, suggesting there could be more possible closed vortex configurations in 4D.

It would also be interesting to study vortex surface configurations for even higher rotation frequencies. The presence of intersection, curvature, and avoided crossings in our vortex core results suggests that vortices can lose their individual character in 4D. It is therefore not entirely clear, even in some low energy stationary states, whether we can meaningfully assign an integer to the number of vortices in the system. In lower dimensions the number of vortices becomes very large in the rapidly rotating limit, where the vortices form an Abrikosov lattice [9]. Investigating the limit of high frequency in one or both planes of rotation in 4D is therefore an interesting and open problem, due to the more malleable nature of the vortex core(s).

This work can also be extended to consider more interesting order parameters in 4D. Certain phases of spinor condensates in 3D are known to host non-Abelian vortices [138, 139], which have more interesting behaviour when they intersect and reconnect. Given that intersection and reconnection are also relevant for the behaviour of vortex planes, it is natural to ask what phenomena would arise for non-Abelian vortices in 4D. Finally, this work also represents a small step towards the strongly interacting fractional quantum Hall effect in 4D [133], thanks to the analogy between a rotating superfluid and a quantum Hall system [4].

Acknowledgements: We thank Tomoki Ozawa, Mike Gunn, Iacopo Carusotto, Mark Dennis and Russell Bisset for helpful discussions. This work is supported by the Royal Society via grants UF160112, RGF\EA\180121 and RGF\R1\180071.

IX. GENERAL ROTATION OF A PLANE IN 4D

We want to derive the simplest rotation to describe a plane tilting in 4D without loss of generality. Consider the plane P defined in 4D Cartesian coordinates as the set of solutions to $x = y = 0$, and another plane P' as the image of P under a double rotation. We will represent P' as the set of solutions to $x' = y' = 0$, where the primed coordinates are related to the original coordinates by double rotation with matrix M, that is, $\mathbf{r}' = M\mathbf{r}$. It will be useful to write this in a block form such that

$$\begin{pmatrix} x' \\ y' \\ z' \\ w' \end{pmatrix} = \begin{pmatrix} A & B \\ C & D \end{pmatrix} \begin{pmatrix} x \\ y \\ z \\ w \end{pmatrix},$$

where A, B, C, D are the 2×2 blocks of M. Rotations in 4D generally have six free parameters, but we can reduce this down to two for the matrix M by exploiting the symmetry of P under certain rotations, and by using our freedom to choose a basis. Firstly, using the following shorthand for a 2D rotation matrix

$$R(\phi) = \begin{pmatrix} \cos\phi & -\sin\phi \\ \sin\phi & \cos\phi \end{pmatrix},$$

note that, for arbitrary $\phi_{1,2}$, we can redefine M to be

$$M = \begin{pmatrix} A & B \\ C & D \end{pmatrix} \begin{pmatrix} R(\phi_1) & 0 \\ 0 & R(\phi_2) \end{pmatrix}, \tag{94}$$

without changing P'. The reason for this is that the initial rotation we have added is a double rotation in the x–y and z–w planes [c.f. Section III], which leaves the plane P invariant, such that the combined transformation results in the same transformed plane P'. Secondly, we will use another double rotation in the x–y and z–w

planes to change basis, as follows

$$\begin{pmatrix} x \\ y \\ z \\ w \end{pmatrix} \rightarrow \begin{pmatrix} R(\phi_3) & 0 \\ 0 & R(\phi_4) \end{pmatrix} \begin{pmatrix} x \\ y \\ z \\ w \end{pmatrix}.$$

Denoting this matrix as $R(\phi_3, \phi_4)$, we have that $M \rightarrow R(\phi_3, \phi_4) M R(-\phi_3, -\phi_4)$ under this transformation. Combining this with the redefinition from Eq. (94) we can write, for arbitrary ϕ_j, $j = 1, 2, 3, 4$

$$M = \begin{pmatrix} R(\phi_3) & 0 \\ 0 & R(\phi_4) \end{pmatrix} \begin{pmatrix} A & B \\ C & D \end{pmatrix} \begin{pmatrix} R(\phi_1) & 0 \\ 0 & R(\phi_2) \end{pmatrix}, \tag{95}$$

without any loss of generality. Note that we have made the shifts $\phi_1 \rightarrow \phi_1 + \phi_3$, and $\phi_2 \rightarrow \phi_2 + \phi_4$ for simplicity. We can use these four free parameters to transform the upper left (A) and lower right (D) blocks into diagonal 2×2 matrices. To see this, start by expanding the product in Eq. (95)

$$M = \begin{pmatrix} R(\phi_3) A R(\phi_1) & R(\phi_3) B R(\phi_2) \\ R(\phi_4) C R(\phi_1) & R(\phi_4) D R(\phi_2) \end{pmatrix}.$$

Denoting the elements of A in the standard fashion

$$A = \begin{pmatrix} a_{11} & a_{12} \\ a_{21} & a_{22} \end{pmatrix},$$

and employing the shorthand $s_j = \sin\phi_j$, $c_j = \cos\phi_j$, the off-diagonal elements of $A' = R(\phi_3) A R(\phi_1)$ are given by

$$\begin{aligned} [A']_{12} &= -a_{11} s_1 c_3 + a_{12} c_1 c_3 + a_{21} s_1 s_3 - a_{22} c_1 s_3, \\ [A']_{21} &= a_{11} c_1 s_3 + a_{12} s_1 s_3 + a_{21} c_1 c_3 + a_{22} s_1 c_3. \end{aligned}$$

Setting these both to zero and taking the sum and difference of the two gives the following simultaneous equations

$$\begin{aligned} (a_{11} - a_{22}) \sin(\phi_3 - \phi_1) + (a_{21} + a_{12}) \cos(\phi_3 - \phi_1) = 0, \\ (a_{11} + a_{22}) \sin(\phi_3 + \phi_1) + (a_{21} - a_{12}) \cos(\phi_3 + \phi_1) = 0, \end{aligned}$$

which always have solutions for $\phi_{1,3}$. Similarly $R(\phi_4) D R(\phi_2)$ can be made diagonal by choosing particular values for $\phi_{2,4}$. We now look at the full transformed matrix M to see what form the off-diagonal blocks must take. The matrix now reads

$$M = \begin{pmatrix} a_1 & 0 & b_{11} & b_{12} \\ 0 & a_2 & b_{21} & b_{22} \\ c_{11} & c_{12} & d_1 & 0 \\ c_{21} & c_{22} & 0 & d_2, \end{pmatrix}$$

where $a_{1,2}$ and $d_{1,2}$ now denote the only non-zero elements of the upper left and lower right blocks after these blocks have been made diagonal. To proceed further, we will first focus on the upper right B block. Normalization of the first two rows of M can be ensured, without loss of generality, by the following form

$$M = \begin{pmatrix} \cos\alpha_1 & 0 & -\sin\alpha_1 \cos\beta_1 & -\sin\alpha_1 \sin\beta_1 \\ 0 & \cos\alpha_2 & -\sin\alpha_2 \cos\beta_2 & -\sin\alpha_2 \sin\beta_2 \\ c_{11} & c_{12} & d_1 & 0 \\ c_{21} & c_{22} & 0 & d_2 \end{pmatrix},$$

such that orthogonality of the first two rows now implies

$$\sin\alpha_1 \sin\alpha_2 \cos(\beta_1 - \beta_2) = 0.$$

This has $\sin\alpha_1 = 0$ or $\sin\alpha_2 = 0$ as special cases, which we ignore for now since these each lead to a simple rotation of the plane P [c.f. Section III]. What we will derive instead is the general case for double rotation by requiring $\beta_2 = \beta_1 + \pi/2$, and this general case will actually include the simple rotation as a special case. Proceeding, we have

$$M = \begin{pmatrix} \cos\alpha_1 & 0 & -\sin\alpha_1 \cos\beta_1 & -\sin\alpha_1 \sin\beta_1 \\ 0 & \cos\alpha_2 & \sin\alpha_2 \sin\beta_1 & -\sin\alpha_2 \cos\beta_1 \\ c_{11} & c_{12} & d_1 & 0 \\ c_{21} & c_{22} & 0 & d_2 \end{pmatrix}.$$

Orthogonality of the last two columns gives

$$\left(\sin^2\alpha_1 - \sin^2\alpha_2\right) \cos\beta_1 \sin\beta_1 = 0.$$

Again, we have a special case, given by $\alpha_2 = \alpha_1$, which will give an isoclinic rotation of the plane P [c.f. Section III]. We will ignore this solution for now, and again find that it can be found as a particular case of the remaining solution. We therefore require either $\cos\beta_1 = 0$ or $\sin\beta_1 = 0$. This leads to the following two forms

$$M = \begin{pmatrix} \cos\alpha_1 & 0 & 0 & -\sin\alpha_1 \\ 0 & \cos\alpha_2 & \sin\alpha_2 & 0 \\ c_{11} & c_{12} & d_1 & 0 \\ c_{21} & c_{22} & 0 & d_2 \end{pmatrix},$$

$$M = \begin{pmatrix} \cos\alpha_1 & 0 & -\sin\alpha_1 & 0 \\ 0 & \cos\alpha_2 & 0 & -\sin\alpha_2 \\ c_{11} & c_{12} & d_1 & 0 \\ c_{21} & c_{22} & 0 & d_2 \end{pmatrix},$$

respectively, up to an unimportant common sign in the upper right block which can be absorbed in to the definition of α_1 and α_2. Furthermore, these two forms are related to each other by a change of basis and redefinition of parameters. We therefore choose the second form without loss of generality. Orthonormality of the columns and the last two rows now allows us to determine the remaining unknowns, such that we finally have

$$\begin{pmatrix} \cos\alpha_1 & 0 & -\sin\alpha_1 & 0 \\ 0 & \cos\alpha_2 & 0 & -\sin\alpha_2 \\ \sin\alpha_1 & 0 & \cos\alpha_1 & 0 \\ 0 & \sin\alpha_2 & 0 & \cos\alpha_2 \end{pmatrix},$$

as is used in the main text.

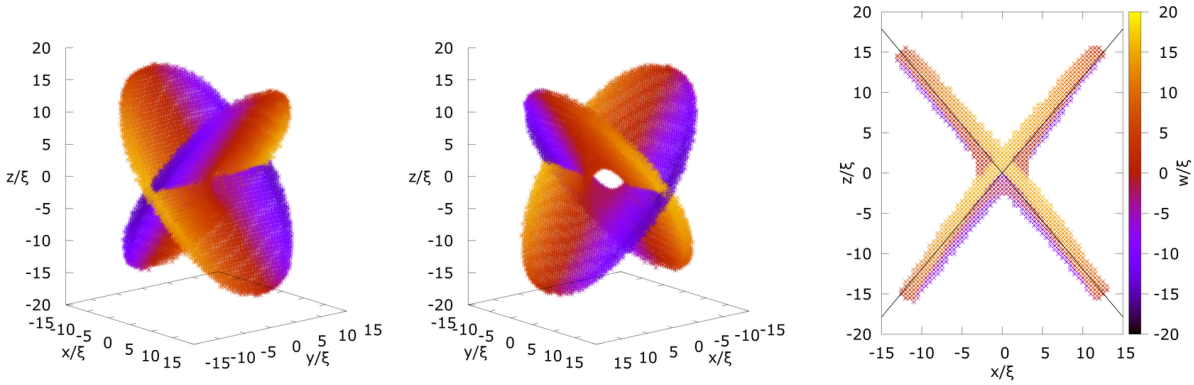

FIG. 16. As in Fig. 7, except with rotation frequencies of $\Omega_{zw} = 1.25\Omega_c$ and $\Omega_{xy} \approx 1.35\Omega_c$, corresponding to a predicted skewness of $\eta = 10^\circ$. The overall structure is essentially the same as in Fig. 7, and the agreement with theory is still very good as shown in panel three. However, this panel also shows that the data has a slight mirror asymmetry in the vertical axis that is not visibly present in Fig. 7 or accounted for in the theory.

X. INTEGRATION IN SKEW DOUBLE POLAR COORDINATES

In this Appendix we derive an integral transformation from 4D Cartesian coordinates (x, y, z, w) into a non-orthogonal coordinate system given by (x, y, z', w'), where the primed coordinates form another Cartesian framed related to the unprimed one by a double rotation. If we are only interested in preserving the relationship between the two planes defined by $x = y = 0$ and $z' = w' = 0$ respectively, then without loss of generality we can choose this double rotation to have the form

$$\begin{pmatrix} x' \\ y' \\ z' \\ w' \end{pmatrix} = \begin{pmatrix} \cos\alpha_1 & 0 & -\sin\alpha_1 & 0 \\ 0 & \cos\alpha_2 & 0 & -\sin\alpha_2 \\ \sin\alpha_1 & 0 & \cos\alpha_1 & 0 \\ 0 & \sin\alpha_2 & 0 & \cos\alpha_2 \end{pmatrix} \begin{pmatrix} x \\ y \\ z \\ w \end{pmatrix},$$

as derived in Appendix IX. As discussed in the main text, here we will only deal with the special case where this double rotation is isoclinic, such that $\alpha_2 = \nu\alpha_1$, with $\nu = \pm 1$. From here on we will employ the shorthand $c = \cos\alpha_1$, $s = \sin\alpha_1$. We will derive this integration over non-orthogonal coordinates for the case of a 4D ball of unit radius, since this geometry preserves the symmetry between the primed and unprimed coordinates. The primed coordinates can be introduced into the integral using Dirac deltas as follows

$$\begin{aligned} \int_{B^4(1)} \mathrm{d}x\mathrm{d}y\mathrm{d}z\mathrm{d}w &= \int_{B^4(1)} \mathrm{d}z\mathrm{d}w\mathrm{d}x\mathrm{d}y \int_{\mathbb{R}^2} \mathrm{d}z'\mathrm{d}w'\delta(z' - cz - sx)\delta(w' - cw - \nu sy) \\ &= \frac{1}{c^2} \int_{B^2(1)} \mathrm{d}x\mathrm{d}y \int_{\mathbb{R}^2} \mathrm{d}z'\mathrm{d}w' \int_{B^2(R)} \mathrm{d}z\mathrm{d}w\delta\left(z - \frac{z' - sx}{c}\right)\delta\left(w - \frac{w' - \nu sy}{c}\right), \end{aligned}$$

where $B^d(R)$ is the ball of radius R centred at the origin in d dimensions, and here $R^2 = 1^2 - x^2 - y^2$.

Our goal now is to eliminate z and w by evaluating the corresponding integrals. This in turn will define the limits of integration for their primed counterparts. However, this is more easily accomplished in double polar coordinates, whereby

$$\int_{B^2(1)} \mathrm{d}x\mathrm{d}y = \int_0^1 r_1\mathrm{d}r_1 \int_{-\pi}^{\pi} \mathrm{d}\theta_1, \quad \int_{\mathbb{R}^2} \mathrm{d}z'\mathrm{d}w' = \int_0^\infty r_2'\mathrm{d}r_2' \int_{-\pi}^{\pi} \mathrm{d}\theta_2',$$

$$\int_{B^2(R)} \mathrm{d}z\mathrm{d}w\delta(z - z_0)\,\delta(w - w_0) = \int_0^R r_2\mathrm{d}r_2 \int_{-\pi}^{\pi} \mathrm{d}\theta_2 \frac{1}{r_2}\delta(r_2 - r_0)\,\delta(\theta_2 - \theta_0),$$

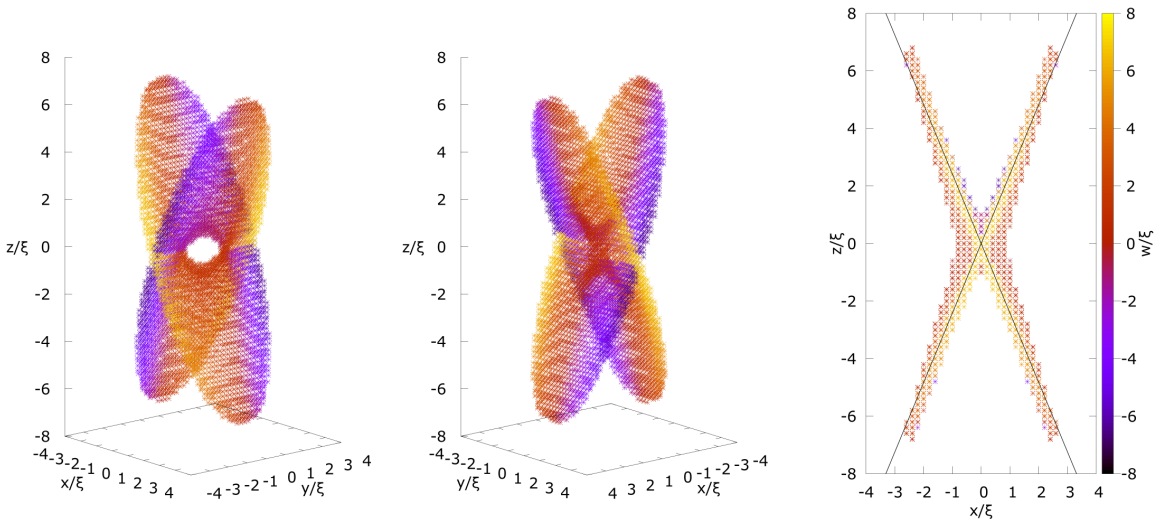

FIG. 17. As in Fig. 16, except with a higher resolution of $\Delta x = 0.2\xi$, and with $\Omega_{xy} \approx 2.25\Omega_c$, corresponding to a predicted skewness of $\eta = 45^\circ$. The agreement with the theoretical planes is still excellent, as seen in the third panel, and there is no visible asymmetry about the vertical axis. Interestingly, the avoided crossing at the origin has a different orientation to that seen in Figs 7 and 16, and appears to be smaller.

where we have defined $z_0 = (z' - sx)/c$, $w_0 = (w' - \nu sy)/c$, $r_0^2 = z_0^2 + w_0^2$, and $\theta_0 = \arctan(z_0, w_0)$. We now integrate out r_2 and θ_2 as follows

$$\int_0^R \mathrm{d}r_2 \delta\left(r_2 - r_0\right) = \Theta\left(R^2 - r_0^2\right), \tag{96}$$

$$\int_{-\pi}^{\pi} \mathrm{d}\theta_2 \delta\left(\theta_2 - \theta_0\right) = 1,$$

where we have used that $\Theta(R - r_0) = \Theta(R^2 - r_0^2)$ since both R and r_0 are non-negative. In double polar coordinates we have that $R^2 = 1 - r_1^2$, and $r_0^2 = [r_2'^2 + s^2 r_1^2 - 2sr_1 r_2' \cos\left(\theta_2' - \nu\theta_1\right)]/c^2$. Substituting this into the Theta function on the RHS of Eq. (96) gives

$$\Theta(R^2 - r_0^2) = \Theta\left[c^2 - r_1^2 - r_2'^2 + 2sr_1 r_2' \cos\left(\theta_2' - \nu\theta_1\right)\right],$$

where we have used that $\Theta(c^2\,\cdot) = \Theta(\cdot)$. Altogether this gives

$$\int_{B^4(1)} \mathrm{d}x\mathrm{d}y\mathrm{d}z\mathrm{d}w = \frac{1}{c^2} \int_0^1 r_1 \mathrm{d}r_1 \int_{-\pi}^{\pi} \mathrm{d}\theta_1 \int_0^1 r_2' \mathrm{d}r_2' \int_{-\pi}^{\pi} \mathrm{d}\theta_2' \Theta\left[c^2 - r_1^2 - r_2'^2 + 2sr_1 r_2' \cos\left(\theta_2' - \nu\theta_1\right)\right],$$

where we have also used the spherical symmetry to restrict the upper limit of r_2' to 1, by comparison to that of r_1. (This is unnecessary, since the step function will ultimately control the limits of whichever radius is integrated over first, but it makes the equivalence between the primed and unprimed coordinates fully clear.)

From now we will assume that the primed coordinates will be integrated over first, so let us make the substitution $\theta_2' = \theta + \nu\theta_1$, treating θ_1 as a constant within the θ_2' integral, in order to simplify the cosine. The limits of the θ integral will be $(-\nu\theta_1 - \pi, -\nu\theta_1 + \pi)$, but this is arbitrary since we are integrating over a full circle, so we can just as easily write $\theta \in (-\pi, \pi)$. In order to figure out exactly how the step function translates into integration limits, consider the inequality it enforces

$$c^2 - r_1^2 - r_2'^2 + 2sr_1 r_2' \cos\theta > 0. \tag{97}$$

This form is ideal for integrating over θ first, but it will actually be easier to integrate over r_2' first. For this reason we will rewrite Eq. (97) by completing the square for r_2' as

$$\left(r_2' - sr_1 \cos\theta\right)^2 < c^2\left(1 - r_1^2\right) - s^2 r_1^2 \sin^2\theta \tag{98}$$

This inequality has no solutions for r_2' where the RHS is

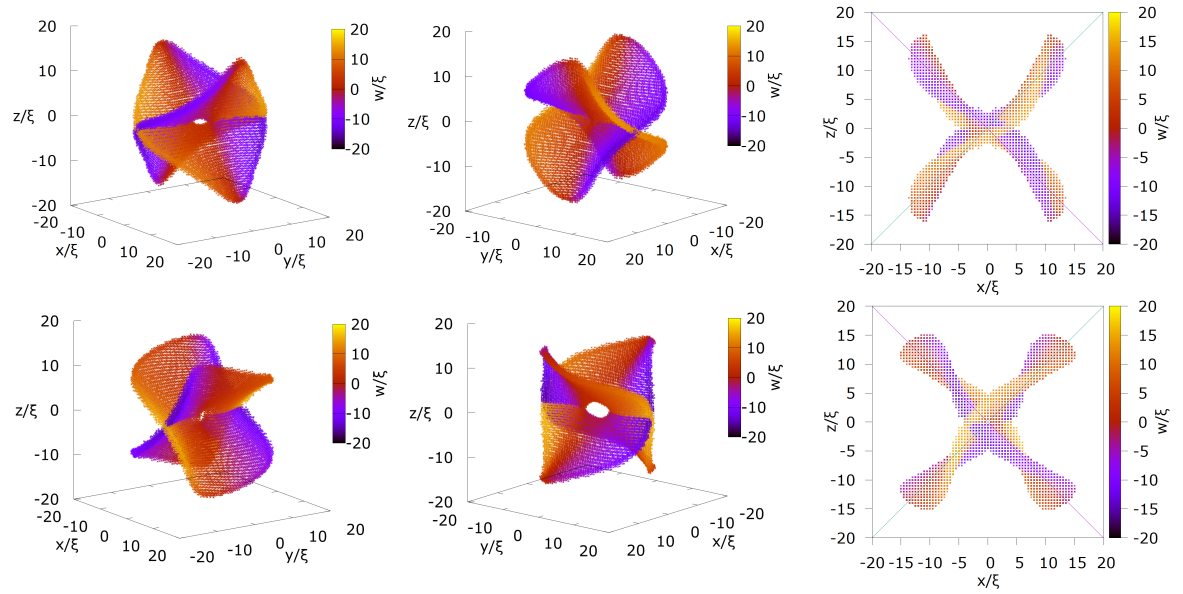

FIG. 18. (Top and bottom) Two different unusual vortex core structures observed in final states of ITEM runs with the same parameters. The frequencies were set at the isoclinic point, $\Omega_{zw} = \Omega_{xy} = 1.3\Omega_c$, and the spatial resolution was equal to $\Delta x = 0.5\xi$, corresponding to system radius of $R \approx 20.6\xi$. These simulations were the final iteration in a series of ITEM runs similar to those that generated Fig. 8. That is, we fixed Ω_{zw}, and varied $\Delta\Omega$ starting from Ω_c and stepping down to the isoclinic point in units of $0.1\Omega_c$. We used the final state of each run as the initial state of the next. These two states started out very close to the predicted skew planes at high frequency difference, however as we decreased $\Delta\Omega$ these planes began to increasingly curve, up to the maximum amount shown in this figure at $\Delta\Omega = 0$. These states have energies given by $E \approx 0.654949\mu N$ (Top) and $E \approx 0.654936\mu N$ (Bottom), respectively. This is similar to, but slightly higher than the orthogonal state energy at these frequencies, which is $E \approx 0.654764\mu N$, suggesting that these are metastable excited states. Furthermore the fact that we found two such different states for identical runs suggests that there may be many different low-lying excitations of this kind, perhaps due to the isoclinic symmetry at $\Delta\Omega = 0$.

negative, so we immediately obtain

$$|\sin\theta| < \frac{c\left(1-r_1^2\right)^{\frac{1}{2}}}{sr_1}, \tag{99}$$

as a constraint for θ. Note that this constraint is trivially satisfied whenever $c\left(1-r_1^2\right)^{1/2} > sr_1$, which occurs when $r_1 < c$. Given this condition for θ, we can then satisfy the inequality (98) when $r_2' \in (r_-, r_+)$, where

$$r_\pm = sr_1\cos\theta \pm \left[c^2\left(1-r_1^2\right) - s^2 r_1^2\sin^2\theta\right]^{\frac{1}{2}}.$$

The last step is to enforce the constraint $r_\pm \geq 0$, since r_2' cannot be negative. Rearranging each inequality gives

$$\begin{aligned} r_- \geq 0 \quad &\Longleftrightarrow \quad \cos\theta \geq \left(\chi^2 - \sin^2\theta\right)^{\frac{1}{2}}, \\ r_+ \geq 0 \quad &\Longleftrightarrow \quad -\cos\theta \leq \left(\chi^2 - \sin^2\theta\right)^{\frac{1}{2}}, \end{aligned}$$

where $\chi = c\left(1-r_1^2\right)^{1/2}/sr_1$. Note that the quantity on the RHS of both of these inequalities is always non-negative, so $r_- \geq 0$ requires $\theta \in [-\pi/2, \pi/2]$, while $r_+ \geq 0$ is automatically satisfied in this same region. With this consideration of the sign of the LHS in mind, we can square both inequalities and rearrange to find

$$\begin{aligned} r_- \geq 0: \quad 1 \geq \chi^2 \quad &\Longrightarrow \quad r_1^2 \geq c^2, \\ r_+ \geq 0: \quad 1 \leq \chi^2 \quad &\Longrightarrow \quad r_1^2 \leq c^2, \end{aligned}$$

Combining all of this with the inequality (99), gives us two separate integration regions. We have

$$r_1 \in (0, c), \quad r_2' \in (0, r_+), \quad \theta \in (-\pi, \pi),$$

and

$$r_1 \in (c, 1), \quad r_2' \in (r_-, r_+) \quad \theta \in (-\theta_*, \theta_*),$$

where $\theta_* = \arcsin\chi$. Finally, we can write the full result as

$$\int_{B^4(1)} \mathrm{d}x\mathrm{d}y\mathrm{d}z\mathrm{d}w = \frac{1}{c^2}\int_0^c r_1\mathrm{d}r_1 \int_{-\pi}^{\pi}\mathrm{d}\theta_1 \int_{-\pi}^{\pi}\mathrm{d}\theta \int_0^{r_+} r_2'\mathrm{d}r_2' + \frac{1}{c^2}\int_c^1 r_1\mathrm{d}r_1 \int_{-\pi}^{\pi}\mathrm{d}\theta_1 \int_{-\theta_*}^{\theta_*}\mathrm{d}\theta \int_{r_-}^{r_+} r_2'\mathrm{d}r_2',$$

as is used in the main text.

XI. THE MINIMUM DISTANCE BETWEEN TWO CIRCLES OF COMMON CENTRE AND RADIUS IN 4D

Consider a pair of circles (C_1, C_2) in $\mathbb{R}^4$ with the same radius and centre, but occupying different planes, and let these two planes be related by an isoclinic rotation. In this Appendix we will derive an expression for the minimum distance between two such circles. Without loss of generality, we may encode the two circles in the following vector equations:

$$\begin{aligned}\boldsymbol{r}_{C_1} &= R\left(\cos\theta_1\hat{\boldsymbol{x}} + \sin\theta_1\hat{\boldsymbol{y}}\right)\\ \boldsymbol{r}_{C_2} &= R\left[\cos\theta_2'\left(c\hat{\boldsymbol{z}} - s\hat{\boldsymbol{x}}\right) + \sin\theta_2'\left(c\hat{\boldsymbol{w}} - \nu s\hat{\boldsymbol{y}}\right)\right].\end{aligned}$$

The vector between an arbitrary point on C_1 and an arbitrary point on C_2 is given by $\boldsymbol{d} = \boldsymbol{r}_{C_1} - \boldsymbol{r}_{C_2}$. All we have to do is compute the length of this vector and minimize it with respect to θ_1 and θ_2'. Evaluating the modulus squared of d, we have

$$\begin{aligned}d^2 &= 2R^2\left[1 + s\left(\cos\theta_1\cos\theta_2' + \nu\sin\theta_1\sin\theta_2'\right)\right]\\ d &= \sqrt{2}R\left[1 + s\cos\left(\theta_1 - \nu\theta_2'\right)\right]^{\frac{1}{2}}\end{aligned}$$

The minimum value of d is therefore $\sqrt{2}R(1-s)^{1/2}$, which occurs when $\theta_1 = \nu\theta_2' + \pi$.

XII. ADDITIONAL NUMERICAL RESULTS

In this Appendix, we will present extra numerical results to supplement those in the main text. Some of these data are from simulations not mentioned in the text, and others are additional data from simulations described in the text, to aid in explanation and visualisation.

XII.1. Unequal Frequency

Fig. 16 shows the final state vortex core for a run of the ITEM with frequencies $\Omega_{zw} = 1.25\Omega_c$, and $\Omega_{xy} \approx 1.35\Omega_c$, which gives a predicted skewness angle of $\eta = 10°$. Just as in Fig. 7, the agreement between theory and numerics is still very good apart from the avoided crossing region near the origin. In particular, the third panel shows a side on view in which the vortex cores lies roughly along a pair of lines, on top of which we have plotted the theoretically predicted lines we expect. As can be seen, the data is still very close to the predicted values, although interestingly there is a small degree of asymmetry visible in the third panel of Fig. 16 — the data points are not symmetric about the vertical axis — that can't be seen in Fig. 7. However, without further investigation we cannot tell whether this is due to numerical inaccuracy or some genuine physical phenomena.

Fig. 17 shows the final state for $\eta = 45°$, with a spatial resolution of $\Delta x = 0.2\xi$, compared to 0.5ξ for the previous figures. The agreement between these data and our predictions is as good as before, as can be seen in the third panel, and the data does have mirror symmetry about the vertical axis. However, there are also some interesting qualitative differences to the lower resolution results. For example, the avoided crossing between the planes has a different orientation to that in the previous two figures, as can be seen by comparing the first two panels. In our reconnection analysis of Sec. V.2 this property of the avoided crossing was controlled by the phase of the added perturbation, so this could be an instance of spontaneous symmetry breaking driven by the noise we add to the initial state. Finally, the size of the reconnected region is smaller, which is most likely due to the smaller system size, but could be due to the higher resolution.

Fig. 18 shows two strange curved vortex surfaces observed at the isoclinic point for identical parameters. The frequencies were $\Omega_{zw} = \Omega_{xy} = 1.3\Omega_c$, and the spatial step size was $\Delta x = 0.5\xi$, which corresponds to a radius of $R \approx 20.6\xi$. Both of these final states were the last iteration in a sequence of ITEM runs, starting from $\Delta\Omega = \Omega_c$ down to $\Delta\Omega = 0$ in steps of $0,1\Omega_c$, with $\Omega_{zw} = 1.3\Omega_c$ fixed. The final state of each run was used as the initial state of the next, so that we could follow the evolution of a particular energy branch. We were attempting to track the predicted skew plane states for a fixed $\Omega_{zw} = 1.3\Omega_c$ and find their energies [c.f. Fig. 8], and the two final states at $\Delta\Omega = \Omega_c$ did in fact closely correspond to these predicted planes. However, both of these states began to deviate from the theoretical states as we decreased $\Delta\Omega$, becoming more and more curved all the way to the isoclinic point. Both these isoclinic curved states have a similar but slightly higher energy ($\approx 0.654949\mu N$ and $\approx 0.654936\mu N$, respectively) than the orthogonal state at the same frequencies ($\approx 0.654764\mu N$), suggesting they are metastable excitations. It is interesting that we have found two different such low lying excitations, this may be due to the degeneracy associated with isoclinic symmetry, in which case we may expect many more such

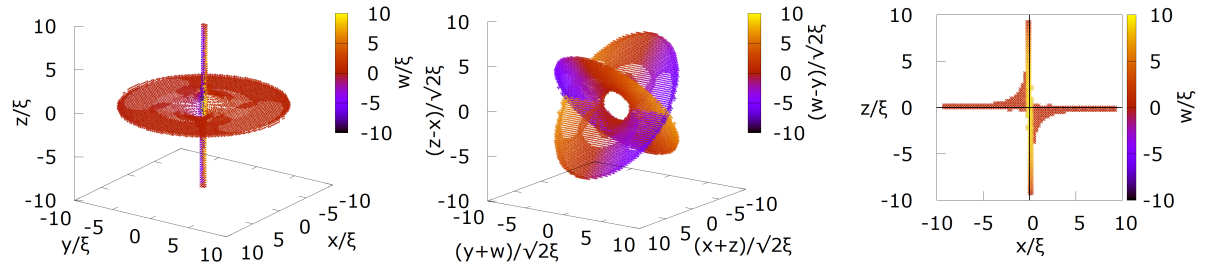

FIG. 19. As Fig. 14 but at a spatial step of $\Delta x = 0.25\xi$, corresponding to a radius of $R \approx 10.3\xi$. Again, we have an avoided crossing but not visible skewness, with the lines $x = 0$ and $z = 0$ plotted on the figure as guides to the eye to show this. While it is not clear from comparing this figure to Fig. 14, the avoided crossing region is in fact smaller in this smaller system [c.f. Fig. 13]

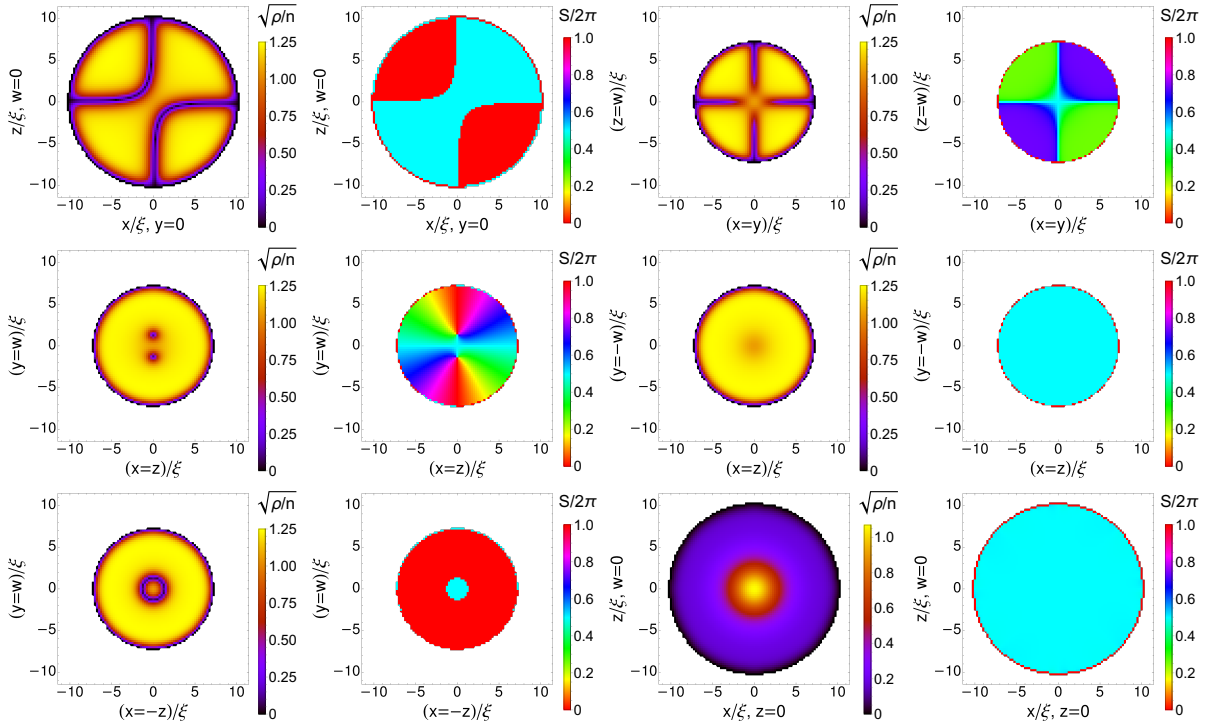

FIG. 20. 2D cuts of the density and phase profile of the state whose vortex core is shown in Fig. 19. The top and center rows show cuts that were previously used to visualise the orthogonal intersecting state in Ref [1], allowing us to compare these two states. The bottom row shows cuts that were not previously used, since, by symmetry, they gave density and phas profiles that were seen before. Now these symmetries are broken and these cuts give useful information.

states.

XII.2. Equal Frequency

Fig. 19 shows the core plot for a final state with the same frequencies ($\Omega = 1.5\Omega_c$) as Fig. 14 but with a spatial step of $\Delta x = 0.25\xi$, corresponding to a smaller radius of $R \approx 10.3\xi$. As we can see in the third panel, this state also has no visible skewness. Also, this state exhibits the same kind of avoided crossing, as in Fig. 14, but with a smaller value for $r_m in$ as shown in Fig. 13.

Fig. 20 shows the density and phase profiles of this same state along 2D cuts given by $y = 0$ & $w = 0$, $x = y$ & $z = w$, $x = z$ & $y = w$, $x = z$ & $y = -w$. Note that a cut given by $x = y$ & $z = w$ would show the same overall structure as that in the $y = 0$ & $w = 0$ cut, but in a smaller disc due to the cut being diagonal. These particular cuts were chosen as they were used in the Appendix of our previous paper [1] to visualise the orthogonal intersecting state. Comparing those previous plots to those in Fig. 20 gives us an idea of how the avoided crossing affects the phase as well as the density.

In more detail, firstly, the top left density plot in Fig. 20 has gone from showing orthogonal intersecting lines of depletion in Ref. [1] to what look hyperbolae,

while the top left phase plot shows that the phase jumps across these lines in the exact same way as before. Secondly, the top right plots show a cut that has gone from orthogonal intersecting vortex lines to density depletions that do not quite reach zero and smoothly vanish near the origin. This is because the vortex cores are curving out of the plane of the cut in this case, and the corresponding phase jumps become smooth variations. Thirdly, the center left plots show a cut that was previously essentially a plot of a doubly charged point vortex but now appears to be a pair of singly like-charged point vortices with a small separation. Fourthly, the center right cut was previously in Ref. [1] a strange case where the density showed what looked like a point vortex, but because of the cut chosen the phase was constant. Now the perturbed version shows that this density depletion no longer goes to zero. Finally, the bottom row shows two more 2D cuts of this state which did not show any new features for the intersecting orthogonal state due to its symmetries. Since the avoided crossing state has fewer symmetries these plots are now interesting. The bottom left plots correspond to a cut ($x = -z$ & $y = w$) that previously had a zero in density but no phase winding, but now show a vortex ring, with a corresponding phase jump. The top right shows plots that are centred on the x–y plane, and hence would have shown very low density (up to numerical accuracy) for the orthogonal state. Now, due to the avoided crossing, we see a region of nonzero density around the origin that reduces to zero as the radius increases, with the corresponding phase plot being constant.

[1] B. McCanna and H. M. Price, Phys. Rev. Research **3**, 023105 (2021).
[2] L. Pitaevskii, S. Stringari, and O. U. Press, *Bose-Einstein Condensation*, International Series of Monographs on Physics (Clarendon Press, 2003).
[3] C. Pethick and H. Smith, *Bose-Einstein Condensation in Dilute Gases* (Cambridge University Press, 2002).
[4] N. R. Cooper, Advances in Physics **57**, 539 (2008).
[5] A. L. Fetter, Rev. Mod. Phys. **81**, 647 (2009).
[6] K. W. Madison, F. Chevy, W. Wohlleben, and J. Dalibard, Phys. Rev. Lett. **84**, 806 (2000).
[7] K. W. Madison, F. Chevy, V. Bretin, and J. Dalibard, Phys. Rev. Lett. **86**, 4443 (2001).
[8] M. R. Matthews, B. P. Anderson, P. C. Haljan, D. S. Hall, C. E. Wieman, and E. A. Cornell, Phys. Rev. Lett. **83**, 2498 (1999).
[9] J. R. Abo-Shaeer, C. Raman, J. M. Vogels, and W. Ketterle, Science **292**, 476 (2001).
[10] N. Verhelst and J. Tempere, Vortex Dynamics. Intech , 1 (2017).
[11] J. Dalibard, F. Gerbier, G. Juzeliūnas, and P. Öhberg, Reviews of Modern Physics **83**, 1523 (2011).
[12] N. Cooper, J. Dalibard, and I. Spielman, Rev. Mod. Phys. **91**, 015005 (2019).
[13] T. Ozawa, H. M. Price, A. Amo, N. Goldman, M. Hafezi, L. Lu, M. C. Rechtsman, D. Schuster, J. Simon, O. Zilberberg, and I. Carusotto, Rev. Mod. Phys. **91**, 015006 (2019).
[14] Y. E. Kraus, Z. Ringel, and O. Zilberberg, Phys. Rev. Lett. **111**, 226401 (2013).
[15] H. Price, O. Zilberberg, T. Ozawa, I. Carusotto, and N. Goldman, Phys. Rev. Lett. **115**, 195303 (2015).
[16] T. Ozawa, H. M. Price, N. Goldman, O. Zilberberg, and I. Carusotto, Phys. Rev. A **93**, 043827 (2016).
[17] M. Lohse, C. Schweizer, H. M. Price, O. Zilberberg, and I. Bloch, Nature **553**, 55 (2018).
[18] O. Zilberberg, S. Huang, J. Guglielmon, M. Wang, K. P. Chen, Y. E. Kraus, and M. C. Rechtsman, Nature **553**, 59 (2018).
[19] S. Sugawa, F. Salces-Carcoba, A. R. Perry, Y. Yue, and I. Spielman, Science **360**, 1429 (2018).
[20] L. Lu, H. Gao, and Z. Wang, Nature communications **9**, 1 (2018).
[21] M. Kolodrubetz, Physical review letters **117**, 015301 (2016).
[22] Q. Wang, K. Ding, H. Liu, S. Zhu, and C. T. Chan, Optics Express **28**, 1758 (2020).
[23] Y. Wang, H. M. Price, B. Zhang, and Y. Chong, arXiv preprint arXiv:2001.07427 (2020).
[24] H. M. Price, Four-dimensional topological lattices without gauge fields (2018), arXiv:1806.05263.
[25] R. Yu, Y. Zhao, and A. P. Schnyder, arXiv preprint arXiv:1906.00883 (2019).
[26] L. Li, C. H. Lee, and J. Gong, Communications Physics **2**, 1 (2019).
[27] M. Ezawa, Physical Review B **100**, 075423 (2019).
[28] O. Boada, A. Celi, J. I. Latorre, and M. Lewenstein, Phys. Rev. Lett. **108**, 133001 (2012).
[29] A. Celi, P. Massignan, J. Ruseckas, N. Goldman, I. B. Spielman, G. Juzeliūnas, and M. Lewenstein, Phys. Rev. Lett. **112**, 043001 (2014).
[30] M. Mancini, G. Pagano, G. Cappellini, L. Livi, M. Rider, J. Catani, C. Sias, P. Zoller, M. Inguscio, M. Dalmonte, and L. Fallani, Science **349**, 1510 (2015).
[31] B. K. Stuhl, H.-I. Lu, L. M. Aycock, D. Genkina, and I. B. Spielman, Science **349**, 1514 (2015).
[32] B. Gadway, Physical Review A **92**, 043606 (2015).
[33] F. A. An, E. J. Meier, and B. Gadway, Science Advances **3**, e1602685 (2017).
[34] H. M. Price, T. Ozawa, and N. Goldman, Phys. Rev. A **95**, 023607 (2017).
[35] G. Salerno, H. M. Price, M. Lebrat, S. Häusler, T. Esslinger, L. Corman, J.-P. Brantut, and N. Goldman, Physical Review X **9**, 041001 (2019).
[36] K. Viebahn, M. Sbroscia, E. Carter, J.-C. Yu, and U. Schneider, Physical Review Letters **122**, 110404 (2019).
[37] L. Barbiero, L. Chomaz, S. Nascimbene, and N. Goldman, arXiv preprint arXiv:1907.10555 (2019).
[38] T. Chalopin, T. Satoor, A. Evrard, V. Makhalov, J. Dalibard, R. Lopes, and S. Nascimbene, arXiv preprint arXiv:2001.01664 (2020).
[39] L. Yuan, Y. Shi, and S. Fan, Opt. Lett. **41**, 741 (2016).
[40] T. Ozawa and I. Carusotto, Physical review letters **118**, 013601 (2017).
[41] E. Lustig, S. Weimann, Y. Plotnik, Y. Lumer, M. A.

Bandres, A. Szameit, and M. Segev, Nature **567**, 356 (2019).
[42] L. Yuan, M. Xiao, Q. Lin, and S. Fan, Phys. Rev. B **97**, 104105 (2018).
[43] L. Yuan, Q. Lin, M. Xiao, and S. Fan, Optica **5**, 1396 (2018).
[44] L. Yuan, Q. Lin, A. Zhang, M. Xiao, X. Chen, and S. Fan, Phys. Rev. Lett. **122**, 083903 (2019).
[45] L. Yuan, A. Dutt, M. Qin, S. Fan, and X. Chen, Photonics Research **8**, B8 (2020).
[46] A. Dutt, Q. Lin, L. Yuan, M. Minkov, M. Xiao, and S. Fan, Science **367**, 59 (2020).
[47] Y. Baum and G. Refael, Physical review letters **120**, 106402 (2018).
[48] H. M. Price, T. Ozawa, and H. Schomerus, arXiv preprint arXiv:1907.04231 (2019).
[49] P. J. Crowley, I. Martin, and A. Chandran, arXiv preprint arXiv:1908.08062 (2019).
[50] E. Boyers, P. J. Crowley, A. Chandran, and A. O. Sushkov, arXiv preprint arXiv:2004.03457 (2020).
[51] T. Ozawa and H. M. Price, Nature Reviews Physics , 1 (2019).
[52] C. Oliver, A. Smith, T. Easton, G. Salerno, V. Guarrera, N. Goldman, G. Barontini, and H. M. Price, arXiv preprint arXiv:2112.10648 (2021).
[53] J. R. Abo-Shaeer, C. Raman, J. M. Vogels, and W. Ketterle, Science **292**, 476 (2001).
[54] A. A. Abrikosov, Journal of Physics and Chemistry of Solids **2**, 199 (1957).
[55] B. P. Anderson, P. C. Haljan, C. A. Regal, D. L. Feder, L. A. Collins, C. W. Clark, and E. A. Cornell, Phys. Rev. Lett. **86**, 2926 (2001).
[56] P. Rosenbusch, V. Bretin, and J. Dalibard, Physical review letters **89**, 200403 (2002).
[57] S. Komineas, The European Physical Journal Special Topics **147**, 133 (2007).
[58] R. Carretero-González, D. Frantzeskakis, and P. Kevrekidis, Nonlinearity **21**, R139 (2008).
[59] R. Bisset, W. Wang, C. Ticknor, R. Carretero-González, D. Frantzeskakis, L. A. Collins, and P. G. Kevrekidis, Physical Review A **92**, 063611 (2015).
[60] W. Wang, R. Bisset, C. Ticknor, R. Carretero-González, D. Frantzeskakis, L. A. Collins, and P. Kevrekidis, Physical Review A **95**, 043638 (2017).
[61] K. Schwarz, Physical Review B **38**, 2398 (1988).
[62] W. Vinen and J. Niemela, Journal of low temperature physics **128**, 167 (2002).
[63] J. Koplik and H. Levine, Physical Review Letters **71**, 1375 (1993).
[64] S. Nazarenko and R. West, Journal of low temperature physics **132**, 1 (2003).
[65] R. Tebbs, A. J. Youd, and C. F. Barenghi, Journal of Low Temperature Physics **162**, 314 (2011).
[66] S. Zuccher, M. Caliari, A. W. Baggaley, and C. F. Barenghi, Physics of fluids **24**, 125108 (2012).
[67] S. M. W, K. Dustin, P. Davide, K. G. L, and I. W. T. M, Proceedings of the National Academy of Sciences **111**, 15350 (2014), doi: 10.1073/pnas.1407232111.
[68] A. Allen, S. Zuccher, M. Caliari, N. Proukakis, N. Parker, and C. Barenghi, Physical Review A **90**, 013601 (2014).
[69] A. Villois, D. Proment, and G. Krstulovic, Phys. Rev. Fluids **2**, 044701 (2017).
[70] A. Villois, D. Proment, and G. Krstulovic, Phys. Rev. Lett. **125**, 164501 (2020).
[71] G. P. Bewley, M. S. Paoletti, K. R. Sreenivasan, and D. P. Lathrop, Proceedings of the National Academy of Sciences **105**, 13707 (2008).
[72] S. Serafini, M. Barbiero, M. Debortoli, S. Donadello, F. Larcher, F. Dalfovo, G. Lamporesi, and G. Ferrari, Phys. Rev. Lett. **115**, 170402 (2015).
[73] S. Serafini, L. Galantucci, E. Iseni, T. Bienaimé, R. N. Bisset, C. F. Barenghi, F. Dalfovo, G. Lamporesi, and G. Ferrari, Phys. Rev. X **7**, 021031 (2017).
[74] P. Lounesto, *Clifford Algebras and Spinors*, 2nd ed., London Mathematical Society Lecture Note Series (Cambridge University Press, 2001).
[75] H. Kim and G. Rote, arXiv preprint arXiv:1603.07269 (2016).
[76] K. Wódkiewicz, Physical review. A, Atomic, molecular, and optical physics **43**, 68 (1991).
[77] F. Stampfer and P. Wagner, Phys. Rev. A **81**, 052710 (2010).
[78] T. T. Lê, Z. Osman, D. K. Watson, M. Dunn, and B. A. McKinney, Physica Scripta **94**, 065203 (2019).
[79] M. Mochol-Grzelak, A. Dauphin, A. Celi, and M. Lewenstein, Quantum Science and Technology **4**, 014009 (2018).
[80] V. A. Andryushchenko and L. P. Kondaurova, Low Temperature Physics **44**, 1020 (2018), https://doi.org/10.1063/1.5055838.
[81] D. Proment and G. Krstulovic, Phys. Rev. Fluids **5**, 104701 (2020).
[82] P. K. Newton, *The N-vortex problem : analytical techniques / Paul K. Newton.*, Applied mathematical sciences ; vol.145 (Springer, New York, 2001).
[83] D. J. Thouless, Phys. Rev. B **27**, 6083 (1983).
[84] M. Verbin, O. Zilberberg, Y. E. Kraus, Y. Lahini, and Y. Silberberg, Phys. Rev. Lett. **110**, 076403 (2013).
[85] Y. E. Kraus, Y. Lahini, Z. Ringel, M. Verbin, and O. Zilberberg, Phys. Rev. Lett. **109**, 106402 (2012).
[86] Y. E. Kraus and O. Zilberberg, Phys. Rev. Lett. **109**, 116404 (2012).
[87] Y. E. Kraus, Z. Ringel, and O. Zilberberg, Phys. Rev. Lett. **111**, 226401 (2013).
[88] M. Verbin, O. Zilberberg, Y. Lahini, Y. E. Kraus, and Y. Silberberg, Phys. Rev. B **91**, 064201 (2015).
[89] M. Lohse, C. Schweizer, O. Zilberberg, M. Aidelsburger, and I. Bloch, Nature Physics **12**, 350 (2016).
[90] S. Nakajima, T. Tomita, S. Taie, T. Ichinose, H. Ozawa, L. Wang, M. Troyer, and Y. Takahashi, Nature Physics **12**, 296 (2016).
[91] M. Lohse, C. Schweizer, H. M. Price, O. Zilberberg, and I. Bloch, Nature **553**, 55 (2018).
[92] O. Zilberberg, S. Huang, J. Guglielmon, M. Wang, K. P. Chen, Y. E. Kraus, and M. C. Rechtsman, Nature **553**, 59 (2018).
[93] W. Cheng, E. Prodan, and C. Prodan, Phys. Rev. Applied **16**, 044032 (2021).
[94] Z.-G. Chen, W. Zhu, Y. Tan, L. Wang, and G. Ma, Phys. Rev. X **11**, 011016 (2021).
[95] A. Schreiber, K. N. Cassemiro, V. Potoček, A. Gábris, P. J. Mosley, E. Andersson, I. Jex, and C. Silberhorn, Phys. Rev. Lett. **104**, 050502 (2010).
[96] A. Regensburger, C. Bersch, B. Hinrichs, G. Onishchukov, A. Schreiber, C. Silberhorn, and U. Peschel, Phys. Rev. Lett. **107**, 233902 (2011).
[97] X.-W. Luo, X. Zhou, C.-F. Li, J.-S. Xu, G.-C. Guo, and

Z.-W. Zhou, Nature Communications **6**, 7704 (2015).
[98] D.-W. Wang, R.-B. Liu, S.-Y. Zhu, and M. O. Scully, Phys. Rev. Lett. **114**, 043602 (2015).
[99] L. Livi, G. Cappellini, M. Diem, L. Franchi, C. Clivati, M. Frittelli, F. Levi, D. Calonico, J. Catani, M. Inguscio, and L. Fallani, Phys. Rev. Lett. **117**, 10.1103/PhysRevLett.117.220401 (2016).
[100] E. J. Meier, F. A. An, and B. Gadway, Phys. Rev. A **93**, 051602 (2016).
[101] S. Kolkowitz, S. L. Bromley, T. Bothwell, M. L. Wall, G. E. Marti, A. P. Koller, X. Zhang, A. M. Rey, and J. Ye, Nature **542**, 66 (2017).
[102] F. Cardano, A. D'Errico, A. Dauphin, M. Maffei, B. Piccirillo, C. de Lisio, G. D. Filippis, V. Cataudella, E. Santamato, L. Marrucci, M. Lewenstein, and P. Massignan, Nature Communications **8**, 15516 (2017).
[103] T. Ozawa and I. Carusotto, Phys. Rev. Lett. **118**, 013601 (2017).
[104] M. Wimmer, H. M. Price, I. Carusotto, and U. Peschel, Nature Physics **13**, 545 (2017).
[105] I. Martin, G. Refael, and B. Halperin, Phys. Rev. X **7**, 041008 (2017).
[106] A. Signoles, E. K. Dietsche, A. Facon, D. Grosso, S. Haroche, J. M. Raimond, M. Brune, and S. Gleyzes, Phys. Rev. Lett. **118**, 253603 (2017).
[107] B. Sundar, B. Gadway, and K. R. A. Hazzard, Scientific Reports **8**, 3422 (2018).
[108] B. Wang, T. Chen, and X. Zhang, Phys. Rev. Lett. **121**, 100501 (2018).
[109] C. Chen, X. Ding, J. Qin, Y. He, Y.-H. Luo, M.-C. Chen, C. Liu, X.-L. Wang, W.-J. Zhang, H. Li, L.-X. You, Z. Wang, D.-W. Wang, B. C. Sanders, C.-Y. Lu, and J.-W. Pan, Phys. Rev. Lett. **121**, 100502 (2018).
[110] Y. Baum and G. Refael, Physical review letters **120**, 106402 (2018).
[111] Y. Peng and G. Refael, Phys. Rev. B **97**, 134303 (2018).
[112] H. M. Price, Phys. Rev. B **101**, 205141 (2020).
[113] D. Cheng, B. Peng, D.-W. Wang, X. Chen, L. Yuan, and S. Fan, Phys. Rev. Research **3**, 033069 (2021).
[114] S. K. Kanungo, J. D. Whalen, Y. Lu, M. Yuan, S. Dasgupta, F. B. Dunning, K. R. A. Hazzard, and T. C. Killian, Nature Communications **13**, 972 (2022).
[115] L. Yuan, M. Xiao, Q. Lin, and S. Fan, Phys. Rev. B **97**, 104105 (2018).
[116] L. Chen, P. Wang, Z. Meng, L. Huang, H. Cai, D.-W. Wang, S.-Y. Zhu, and J. Zhang, Phys. Rev. Lett. **120**, 193601 (2018).
[117] H. Cai, J. Liu, J. Wu, Y. He, S. Zhu, J. Zhang, and D. Wang, Phys. Rev. Lett. **122**, 023601 (2019).
[118] M. Wimmer, M. Monika, I. Carusotto, U. Peschel, and H. M. Price, Physical review letters **127**, 163901 (2021).
[119] V. Lienhard, P. Scholl, S. Weber, D. Barredo, S. de Léséleuc, R. Bai, N. Lang, M. Fleischhauer, H. Büchler, T. Lahaye, and A. Browaeys, Phys. Rev. X **10**, 021031 (2020).
[120] J. H. Kang, J. H. Han, and Y. Shin, New Journal of Physics **22**, 013023 (2020).
[121] A. Balčytis, T. Ozawa, Y. Ota, S. Iwamoto, J. Maeda, and T. Baba, Synthetic dimension band structures on a Si CMOS photonic platform (2021), arXiv:2105.13742 [physics.optics].
[122] H. Chen, N. Yang, C. Qin, W. Li, B. Wang, T. Han, C. Zhang, W. Liu, K. Wang, H. Long, X. Zhang, and L. Peixiang, Light Sci. Appl. **10**, 1 (2021).
[123] N. Englebert, N. Goldman, M. Erkintalo, N. Mostaan, S.-P. Gorza, F. Leo, and J. Fatome, arXiv preprint arXiv:2112.10756 (2021).
[124] Y.-Q. Zhu, N. Goldman, and G. Palumbo, Phys. Rev. B **102**, 081109 (2020).
[125] G. Palumbo and N. Goldman, Phys. Rev. Lett. **121**, 170401 (2018).
[126] M. Chen, C. Li, G. Palumbo, Y.-Q. Zhu, N. Goldman, and P. Cappellaro, Science **375**, 1017 (2022).
[127] A. Schwartz and B. Fischer, Optics Express **21**, 6196 (2013).
[128] B. A. Bell, K. Wang, A. S. Solntsev, D. N. Neshev, A. A. Sukhorukov, and B. J. Eggleton, Optica **4**, 1433 (2017).
[129] X.-F. Zhou, X.-W. Luo, S. Wang, G.-C. Guo, X. Zhou, H. Pu, and Z.-W. Zhou, Phys. Rev. Lett. **118**, 083603 (2017).
[130] H. Price, Y. Chong, A. Khanikaev, H. Schomerus, L. J. Maczewsky, M. Kremer, M. Heinrich, A. Szameit, O. Zilberberg, Y. Yang, *et al.*, Journal of Physics: Photonics (2022).
[131] T. Chalopin, T. Satoor, A. Evrard, V. Makhalov, J. Dalibard, R. Lopes, and S. Nascimbene, Nature Physics **16**, 1017 (2020).
[132] E. Meier, F. An, and B. Gadway, Nat. Commun. **7**, 13986 (2016).
[133] S.-C. Zhang, Science **294**, 823 (2001).
[134] D. Karabali and V. P. Nair, Nuclear Physics B **641**, 533 (2002).
[135] D. Prument, M. Onorato, and C. F. Barenghi, Phys. Rev. E **85**, 036306 (2012).
[136] D. Prument, M. Onorato, and C. F. Barenghi, Journal of Physics: Conference Series **544**, 012022 (2014).
[137] J. Gallier and D. Xu, *A Guide to the Classification Theorem for Compact Surfaces*, Geometry and Computing (Springer Berlin Heidelberg, 2013).
[138] Y. Kawaguchi and M. Ueda, Physics Reports **520**, 253 (2012), spinor Bose–Einstein condensates.
[139] T. Machon and G. P. Alexander, Proceedings of the Royal Society A: Mathematical, Physical and Engineering Sciences **472**, 10.1098/rspa.2016.0265 (2016).

Chapter 4

Conclusions

"One never notices what has been done; one only sees what remains to be done."

Marie Curie

In this thesis we have studied the low energy behaviour of a hypothetical 4D superfluid undergoing double rotation. We found that the resulting vortex phenomena differed from that seen in two and three dimensions in many important and interesting ways. Perhaps, the common theme of this new physics is that vortices are able to lose their individual character in 4D, and idea of "the number of vortices in a system" can become somewhat meaningless. Hints of this could be seen in our first paper, where we showed that a pair of orthogonal intersecting vortex planes form a low-energy stationary state under generic double rotations. In our second paper this became even clearer, as we showed analytically that skew intersecting vortex planes evolve dynamically into a single curved surface with no self intersection, and found numerical stationary states containing similar curved core structures with avoided crossings. This is a very brief summary of our results, which we will now expand upon and discuss further.

The second chapter consists of a paper detailing our initial results, which are a first step into the physics of quantum vortices in 4D. We showed that the natural 4D extension of a vortex line in 3D is a vortex plane stabilised by simple rotation of a 4D superfluid. Building on this intuition, we introduced the concept of a double rotation, through two

independent and orthogonal rotation planes simultaneously. This means that a doubly-rotating 4D superfluid has two independent frequency parameters, and we chose to focus on the simplest nontrivial case where these frequencies were equal. Our ansatz for the optimal vortex configuration under this type of rotation was a pair of orthogonal intersecting vortex planes. By viewing the double rotation as a combination of simple rotations in the two respective planes, we reasoned that the ground state under the double rotation could be just a combination of the two vortex planes that would be generated by each of these simple rotations separately.

Using this ansatz, we then presented numerical results that this intersecting state is a stationary state with lower energy than a single vortex plane for sufficiently high frequencies. We also found that the vortex-vortex interaction vanished, due to the orthogonality. The existence of stable intersecting vortices that do not interact is already a departure from the physics of vortices in two and three dimensions. The paper then concludes with a discussion of the questions raised by these results, including the possible existence and nature of reconnection dynamics for intersecting vortex planes, and of the behaviour of vortices at low energy under double rotation of unequal frequencies.

These particular questions were addressed in the fourth chapter, which is a manuscript for a forthcoming paper. Here we gave a fuller description of the mathematical structure of 4D rotations, including an explanation of isoclinic rotations as these were useful to describe more complex vortex structures in 4D. This allowed us to build on our initial results by developing a theory of intersecting, non orthogonal (or skew) vortex planes based on competition between rotational and vortex-vortex interaction energy.

We calculated the hydrodynamic interaction between skew vortex planes in a few special cases, using an integral transformation into skew double polar coordinates which we derived. For two planes related by a simple rotation the interaction vanishes as before, but if the rotation is isoclinic then the two planes are tilting in either a purely aligning or anti-aligning sense and they begin to interact. In this case the interaction varies monotonically with the tilt angle and is repulsive (resp. attractive) if the vortices are

approaching an aligned (resp. anti-aligned) state.

We also used linearised GPE dynamics to investigate the possible reconnection of skew vortex planes. These analytics predicted that purely aligning planes still formed a stationary state, although we suspect this is not true for the full nonlinear dynamics. For generic tilting we found that skew planes do not form a stationary state, and the resulting evolution was such that the vortex core curved and expanded away from the intersection point, we referred to this as an avoided crossing. Away from the former intersection, the core approached a pair of planes as before.

Next, we sought to understand the problem of unequal frequencies using skew vortex planes as an ansatz, ignoring any of these dynamics. This was based on the result that a single vortex plane always wants to fully align with the higher rotation frequency. In the case of two planes, each wants to align in this way but to do so they must begin to align with each other. This introduces a nonzero repulsive interaction limiting the tilt angle. Calculating the rotational energy from this ansatz, we then minimized the sum of rotational and hydrodynamic energies to find the optimal configuration of the two planes. This gave us a unique, nontrivial minimum for each value of the difference between the rotation frequencies. Furthermore, this optimal state was predicted to be lower in energy than the orthogonal state.

Testing this prediction numerically, we found very good agreement except for the existence of an avoided intersection in the vortex core. At large distances, the core approached the predicted skew planes, but at small radii the core curved away from the origin such that the two planes no longer intersected but formed a single curved surface. Interestingly, these numerical results suggest that such curved vortex structures can form stationary states in 4D.

Finally we sought to apply this theory to the case of equal frequency rotation, reasoning that vortex planes tilted to anti-align may gain more from attractive interaction than they lose from not aligning with the rotation. In this case we predicted that, at frequencies near and above the critical frequency, the orthogonal state is always preferred. Again, we

compared this result to numerics and found approximate agreement, in that the final states we obtained had a small degree of skewness that decreased with frequency, eventually to zero. However, there was again a sizeable avoided crossing in the vortex cores, which also decreased with frequency but did not disappear. We found that these final states were generally lower energy than the orthogonal state even above the critical frequency, but the energy difference between these states was very small and decreased with system size. This suggests that for large enough systems the orthogonal state is either lower energy, or degenerate with, these avoided crossing states.

This work opens up many exciting future research directions. Firstly, there is clearly much more to be understood about the physics of vortices in 4D just from the minimal GPE model that we have considered. The presence of curved vortex stationary states raises interesting questions that are worth exploring, such as whether closed vortex surfaces can be stable, and what the ground state configuration looks like for higher values of one or both frequencies. Secondly, much more work needs to be done to connect to experiments, and we hope that the research we have presented can provide a foundation for these future works. Finally, in the long term this work could be adapted to study more complex topological defects in 4D, and may inspire future research towards the 4D fractional quantum Hall effect.

Appendix A

Imaginary time evolution method

Here we will explain the imaginary time evolution method (ITEM), and demonstrate how it works using linear quantum evolution as an example. With that in mind, consider the Schrödinger equation, given by ($\hbar = 1$ in this Appendix)

$$i\frac{\partial}{\partial t}\left|\psi\right\rangle = H\left|\psi\right\rangle . \tag{A.1}$$

Its solution for a given initial state $|\psi(0)\rangle$ can be written formally as

$$\left|\psi(t)\right\rangle = e^{-iHt}\left|\psi(0)\right\rangle . \tag{A.2}$$

The Hamiltonian H is a Hermitian linear operator, so its eigenfunctions form an orthonormal set with real eigenvalues

$$H\left|n\right\rangle = E_n\left|n\right\rangle , \qquad \langle n|m|n|m\rangle = \delta_{nm}, \tag{A.3}$$

and we can write any state $|\psi(t)\rangle$ in terms of this basis as

$$\left|\psi(t)\right\rangle = \sum_n \psi_n(t)\left|n\right\rangle , \qquad \psi_n(t) \equiv \langle n|\psi(t)|n|\psi(t)\rangle . \tag{A.4}$$

The operator exponential in Eq. (A.2), which is nontrivial to compute in general, acts

straightforwardly in the eigenbasis

$$e^{-iHt}\left|n\right\rangle = e^{-iE_n t}\left|n\right\rangle . \tag{A.5}$$

This means if we know the overlap coefficients ψ_n for our initial data at time $t = 0$, we can in principle write down the solution at any future time as an infinite series

$$\left|\psi(t)\right\rangle = \sum_n \psi_n(0) e^{-iE_n t}\left|n\right\rangle . \tag{A.6}$$

Let us now think about finding the eigenfuctions, or *stationary states* of a system. In other words we are solving the time independent Schrödinger equation given by Eq. (A.3). Of particular interest is the ground state, the state of lowest energy E_n, as this determines much of the low temperature behaviour of a system described by H. We will denote this state by $n = 0$, and assume that it is non-degenerate - there is no other eigenstate $|n\rangle$ with energy $E_n = E_0$. The imaginary time evolution method (ITEM) is a simple numerical procedure to obtain ground states of these equations. Let $t \to -it$ such that the solution now reads

$$\left|\psi(t)\right\rangle = e^{-Ht}\left|\psi(0)\right\rangle = \sum_n \psi_n(0) e^{-E_n t}\left|n\right\rangle \tag{A.7}$$

an infinite sum of exponentially decaying terms. Now the condition that E_0 is the unique lowest energy translates into the fact that the $n = 0$ term in Eq. (A.7) decays slower than any other. More rigorously, in terms of ratios of overlap integrals

$$\lim_{t\to\infty} \frac{\langle n|\psi(t)|n|\psi(t)\rangle}{\langle 0|\psi(t)|0|\psi(t)\rangle} = \lim_{t\to\infty} \frac{\langle n|\psi(0)|n|\psi(0)\rangle}{\langle 0|\psi(0)|0|\psi(0)\rangle} e^{-(E_n - E_0)t} = \begin{cases} 1 & \text{if } n = 0 \\ 0 & \text{otherwise} \end{cases} \tag{A.8}$$

provided that our initial data is not orthogonal to the ground state. This means that we can take a generic initial state and evolve it in imaginary time into a configuration that is dominated by the ground state. There are two main difficulties: we still need a representation of the operator e^{-Ht}, and the solution we obtain is exponentially approaching

zero. One way to solve both of these problems involves picking a discrete set of times $\{t_n : n = 0, 1, 2, ..., N\}$ with associated intervals $\Delta t_n = t_{n+1} - t_n$. Provided that $\max_n \Delta t_n$ is small in some sense compared to the operator H, we can Taylor expand the exponential. For the numerical results in this project we use a constant interval $\Delta t_n = \Delta t$ and a simple first-order expansion

$$e^{-\Delta t H} = 1 - \Delta t H + O(\Delta t^2 H^2). \tag{A.9}$$

Now that we have discretized time, we can alternate between applying the operator $e^{-\Delta t H}$, and another operator which corrects the exponential decay. Labeling $|\psi^n\rangle = |\psi(t_n)\rangle$ for convenience, we may write the full procedure as follows

$$\left|\widetilde{\psi}^{n+1}\right\rangle = (1 - \Delta t H)\left|\psi^n\right\rangle, \tag{A.10}$$

$$\left|\psi^{n+1}\right\rangle = \sqrt{\frac{\langle\psi^n|\psi^n|\psi^n|\psi^n\rangle}{\left\langle\widetilde{\psi}^{n+1}|\widetilde{\psi}^{n+1}\middle|\widetilde{\psi}^{n+1}|\widetilde{\psi}^{n+1}\right\rangle}}\left|\widetilde{\psi}^{n+1}\right\rangle. \tag{A.11}$$

In this project we have been using this method to solve the GPE. This means we take the position representation $\langle \boldsymbol{r}|\psi(t)|\boldsymbol{r}|\psi(t)\rangle = \psi(\boldsymbol{r}, (t))$ in which the "Hamiltonian" is given by the right-hand side of Eq. (1.7). We also discretize space into a grid such that for each coordinate x we have $x_i = i\Delta s$, with the same step size in each direction. For example in 1D we define $\psi_i^n = \psi(i\Delta s, n\Delta t)$, so that the second derivative becomes

$$\left(\nabla^2\psi\right)_i = \frac{\psi_{i+1} - 2\psi_i + \psi_{i-1}}{\Delta s^2} + O(\Delta s^2), \tag{A.12}$$

and in Cartesian coordinates in higher dimensions the finite-difference Laplacian is a sum of these terms for each coordinate. In 1D the procedure for solving the GPE this way is

$$\widetilde{\psi}_i^{n+1} = \left(1 - \Delta t V_i - \Delta t|\psi_i^n|^2 + \frac{\Delta t}{\Delta s^2}\right)\psi_i^n - \frac{\Delta t}{2\Delta s^2}\left(\psi_{i+1}^n + \psi_{i-1}^n\right), \tag{A.13}$$

$$\psi_i^{n+1} = \left[\frac{\sum_j \left|\psi_j^n\right|^2}{\sum_j \left|\widetilde{\psi}_j^{n+1}\right|^2}\right]^{\frac{1}{2}}\widetilde{\psi}_i^{n+1}, \tag{A.14}$$

where we have already de-dimensionalized[1], such that $V_i = V_{\text{ext}}(\xi x_i)/\mu$. We have also made an explicit choice to evaluate the ψ-dependent operator H at time $n\Delta t$ rather than at the next time-step.

[1]When using this method to simulate trapped condensates it is more standard to work in the units defined by the trap, and have the free parameter on the nonlinear term.

Appendix B

Homotopy theory

Topological invariants in physics are, informally, quantities that are not affected by continuous deformations of space or of physical configurations. These quantities can prove very useful for characterizing and understanding the behaviour of certain systems. One powerful tool for predicting the existence of topological invariants is *homotopy theory*, which we will demonstrate using vortices in superfluids as an example.

To begin, we consider a complex order parameter $\psi(\boldsymbol{r})$ defined on n dimensional space $\mathbb{R}^n$. We can continuously deform ψ to a unit complex number everywhere except for a set $U = \bigcup_i U_i$ of neighbourhoods of the zeroes of ψ. What this means is that we index by i all the regions V_i where ψ vanishes, and that each of these is a subset of the interior, and not the boundary, of a set U_i. We then take the union U of these U_i, such that ψ is nonzero outside U. After the deformation we have that $\psi = e^{i\phi}$ in $U^c = \mathbb{R}^n/U$ (everywhere except U). A unit complex number is a point on a circle, S^1, so we can think of ψ as a continuous *mapping* (or simply map) from U^c to S^1.

Suppose we take a particular map $\psi_0 : \boldsymbol{r} \in U^c \to e^{i\phi_0(\boldsymbol{r})}$ and ask what is the set of all other physical phase profiles we can access with further arbitrary continuous deformations. This is called the *homotopy class* of the map ψ_0, denoted $[\psi_0]$, and these continuous deformations between maps are called homotopies. Maps that can be connected by a homotopy, that is maps in the same homotopy class, are called *homotopic*. If every map

from U^c to S^1 is homotopic to every other, then the set of all homotopy classes of these maps, denoted $[U^c, S^1]$, contains just a single element. In this case we could continuously deform any order parameter on U_c to any other. We can always construct a *constant map* c that sends every point in U^c to a given point in S^1, so when $[U^c, S^1]$ has one element it must be $[c]$, the set of maps that are homotopic to a constant, or *null-homotopic* maps. One way for a map not to be null-homotopic is if it contains a *topological defect*: a connected region of zeroes of an order parameter that cannot be removed by continuous deformations. These deformations can include moving topological defects around and combining defects by moving them to the same point.

There is often a natural way to combine two maps from a space A to a space B, in particular this is guaranteed when A is an n dimensional sphere S^n. The case of $A = S^2$ is shown in Fig. B.1. As we can see, for an S^n we can always shrink the equator to a point and end up with two copies of S^n touching at a point. We are then able to apply the two maps to each copy individually. [1] The resulting total map is then defined as the combination $f \cdot g$. This combination of maps can then be used to define a combination rule for homotopy classes, via $[f \cdot g] = [f][g]$.

We now come to an important definition. The set $[A, B]$ forms a *group* if this composition of homotopy classes satisfies two rules:

- $[c][f] = [f][c] = [f]$ for all maps f if and only if c is null-homotopic
- for every map f, there is a class of inverse maps $[f]^{-1}$ such that $[f]^{-1}[f] = [f][f]^{-1} = [c]$, the class of null-homotopic maps

In particular, such a group structure is always guaranteed if $A = S^n$, and the resulting group is known as the *nth* homotopy group of B, denoted $\pi_n(B)$.

In many physical cases our homotopy classes of configurations do form a group, and the structure of this group tells us how defects combine. If we have ψ_1, ψ_2, and ψ_3 each

[1] Note that this requires that the two maps agree at the touching point, otherwise the overall map is one-to-many there. This means we are actually dealing with spaces A and B that have a basepoint, and that the maps are basepoint-prerserving [99]

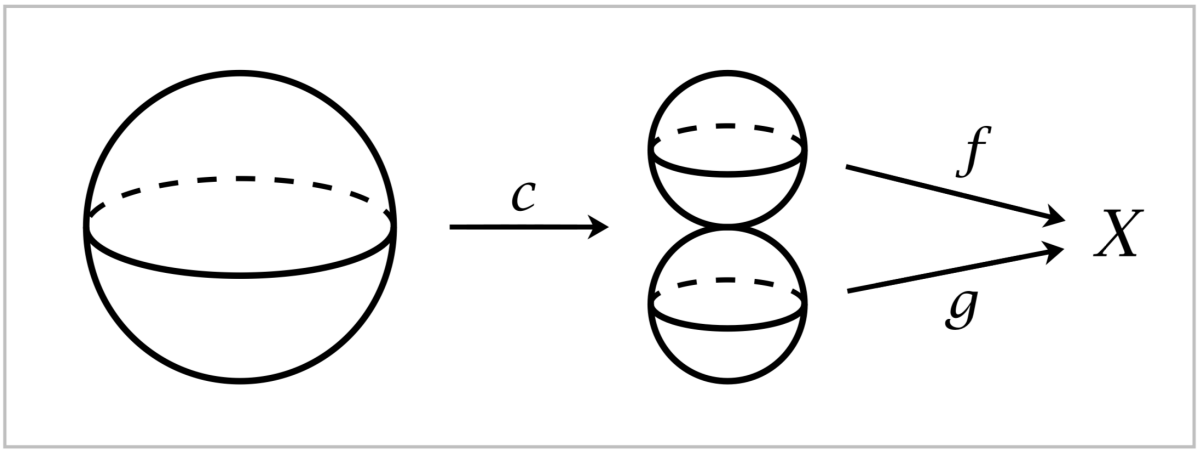

Figure B.1: Two maps f and g from a sphere to a space X can be combined in a canonical way. First we take a single sphere and apply the map c which shrinks the equator to a point. We now have two spheres touching at that point, and we will apply the map f to the top sphere and g to the bottom sphere such that every point ends up somewhere in X. The total map is then defined as the combination $f \cdot g$

with one defect, then $\psi_3 \in [\psi_1][\psi_2]$ means that combining the defects of $\psi_{1,2}$ generates the defect represented by ψ_3. Also, if we have a pair of single-defect functions $\psi_\pm$ such that their homotopy classes are inverses, i.e. $[\psi_-] = [\psi_+]^{-1}$, then these two defects annihilate each other leaving none behind. If the group $[A, B]$ contains any elements $[f]$ and $[g]$ such that $[f][g] \neq [g][f]$ then it is said to be *non-abelian*. When this occurs in a physical setting it can give rise to vortices which cannot pass through each other but instead stick together forming a "rung" [4, 100].

Let's now apply this mathematical machinery to derive something: the winding number of a vortex. Consider an isolated point zero of a 2D complex order parameter ψ. As shown in Fig. B.2, we can continuously deform the complement of this zero to a circle S^1, and as argued before, we can deform the values of ψ in this complement to points on the complex unit circle. The set of topological point defects in this case is therefore described by the homotopy class of maps $[S^1, S^1]$, or the first homotopy group of S_1, $\pi_1(S^1$. The first homotopy group $\pi_1(X$ of any space X describes the behaviour of loops in X, and is such an important object that it gets its own name: $\pi_1(X)$ is known as the *fundamental group* of X. The fundamental group of a circle is a textbook exercise [99], and is equal to $\mathbb{Z}$, the group of integers under addition. These integers are precisely the

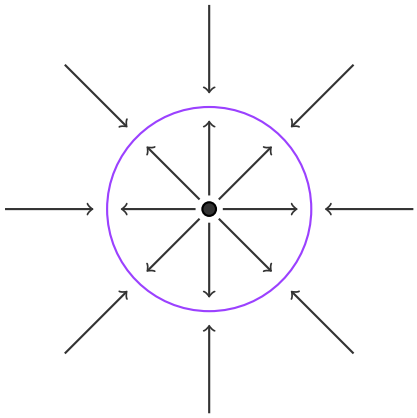

Figure B.2: The punctured plane $R^2/\{0\}$ can be continuously deformed into a circle

possible winding numbers of a point vortex in two dimensions. The fact that the group operation is addition is telling us what we derived in Chapter 1: combining vortices is the same as adding their winding numbers.

We will now try a more interesting example, a vortex ring in 3D. A naive guess for the complement of a ring in 3D might be a torus T^2, which would imply that we need to find $[T^2, S^1]$, the homotopy classes of maps from a torus to a circle. It turns out that this is incorrect, and the complement of a ring actually deforms to a sphere with two points identified, or a "degenerate" torus where the hole in the middle is shrunk to a point [9]. However, it is helpful to see how this naive guess fails, so we proceed anyway. Maps from a torus are not straightforward, in general one can write [8]

$$[T^2, X] = \pi_1(X)^2 \times \pi_2(X), \tag{B.1}$$

where $\times$ denotes the Cartesian product of the πs as sets, meaning that $[T^2, X$ does not necessarily form a group. In our case we are lucky as $\pi_2(S^1)$ is the trivial group, and we have $[T^2, S^1] = \pi_1(S^1)^2 = \mathbb{Z}^2$ [101], pairs of integers under addition. Does this mean that a single vortex ring has two winding numbers? No, clearly we have made a mistake. The key is that a torus has two holes: there is the inside of the torus, into which we have put the ring; and there is the "doughnut hole" in the middle. By including this second hole we have not eliminated the possibility that our vortex ring is threaded by a vortex line,

or another vortex ring [9]. In other words, we have actually just computed the homotopy classification of two linked vortex lines.[2]

Oddly enough, this pair of linked rings has the same "enclosing space", that is T^2, as a pair of orthogonal intersecting vortex planes in 4D. Using double polar coordinates, we can enclose one plane inside the region $r_1^2 = R_1^2$, and the other inside $r_2^2 = R_2^2$, where the R_j are arbitrary constants. The intersection of these two spaces is a *flat torus*, (a torus with no curvature) another peculiarity of four dimensions. We can understand this duality even better if we look at the image of the orthogonal planes in a 3-sphere S^3 surrounding the intersection point, that is $r_1^2 + r_2^2 = R^2$. Inside this S^3, the plane $r_1 = 0$ is given by $r_2^2 = R^2$, and vice-versa. In other words, each plane forms a circle of intersection with the 3-sphere. The benefit of restricting to a 3-sphere in this way is that we can now use stereographic projection to map the S^3 to $\mathbb{R}^3$ and gain a better visual understanding of the vortex planes. If we let the point $w = R, z = x = y = 0$ get mapped to infinity, then the new coordinates in $\mathbb{R}^3$ are given by

$$X = \frac{x}{R - w} \tag{B.2}$$

$$Y = \frac{y}{R - w} \tag{B.3}$$

$$Z = \frac{z}{R - w} \tag{B.4}$$

The circle $r_2 = 0$, $r_1 = R$ then gets mapped to the circle $Z = 0$, $X^2 + Y^2 = 1$, while the the circle $r_1 = 0$, $r_2 = R$ gets mapped to the z axis: $X = Y = 0$. What is now clear from this is that these two circles are linked. The orthogonal intersecting planes form a Hopf link in any 3-sphere that encloses their intersection point. This is of course the reason why the homotopy classification of these planes was idential to that of the linked rings. Most importantly the classification is the same regardless of the type of order parameter, provided that it can host line defects in 3D and surface defects in 4D. This means that a pair of intersecting vortex plane defects can realise the same homotopy classification as a

[2] More precisely two vortex lines forming a Hopf link

pair of linked vortex rings in 3D, for arbitrary order parameter manifolds, not just S^1.

Bibliography

[1] B. McCanna and H. M. Price, "Superfluid vortices in four spatial dimensions," *Phys. Rev. Res.*, vol. 3, p. 023 105, 2021. DOI: 10.1103/PhysRevResearch.3.023105.

[2] ——, "Skewed and curved vortex surfaces in stationary states of four dimensional superfluids," 2022, in preparation.

[3] P. M. Chaikin and T. C. Lubensky, *Principles of Condensed Matter Physics*. Cambridge University Press, 1995, ISBN: 9780511813467. DOI: 10.1017/CBO9780511813467.

[4] Y. Kawaguchi and M. Ueda, "Spinor Bose–Einstein condensates," *Phys. Rep.*, vol. 520, pp. 253–381, 2012. DOI: https://doi.org/10.1016/j.physrep.2012.07.005.

[5] L. Piatevskii and S. Stringari, *Bose-Einstein Condensation and Superfluidity*, ser. International Series of Monographs on Physics. Oxford University Press, 2016, ISBN: 9780198758884. DOI: 10.1093/acprof:oso/9780198758884.001.0001.

[6] C. Pethick and H. Smith, *Bose-Einstein Condensation in Dilute Gases*. Cambridge University Press, 2008, p. 569, ISBN: 9780511802850. DOI: 10.1017/CBO9780511802850.

[7] A. L. Fetter, "Rotating trapped Bose-Einstein condensates," *Rev. Mod. Phys.*, vol. 81, pp. 647–691, 2009. DOI: 10.1103/RevModPhys.81.647.

[8] J. E. Avron, R. Seiler, and B. Simon, "Homotopy and Quantization in Condensed Matter Physics," *Phys. Rev. Lett.*, vol. 51, pp. 51–53, 1983. DOI: 10.1103/PhysRevLett.51.51.

[9] H. Nakanishi, K. Hayashi, and H. Mori, "Topological classification of unknotted ring defects," *Commun. Mat. Phys.*, vol. 117, pp. 203–213, 1988. DOI: 10.1007/BF01223590.

[10] Y. Shen *et al.*, "Optical vortices 30 years on: OAM manipulation from topological charge to multiple singularities," *Light Sci. Appl.*, vol. 8, p. 90, 2019. DOI: 10.1038/s41377-019-0194-2.

[11] T. Machon and G. P. Alexander, "Global defect topology in nematic liquid crystals," *Proc. Phys. Soc. London, Sect. A*, vol. 472, 2016. DOI: 10.1098/rspa.2016.0265.

[12] W. Bao and Y. Cai, "Mathematical theory and numerical methods for Bose-Einstein condensation," *Kinet. Rel. Models*, vol. 6, pp. 1–135, 2012. DOI: 10.3934/krm.2013.6.1.

[13] A. A. Abrikosov, "The magnetic properties of superconducting alloys," *J. Phys. Chem. Solids*, vol. 2, pp. 199–208, 1957. DOI: 10.1016/0022-3697(57)90083-5.

[14] E. J. Yarmchuk, M. J. V. Gordon, and R. E. Packard, "Observation of Stationary Vortex Arrays in Rotating Superfluid Helium," *Phys. Rev. Lett.*, vol. 43, pp. 214–217, 1979. DOI: 10.1103/PhysRevLett.43.214.

[15] J. R. Abo-Shaeer, C. Raman, J. M. Vogels, and W. Ketterle, "Observation of Vortex Lattices in Bose-Einstein Condensates," *Science*, vol. 292, pp. 476–479, 2001. DOI: 10.1126/science.1060182.

[16] P. Engels, I. Coddington, P. C. Haljan, V. Schweikhard, and E. A. Cornell, "Observation of Long-Lived Vortex Aggregates in Rapidly Rotating Bose-Einstein Condensates," *Phys. Rev. Lett.*, vol. 90, p. 170 405, 2003. DOI: 10.1103/PhysRevLett.90.170405.

[17] Y.-J. Lin, R. L. Compton, K. Jiménez-García, J. V. Porto, and I. B. Spielman, "Synthetic magnetic fields for ultracold neutral atoms," *Nature*, vol. 462, pp. 628–632, 2009. DOI: 10.1038/nature08609.

[18] J. Dalibard, F. Gerbier, G. Juzeliūnas, and P. Öhberg, "Colloquium: Artificial gauge potentials for neutral atoms," *Rev. Mod. Phys.*, vol. 83, pp. 1523–1543, 2011. DOI: 10.1103/RevModPhys.83.1523.

[19] J. Struck *et al.*, "Tunable Gauge Potential for Neutral and Spinless Particles in Driven Optical Lattices," *Phys. Rev. Lett.*, vol. 108, p. 225 304, 2012. DOI: 10.1103/PhysRevLett.108.225304.

[20] A. Celi *et al.*, "Synthetic Gauge Fields in Synthetic Dimensions," *Phys. Rev. Lett.*, vol. 112, p. 043 001, 2014. DOI: 10.1103/PhysRevLett.112.043001.

[21] N. Goldman, G. Juzeliūnas, P. Öhberg, and I. B. Spielman, "Light-induced gauge fields for ultracold atoms," *Rep. Prog. Phys.*, vol. 77, p. 126 401, 2014. DOI: 10.1088/0034-4885/77/12/126401.

[22] V. Galitski, G. Juzeliūnas, and I. B. Spielman, "Artificial gauge fields with ultracold atoms," *Phys. Today*, vol. 72, pp. 38–44, 2019. DOI: 10.1063/PT.3.4111.

[23] T. Ozawa *et al.*, "Topological photonics," *Rev. Mod. Phys.*, vol. 91, p. 015 006, 2019. DOI: 10.1103/RevModPhys.91.015006.

[24] R. M. Price, D. Trypogeorgos, D. L. Campbell, A. Putra, A. Valdés-Curiel, and I. B. Spielman, "Vortex nucleation in a Bose–Einstein condensate: from the inside out," *New J. Phys.*, vol. 18, p. 113 009, 2016. DOI: 10.1088/1367-2630/18/11/113009.

[25] L. J. LeBlanc, K. Jiménez-García, R. A. Williams, M. C. Beeler, W. D. Phillips, and I. B. Spielman, "Gauge matters: observing the vortex-nucleation transition in a Bose condensate," *New Journal of Physics*, vol. 17, p. 065 016, 2015. DOI: 10.1088/1367-2630/17/6/065016.

[26] N. Cooper, "Rapidly rotating atomic gases," *Adv. Phys.*, vol. 57, pp. 539–616, 2008. DOI: 10.1080/00018730802564122.

[27] K. v. Klitzing, G. Dorda, and M. Pepper, "New Method for High-Accuracy Determination of the Fine-Structure Constant Based on Quantized Hall Resistance," *Phys. Rev. Lett.*, vol. 45, pp. 494–497, 1980. DOI: 10.1103/PhysRevLett.45.494.

[28] B. Bernevig and T. Hughes, *Topological Insulators and Topological Superconductors*. Princeton University Press, 2013, ISBN: 9780691151755. DOI: 10.1515/9781400846733.

[29] L. D. LANDAU and E. M. LIFSHITZ, "MOTION IN A MAGNETIC FIELD," *Quantum Mechanics (Third Edition)*. Pergamon, 1977, ch. XV, pp. 453–471, ISBN: 978-0-08-020940-1. DOI: https://doi.org/10.1016/B978-0-08-020940-1.50022-0.

[30] D. Tong, *Lectures on the Quantum Hall Effect*, 2016. DOI: 10.48550/ARXIV.1606.06687.

[31] P. G. Harper, "Single Band Motion of Conduction Electrons in a Uniform Magnetic Field," *Proc. Phys. Soc. London, Sect. A*, vol. 68, pp. 874–878, 1955. DOI: 10.1088/0370-1298/68/10/304.

[32] D. R. Hofstadter, "Energy levels and wave functions of Bloch electrons in rational and irrational magnetic fields," *Phys. Rev. B*, vol. 14, pp. 2239–2249, 1976. DOI: 10.1103/PhysRevB.14.2239.

[33] D. J. Thouless, M. Kohmoto, M. P. Nightingale, and M. den Nijs, "Quantized Hall Conductance in a Two-Dimensional Periodic Potential," *Phys. Rev. Lett.*, vol. 49, pp. 405–408, 1982. DOI: 10.1103/PhysRevLett.49.405.

[34] K. von Klitzing, "Essay: Quantum Hall Effect and the New International System of Units," *Phys. Rev. Lett.*, vol. 122, p. 200 001, 2019. DOI: 10.1103/PhysRevLett.122.200001.

[35] H. L. Stormer, D. C. Tsui, and A. C. Gossard, "The fractional quantum Hall effect," *Rev. Mod. Phys.*, vol. 71, S298–S305, 1999. DOI: 10.1103/RevModPhys.71.S298.

[36] F. D. M. Haldane, "Model for a Quantum Hall Effect without Landau Levels: Condensed-Matter Realization of the "Parity Anomaly"," *Phys. Rev. Lett.*, vol. 61, pp. 2015–2018, 1988. DOI: 10.1103/PhysRevLett.61.2015.

[37] G. Juzeliūnas, J. Ruseckas, P. Öhberg, and M. Fleischhauer, "Light-induced effective magnetic fields for ultracold atoms in planar geometries," *Phys. Rev. A*, vol. 73, p. 025 602, 2006. DOI: 10.1103/PhysRevA.73.025602.

[38] D. Jaksch and P. Zoller, "Creation of effective magnetic fields in optical lattices: the Hofstadter butterfly for cold neutral atoms," *New J. Phys.*, vol. 5, pp. 56–56, 2003. DOI: 10.1088/1367-2630/5/1/356.

[39] M. Aidelsburger, M. Atala, M. Lohse, J. T. Barreiro, B. Paredes, and I. Bloch, "Realization of the Hofstadter Hamiltonian with Ultracold Atoms in Optical Lattices," *Phys. Rev. Lett.*, vol. 111, p. 185 301, 2013. DOI: 10.1103/PhysRevLett.111.185301.

[40] H. Miyake, G. A. Siviloglou, C. J. Kennedy, W. C. Burton, and W. Ketterle, "Realizing the Harper Hamiltonian with Laser-Assisted Tunneling in Optical Lattices," *Phys. Rev. Lett.*, vol. 111, p. 185 302, 2013. DOI: 10.1103/PhysRevLett.111.185302.

[41] G. Jotzu *et al.*, "Experimental realization of the topological Haldane model with ultracold fermions," *Nature*, vol. 515, pp. 237–240, 2014. DOI: 10.1038/nature13915.

[42] A. Kitaev, "Periodic table for topological insulators and superconductors," *AIP Conference Proceedings*, vol. 1134, pp. 22–30, 2009. DOI: 10.1063/1.3149495.

[43] S. Ryu, A. P. Schnyder, A. Furusaki, and A. W. W. Ludwig, "Topological insulators and superconductors: tenfold way and dimensional hierarchy," *New J. Phys.*, vol. 12, p. 065 010, 2010. DOI: 10.1088/1367-2630/12/6/065010.

[44] H. M. Price, O. Zilberberg, T. Ozawa, I. Carusotto, and N. Goldman, "Four-Dimensional Quantum Hall Effect with Ultracold Atoms," *Phys. Rev. Lett.*, vol. 115, p. 195 303, 2015. DOI: 10.1103/PhysRevLett.115.195303.

[45] S.-C. Zhang, "A Four-Dimensional Generalization of the Quantum Hall Effect," *Science*, vol. 294, pp. 823–828, 2001. DOI: 10.1126/science.294.5543.823.

[46] X.-L. Qi, T. L. Hughes, and S.-C. Zhang, "Topological field theory of time-reversal invariant insulators," *Phys. Rev. B*, vol. 78, p. 195 424, 2008. DOI: 10.1103/PhysRevB.78.195424.

[47] D. J. Thouless, "Quantization of particle transport," *Phys. Rev. B*, vol. 27, pp. 6083–6087, 1983. DOI: 10.1103/PhysRevB.27.6083.

[48] M. Verbin, O. Zilberberg, Y. E. Kraus, Y. Lahini, and Y. Silberberg, "Observation of Topological Phase Transitions in Photonic Quasicrystals," *Phys. Rev. Lett.*, vol. 110, p. 076 403, 2013. DOI: 10.1103/PhysRevLett.110.076403.

[49] Y. E. Kraus, Y. Lahini, Z. Ringel, M. Verbin, and O. Zilberberg, "Topological States and Adiabatic Pumping in Quasicrystals," *Phys. Rev. Lett.*, vol. 109, p. 106 402, 2012. DOI: 10.1103/PhysRevLett.109.106402.

[50] Y. E. Kraus and O. Zilberberg, "Topological Equivalence between the Fibonacci Quasicrystal and the Harper Model," *Phys. Rev. Lett.*, vol. 109, p. 116 404, 2012. DOI: 10.1103/PhysRevLett.109.116404.

[51] Y. E. Kraus, Z. Ringel, and O. Zilberberg, "Four-Dimensional Quantum Hall Effect in a Two-Dimensional Quasicrystal," *Phys. Rev. Lett.*, vol. 111, p. 226 401, 2013. DOI: 10.1103/PhysRevLett.111.226401.

[52] M. Verbin, O. Zilberberg, Y. Lahini, Y. E. Kraus, and Y. Silberberg, "Topological pumping over a photonic Fibonacci quasicrystal," *Phys. Rev. B*, vol. 91, p. 064 201, 2015. DOI: 10.1103/PhysRevB.91.064201.

[53] M. Lohse, C. Schweizer, O. Zilberberg, M. Aidelsburger, and I. Bloch, "A Thouless quantum pump with ultracold bosonic atoms in an optical superlattice," *Nat. Phys.*, vol. 12, pp. 350–354, 2016. DOI: 10.1038/nphys3584.

[54] S. Nakajima *et al.*, "Topological Thouless pumping of ultracold fermions," *Nat. Phys.*, vol. 12, pp. 296–300, 2016. DOI: 10.1038/nphys3622.

[55] M. Lohse, C. Schweizer, H. M. Price, O. Zilberberg, and I. Bloch, "Exploring 4D quantum Hall physics with a 2D topological charge pump," *Nature*, vol. 553, pp. 55–58, 2018. DOI: 10.1038/nature25000.

[56] O. Zilberberg *et al.*, "Photonic topological boundary pumping as a probe of 4D quantum Hall physics," *Nature*, vol. 553, pp. 59–62, 2018. DOI: 10.1038/nature25011.

[57] W. Cheng, E. Prodan, and C. Prodan, "Revealing the Boundary Weyl Physics of the Four-Dimensional Hall Effect via Phason Engineering in Metamaterials," *Phys. Rev. Appl.*, vol. 16, p. 044 032, 2021. DOI: 10.1103/PhysRevApplied.16.044032.

[58] ——, "Experimental Demonstration of Dynamic Topological Pumping across Incommensurate Bilayered Acoustic Metamaterials," *Phys. Rev. Lett.*, vol. 125, p. 224 301, 2020. DOI: 10.1103/PhysRevLett.125.224301.

[59] Z.-G. Chen, W. Zhu, Y. Tan, L. Wang, and G. Ma, "Acoustic Realization of a Four-Dimensional Higher-Order Chern Insulator and Boundary-Modes Engineering," *Phys. Rev. X*, vol. 11, p. 011 016, 2021. DOI: 10.1103/PhysRevX.11.011016.

[60] D. I. Tsomokos, S. Ashhab, and F. Nori, "Using superconducting qubit circuits to engineer exotic lattice systems," *Phys. Rev. A*, vol. 82, p. 052 311, 2010. DOI: 10.1103/PhysRevA.82.052311.

[61] D. Jukić and H. Buljan, "Four-dimensional photonic lattices and discrete tesseract solitons," *Phys. Rev. A*, vol. 87, p. 013 814, 2013. DOI: 10.1103/PhysRevA.87.013814.

[62] H. M. Price, "Four-dimensional topological lattices through connectivity," *Phys. Rev. B*, vol. 101, p. 205 141, 2020. DOI: 10.1103/PhysRevB.101.205141.

[63] Y. Wang, H. M. Price, B. Zhang, and Y. D. Chong, "Circuit implementation of a four-dimensional topological insulator," *Nat. Commun.*, vol. 11, p. 2356, 2020. DOI: 10.1038/s41467-020-15940-3.

[64] A. Schreiber *et al.*, "Photons Walking the Line: A Quantum Walk with Adjustable Coin Operations," *Phys. Rev. Lett.*, vol. 104, p. 050 502, 2010. DOI: 10.1103/PhysRevLett.104.050502.

[65] A. Regensburger *et al.*, "Photon Propagation in a Discrete Fiber Network: An Interplay of Coherence and Losses," *Phys. Rev. Lett.*, vol. 107, p. 233 902, 2011. DOI: 10.1103/PhysRevLett.107.233902.

[66] O. Boada, A. Celi, J. I. Latorre, and M. Lewenstein, "Quantum Simulation of an Extra Dimension," *Phys. Rev. Lett.*, vol. 108, pp. 2–7, 2012. DOI: 10.1103/PhysRevLett.108.133001.

[67] B. K. Stuhl, H.-I. Lu, L. M. Aycock, D. Genkina, and I. B. Spielman, "Visualizing edge states with an atomic Bose gas in the quantum Hall regime," *Science*, vol. 349, pp. 1514–1518, 2015. DOI: 10.1126/science.aaa8515.

[68] M. Mancini *et al.*, "Observation of chiral edge states with neutral fermions in synthetic Hall ribbons," *Science*, vol. 349, pp. 1510–1513, 2015. DOI: 10.1126/science.aaa8736.

[69] X.-W. Luo, X. Zhou, C.-F. Li, J.-S. Xu, G.-C. Guo, and Z.-W. Zhou, "Quantum simulation of 2D topological physics in a 1D array of optical cavities," *Nat. Commun.*, vol. 6, p. 7704, 2015. DOI: 10.1038/ncomms8704.

[70] B. Gadway, "Atom-optics approach to studying transport phenomena," *Phys. Rev. A*, vol. 92, p. 043 606, 2015. DOI: 10.1103/PhysRevA.92.043606.

[71] L. Livi *et al.*, "Synthetic Dimensions and Spin-Orbit Coupling with an Optical Clock Transition," *Phys. Rev. Lett.*, vol. 117, p. 220 401, 2016. DOI: 10.1103/PhysRevLett.117.220401.

[72] E. J. Meier, F. A. An, and B. Gadway, "Atom-optics simulator of lattice transport phenomena," *Phys. Rev. A*, vol. 93, p. 051 602, 2016. DOI: 10.1103/PhysRevA.93.051602.

[73] T. Ozawa, H. M. Price, N. Goldman, O. Zilberberg, and I. Carusotto, "Synthetic dimensions in integrated photonics: From optical isolation to four-dimensional quantum Hall physics," *Phys. Rev. A*, vol. 93, p. 043 827, 2016. DOI: 10.1103/PhysRevA.93.043827.

[74] L. Yuan, Y. Shi, and S. Fan, "Photonic gauge potential in a system with a synthetic frequency dimension," *Opt. Lett.*, vol. 41, pp. 741–744, 2016. DOI: 10.1364/OL.41.000741.

[75] S. Kolkowitz *et al.*, "Spin–orbit-coupled fermions in an optical lattice clock," *Nature*, vol. 542, pp. 66–70, 2017. DOI: 10.1038/nature20811.

[76] F. Cardano *et al.*, "Detection of Zak phases and topological invariants in a chiral quantum walk of twisted photons," *Nat. Commun.*, vol. 8, p. 15 516, 2017. DOI: 10.1038/ncomms15516.

[77] T. Ozawa and I. Carusotto, "Synthetic Dimensions with Magnetic Fields and Local Interactions in Photonic Lattices," *Phys. Rev. Lett.*, vol. 118, p. 013 601, 2017. DOI: 10.1103/PhysRevLett.118.013601.

[78] M. Wimmer, H. M. Price, I. Carusotto, and U. Peschel, "Experimental measurement of the Berry curvature from anomalous transport," *Nat. Phys.*, vol. 13, pp. 545–550, 2017. DOI: 10.1038/nphys4050.

[79] I. Martin, G. Refael, and B. Halperin, "Topological Frequency Conversion in Strongly Driven Quantum Systems," *Phys. Rev. X*, vol. 7, p. 041 008, 2017. DOI: 10.1103/PhysRevX.7.041008.

[80] A. Signoles *et al.*, "Coherent Transfer between Low-Angular-Momentum and Circular Rydberg States," *Phys. Rev. Lett.*, vol. 118, p. 253 603, 2017. DOI: 10.1103/PhysRevLett.118.253603.

[81] B. Sundar, B. Gadway, and K. R. A. Hazzard, "Synthetic dimensions in ultracold polar molecules," *Sci. Rep.*, vol. 8, p. 3422, 2018. DOI: 10.1038/s41598-018-21699-x.

[82] B. Wang, T. Chen, and X. Zhang, "Experimental Observation of Topologically Protected Bound States with Vanishing Chern Numbers in a Two-Dimensional Quantum Walk," *Phys. Rev. Lett.*, vol. 121, p. 100 501, 2018. DOI: 10.1103/PhysRevLett.121.100501.

[83] C. Chen *et al.*, "Observation of Topologically Protected Edge States in a Photonic Two-Dimensional Quantum Walk," *Phys. Rev. Lett.*, vol. 121, p. 100 502, 2018. DOI: 10.1103/PhysRevLett.121.100502.

[84] Y. Baum and G. Refael, "Setting Boundaries with Memory: Generation of Topological Boundary States in Floquet-Induced Synthetic Crystals," *Phys. Rev. Lett.*, vol. 120, p. 106 402, 2018. DOI: 10.1103/PhysRevLett.120.106402.

[85] Y. Peng and G. Refael, "Topological energy conversion through the bulk or the boundary of driven systems," *Phys. Rev. B*, vol. 97, p. 134 303, 2018. DOI: 10.1103/PhysRevB.97.134303.

[86] T. Chalopin *et al.*, "Probing chiral edge dynamics and bulk topology of a synthetic Hall system," *Nat. Phys.*, vol. 16, pp. 1017–1021, 2020. DOI: 10.1038/s41567-020-0942-5.

[87] D. Cheng, B. Peng, D.-W. Wang, X. Chen, L. Yuan, and S. Fan, "Arbitrary synthetic dimensions via multiboson dynamics on a one-dimensional lattice," *Phys. Rev. Res.*, vol. 3, p. 033 069, 2021. DOI: 10.1103/PhysRevResearch.3.033069.

[88] S. K. Kanungo *et al.*, "Realizing topological edge states with Rydberg-atom synthetic dimensions," *Nat. Commun.*, vol. 13, p. 972, 2022. DOI: 10.1038/s41467-022-28550-y.

[89] T. Ozawa and H. M. Price, "Topological quantum matter in synthetic dimensions," *Nat. Rev. Phys.*, vol. 1, pp. 349–357, 2019. DOI: 10.1038/s42254-019-0045-3.

[90] I. Dotsenko, "Raman spectroscopy of single atoms," M.S. thesis, Institut für Angewandte Physik der Universität Bonn, 2002. [Online]. Available: http://quantum-technologies.iap.uni-bonn.de/en/diplom-theses.html?task=download&file=89&token=61410be31efd891035e7832a473728af (visited on 03/24/2021).

[91] H. M. Price, T. Ozawa, and N. Goldman, "Synthetic dimensions for cold atoms from shaking a harmonic trap," *Phys. Rev. A*, vol. 95, p. 023 607, 2017. DOI: 10.1103/PhysRevA.95.023607.

[92] E. Lustig *et al.*, "Photonic topological insulator in synthetic dimensions," *Nature*, vol. 567, p. 356, 2019. DOI: 10.1038/s41586-019-0943-7.

[93] M. Hafezi, S. Mittal, J. Fan, A. Migdall, and J. M. Taylor, "Imaging topological edge states in silicon photonics," *Nat. Photonics*, vol. 7, pp. 1001–1005, 2013. DOI: 10.1038/nphoton.2013.274.

[94] J. Koplik and H. Levine, "Vortex reconnection in superfluid helium," *Phys. Rev. Lett.*, vol. 71, pp. 1375–1378, 1993. DOI: 10.1103/PhysRevLett.71.1375.

[95] V. I. Arnold and B. A. Khesin, *Topological Methods in Hydrodynamics*. Berlin, Heidelberg: Springer-Verlag, 1998, ISBN: 038794947x.

[96] H. Salman, "Helicity conservation and twisted Seifert surfaces for superfluid vortices," *Proc. R. Soc. A*, vol. 473, p. 20 160 853, 2017. DOI: 10.1098/rspa.2016.0853.

[97] H. Kedia, D. Kleckner, M. W. Scheeler, and W. T. M. Irvine, "Helicity in superfluids: Existence and the classical limit," *Phys. Rev. Fluids*, vol. 3, p. 104 702, 2018. DOI: 10.1103/PhysRevFluids.3.104702.

[98] B. N. Shashikanth, "Vortex dynamics in R4," *J. Math. Phys.*, vol. 53, p. 013 103, 2012. DOI: 10.1063/1.3673800.

[99] A. Hatcher, *Algebraic Topology*. Cambridge University Press, 2002. [Online]. Available: https://pi.math.cornell.edu/~hatcher/AT/AT+.pdf (visited on 03/24/2021).

[100] S. Serafini *et al.*, "Vortex reconnections and rebounds in trapped atomic Bose-Einstein condensates," *Phys. Rev. X*, vol. 7, pp. 1–12, 2017. DOI: 10.1103/PhysRevX.7.021031.

[101] A. T. Garel, "Boundary conditions for textures and defects," *Journal De Physique*, vol. 39, pp. 225–229, 1978. DOI: 10.1051/jphys:01978003902022500.